L. KOLLÁR and E. DULÁCSKA
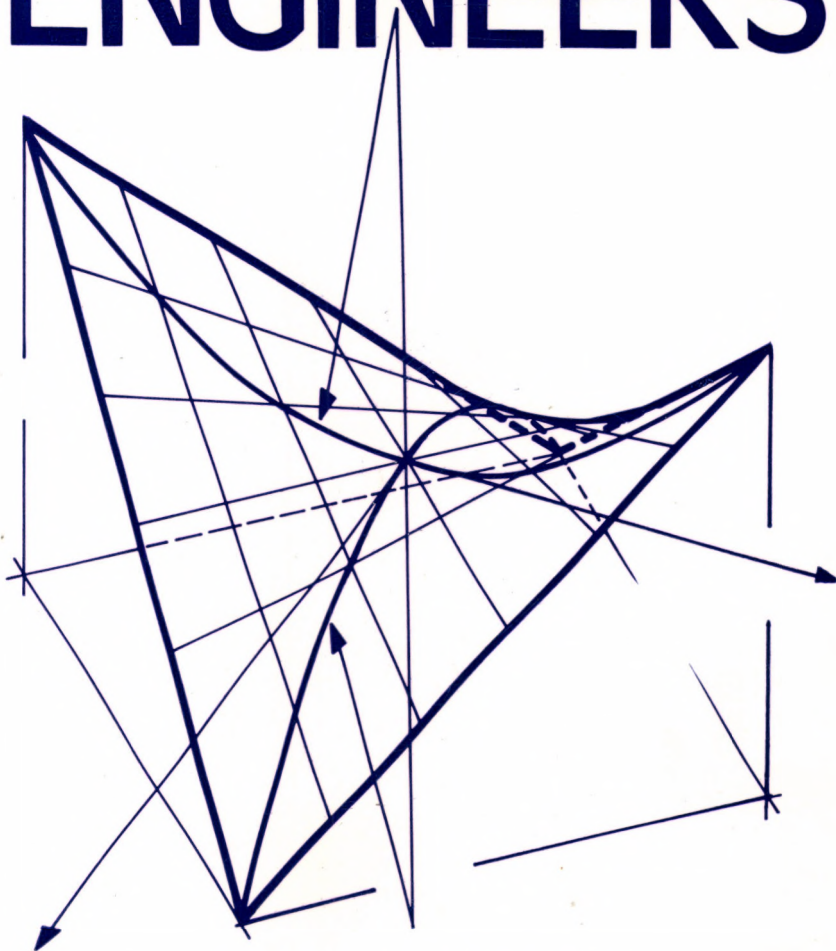
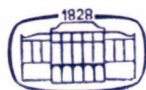# BUCKLING OF SHELLS FOR ENGINEERS

BUCKLING OF SHELLS
FOR ENGINEERS

By L. Kollár and E. Dulácska

This book provides a new approach to the design of shell structures against buckling, without the extensive and complicated mathematical detail usually associated with the treatment of this intricate engineering problem. The results of shell buckling theory are given in the form of diagrams, tables or simple formulae — which can be used directly in practical design. Problems of the application of theoretically derived critical loads to shells made of steel, concrete, etc. and the choice of the safety factors are discussed, providing information for engineers designing roofs, silos, hulls of ships, bodies of vehicles, aeroplanes, rockets and industrial containers.

List of Contents

Buckling of Shells
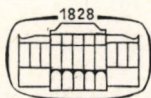## for Engineers

Buckling of Shells
for Engineers

Dr. L. Kollár D. Sc. (techn.)

Budapest City Council's Architectural
and Town Planning Office
Budapest, Hungary

and

Dr. E. Dulácska D. Sc. (techn.)

Institute of Building Types Design
Budapest, Hungary

Contents

Preface

The progress in any branch of science may perhaps be best demonstrated if a body of knowledge that was earlier rather complicated to analyze can now be treated in a much simpler way. This work aims at illustrating this principle in a special field: it endeavours to summarize the problems of shell buckling in an easily understandable manner, in a way that can be put to immediate practical use.

Chapters 1 to 4, 6, Sections 5.1, 5.2, 8.2, 8.3 and 10.1 were written by the first author; Chapters 7, 9, Sections 5.3, 5.4, 8.1, 8.4 and 10.2 by the second. Nevertheless, they assume common responsibility for the whole book. We note that the contents of Chapters 8 and 9 are rather complex, so that we have edited them by considering each Section as a separate unit.

The Hungarian and the German editions (both published in 1973) have been significantly expanded. Sections 4.3, 5.3, 5.4, 9.5, 9.7, 10.1 and 10.2 are new, and the other sections and chapters have been brought up to date.

The authors are indebted to Professor Dr. I. Korányi, who first suggested the work, to all the authors and publishers who have given permission for the reproduction of the figures listed on pp. 277, to the publishers for making the English edition available, and to Mr. G. R. Thompson who revised the translation.

Finally, they would like to pay tribute to Dr. I. Menyhárd, who taught them how scientific thoroughness and practical usefulness can be reconciled. If this has been achieved in this book, it is mainly due to him.

Dr. L. Kollár
Dr. E. Dulácska

1. Introduction

1.1. Setting of Objectives

The structural engineer prefers general methods of calculation by which static and stability analyses of the structure can be made, preferably with a limited amount of computational work. Although for bar structures such static methods are available, stability problems, being described by differential equations subject to boundary conditions, or by eigenvalue problems of matrices have to be solved separately in every case. There are, however, reference books containing a great variety of ready solutions facilitating the design of structures.

The stability problems of shells are, in fact, much more complicated than those of bar structures; hence, general computational methods may be even less expected. Although the literature presents solutions for a great variety of special problems, these are difficult to survey for the designer, if only for lack of time. In addition, the individual papers mostly emphasize the special features of the particular problem dealt with, omitting an overall view of the phenomenon.

The construction of high-speed computers has made it possible to develop programmes by which complicated shell buckling phenomena can be followed very accurately. However, not every design engineer has access to these programmes, moreover, there is very often not enough time and money to perform such comprehensive computations. It is therefore desirable to provide the designers with more simple, easy-to-survey and easy-to-use methods. We have tried to comply with this demand in the present book, utilizing, of course, the results of intricate calculations performed by many authors.

We set ourselves two objects when writing this book. On the one hand, we wanted to give a clear picture of the physical phenomena of shell buckling. On the other, we tried to collect the main results from the rather voluminous literature and present them in a form ready for practical use.

In the survey we neither wanted to process the literature completely, nor to report on the theory in detail, but rather to make known and describe clearly all phenomena and kinds of problems involved. We present the results in the form

of formulas and diagrams in order to facilitate practical application. Ample reference is made to the literature where the detailed analyses of special problems can be found. In many cases approximate methods are given, especially when they are more illuminating and simpler than the exact ones, but we always try to define the limits of their validity.

Because of their complexity, we show the details of analysis of the elastic stability theory only for some characteristic cases, while we only report on the results of the others.

The following works included in the References deal with shell buckling problems in a comprehensive way:

[1.1] gives an overall view of shell-buckling problems;

[1.2] summarizes the theoretical results of the buckling of cylindrical and spherical shells;

[1.3] and [1.3a] report on investigations concerning post-buckling behaviour with special emphasis on shells, based mainly on Koiter's theory;

[1.4] and [1.4a] review several hundred papers concerning shell-buckling;

[1.5] presents a comprehensive collection of the results of various stability problems;

[1.6] gives an excellent introduction to nonlinear instability theory, also displaying the necessary mathematical methods;

[1.7] treats the general principles and theory of elastic stability systematically, with special emphasis on post-buckling behaviour;

[1.8] presents a concise survey on principles and results in the field of plate and shell buckling.

1.2. Survey of Shell-Buckling Phenomena

As in the stability theory of centrally compressed bars, we can look for the critical value of load intensity at which, besides the original, unbuckled state, another "neighbouring" shape, infinitely close to the first one, also becomes possible ("bifurcation"). In this investigation only the first powers of the (infinitely small) displacements, and/or of their derivatives, are taken into account, while their second powers, being smaller by one order of magnitude, are neglected. This will be called *linear theory* in what follows.

The critical load (P_{cr}^{lin}) determined in this way is, however, in many cases much greater than those given by experiments. Hence, we have to consider deflections of finite magnitude, occurring after buckling, resulting in the *nonlinear*

theory, which includes "large deformations". This is characterized by also taking into account the second (or sometimes even higher) powers of displacements, which determine the buckling shape ("geometrical nonlinearity"). According to the basic papers of Koiter [2.24], [2.25], this nonlinear stability theory can be set up in such a way that the buckling shape(s) are expanded into power series of displacements, measured from the unbuckled state, and from this series as many terms are taken as the computing possibilities allow. In the simplest case we consider the squares of the greatest displacement component w, perpendicular to the shell surface, while only the first powers of the other two displacement components, tangential to the shell surface, are taken into account. The latter are much smaller than w, having the same order of magnitude as w^2. By so doing, we can describe the behaviour of the buckled shell up to displacements several times the shell thickness. Investigations show that most structures behave according to one of the diagrams plotted in Figs 1.1 (a)—(e) (see e.g., in [1.6] or [1.7]). In the Figures the load P is plotted against the buckling displacement w. Curves of
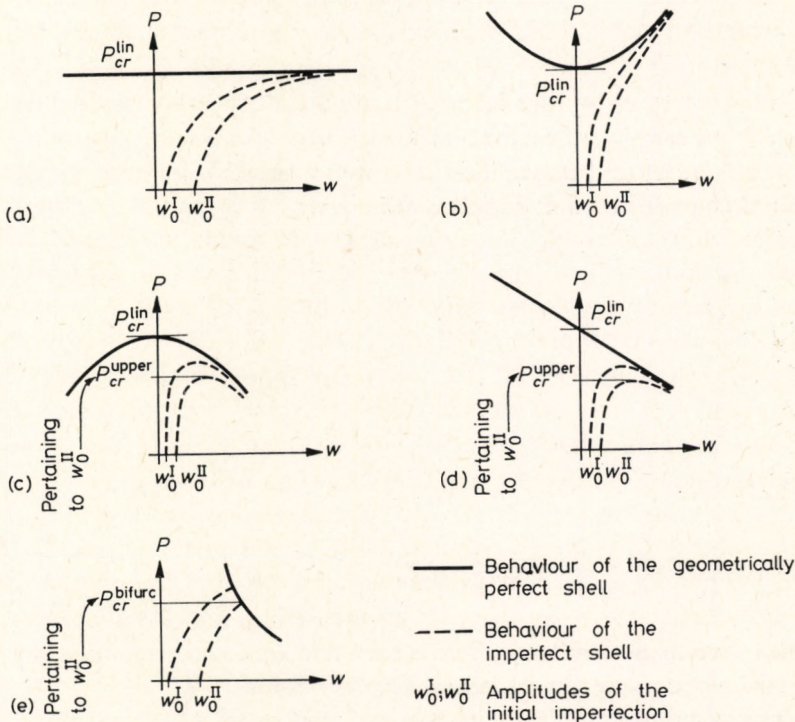
Fig. 1.1. Characteristic cases of post-buckling load bearing behaviour plotted against the buckling deformation

type Fig. 1.1 (a) show that after reaching the critical load, the equilibrium of the centrally compressed structure becomes indifferent, i.e. its *load bearing capacity* remains *constant*. Initial imperfections increase the deformations, but the curves will have no peak points, approaching the horizontal line of the centrally compressed structure asymptotically. Thus, the excentrically compressed structures of this type have no "critical" load. This kind of diagram is obtained rather seldom with shells; however, it describes fairly accurately the behaviour of many bar structures. For shells the other types of diagrams are much more characteristic.

Figure 1.1 (b) shows the *increasing load bearing capacity* in the post-buckling range. In the case of central compression there is a definite critical load at which bifurcation occurs, but with eccentric compression this becomes "blurred": the buckling deformation of the structure gradually increases with the increasing load. Consequently, this type of structure is insensitive to imperfections. Hitherto well-known examples are plates. These behave symmetrically with respect to $+w$ and $-w$ displacements ("symmetric behaviour"). The physical conditions necessary for increasing the load bearing capacity are dealt with in Section 6.1. Other examples are — for certain geometric proportions — ring-compressed and twisted cylindrical shells (Sections 2.3 and 2.6), as well as most shells with negative Gaussian curvature (Chapter 5).

Structures described by Figs 1.1 (c), (d), (e) are characterized by the fact that after reaching a certain critical load intensity their *load bearing capacity decreases*. The shell of Fig. 1.1 (c) behaves identically with respect to $+w$ and $-w$ displacements: it is "symmetric" with respect to the buckling deformation. If disturbances are present, either as geometrical imperfections of shape or as initial bending deformations (indicated as "imperfections" in the Figures), then the maximum load bearing capacity of the structure at which the shell snaps through, P_{cr}^{upper}, lies lower than that of the perfect shell (P_{cr}^{lin}). Thus, this P_{cr}^{upper} becomes the critical load, markedly dependent on the amplitude w_0 of the initial imperfection. Hence, these structures are very sensitive to initial imperfections and can by no means be designed on the basis of P_{cr}^{lin}. The hydrostatically compressed cylinder behaves this way (see Section 2.3).

The structures of Fig. 1.1 (d) behaves "asymmetrically" with respect to $+w$ and $-w$. Practically, however, only the falling (right-hand side) branch of the diagram is important: if the imperfection of the structure has a sign corresponding to this branch, it behaves in a similar way to that of Fig. 1.1 (c), except that the drop in the load bearing capacity is more sudden. The physical explanation of the asymmetric behaviour is that the structure "stiffens" during buckling deformation in one direction, while in the other it "unstiffens". The axially compressed cylindrical panel behaves in this way (see p. 305 in [2.57]) provided that it buckles in both the axial and ring directions in one half wave (Fig. 1.2); if it buckles

outwards, its curvature increases, causing stiffening; if inwards, it unstiffens. The shell-arches discussed in Chapter 6 also behave differently under bending in their planes in opposite directions, but the centrally compressed arch — since its two halves are bent in opposite directions — behaves "symmetrically" with respect to the buckling deformation.
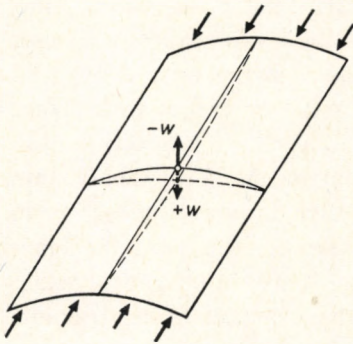
Fig. 1.2. Example of the structure with "asymmetric" post-critical behaviour
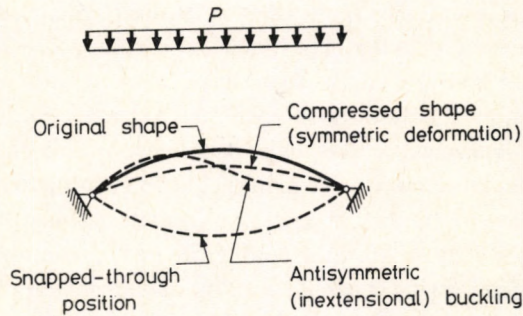
Fig. 1.3. Antisymmetric buckling, bifurcating from the symmetric deflection of the flat arch

Figure 1.1 (e) shows a "composite" kind of behaviour: the shell deforms according to the shape of a certain initial imperfection (e.g., according to one of the dashed lines of Fig. 1.1 (c)) but before reaching the "snapping load intensity" P_{cr}^{upper}, corresponding to the peak of this curve, another buckling shape bifurcates from this deformation, causing failure of the shell. The bifurcation point of this latter buckling shape lies so low only if the shell has previously deformed in another shape. An undeformed shell would exhibit a higher branching point into this latter shape.

This branching of bifurcating phenomenon may also start from the dashed lines of Fig. 1.1 (a), and the bifurcating deformation itself can have — besides a falling (asymmetric) character — a symmetric shape as well, as shown in Figs. 1.1 (b) or 1.1 (c). This kind of behaviour is illustrated by the uniformly loaded flat arch (Fig. 1.3). It is well known [2.51] that such a flat arch may buckle in two ways: after being sufficiently compressed it can snap downwards in a symmetric shape (according to one of the dashed lines of Fig. 1.1 (c)), or it can buckle (by bifurcation) in an antisymmetric shape with inextensional deformation. Now it may happen that the arch is compressed symmetrically due to the load, not to such an

extent that snapping occurs, but sufficiently to allow the increased compressive force to cause antisymmetric buckling. (This bifurcation itself may correspond to Fig. 1.1 (a), (b) or (c), i.e., it is "symmetric" with respect to $+w$ and $-w$). The load intensity causing this type of buckling will obviously be smaller than that causing antisymmetric buckling of the undeformed, i.e. incompressible, arch.

It also follows from what has been said in connection with Fig. 1.1 (e) that for shells – in contrast to bars and plates – it is not always an initial imperfection similar to the buckling shape that is most detrimental, but perhaps some other, quite different from the "bifurcating" shape. As will be shown, the axially compressed cylinder (Section 2.1), for example, may behave in this way.

Finally, we have to mention a more complex kind of behaviour which comes about if several buckling modes are associated with the same (linear) critical load *(multimode or compound buckling)*. Within the frame of the linear theory, these buckling modes are orthogonal to each other, i.e. they do not combine, but due to the nonlinear relations governing post-buckling deformations, no longer infinitely small, they couple (interact), resulting in a sharp drop in post-buckling load bearing capacity, even more detrimental than that exhibited by the structures, represented by Fig. 1.1 (d), with "asymmetric" behaviour. This drop comes about even if the individual buckling modes have a constant or ascending post-buckling character. The axially compressed cylinder and the radially compressed sphere exhibit compound buckling, but the composite shell structures of Chapter 8 may also show this kind of behaviour, if the critical load of the "local" buckling coincides with that of the "overall" buckling.

Compound buckling may also be associated with imperfections or pre-buckling deformations similar to or different from the buckling modes, resulting in a deformation path as shown in Fig. 1.1 (e).

The diagrams of Fig. 1.1 can be plotted — instead of against the buckling displacement w — as a function of the "average" displacement f parallel to the direction of the load. Since f is in the first approximation proportional to w^2 (see e.g. in [2.51]), the shapes of the curves change to some extent and will correspond to Fig. 1.4. Figure 1.4 (a) needs no explanation. The curves of Fig. 1.4 (b) may have different "kinks" (abrupt changes in slope), i.e. they may continue beyond P_{cr}^{lin} with different slopes. Figure 1.4. (c) may correspond to both Figs 1.1 (c) and 1.1 (d), with different initial tangents to the descending section of the curves at P_{cr}^{lin} (cf. Fig. 8.2.3 (a)). We have also drawn the ascending section of this diagram, because it has been computed for several cases. Finally, Fig. 1.4 (d) corresponds to Fig. 1.1 (e).

For the practical design of shell structures with decreasing post-buckling load bearing capacity (Figs 1.1. (c), (d), (e) or Figs. 1.4 (c), (d)) it is expedient to plot the critical force P_{cr}^{upper} referred to P_{cr}^{lin} against the ratio of imperfection-amplitude
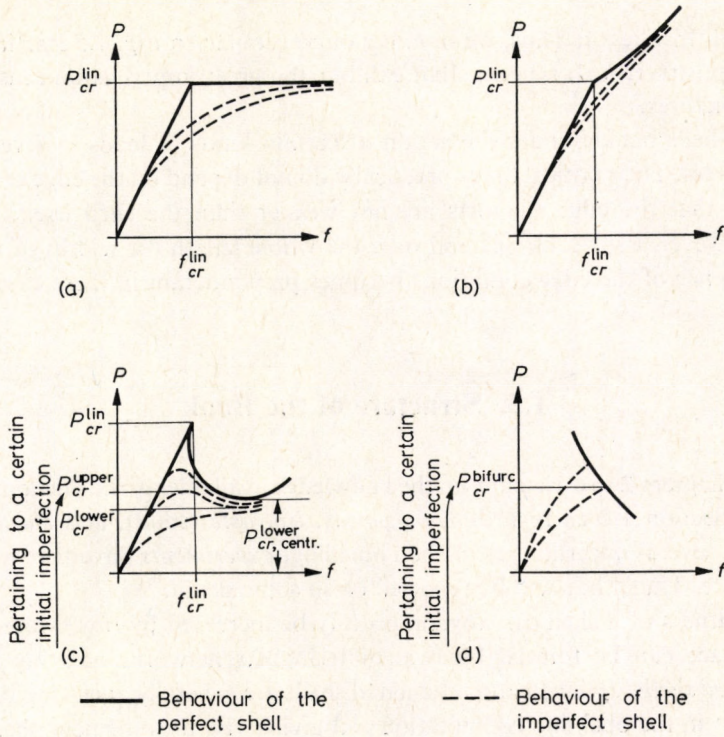
Fig. 1.4. Characteristic cases of post-buckling load bearing behaviour plotted against the displacement in the direction of the load
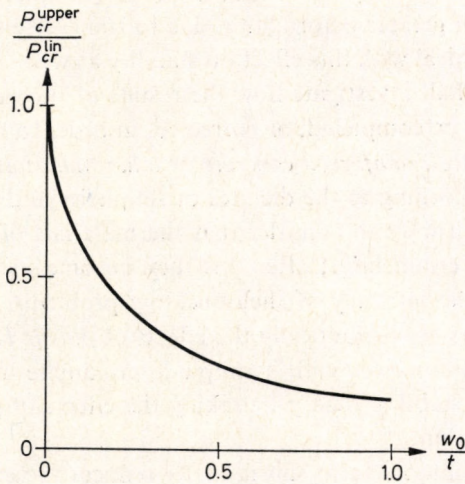
Fig. 1.5. The critical load causing snapping plotted against the initial imperfection amplitude

w_0 to wall-thickness t. Thus, we obtain a curve similar to Fig. 1.5 starting with a very steep (or vertical) tangent, that exhibits the great imperfection sensitivity of these structures.

Some shells buckle under the action of certain kinds of loads in several small local buckles. Their critical loads practically do not depend on the edge conditions, provided that the edge supports are not weaker than the shell itself. In other cases, however, the buckles extend over the whole length (or width) of the shell. The influence of the edge conditions becomes preponderant in these cases.

1.3. Structure of the Book

In Chapters 2 to 6 we sum up the knowledge available on the phenomena outlined in Section 1.2 as regards *homogenous, isotropic* (solid), and *elastic* shells.

Due to several uncertainties in shell buckling, *experiments* have here a primary importance. Thus, they will be reported on in some detail.

The stiffness of a shell can advantageously be increased by *ribs*. Moreover, the shell surface can be formed by bars of triangular network, omitting the skin *(reticulated shells)*. Ribbed and reticulated shells are generally anisotropic, causing difficulties in the buckling computation and giving rise to some new phenomena. Thus, in Chapter 7 we shall report on the most important results of the stability theory of *anisotropic shells*. These allow the treatment of *corrugated* and *sandwich shells*, in addition to ribbed and reticulated ones (Chapter 8). Since sandwich shells exhibit a much greater deformation due to transverse shear than ordinary, solid shells, we shall deal with this effect on stability as well.

In Chapter 9 we shall investigate how the results of the elastic stability theory given hitherto are to be completed, or corrected, in order to make them utilizable for shells made of *steel, reinforced concrete* or *other materials*. These completions will also be made according to the dictates of simplicity and practical usefulness.

First of all, we will have to consider that the materials of shells are elastic at most only up to a certain limit; after this they become plastic ("physical non-linearity"). Due to the intricacy of shell-buckling problems, only a few attempts have been made to assess theoretically the effects of *plastic behaviour*. Hence, we will have to content ourselves with a simple approximate method that corrects the results of elastic stability theory by taking the effects of plastic behaviour of the material into account.

The *creep* of the materials also substantially reduces the critical load intensity of shells. Due to difficulties similar to those connected with plasticity, we take this into account only approximately.

Cracks occurring in concrete diminish the stiffness of reinforced concrete shells considerably, as compared to the uncracked section, so they reduce the critical load intensity as well. We shall show how this unstiffening effect of cracks (together with the stiffening effect of the reinforcement) can be taken into account.

The *experimental determination* of the critical load will also be treated briefly.

Finally, all circumstances (post-buckling behaviour of the shell, etc.) determining a suitable magnitude for the *safety factor* will be examined in turn.

The procedure outlined in Chapters 2 to 9 will be elucidated by means of some *numerical examples*.

2. Buckling of Cylindrical Shells

Here, we present the solutions for the following loading cases:

— axial compression (and the related case of bending);
— compression in the circumferential direction (due to lateral or hydrostatic pressure);
— torsion.

We also deal with the simultaneous action of several loads.

2.1. Axial Compression

According to *experiments* the axially compressed shell buckles in small, local waves. The end supports (edge conditions) generally influence buckling only if the cylinder is short. Basically two kinds of buckles can develop: axisymmetric ("ring") ones or a reticulated ("chessboard") pattern of inward and outward buckles (Fig. 2.1 (a)).

In some experiments buckles of the shape shown in Figs 2.1 (a), (b), (c) developed. This is partly due to the fact that testing machines mostly apply a given strain to the shell that can be met by the latter with buckling of its middle section alone. The other cause may be the stiffening effect of the edges. (In the case of gravity loading only this latter applies [2.41]).

For developing the critical load according to the *linear theory* we present here a simplified analysis based on [2.12], making use of the experimental result that, in the case of a *reticulated* buckling pattern, one buckle extends over a small area only, inside which the shell can be regarded as *shallow*.
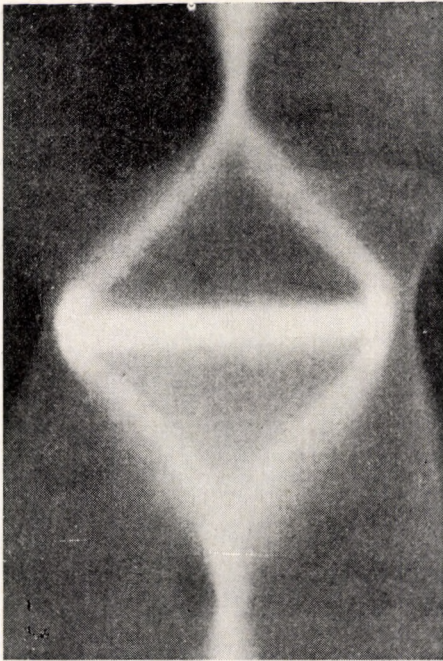
(a)
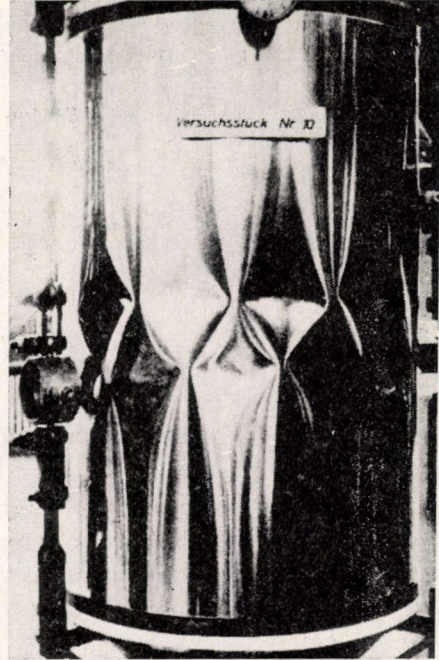
(b)

(c)

Fig. 2.1. Buckling patterns of the axially compressed cylindrical shell

The equilibrium and compatibility equations of shallow shells run in cartesian co-ordinates x, y as follows [2.17], [2.17a], [2.35], [2.56]:

$$B \Delta \Delta w - L_P F = p, \tag{2.1a}$$

$$\Delta \Delta F + T(1 - v^2) L_P w = 0. \tag{2.1b}$$

Here,

$$\Delta = \frac{\partial^2}{\partial x^2} + \frac{\partial^2}{\partial y^2} \tag{2.2a}$$

and

$$L_P = \frac{\partial^2 z}{\partial y^2} \frac{\partial^2}{\partial x^2} - 2 \frac{\partial^2 z}{\partial x \partial y} \frac{\partial^2}{\partial x \partial y} + \frac{\partial^2 z}{\partial x^2} \frac{\partial^2}{\partial y^2} \tag{2.2b}$$

the Laplace and Pucher differential operators, respectively;

$z(x, y)$ — equation of the shell surface;

w — displacement perpendicular to the shell surface (buckling deformation);

F — stress function;

$B = \dfrac{Et^3}{12(1 - v^2)}$ — bending stiffness of the shell;

$T = \dfrac{Et}{1 - v^2}$ — tensile stiffness of the shell;

E — Young's modulus;

t — shell thickness;

v — Poisson's ratio;

p — load perpendicular to the shell surface.

The second derivatives of the stress function give the specific membrane forces:

$$\frac{\partial^2 F}{\partial y^2} = n_x, \tag{2.3a}$$

$$\frac{\partial^2 F}{\partial x^2} = n_y, \tag{2.3b}$$

$$\frac{\partial^2 F}{\partial x \partial y} = - n_{xy}. \tag{2.3c}$$

When setting up Eqs (2.1a, b), from the expressions of the strains only the linear terms of displacements were taken into account. Hence, Eqs (2.1a, b) are linear and the critical load to be obtained from them will be that of the linear theory.

Equations (2.1a, b) are of general validity. Therefore, they may contain the load and internal forces of the pre-buckling state, being in equilibrium, and, furthermore, the infinitesimally small increments of internal forces arising during buckling, together with the also infinitesimally small load increments $\bar{p}$, perpendicular to the shell surface, resulting from the pre-buckling internal forces of finite magnitude multiplied by the changes in curvatures during buckling. In the following we omit from Eqs (2.1a, b) the pre-buckling load and internal forces (being in equilibrium), and retain only those parts of the load and the internal forces that arise during buckling.

We eliminate F from Eqs (2.1a, b). For this purpose the first equation will be multiplied by $\varDelta\varDelta$, the second one by L_P, and they will be added:

$$B\varDelta^4 w + T(1-v^2)L_P^2 w = \varDelta^2 \bar{p}. \tag{2.4}$$

In the case of a cylindrical shell (Fig. 2.2):

$$\frac{\partial^2 z}{\partial x^2} = \frac{\partial^2 z}{\partial x \partial y} = 0$$

and (supposing the positive z axis to be pointing inwards):

$$\frac{\partial^2 z}{\partial y^2} = \frac{1}{R},$$

so that

$$L_P = \frac{1}{R}\frac{\partial^2}{\partial x^2}. \tag{2.5a}$$

In the case of buckling due to axial compression, the load $\bar{p}$, perpendicular to the shell surface, is given by the pre-buckling internal force n_x multiplied by the
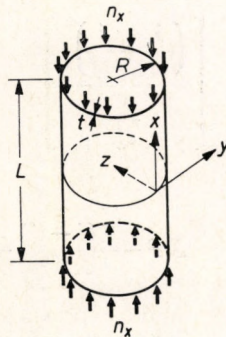
Fig. 2.2. The axially compressed cylinder

change in curvature during buckling:

$$\bar{p} = n_x \frac{\partial^2 w}{\partial x^2}. \qquad (2.5b)$$

Substituting these expressions into Eq. (2.4) results in the following homogeneous differential equation for w:

$$B\Delta^4 w + T(1 - v^2) \frac{1}{R^2} \frac{\partial^4 w}{\partial x^4} = n_x \Delta^2 \frac{\partial^2 w}{\partial x^2}. \qquad (2.6)$$

This equation represents a so-called "eigenvalue-problem": those values of n_x have to be determined which allow a nonzero ("nontrivial") solution for w. Assuming for w a reticulated ("chessboard") buckling pattern:

$$w = w_1 \sin \frac{\pi}{l_x} x \sin \frac{\pi}{l_y} y \qquad (2.7)$$

— where l_x and l_y denote the half buckling wavelengths — and substituting (2.7) into (2.6), we arrive, after simplifying with w, at the following expression for the critical axial force (omitting the negative sign):

$$n_x = B\pi^2 \frac{\left(\frac{1}{l_x^2} + \frac{1}{l_y^2}\right)^2}{\frac{1}{l_x^2}} + \frac{T(1-v^2)}{R^2\pi^2} \frac{\frac{1}{l_x^2}}{\left(\frac{1}{l_x^2} + \frac{1}{l_y^2}\right)^2}. \qquad (2.8)$$

In this, the half buckling lengths in the directions x and y are still unknown. Assuming their ratio provisionally as constant, let us minimize n_x with respect Io the expression

$$\left[\frac{\left(\frac{1}{l_x^2} + \frac{1}{l_y^2}\right)^2}{\frac{1}{l_x^2}} \right]$$

as follows:

$$\frac{\partial n_x}{\partial \left[\dfrac{\left(\frac{1}{l_x^2} + \frac{1}{l_y^2}\right)^2}{\frac{1}{l_x^2}} \right]} = B\pi^2 - \frac{T(1-v^2)}{R^2\pi^2} \frac{\frac{1}{l_x^4}}{\left(\frac{1}{l_x^2} + \frac{1}{l_y^2}\right)^4} = 0. \qquad (2.9)$$

Arranging we obtain:

$$\frac{\left(\frac{1}{l_x^2} + \frac{1}{l_y^2}\right)^2}{\frac{1}{l_x^2}} = \frac{1}{\pi^2}\sqrt{\frac{T(1-v^2)}{BR^2}}. \tag{2.10}$$

Substituting (2.10) into Eq. (2.8) furnishes the minimum value of the critical axial force:

$$n_{x,\,cr}^{\text{lin}} = 2\sqrt{\frac{BT(1-v^2)}{R^2}} = \frac{Et^2}{\sqrt{3(1-v^2)}R}. \tag{2.11}$$

This yields for $v=0.3$ the value:

$$n_{x,\,cr}^{\text{lin}} = 0.606\,\frac{Et^2}{R}, \tag{2.12}$$

i.e. the critical stress:

$$\sigma_{x,\,cr}^{\text{lin}} = \frac{n_{x,\,cr}^{\text{lin}}}{t} = \frac{Et}{\sqrt{3(1-v^2)}R}. \tag{2.13}$$

It can be seen that the ratio of the two half buckling wavelengths has disappeared from the result. Though restriction (2.10) remains valid for the magnitude of the buckle, the critical stress is independent of the shape of the buckle. This can be demonstrated physically — with the aid of the energy method — by considering that, e.g., in the case of a square buckle ($l_x=l_y$), the strain energy of the bending is great, but that of the circumferential tension is small, while for $l_y \to \infty$ (axisymmetric buckle) the strain energy of the circumferential forces predominates with simultaneous decrease of that of the bending.

Since several buckling modes are associated with the same linear critical load, we have to deal with the phenomenon called "compound buckling" (see Section 1.2). The consequences of this phenomenon will be treated later.

The derivation of the linear (also called "classical") critical load shown above is not of general validity. On the one hand, the shallowness of the shell surface was assumed; on the other, the buckling pattern was restricted to that described by Eq. (2.7). Nevertheless, we also obtain the same critical stress if, instead of Eq. (2.7), we assume a reticulated buckling pattern rotated by 45°, even if we assume an axisymmetric buckling shape. In this latter case a definite expression for the buckling length in the axial direction is obtained:

$$l_x = \frac{\pi}{\sqrt[4]{12(1-v^2)}}\sqrt{Rt} \approx 1.72\sqrt{Rt} \tag{2.14}$$

(for $v=0.3$).

It should be noted, however, that only the isotropic shell under pure axial compression exhibits this peculiarity, namely, that its linear critical load is independent of the buckling shape, or, to put it in another way, that several buckling modes are associated with the same linear critical load. Buckling with reticulated and axisymmetric patterns differs already in post-buckling behaviour. Moreover, orthotropy of the shell or circumferential tension (due to internal pressure) acting simultaneously with axial compression causes the linear critical loads pertaining to different buckling patterns to differ from each other (Section 2.5).

The exact derivation of general validity is to be found in [2.6], [2.17], [2.17a], [2.43] or [2.51], giving the same result as Eq. (2.13).

However, the test results yielded only about 15–60% of this linear critical stress. In Figs 2.3 (a), (b), (c) we compiled the buckling stresses of the tests reported on in [2.9], [2.33], [2.53], [2.57]. (The results of Fig. 2.3 (d), which refer to "near-perfect" models fabricated by sophisticated methods, will be discussed later.)

This great discrepancy can be explained in several ways.

It can be shown that even the linear theory may give lower critical stresses if the boundary conditions are modified. Hoff and Soong [2.19] solved the buckling problem of the axially compressed cylinder for several boundary conditions and found that the critical stresses of cylinders with *built-in edges* are equal to or greater than (2.13), while the critical stresses of cylinders with *hinged edges* can be equal to or greater than Eq. (2.13) only if "hinged edges" mean a constraint preventing circumferential displacement v of the edge points. If we stipulate, instead of $v=0$, that the edge shearing forces n_{xy} should be equal to zero, the critical stress drops to half the value given by Eq. (2.13). The critical stress of a cylinder with *free edges* is 0.38 of Eq. (2.13), and in the case of very short cylinders it is even less.

The above results of Hoff and Soong were confirmed by the calculations of Thielemann and Esslinger [2.49]: if for the hinged edge we stipulate $n_{xy}=0$ and $m_x=0$ (no axial bending moment), the linear critical stress decreases to half the value of (2.13).

The linear critical load may also be diminished by *pre-buckling deformations* [2.16], [2.46]. The method of taking these into account is called the "consistent theory", because it applies the same boundary conditions to the pre-buckling deformations as to the buckling itself. This means physically that during the compression prior to buckling the shell expands radially (due to a nonzero Poisson's ratio), and since the supports cannot follow this expansion, the originally straight generatrices of the cylinder become curved. Hence, this theory investigates, in fact, the buckling of a deformed cylinder. Since in this method of calculation the pre-buckling deformations are not regarded as being infinitely small, these diminish the critical stress even if they were orthogonal to the buckling shape (e.g. a cylinder that buckles in a reticulated pattern undergoes axisymmetric
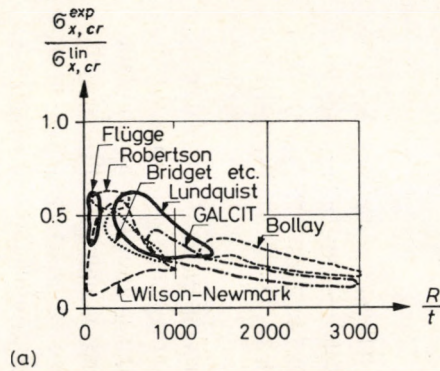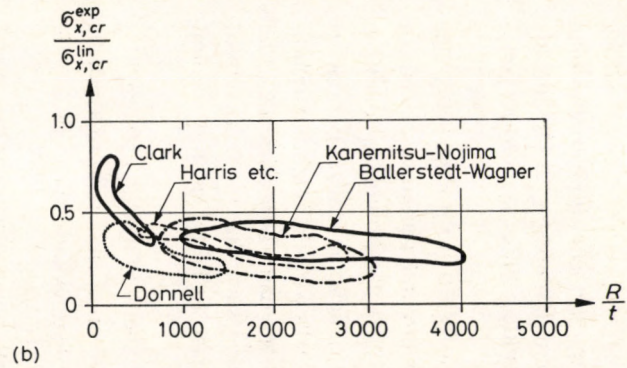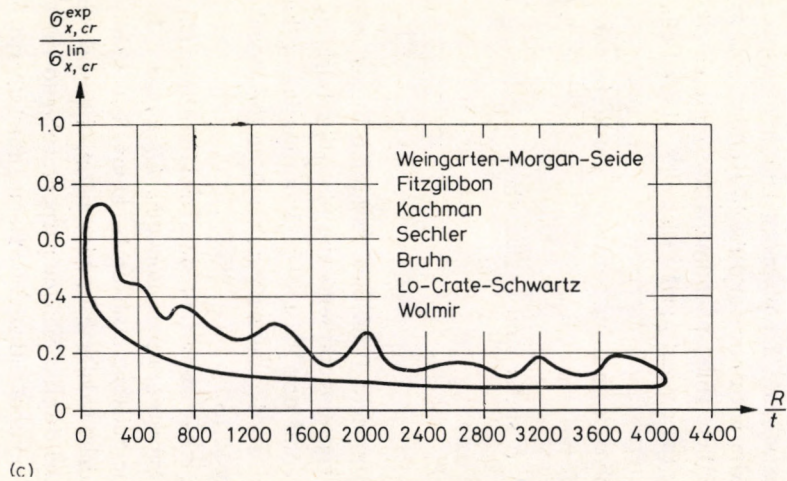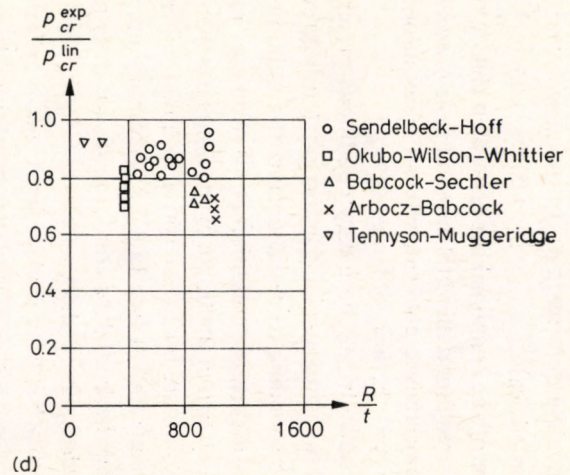
Fig. 2.3. Experimental results on axially compressed cylindrical shells.
(a), (b), (c) – Models manufactured by usual methods, (d) – "near-perfect" models

pre-buckling deformation). In this way $0.93\,\sigma_{x,cr}^{lin}$ was obtained for cylinders with built-in edges.

Almroth [2.2] applied the consistent theory to boundary conditions prescribing $n_{xy}=0$ and found that in the case of *built-in edges* the requirement $n_{xy}=0$ practically does not reduce the value $0.93\sigma_{x,cr}^{lin}$ mentioned above, while for *hinged edges* with $n_{xy}=0$ he also obtained $0.5\sigma_{x,cr}^{lin}$.

Fortunately, the boundary conditions prescribing $n_{xy}=0$ are not realistic. The "classical" hinged-edge support obviously prevents circumferential displacement v, corresponding to realistic support conditions. In fact, the boundary condition $n_{xy}=0$ or even the condition $m_x=0$ would be rather difficult to realize. Besides, as will be shown in the frame of the nonlinear theory, shells with the boundary condition $n_{xy}=0$ are far less sensitive to initial imperfections than those with the usual requirement $v=0$ (see Fig. 2.9). Summing up, we may state that the reduction of $\sigma_{x,cr}^{lin}$ by the boundary condition $n_{xy}=0$ does not have to be taken into account when designing a shell.

All that has been said so far refers to cylindrical shells of medium length.

For the sake of completeness it should be mentioned that *very short* shells buckle as wide flat plates of length L; while *very long* cylindrical shells buckle like bars with circular tube-like cross sections.

All these three phenomena are represented by the diagram of Flügge [2.17], giving the critical axial stress $\sigma_{x,cr}^{lin}$ plotted against the geometric parameter

$$\omega_1 = \frac{\sqrt[4]{12(1-v^2)}}{\pi}\,\frac{L}{\sqrt{Rt}},\tag{2.15a}$$

for short shells, and against the parameter

$$\omega_2 = \frac{1}{\pi\sqrt[4]{12(1-v^2)}}\,\frac{L}{R}\sqrt{\frac{t}{R}}\tag{2.15b}$$

for long shells (Fig. 2.4), assuming hinged edges. The ascending branch of the first diagram represents the plate-like buckling, while the descending section of the second one the bar buckling (assuming hinged bar ends). The middle part of the two diagrams corresponds to the "local shell buckling" dealt with so far, see Eq. (2.13).

The most important step towards the explanation of the test results was the development of the *nonlinear buckling theory*. Its basic equations for geometrically perfect shells were set up by Donnell in 1934 [2.8]. The nonlinear theory differs from the linear one by also taking into account the second power terms of at least the displacement w perpendicular to the shell surface, which appear in the expressions of the strains. Hence, the hitherto linear formulas of the strains, ex-
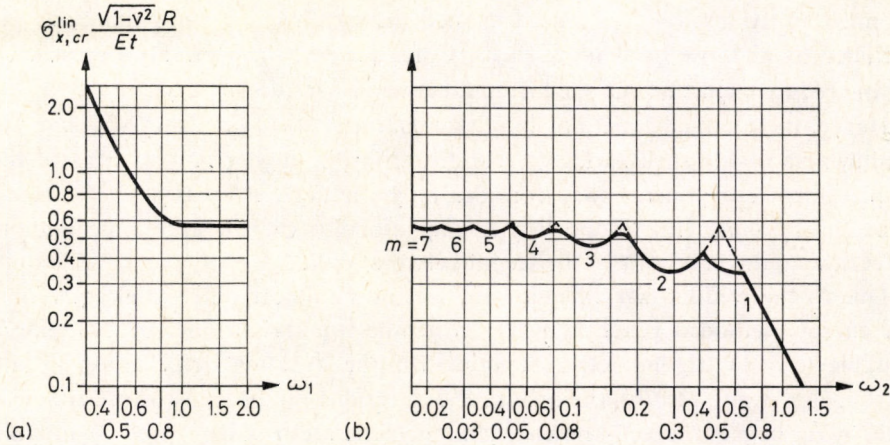
Fig. 2.4. Exact diagram for the axial linear critical stress of the cylinder.
(a) – Short shells, (b) – long shells

pressed by the displacements (see. e.g. p. 286 in [2.6] or p. 201 in [2.17]), become enlarged by the following terms (cf. p. 303 in [2.6] or p. 338 in [2.51]):

$$\varepsilon_x'' = \frac{1}{2}\left(\frac{\partial w}{\partial x}\right)^2, \tag{2.16a}$$

$$\varepsilon_y'' = \frac{1}{2}\left(\frac{\partial w}{\partial y}\right)^2, \tag{2.16b}$$

$$\gamma_{xy}'' = \frac{\partial w}{\partial x}\left(\frac{\partial w}{\partial y}\right). \tag{2.16c}$$

If we develop the equilibrium (2.1a) and the compatibility equations (2.1b) from the expressions completed by these quadratic terms, and if we substitute the curvatures and twist of the deformed surface, instead of those of the undeformed one, into the Pucher operator (2.2b) of the equilibrium equation, then — taking the relations (2.5a, b) into account — we obtain:

$$B\varDelta\varDelta w - \frac{1}{R}\frac{\partial^2 F}{\partial x^2} - \frac{\partial^2 w}{\partial x^2}\frac{\partial^2 F}{\partial y^2} + 2\frac{\partial^2 w}{\partial x \partial y}\frac{\partial^2 F}{\partial x \partial y} - \frac{\partial^2 w}{\partial y^2}\frac{\partial^2 F}{\partial x^2} = n_x\frac{\partial^2 w}{\partial x^2}, \tag{2.17a}$$

$$\varDelta\varDelta F + T(1-v^2)\left[\frac{1}{R}\frac{\partial^2 w}{\partial x^2} + \frac{\partial^2 w}{\partial x^2}\frac{\partial^2 w}{\partial y^2} - \left(\frac{\partial^2 w}{\partial y\partial y}\right)^2\right] = 0. \tag{2.17b}$$

These two equations are identical with those of Donnel, that were developed from the more exact relations, i.e. *not* assuming the shallowness of the shell, but omitting those terms that were small in comparison to the others. Thus, in the

Donnell equations frequently used in shell theory the same approximations are included as in those of shallow shells. Consequently, their validity is restricted by the requirement that the shell should be shallow inside one buckle.

Hence, the Donnell equations have two characteristics: first, they stipulate the shallowness of the shell surface; secondly, from the higher power terms of the displacement components they consider only those given by Eqs (2.16a, b, c). When mentioning the "Donnell-type" equations in the literature, the authors refer now to the first, now to the second, characteristic.

Due to the well-known difficulties of solving nonlinear differential equations, the energy method is generally preferred to the equilibrium one. By assuming a suitable (mostly trigonometric) function for the buckling deformation w and introducing it into (2.17b), the quadratic expressions can be transformed to linear ones by the help of the well-known trigonometric relations. Then F and the internal forces (2.3a, b, c) can be computed. Thus, the expression of the total potential energy of the buckled shell might be written down, which, when minimized, replaces the equilibrium equation. The more terms we take from the series of w, with respect to whose coefficients the potential energy had to be minimized [2.6], [2.51], the more exact results we obtain.

Kármán and Tsien [2.21] investigated the post-buckling behaviour of the geometrically perfect cylinder as described above, assuming a combined buckling shape with two free parameters, in 1941. It turned out that the buckling shape varies steadily during buckling. (This circumstance also necessitates the assumption of
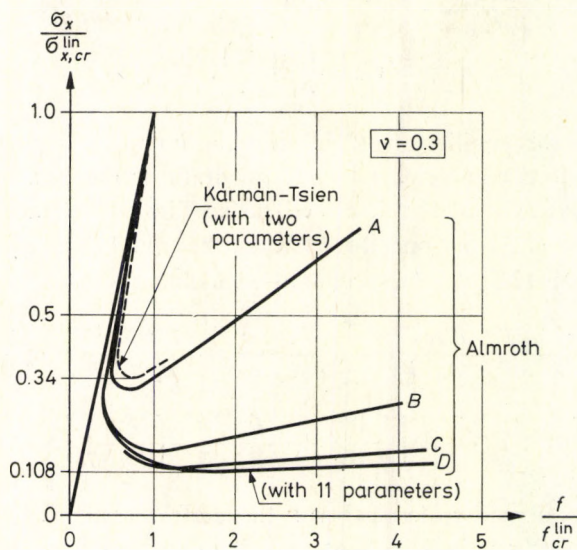
Fig. 2.5. Post-buckling behaviour of the axially compressed perfect cylindrical shell

a combined buckling shape with a possibly large number of free parameters.) They obtained the upper curve of Fig. 2.5, where the ratio of the displacement f of the load in its own direction to the displacement f_{cr} pertaining to the critical load was used as abscissa. The shape of the curve indicates a great sensitivity to initial imperfections. This phenomenon will be discussed later.

Using the Donnell equations, Leggett–Jones [2.29], Michielsen [2.36], Kempner [2.22], and Almroth [2.1] computed with more and more free parameters the curve which describes the post-buckling behaviour of the cylinder. The character of the curve did not change, but its lowest point, i.e. the value of σ_{cr}^{lower}, sank. This reduction, expressed in the percentage of the linear critical load (2.13), varies from 34% as computed by Kármán and Tsien to 10.8%, when the number of the free parameters is increased to 11 (Fig. 2.5, Curves A, B, C, D). According to all these computations, the whole curve, together with the ratio $\sigma_{cr}^{lower}/\sigma_{cr}^{lin}$, is independent of t/R, i.e. of the geometric proportions of the shell.

Hoff, Madsen and Mayers [2.18] took more free parameters (i.e. more terms of the Fourier series of the buckling displacement w) into account than previous investigators. They found that when increasing the number of terms considered to infinity, σ_{cr}^{lower} tends to zero. At the same time, t/R must also tend to zero,
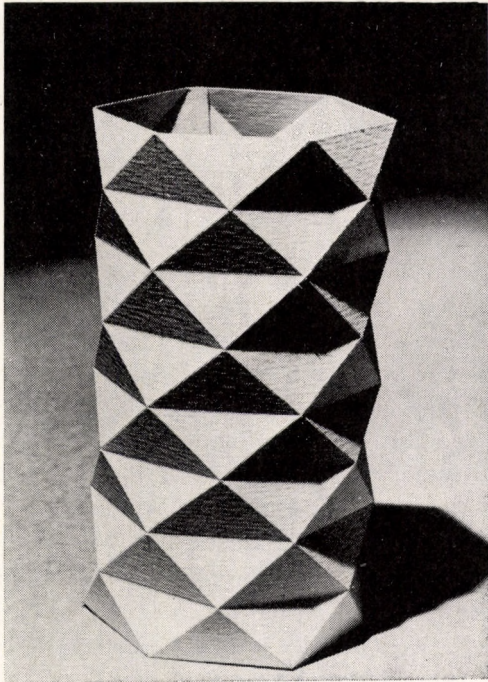
Fig. 2.6. The Yoshimura-pattern

while the buckling shape takes the form of the so-called "Yoshimura-pattern" (Fig. 2.6).

The Yoshimura-pattern clearly demonstrates the propensity of the axially compressed shell to "snapping". The Yoshimura-pattern is, in fact, an inextensional "mapping" of the cylindrical surface: the individual plane triangles came about by straightening the corresponding parts of the cylindrical surface, but infinitely large bending deformations have to develop along the edges [2.18], [2.33]. However, for geometric reasons, the cylindrical surface can reach the Yoshimura-pattern only through *extensional deformation*. This explains the propensity to snapping: the final state represents a smaller resistance than the stage leading to it.

Because of the infinite bending deformations necessary along the edges, the Yoshimura-pattern can develop only if the shell has no bending rigidity, i.e. (bending stiffness being equal to t^3, and tensile stiffness to t) if $t \rightarrow 0$ (or $t/R \rightarrow 0$). In the case of a shell with finite wall thickness ($t/R > 0$) and, consequently, with finite bending stiffness, there will be no sharp "kink", but a curvature with a small but finite radius along the edges. As a result, the triangles will also undergo some bending deformation, all these causing deviation from the Yoshimura-pattern. Accordingly, σ_{cr}^{lower} will also be greater than zero. The experiments show, in fact, that the thinner the shell, the closer the buckling shape to the Yoshimura-pattern.

The Yoshimura-pattern is a limiting case of the "diamond" buckling shape (for $t \rightarrow 0$). The "diamond" pattern can be described in the first approximation by the expression

$$w = w_1 \sin \frac{\pi}{l_x} x \sin \frac{\pi}{l_y} y + w_2 \sin \frac{2\pi}{l_x} x,$$

so that it may be considered as the combination of an axisymmetric and a reticulated (chessboard) shape. It yields the same linear critical load (2.11) as the axisymmetric or reticulated shapes [2.44].

Hoff, Madsen and Mayers explain their result $\sigma_{x,cr}^{lower} \rightarrow 0$ by recalling that the method of Kármán and Tsien requires the minimization of the potential energy with respect to the circumferential wave number (n) too, resulting in $n < 2$, which is, for geometric reasons, obviously impossible. Another cause of $\sigma_{x,cr}^{lower} \rightarrow 0$ might be that the nonlinear computation based on the Donnell equations (2.17) can only describe exactly the buckling deformation of the infinitely thin cylinder. That is, the nonlinear terms appearing in Eqs (2.16a, b, c), comprising second powers of the w-derivatives, describe with sufficient accuracy the strains only up to buckling deformations of limited magnitude. Therefore, they may be sufficient for the initial section of the curve, while they may no longer be sufficient

up to the environment of the lowest point. However, the Yoshimura-pattern of the infinitely thin shell, being inextensional, can correctly be described by the Donnell equations. To describe greater buckling deformations of the shell with finite wall thickness, further terms of higher order should be taken into account. This would tremendously complicate the computational work, which is already intricate enough with the second power Donnell terms, because difficulties arise not only due to the nonlinear character, but also due to the steadily changing buckling shape. On the other hand, the Donnell equations are always accurate enough to determine σ_{cr}^{upper} (Fig. 1.1 (c)) of the imperfect shell, which is necessary for the practical design. In fact, the cylinder undergoes much smaller deformations up to σ_{cr}^{upper} than up to σ_{cr}^{lower}.

The value of σ_{cr}^{lower} related to the geometrically perfect shell has theoretically little significance, because if the cylinder were really perfect, it would buckle at the upper stress value σ_{cr}^{lin} of the linear theory. On the other hand, if initial imperfections are present, it does not buckle at σ_{cr}^{lower} either, but at a stress value σ_{cr}^{upper} depending on the magnitude of the imperfection (Fig. 1.1 (c)).

However, σ_{cr}^{lower} can practically be considered as a lower bound for the value of σ_{cr}^{upper}. That is, the curves of the imperfect shells osculate that of the perfect one, so that if their peak would lie lower than σ_{cr}^{lower}, then, in fact, they have no peak, they rather have a steadily ascending character (Fig. 1.4 (c)), similar to the shells with increasing post-buckling load bearing capacity (Fig. 1.4 (b)).

We still have to deal with the postcritical behaviour of the *axisymmetrically buckled cylindrical shell*. This behaves according to Fig. 1.1 (a) [2.44], i.e. it has an (almost) constant load bearing capacity. That is, the phenomenon is identical with the buckling of bars on elastic foundation, where the bars are formed by the longitudinal fibres, supported elastically by the ring-directed ones [2.51]. This explains why the test cylinders always buckle with reticulated (or diamond) pattern (with decreasing load bearing capacity), and never in axisymmetric form.

Using more exact relations than Eqs (2.16), i.e. taking further nonlinear terms in the expressions for strains (and curvatures) into account, we can, of course, follow the buckling process more closely. By so doing, Mayers and Rehfield [2.34] found that the postcritical behaviour slightly depends on the ratio R/t. Nevertheless, this dependence has hardly any practical relevance.

To make the practical design of cylindrical shells with adequate security against buckling possible, the value σ_{cr}^{upper}, i.e. the actual critical stress pertaining to different amplitudes of initial imperfections, has to be determined.

Taking initial imperfections into account, the deformation curves and the critical stresses of the cylindrical shells were first computed by Donnell and Wan [2.9]. They took five free parameters in the expression of buckling deformation into account and assumed that the initial imperfection has *the same shape* as the current

buckling configuration. Since the latter varies during the buckling process, this assumption of similarity is theoretically wrong, although it could furnish just $\sigma_{cr}^{\text{upper}}$ correctly, if it were true that an imperfection having the same shape as the buckling pattern is the most onerous one.

Donnell and Wan, using the method outlined above for the perfect cylinder, minimizing the potential energy and introducing some approximations, obtained curves similar to the dashed lines of Fig. 1.1 (c). Plotting their peak points against w_0/t as abscissa, we obtain $\sigma_{x,\,cr}^{\text{upper}}$, i.e. the actual critical stress as a function of the amplitude w_0 of the initial imperfection.

Donnell and Wan measured the initial imperfection by an "unevenness factor" U, instead of the ratio w_0/t. Its definition is:

$$w_0/t = U \frac{l_x^{1.5} l_y^{0.5}}{\pi^2 t^2} = U \frac{R^2}{m^{1.5} n^2 t^2}. \tag{2.18}$$

Here l_x and l_y denote the half wavelengths of the initial imperfection,

$$n = \frac{\pi R}{l_y} = \frac{\text{half circumference}}{\text{half wavelength}} = \frac{\text{circumference}}{\text{wavelength}}, \tag{2.19a}$$

$$m = \frac{l_y}{l_x} \quad \text{the ratio of both half wavelengths.} \tag{2.19b}$$

The value of m was assumed by Donnell and Wan, on the basis of experiments, to be 0.75, while for n they obtained a value 10% to 30% smaller than that given by the linear theory (2.10):

$$n = \frac{\sqrt[4]{12(1-\nu^2)}}{m + \dfrac{1}{m}} \sqrt{\frac{R}{t}} \approx 0.87 \sqrt{\frac{R}{t}}. \tag{2.20}$$

Since their n depends not only on R/t but also on U, we substituted, for simplicity, the value (2.20) given by the linear theory for n into (2.18), yielding:

$$\frac{\omega_0}{t} \approx 2U \frac{R}{t}. \tag{2.21}$$

Hence, we "converted" the curve of Donnell and Wan from U to w_0/t in Fig. 2.7 with the aid of the relation (2.21). Since the actual n of Donnell and Wan is smaller than that given by (2.20), the more exact value of w_0/t would be greater than that given by (2.21). Hence, the curve of Fig. 2.7 would lie higher than plotted, but using the approximation described, we are on the safe side and to some extent compensate for the error caused by the small number of free parameters considered.
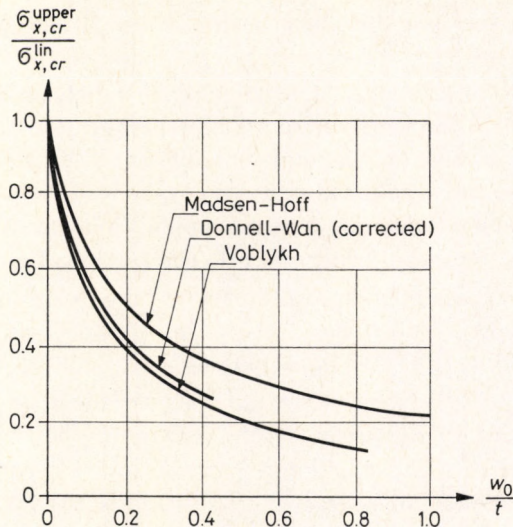
Fig. 2.7. The axial stress causing snapping plotted
against the initial imperfection amplitude

Voblykh [2.52] computed the critical stress in a similar way to Donnell and Wan, assuming a different (axisymmetric) initial imperfection, and with a different number of free parameters. His results lie quite close to those of Donnell and Wan (Fig. 2.7).

Madsen and Hoff [2.33] did not assume that the initial imperfection always has a shape similar to the buckling pattern. After comprehensive computations, taking more free parameters into account, they obtained the upper curve of Fig. 2.7, which somewhat deviates from that of Donnell and Wan.

Each of these calculations gave a unique curve, which is independent of the geometric proportions (R/t) of the cylinder. The tendency of the test results shown in Figs 2.3 (a), (b), (c), according to which the actual buckling stress decreases with increasing R/t, can be accounted for by assuming that the initial imperfection amplitude w_0 is proportional to the radius R of the cylinder and is independent of the wall thickness t (see also [2.41]). In other words, this means that on a more slender shell (with great R/t ratio) we may expect greater initial imperfections in comparison to the wall thickness, as with the common compressed bars, where an initial imperfection in some way proportional to the slenderness ratio is also assumed.

The methods of calculation outlined in the foregoing all have in common that they assume in advance — with a certain number of free parameters — the shape of the initial imperfection and make it probable only with comparative

3*

computations that the assumed imperfection shape indeed yields the lowest σ_{cr}^{upper} value for a given w_0/t.

The general theory of Koiter [2.24], [2.25] outlined in Section 1.2 makes possible the investigation of the influence of the initial imperfections and buckling modes of any shape and the choice of the most onerous one(s) of them, assuming only that the deformations are small in comparison to the wall thickness. For the sake of a shorter treatment we describe here a simplified version of Koiter's method applied to shell buckling, see [2.20] or [4.14]. The computation starts again from Donnell's equations containing among the higher power displacement terms only the second powers of w (and w derivatives). The method essentially agrees with that described after Eqs (2.17a, b) up to the minimization of the potential energy. Then, from the equation system of the third degree, obtained by differentiating the fourth degree energy expression, terms containing the third powers of w/t will be omitted. The resulting equations of second degree become simple enough to make possible the direct investigation of the effect of the various initial imperfections (axisymmetric, asymmetric, i.e. reticulated, and combined) and that of various buckling modes and their combinations. The buckling modes are eigenfunctions of the linear buckling theory, meeting requirement (2.10) for the buckling wavelength ratio. Although they are orthogonal in the frame of the linear theory, they interact due to the nonlinear expressions and appear as combinations.

The general theory of Koiter yielded several important results. It became manifest that with shells it is not always the imperfection shape similar to the buckling mode that proves to be the most onerous. That is, in most cases, to a given w_0/t
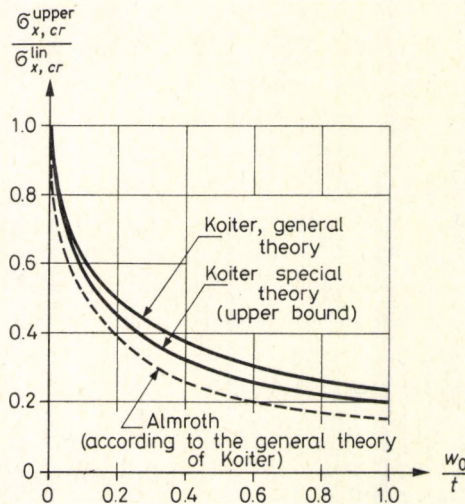
Fig. 2.8. The axial stress causing snapping plotted against the initial imperfection amplitude

the lowest $\sigma_{cr}^{\text{upper}}$ will be obtained in a similar manner to that shown in Fig. 1.1 (e): the shell begins to deform according to an initial imperfection having the shape of one of the eigenfunctions, but before reaching $\sigma_{cr}^{\text{upper}}$ pertaining to the peak point of the load-deflection curve, another (possibly compound) buckling mode bifurcates therefrom. This bifurcation point gives the lowest $\sigma_{cr}^{\text{upper}}$ value.

The general theory of Koiter is — due to the neglecting of higher powers of w/t — the less exact, the greater the buckling deformations are. However, it gives the initial tangent of the curve characterizing the post-buckling behaviour of the perfect shell exactly, since it belongs to $w=0$. It furnishes good results for small w_0/t values, because in this case buckling deformations remain small when reaching $\sigma_{cr}^{\text{upper}}$. To throw light on the accuracy of his method Koiter developed his "special theory" [2.26]. Its main point is that for certain special initial imperfections exact solutions can be found without neglecting the higher terms, contrary to the general theory. Thus, an upper bound for the exact solution can be established. In Fig. 2.8, we show the results of the general and the special theories of Koiter for the axially compressed cylinder. The special theory refers to the axisymmetric initial imperfection from which, according to Fig. 1.1 (e), the asymmetric buckling bifurcates. (For this latter he assumed $v=0.272$.)

It is worthwhile to note that at first sight the axisymmetric imperfection (together with the pertaining axisymmetric deformation) seems to be "harmless", with — as said before — an approximately constant post-buckling load bearing capacity (Fig. 1.1 (a)). Nevertheless, it furnishes — to our present state of knowledge — the lowest critical load, according to our remark referring to Fig. 1.1 (e): the shell "jumps over" into another buckling mode.

Almroth [2.2], using the general theory of Koiter and assuming an axisymmetric imperfection, determined the $\sigma_{cr}^{\text{upper}}$-curve more exactly, and he obtained somewhat lower values (Fig. 2.8).

Figures 2.7 and 2.8 show that for the axially compressed cylinder different computations, assuming various shapes for the initial imperfection (axisymmetric, reticulated, or combined), furnished curves rather close to each other. Accordingly, from the practical point of view, this problem can be considered as solved. The amplitude of the initial imperfection should be assumed according to the erection accuracy to be expected (see Section 9.2). The value of $\sigma_{x,cr}^{\text{upper}}$ determined in this way may be checked by Figs 2.3 (a), (b), (c).

The predominant role of imperfections is also verified by Fig. 2.3 (d), which shows some experimental results performed on "nearly perfect" cylindrical shells in recent years [2.45a]. These models were fabricated by special methods (electroforming, etc.) in order to avoid imperfections and residual stresses. The testing apparatus was also specially designed. The figure shows that, in fact, buckling stresses very close to the linear classical value of $\sigma_{x,cr}^{\text{lin}}$ could be achieved.

Very short or *very long* shells are less prone to snapping, because — as has been said before — in these cases the phenomenon turns into plate or bar buckling showing no snapping but gradually increasing deformations due to eccentric compression. However, it can happen that an eccentrically loaded long cylinder begins to deform as a bar, and on the compressed side the compressive stress increased by bending causes local buckling of the shell (see Section 2.2). This branching and snapping is also described by Fig. 1.1 (e).

Narasimhan and Hoff [2.37] investigated the post-buckling behaviour of a cylinder with hinged edges assuming boundary condition $n_{xy}=0$ and taking initial imperfections into account. Starting from an imperfection shape similar to that of the buckling mode of the linear theory pertaining to these boundary conditions, they obtained the two curves of Fig. 2.9 for two different
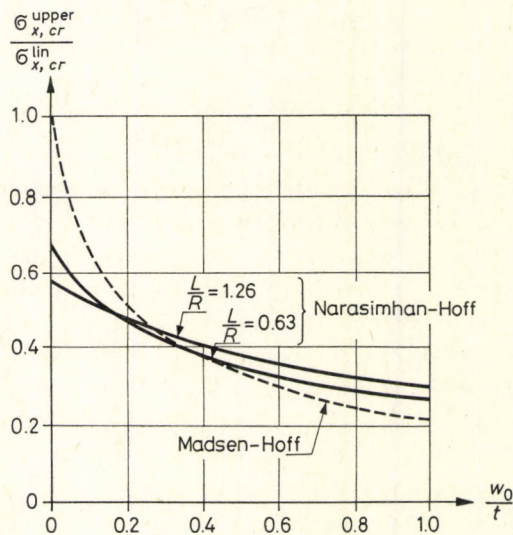
Fig. 2.9. Decrease of the snapping stress of cylinders with
initial imperfection in the cases of
"normal" and of $n_{xy}=0$ boundary conditions

L/R ratios. For comparison, we also plotted the curve of Madsen–Hoff pertaining to shells with "classical" boundary conditions ($v=0$ instead of $n_{xy}=0$) valid for the local buckling of infinitely long shells. It can be seen that the curves of shells with boundary condition $n_{xy}=0$, starting from a lower critical stress value, intersect the curve of the shell with classical boundary conditions, starting from a higher σ_{cr}^{upper}. This also confirms the earlier statement that the reduction of $\sigma_{x,cr}^{lin}$ due to boundary condition $n_{xy}=0$ has no practical significance.

The *buckling wavelength* and the buckling shape has not been clarified to as great an extent as the critical stress. The test results showed that the ratio $m = l_y/l_x$ of the half wavelengths in circumferential and axial directions lies between 0.7 and 1.0, but substantially less circumferential waves develop than predicted by the linear theory (Eq. (2.20)). Thus, empirical formulas were set up. On the basis of 550 experiments made on 47 Mylar cylinders, de Neufville and Connor [2.39] established the following formula for the circumferential full wave number:

$$n \approx 2.7 \sqrt[4]{\frac{R}{t}} \sqrt{\frac{R}{L}} \tag{2.22}$$

containing also the length L of the cylinder, while R/t appears under the fourth root sign. In the experiments R/t varied between 800 and 1600, while R/L was equal to 1, 1/2 or 1/3. Hence, the formula can be considered as reliable only in this range.

For cylinders with $R/t = 540 \sim 760$ and $R/L = 0.1 \sim 2$, Hoff [1.2] found the following relation appropriate:

$$n \approx 0.286 \sqrt{\frac{R}{t} \left(\frac{R}{L}\right)^{0.36}}. \tag{2.23}$$

Both empirical formulas emphasize the fact that the circumferential wave number increases with decreasing cylinder length. This was also shown theoretically when investigating cylinders of finite length [2.14]. Thus, the wave number formulas not containing the length are only valid for "infinitely long" cylinders. (According to the same investigations, the critical stress is practically independent of the length of the cylinder.)

A most important finding on the circumferential wave number is that it varies during the buckling process. This was already shown by computations made on perfect cylinders. On the basis of [2.6], in Fig. 2.10 the post-critical behaviour of a cylinder with $R/t = 1000$ is shown versus w/t, assuming $l_x = l_y$ (square buckles) and $v = 0.3$. It can be seen that the curve describing the behaviour of the shell is practically the lower envelope of the stress-strain curves pertaining to different circumferential wave numbers, and that this wave number n steadily decreases during buckling.

High-speed motion pictures of the buckling process [2.15], [2.48] have shown that, when the cylinder starts buckling near the linear critical stress ("near-perfect" cylinders), first a wave number corresponding to the linear theory develops, which then "jumps over" into shapes having longer and longer wavelengths, while the compressive stress gradually decreases (see Fig. 2.5). Imperfect shells start with greater wavelengths than those of the linear theory, and they exhibit a similar change in buckling pattern during the buckling
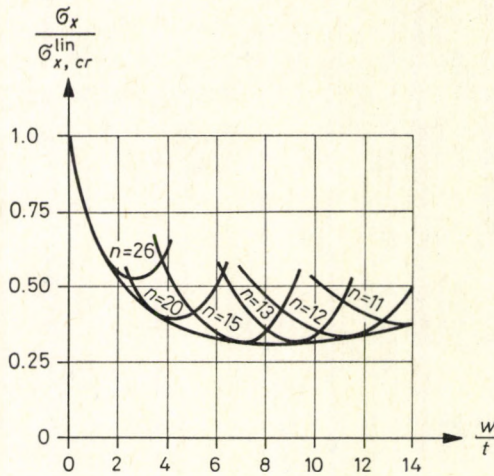
Fig. 2.10. Decrease of the circumferential wave
number during the buckling process

process. When completing the test, the final buckling pattern with greater
wavelengths (pertaining to a comparatively small compressive stress) rather
than the initial one can be observed.

These results were also substantiated by the experiments of Yamaki, Otomo,
and Matsuda [2.58], who followed the post-buckling behaviour by lowering
or returning the loading head of polyester cylinders, and so were able to ob-
serve the changes in the buckling pattern and the varying load taken by the
models.

Therefore, it seems reasonable to relate the circumferential wave number to
the actual compressive stress σ_x. Pflüger [2.41] proposed, on the basis of approxi-
mate calculations, a factor varying with the ratio $\sigma_x/\sigma_{x,cr}^{lin}$ instead of the constant
value of 0.87 in Eq. (2.20). Approximating the curves given by Pflüger for this
factor by a straight line, we obtain the relation

$$n \approx 0.93 \frac{\sigma_x}{\sigma_{x,cr}^{lin}} \sqrt[4]{1-v^2} \sqrt{\frac{R}{t}}. \tag{2.24}$$

2.2. Cylinders in Bending

Two equal couples of opposite sign applied to the ends of the cylinder cause
normal stresses in the cylinder wall, which vary linearly along the diameter
lying in the plane of the couples. Detailed investigations according to the
linear theory [2.45] showed that the critical maximum bending stress is hardly

greater than the critical value of the uniform compressive stress, so this latter can be taken instead. The explanation of this phenomenon is that the cylinder buckles in small, local waves, and so the smaller stresses of other, remote parts hardly relieve the environment of the maximum stress.

2.3. Circumferential Compression

A load acting perpendicularly to the surface of the cylinder (lateral pressure, Fig. 2.11 (a)) causes circumferential (hoop) stress σ_φ in the wall of the shell.
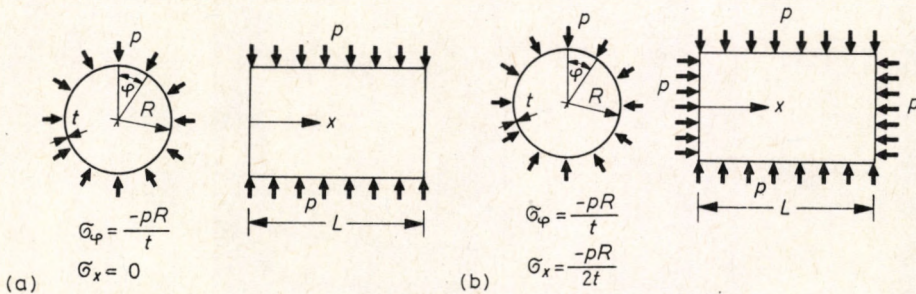
Fig. 2.11. Cylindrical shells under lateral and hydrostatic pressure.
(a) – Lateral pressure only (circumferential compression), (b) – pressure also acting on the end diaphragms (hydrostatic pressure)

Experiments show that when reaching the critical value of the load, the shell buckles in only one half wave in the longitudinal, but in several waves in the circumferential direction (Fig. 2.12). Hence, contrary to the case of axial compression, boundary conditions have here a considerable influence on the critical load: the shell obviously buckles at a smaller critical load when the two supporting *edge rings* are far apart, i.e. the shell is long, than if they are nearer.

In the following — if not stated to the contrary — we always refer to *complete* cylinders connected to the end diaphragms by *hinged edges*.

Assuming that the lateral pressure remains perpendicular to the buckled surface (fluid or air pressure), the linear theory [2.17], [2.17a], [2.43], [2.51] yielded a rather intricate formula for the critical hoop stress $\sigma_{\varphi,cr}$. Using some approximations Flügge [2.17] simplified the result and plotted $\sigma_{\varphi,cr}$ against the parameters ω_1 (Eq. (2.15a)) and ω_2 (Eq. (2.15b)) for short and long shells respectively (Fig. 2.13). The curves have a falling character with increasing shell length L, due to the fact that the stiffening effect owing to bending of the generatrices (and to the associated membrane forces) decreases with increasing cylinder
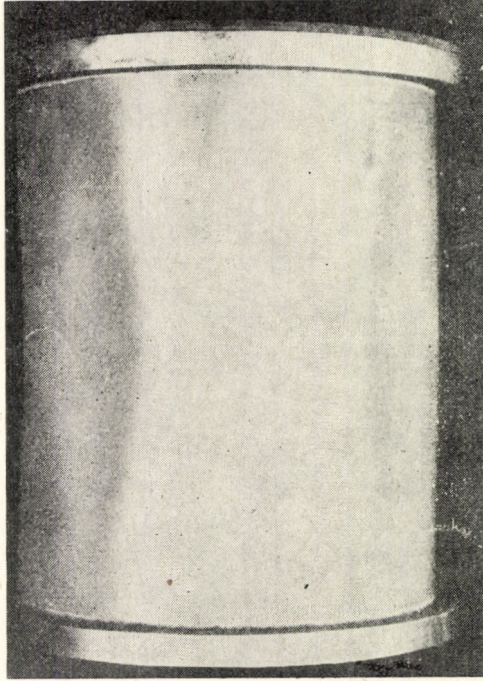
Fig. 2.12. Buckling of a cylindrical shell under hydrostatic pressure

(a)

(b)
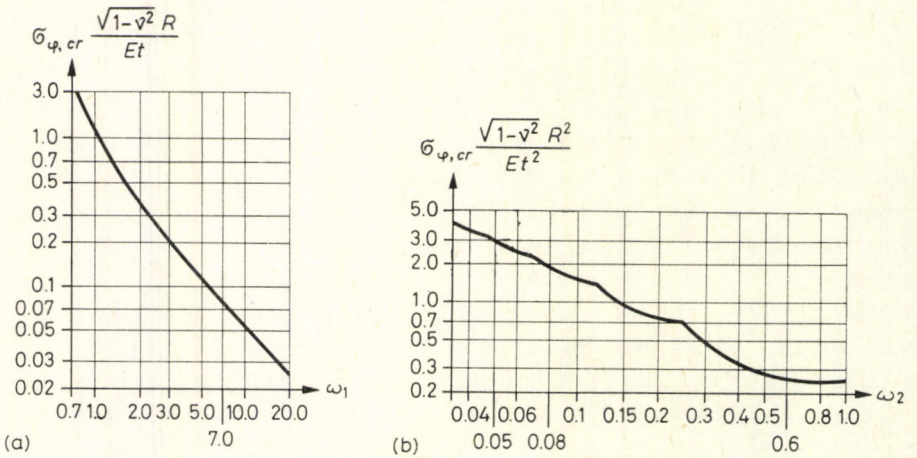
Fig. 2.13. Exact diagram for the linear critical circumferential stress of the cylinder under lateral pressure.
(a) – Short shells, (b) – long shells

length, while the critical hoop stress asymptotically approaches that of a circular ring. On the other hand, very short shells buckle as flat plates.

Lundgren [2.32] approximated the above results by the following formulas, assuming $v=0.2$ (Fig. 2.11 (a)):

for

$$L > 2.3 \sqrt{Rt},$$

$$\sigma_{\varphi, cr} = E \frac{0.89 \frac{t}{L} \sqrt{\frac{t}{R}}}{1 - 1.18 \frac{\sqrt{Rt}}{L}}, \qquad (2.25a)$$

and for

$$L < 2.3 \sqrt{Rt},$$

$$\sigma_{\varphi, cr} = E \left[3.4 \left(\frac{t}{L} \right)^2 + 0.025 \left(\frac{L}{R} \right)^2 \right]. \qquad (2.25b)$$

Batdorf [2.3] took $v=0.3$ and approximated the exact result of the linear theory by a diagram plotted against the geometric parameter $Z=(L^2/Rt)\sqrt{1-v^2}$ (upper curve in Fig. 2.14), which is consistent with Lundgren's results.

The linear theory yields a rather intricate expression for the circumferential
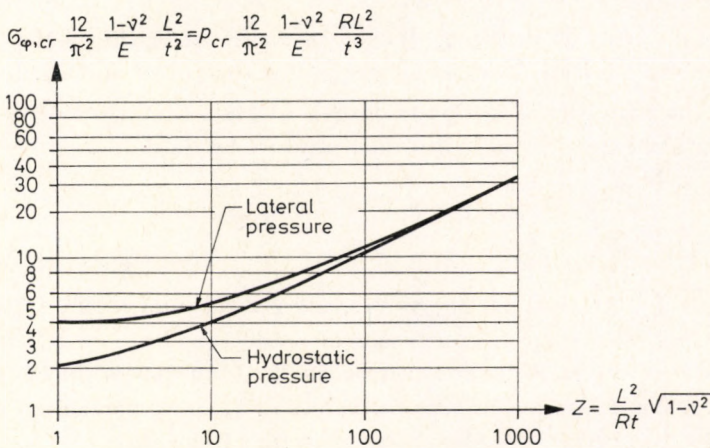
Fig. 2.14. Approximate linear critical stresses of the cylindrical shell subjected to lateral and to hydrostatic pressure

full wave number (2.19a), which can be approximated according to [2.32] as follows (with $v=0.2$):
for

$$L > 2.3 \sqrt{Rt},$$

$$n = \pi \frac{R}{L} \sqrt{0.85 \frac{L}{\sqrt{Rt}} - 1},$$ (2.26a)

and for

$$L < 2.3 \sqrt{Rt},$$

$$n = \pi \frac{R}{L}.$$ (2.26b)

We still have to deal with the buckling of shells subjected to external pressure also on their end diaphragms (hydrostatic pressure, Fig. 2.11 (b)), because several models were loaded in this way. In this case, an axial stress equal to half the hoop stress arises:

$$\sigma_x^{\text{hydrostat}} = \frac{\sigma_\varphi^{\text{hydrostat}}}{2} = -\frac{pR}{2t}.$$ (2.27)

The axial stress evidently diminishes the critical value of the pressure p. The shorter the shell, the greater this reduction is. That is, the influence of the axial compressive stress on the buckling is the greater the closer it comes to the critical axial stress $\sigma_{x,cr}$. On the other hand, $\sigma_{x,cr}$ does not depend on the length of the cylinder but the critical hoop stress $\sigma_{\varphi,cr}$ does. Consequently, the shorter the cylinder (i.e., the smaller the geometric parameter $L/\sqrt{Rt}$), the greater σ_φ can be and at the same time also the influence of σ_x, since $\sigma_x = \sigma_\varphi/2$. The lower curve of Fig. 2.14 shows the results of Batdorf [2.3], approximating to those of the exact linear theory. It can be seen that at $L/\sqrt{Rt} = 4$ the difference between the two critical load intensities is less than 20%. Indeed, for greater values of the parameter $L/\sqrt{Rt}$, Lundgren's formula (2.25a) changes into the approximate one derived for hydrostatic pressure by Batdorf [2.3]:

$$\sigma_{\varphi,cr} \frac{t}{R} = p_{cr}^{\text{hydrostat}} = \frac{0.92 E t^{5/2}}{L R^{3/2}},$$ (2.28)

valid for $v = 0.3$ [2.54], [3.5].

For great $L/\sqrt{Rt}$ or small R/t values, the critical load of the circular ring (2.29a) sets a lower bound for the results of Batdorf (and of Lundgren). That is, the critical load of the shell can never be smaller than that of the circular ring. This circumstance also means that for values of $L/\sqrt{Rt}$ greater than indicated in Fig. 2.14 the cirtical load also depends on the ratio R/t.

As far as the model tests are concerned, there were some series which buckled very close the critical load of the linear theory. Such were the models of Sturm

[2.47], Litle [2.30], Weingarten and Seide [2.54], Windenburg and Trilling [2.55], and Lundgren [2.32]. (Some models of the last author buckled in the plastic range. Accordingly, agreement could be achieved by taking plasticity into account.)

However, other model tests (e.g., the three series of the David Taylor Model Basin, USA (see in [2.10] and [2.11]) show smaller critical loads than the linear one. Soviet tests yielded similar results [2.57]. These models mostly buckled at between 60% and 100% of the linear critical load. All these results indicate that cylindrical shells subjected to circumferential compression are far less sensitive to initial imperfections than those subjected to axial compression.

Among the models mentioned above, those of Weingarten and Seide [2.54] and of the David Taylor Model Basin (see in [2.10] and [2.11]) were subjected to hydrostatic pressure. However, except for one or two cylinders, the geometric parameter $L/\sqrt{Rt}$ was always greater than 4 (maximum 60). The models of Sturm [2.47] were loaded partly by hydrostatic, partly by lateral, pressure, but since the minimum value of $L/\sqrt{Rt}$ was 14, the kind of loading was irrelevant.

Lundgren [2.32] loaded his reinforced concrete barrel vaults by weights. This kind of loading differs from the fluid (or air) pressure in that it maintains its original direction, while the pressure loading remains perpendicular to the (buckled) surface. This difference causes a deviation in the magnitude of the critical load too, which increases in proportion as the circumferential wave number n decreases (i.e., as the shell becomes less shallow inside one buckling half wave). For the limiting cases of a closed ring, corresponding to the infinitely long cylindrical shell, the circumferential wave number is $n=2$. Denoting by EI the flexural rigidity of the ring in its own plane, its critical pressures are for *fluid pressure* [2.51]:

$$p_{cr} = 3.0 \frac{EI}{R^3}, \tag{2.29a}$$

while for *constant directional load* the magnitude of the critical pressure depends on the way the ring is supported against rotation in its own plane, as is explained very clearly in [2.45c]. If two opposite points of the ring are connected to fixed hinges, we obtain the result valid for a semi-circular arch [2.6a]:

$$p_{cr} = 3.265 \frac{EI}{R^3}. \tag{2.29b}$$

This deformation contains a certain rigid-body rotation of the whole ring, expressed by the constant term in the circumferential displacement v, see Fig. 2.15 (a). However, the behaviour of a cylindrical shell supported by end diaphragms corresponds rather to Fig. 2.15 (b) with no rigid-body rotation at all,

and results in a higher critical pressure [2.39a]:

$$p_{cr} = 4.0 \frac{EI}{R^3}.$$

(2.29c)

This difference of 33% between Eqs (2.29a) and (2.29c) decreases with increasing n. Computations in [2.45b] show differences of 11%, 6% and 3% for $n=3$, 4 and 6, respectively.

$$w = C \sin 2\varphi \qquad\qquad w = C \sin 2\varphi$$

$$v = -\frac{C}{2}(1 + \cos 2\varphi) \qquad v = -\frac{C}{2} \cos 2\varphi$$

(a)   (b)
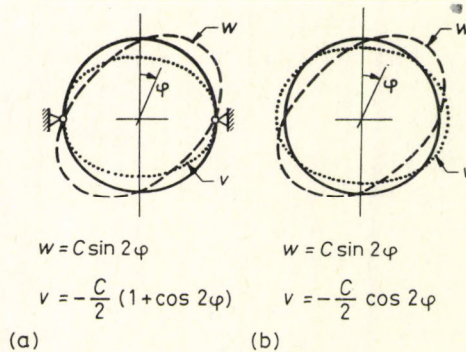
Fig. 2.15. Buckling deformation of a ring under radial pressure.
(a) – With two opposite points fixed (rigid-body rotation), (b) – without rigid-body rotation

These data clearly show that for design we may always use the formulas for fluid pressure, because when so doing we commit an error to the benefit of safety if the loads are constant directional. Nevertheless, for evaluating model tests we always have to consider the difference between the two kinds of critical loads.

As far as the *nonlinear theory* is concerned, up to now every author has started from the Donnell equations described in Section 2.1. As stated earlier, their accuracy is connected with the shallowness of the shell inside one buckling half wave. The error caused by the approximations of the Donnell equations in the nonlinear theory has not been investigated yet. However, some information can be obtained from similar investigations concerning the linear theory. Simitses and Aswani [2.45b] found that Donnell's equations give practically accurate results for very long shells with $n=2$, provided the load is constant directional, while for shorter shells (with $n \geqq 2$) they give lower values with a maximum error of 22.3%. On the other hand, the Donnell equations for fluid pressure acting on very long shells result in critical loads 6.7% higher than the accurate ones, while for shorter shells ($n \geqq 2$) they again yield lower critical loads with a maximum error of 27%.

The linear theory presented before (Fig. 2.13 and Eqs (2.25 (a), (b))) has no

such limitations or errors, since in its derivation no assumptions have been made concerning the shallowness of the shell.

In summary, we have to consider the following viewpoints when evaluating model tests or theoretical investigations:

– whether the pressure acted also on the end diaphragms or only on the lateral surface of the cylinder,
– whether the load maintained its direction during buckling or acted always perpendicularly to the buckled surface,
– whether the derivation was based on the Donnell equations or more accurate relations were used.

The post-critical behaviour of the cylinder subjected to hydrostatic pressure (see Fig. 2.11 (b)) was first investigated by Donnell, who used the nonlinear theory and also took initial imperfections into account. This was done in particular for shells connected to the end diaphragms by hinged edges [2.10] and for those with built-in edges [2.11].

Donnell assumed only three free parameters in the expression for the buckling shape. Presumably, this circumstance explains why he obtained curves with increasing post-buckling load bearing capacity for small $L/\sqrt{Rt}$ values, in contradiction to other results below. Budiansky and Amazigo [2.5] investigated the problem on the basis of the general theory of Koiter, starting also from the Donnell equations. They found that the behaviour of the perfect shell corresponds to Fig. 1.1 (b) or 1.1 (c), i.e., its load-deformation curve can be described for small buckling amplitudes w by the first two terms of the series expansion

$$p/p_{cr}^{lin} = 1 + b(w/t)^2. \tag{2.30}$$

Hence, the variation of the post-buckling load bearing capacity in the initial stage of the buckling process is characterized by the coefficient b: if b is positive, the post-buckling load bearing capacity increases (Fig. 1.1 (b)), if it is negative, it decreases (Fig. 1.1 (c)). The greater the absolute value of b, the quicker the variation. They obtained for b the two curves in Fig. 2.16(a) plotted against the geometric parameter $Z = (L^2/Rt)\sqrt{1-v^2}$. The curve valid for the circumferential compression clearly shows the three sections mentioned above: for small Z-values the shell has an increasing post-buckling load bearing capacity (short shell: "plate buckling"; Fig. 1.1 (b)); for medium Z-values it shows a decreasing behaviour (snapping: Fig. 1.1 (c)); while for $Z \to \infty$, it approaches the behaviour of the circular ring, which, like all bars, exhibits (at least in the initial stage) a constant post-buckling load bearing capacity (Fig. 1.1 (a)).

All these results are in agreement with the computations of Wolmir [2.57], who also obtained the minimum value of p_{cr}^{lower} for medium $L/\sqrt{Rt}$-values.

The test results, in fact, show the same tendency as Fig. 2.16 (a); see the comparisons in [2.5] and [1.1].

The diagrams of Fig. 2.16 (b) give, also on the basis of [2.5], the peak points p_{cr}^{upper} of the post-buckling curve of cylinders with initial imperfections as a

(a)

(b)
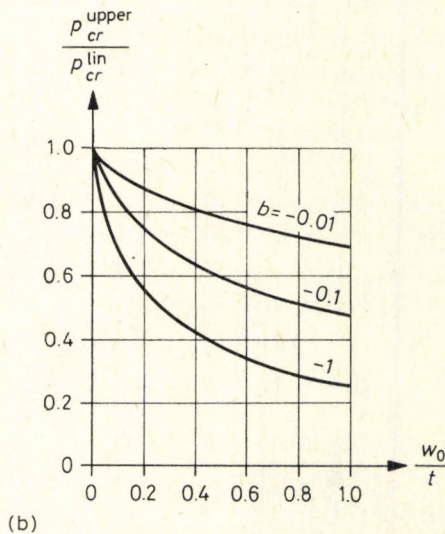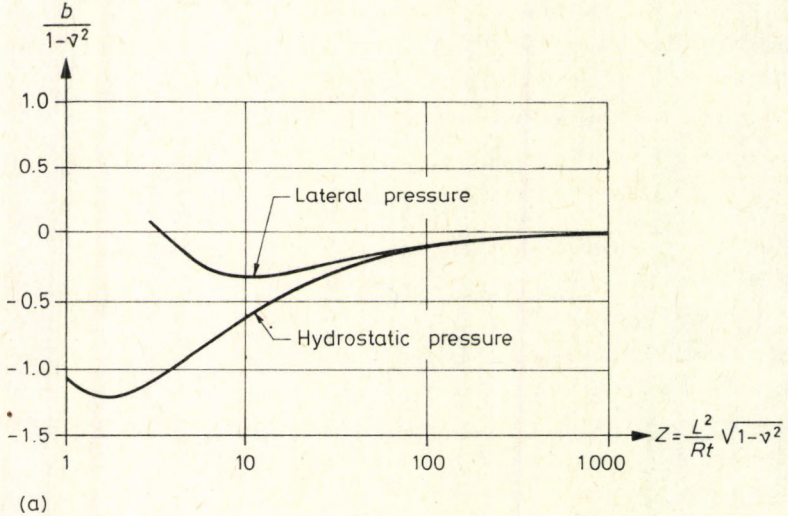
Fig. 2.16. Post-critical behaviour of the cylindrical shell subjected to lateral and to hydrostatic pressure

function of the quantity b, characterizing the initial tangent of this curve, and of the ratio of imperfection amplitude to wall thickness w_0/t. However, these diagrams are only approximate ones (as contrasted to the exact values of Fig. 2.16 (a)).

The post-buckling load-deformation curves themselves were calculated with some approximations (for both perfect and imperfect cylinders of certain geometric ratios) by Dierks [2.7] and by Thielemann and Esslinger [2.50]. Based on computations and experiments, Pflüger [2.42] developed a simple, easy to use design formula for the circumferential compression due to lateral pressure. Figure 2.17 gives with close approximation the snapping stress $\sigma_{\varphi,cr}^{upper}$, assuming
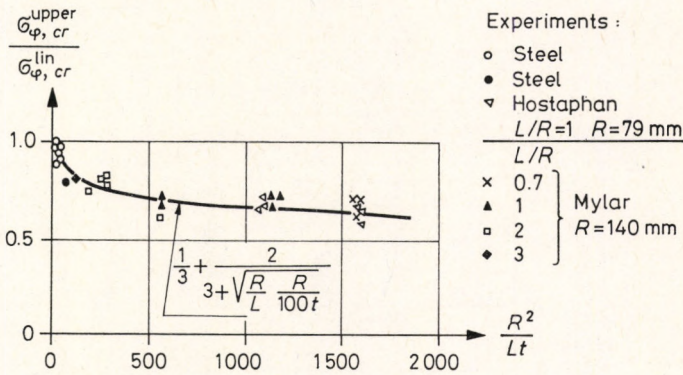
Fig. 2.17. Pflüger's experimental results and proposed design formula

an imperfection amplitude of $1/400$ of the diameter $(w_0 = 2R/400)$, as related to the linear critical stress $\sigma_{\varphi,cr}^{lin}$ determined by Eqs (2.25a) or (2.25b), plotted against the geometric parameter R^2/Lt.

The circumferential wave number observed on test cylinders is generally less than that given by the linear theory (Eq. 2.26a, b)). This phenomenon is due to the fact that the shell "jumps over" to shapes with less and less circumferential wave numbers during buckling, similarly to the case of the axially compressed cylinder (see Fig. 2.10). According to the theoretical investigations of Dierks [2.7] and Pflüger [2.42] the wave number given by Eqs (2.26a, b) is to be reduced by 10 %. Moreover, the tests of Pflüger gave an average wave number about 30 % less than this latter value, with great scatter of the individual test results.

2.4. Simultaneous Action of Axial
and Circumferential Compression

Detailed investigations on the basis of the linear theory [2.17], [2.51] showed that the diagram representing the interaction of both loading types is a broken line consisting of straight sections, concave when seen from the origin. According to [2.54] and [3.6], this may be approximated by a flat curve bulging somewhat outward, not differing very much from a straight line. Figure 2.18 shows
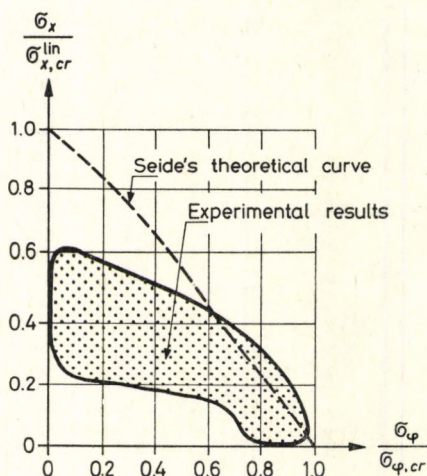
Fig. 2.18. Cylindrical shell compressed in axial and circumferential directions. Theoretical interaction curve and experimental results

the theoretical interaction curve of Seide, together with the experimental results of [2.54] and [2.57]. The more the axial compression prevails, the greater is the discrepancy between the linear theory and the experiments, according to the explanation of Section 2.1. The experimental results indicate a curve starting from about one third of the linear critical axial stress. On the other hand, the outward bulging character of the interaction curve was confirmed by the experiments. (It should be noted that Seide took as abscissa the circumferential compression due to hydrostatic rather than to lateral pressure).

Lundgren [2.32] approximated, to the benefit of safety, this flat curve by the straight line (Fig. 2.19):

$$\frac{\sigma_x}{\sigma_{x,cr}} + \frac{\sigma_\varphi}{\sigma_{\varphi,cr}} = 1. \qquad (2.31)$$
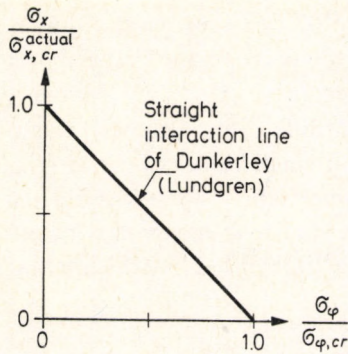
Fig. 2.19. Approximate analysis of simultaneous
action of axial and circumferential compression

This line is also called the "straight interaction line of Dunkerley" [2.27], [2.40]
and can be used in design. The same was also proposed in [2.57]. Here $\sigma_{x,cr}$
denotes the actual critical axial stress (a fraction of the linear critical stress, to
be taken, e.g., from Fig. 2.7 or 2.8 as explained above), and $\sigma_{x,cr}$ is given by
Eq. (2.25a) or (2.25b).

2.5. The Stabilizing Effect of the Circumferential
Tension on the Axial Compression

If in the perfect cylinder circumferential tension (caused by internal pressure)
arises, this hinders the buckling with asymmetric (reticulated, diamond) patterns,
but does not interfere with axisymmetric buckling. The explanation of this
fact is that asymmetric buckling implies waves in the circumferential direction,
which are "ironed out" by the circumferential tension, while during axisym-
metric buckling no circumferential waves develop, so that there is nothing to be
"ironed out". (According to detailed investigations [2.44], in the case of internal
pressure reticulated buckling pattern cannot come about, only diamond or
axisymmetric ones.) Hence, the buckling phenomenon is as shown in Fig. 2.20,
where circumferential tension is characterized by the internal pressure p [2.44].
(If the pressure also acts on both end-diaphragms of the cylinder, causing axial
tension in addition, the axial compression diminished by this latter value has
to be regarded as σ_x.) Increasing circumferential tension causes the axial linear
critical stress of the diamond pattern buckling to increase over that of the
axisymmetric buckling. At the same time, the post-critical load-deformation
curves become flatter and flatter: their lowest points are getting higher and
higher. Thus, the perfect cylinder starts to buckle axisymmetrically. Nevertheless,

when its axial compression f becomes great enough to reach the "diamond" postbuckling curve corresponding to the actual internal pressure, it continues to buckle along this latter curve: the shell "jumps over" from axisymmetric to diamond pattern. According to experiments, this diamond buckling has the shape of Fig. 2.21, even for small values of the internal pressure.

Cylinders with initial imperfections were investigated by Hutchinson [2.20] on the basis of Koiter's theory. He also found that asymmetric (reticulated or diamond) initial imperfections will be "ironed out" by the internal pressure, so that the criti-
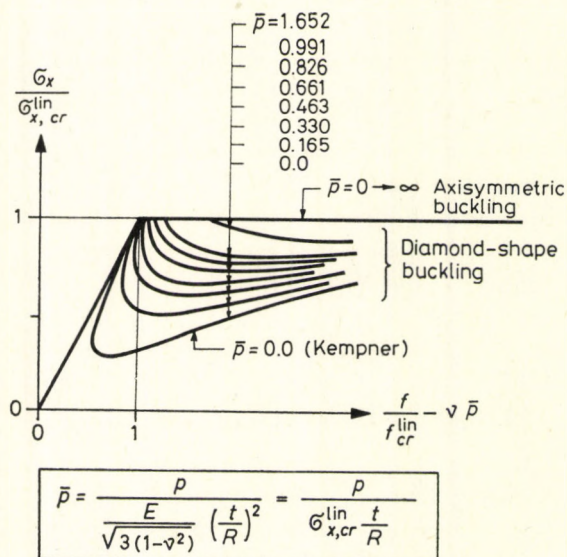
Fig. 2.20. Influence of internal pressure on the axial critical compressive stress of the perfect cylinder
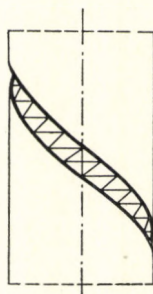
Fig. 2.21. Buckling pattern of the axially compressed and internally pressurized cylinder

(a)

(b)
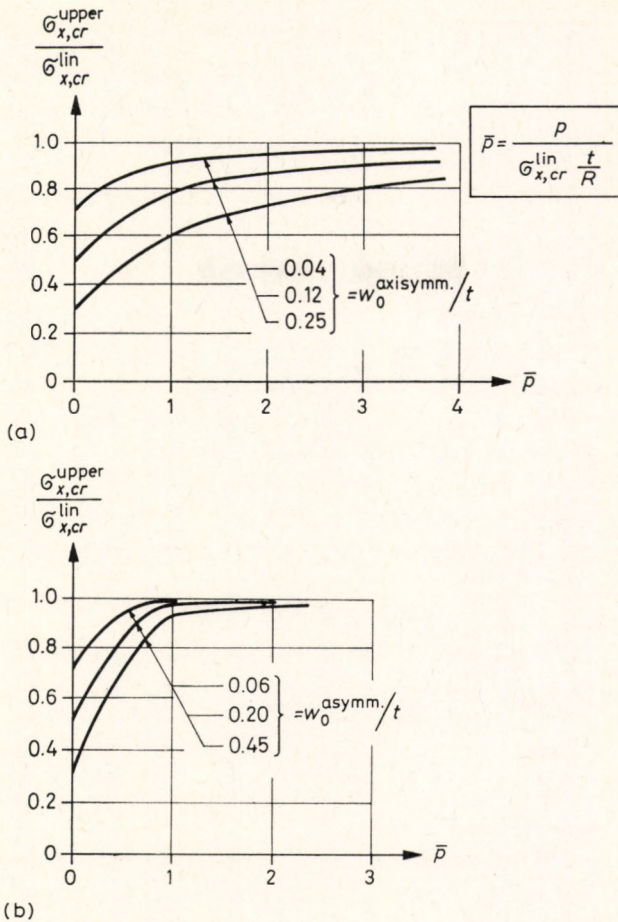
Fig. 2.22. Influence of initial imperfections on the critical axial compressive stress of the internally pressurized cylinder.
(a) – Axisymmetric imperfection, (b) – asymmetric imperfection

cal axial compressive stress becomes markedly greater as compared to the case of $p=0$. However, the axisymmetric imperfection cannot be "ironed out", so that the buckling process starts as if there were no internal pressure: the shell undergoes axisymmetric deformation, from which an asymmetric buckling bifurcates. The internal pressure can only hinder this bifurcating deformation. Consequently, the internal pressure increases the axial critical stress in the case of axisymmetric imperfections to a much smaller extent.

The results of Hutchinson's calculations (assuming $v=0.3$) for axisymmetric imperfections are shown in Fig. 2.22 (a), and those for asymmetric (reticulated) ones in Fig. 2.22 (b). (The curves for diamond-shape imperfections lie in between.)

Hutchinson also checked his results for axisymmetric initial imperfections by the special theory of Koiter and obtained a slight deviation from Fig. 2.22.

Axisymmetric buckling actually occurred on a silo subjected to internal pressure as reported by Hooley at the IASS Symposium in Budapest 1965.

2.6. Cylinders under Torsion

If a cylindrical shell is subjected to two equal and opposite twisting moments applied on both ends, pure shear arises in the cylinder wall, and at a certain value of the shear stress the shell buckles. According to investigations performed on the basis of the linear theory [2.43], [2.51], we have to distinguish between two kinds of cylinders:

1. The cylinder is *long*, if in the case of simply supported edges:

$$\frac{1}{\sqrt{1-v^2}} \frac{L^2 t}{(2R)^3} > 5.5, \tag{2.32}$$

and in the case of clamped edges:

$$\frac{1}{\sqrt{1-v^2}} \frac{L^2 t}{(2R)^3} > 7.8 \tag{2.33}$$

(notations are explained in Fig. 2.11).

The boundary conditions of the "long" cylinder do not influence the critical shearing stress. It can lose its stability due to torsion in two ways:

(a) it may buckle by torsion as a bar at a critical shearing stress;

$$\tau_{cr} = E \frac{\pi R}{L}, \tag{2.34}$$

(b) its wall may buckle as a shell at

$$\tau_{cr} = \frac{E}{3\sqrt{2}\,(1-v^2)^{3/4}} \left(\frac{t}{R}\right)^{3/2}. \tag{2.35}$$

As a rule, Eq (2.35) yields a lower critical stress than Eq. (2.34).

2. The cylinder is *short*, if the unequality sign in Eqs (2.32)–(2.33) is reversed.

The critical shearing stress then becomes, according to Donnell (see in [2.51]), for hinged edges:

$$\tau_{cr} = \frac{E}{1-v^2} \frac{t^2}{L^2} \left[2.8 + \sqrt{2.6 + 1.4(1-v^2)^{3/4} \left(\frac{L}{\sqrt{2Rt}}\right)^3}\right], \tag{2.36}$$

and for clamped edges:

$$\tau_{cr} = \frac{E}{1-v^2}\frac{t^2}{L^2}\left[4.6+\sqrt{7.8+1.67(1-v^2)^{3/4}\left(\frac{L}{\sqrt{2Rt}}\right)^3}\right]. \tag{2.37}$$

Using these formulas Batdorf [2.3] plotted the critical shearing stress against the geometric parameter $Z=\sqrt{1-v^2}\,(L^2/Rt)$, as shown in Fig. 2.23.
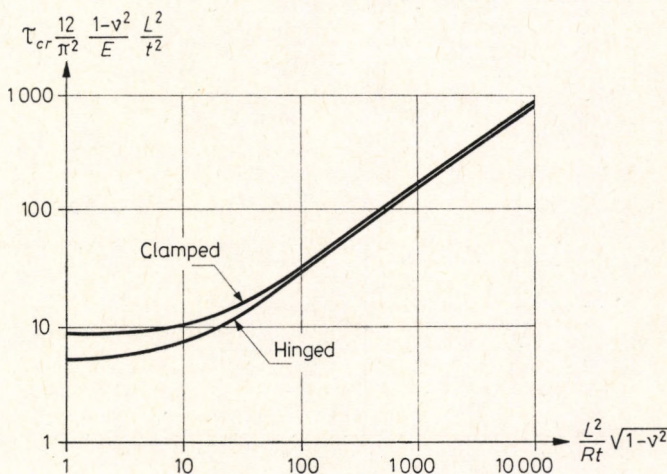
Fig. 2.23. Linear critical shearing stress of the twisted cylinder

The formula for hinged edges was refined by Kromm [2.28] cf. [2.51], resulting in the equation:

$$\tau_{cr} = 4.39\frac{E}{1-v^2}\frac{t^2}{L^2}\sqrt{1+0.0257(1-v^2)^{3/4}\left(\frac{L}{\sqrt{Rt}}\right)^3} \tag{2.38}$$

that yields slightly lower values for τ_{cr}.

The buckling pattern consists of waves of helicoidal shape or of their combinations [2.51].

The experiments [1.1], [2.4], [2.51], [2.57] yielded critical stresses generally 15–20% smaller than that of the linear theory. Hence, in the case of pure shear (twist), the cylinder is hardly sensitive to initial imperfection.

The post-buckling load-deformation curves of the twisted cylinder were first calculated by Loo [2.31], who used the Donnel equations valid for large deflections. He assumed four free parameters in the expression for the buckling shape, and performed the computations for perfect and imperfect cylinders as well. Nash [2.38] improved the accuracy of these computations by taking five free param-

eters in the buckling shape. These calculations showed the circumferential wave number to decrease during the buckling process.

Budiansky [2.4] determined the quantity b, characteristic of the initial tangent of the post-critical load bearing capacity curve of perfect cylinders (cf. Figs 1.1 (b) (c) and Section 2.3), by means of the general theory of Koiter, i.e. exactly. His results are shown in Fig. 2.24 (a) for cylinders with both hinged and clamped edges. For cylinders with initial imperfections, the theory furnishes the approximate values of the snapping stress τ_{cr}^{upper} of Fig. 2.24 (b), defined as in Fig. 1.1 (c).
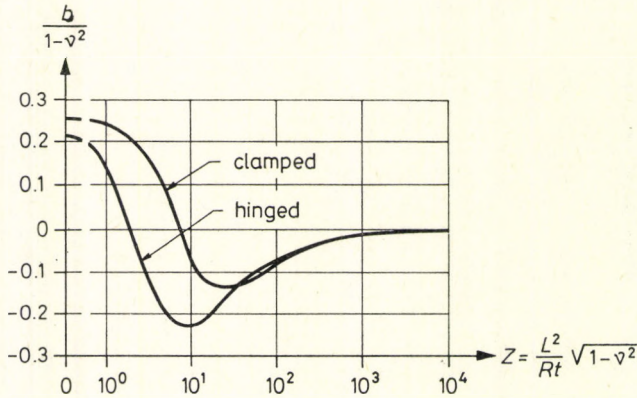
(a)
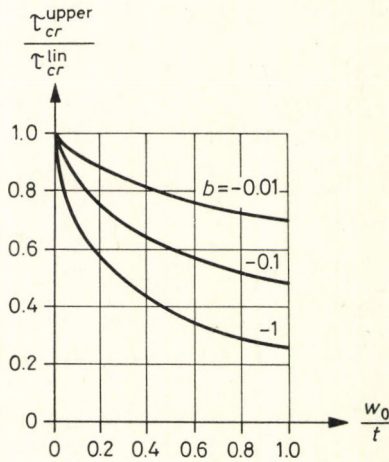
(b)

Fig. 2.24. Initial post-critical behaviour of the twisted cylinder

More elaborate theoretical investigations by Yamaki and Matsuda [2.60] on cylinders with clamped edges showed that the post-buckling behaviour of twisted cylinders is more complicated than the curves similar to Fig. 1.4 (c). Their results for $R/t=406$, $v=0.3$, which were also confirmed by very carefully conducted experiments [2.59], are shown in Fig. 2.25. (Solid lines refer to theoretical, dashed
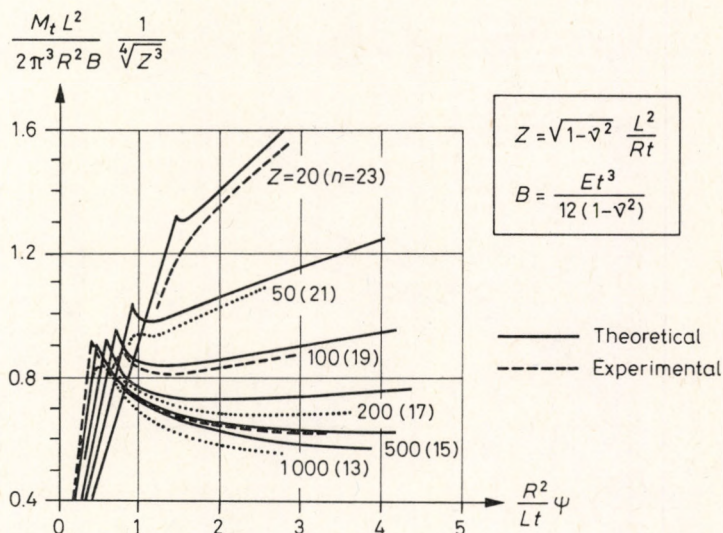
Fig. 2.25. Relations between twisting moment M_t and angle of twist ψ for clamped cylindrical shells in the post-buckling range ($R/t=405$, $v=0.3$)

lines to experimental, results.) It can clearly be seen that the seemingly steep initial drop in the post-buckling load bearing capacity at $Z=20$ (cf. Fig. 2.24 (a)) is compensated to a large extent by the subsequent ascending character of the curve. The shapes of the curves in Fig. 2.25 explain why the test cylinders exhibit critical (snapping) stresses rather close to those of the linear theory, despite the steeply falling initial tangents at some values of Z (see Fig. 2.24 (a)).

Summing up, we may conclude that a cylinder is most sensitive to initial imperfections if subjected to axial compression. The sensitivity is less in the case of lateral (hydrostatic) pressure, while in the case of twist the influence of initial imperfections becomes very small indeed.

2.7. Simultaneous Action of Twist and Axial Compression

The problem of simultaneous action of twist and axial compression was investi-
gated by Kromm [2.28], and cf. [7.21], on the basis of the linear theory. His main
results are shown in Fig. 2.26. Here τ_{cr} denotes the critical shearing stress given
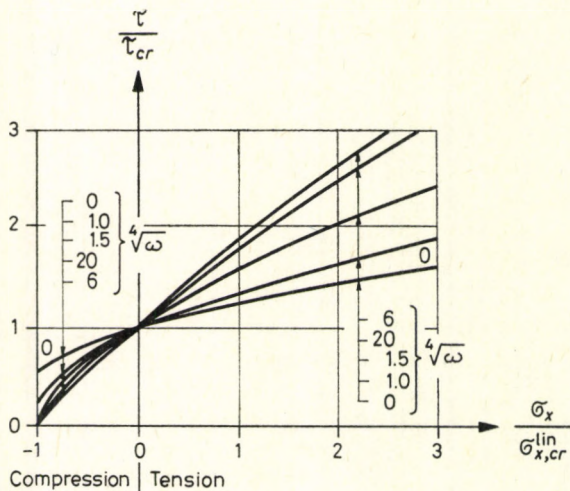
Fig. 2.26. Interaction of axial compression and torsion according to the linear theory

by Eq. (2.36) for pure shear (twist), $\sigma_{x, cr}^{lin}$ is the linear critical axial compressive
stress according to Eq. (2.13), while ω represents a geometric parameter:

$$\omega = \frac{12(1-\nu^2)}{\pi^4} \frac{L^4}{R^2 t^2}. \tag{2.39}$$

A special feature of the diagram in Fig. 2.26 is that the curve pertaining to
$\sqrt[4]{\omega} = 6$ has an extreme position. The curve corresponding to $\sqrt[4]{\omega} = 20$ may be taken
valid as far as $\sqrt[4]{\omega} = \infty$ [7.21].

3. Buckling of Conical Shells

Investigations on the buckling of conical shells showed that they behave in a similar way to cylindrical ones. Therefore, their treatment is fairly simple.

In the following we deal only with circular conical and truncated conical shells of uniform wall thicknesses. It is assumed that the bottom diaphragm of the conical shell, truncated or not, (and the top diaphragm of the truncated one) is infinitely rigid in its own plane and is connected to the shell by a hinged edge.

3.1. Compression along the Generatrices

In this loading case (Fig. 3.1) only generatrix directed stresses of magnitude

$$\sigma_{gen} = \frac{P}{2\pi rt \cos \alpha} \tag{3.1}$$

arise in the cone.

The buckling problem was solved on the basis of the linear theory by Seide [3.4]. The main result of his investigations is that the cone can be substituted for
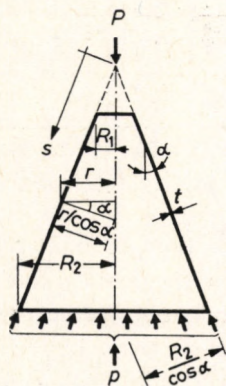
Fig. 3.1. Conical shell compressed along the generatrices

by a cylinder with the radius $r/\cos \alpha$ equal to the actual principal radius of curvature of the cone (Fig. 3.1). This would result in cylinders with different radiuses for every point of the generatrix. However, since the generatrix directed stress varies, according to Eq. (3.1), in inverse proportion to the radius of curvature, just as the critical stress of the cylinder does (see Eq (2.13)), it is — according to the linear theory — irrelevant at which point the substituting cylinder is established.

According to what was said on cylinder buckling, however, the initial imperfection increases with increasing ratio R/t, causing a greater reduction in the critical load (see Fig. 2.3 (a), (b), (c)). Consequently, it is expedient to take the radius of the cylinder equal to the maximum radius of curvature $R_2/\cos \alpha$ of the cone.

The behaviour of the cone is similar to that of the cylinder also in the following respect: if along the edges zero tangential stresses ($n_{xy}=0$) are stipulated instead of zero tangential displacements ($v=0$), then the linear critical load sinks to half its original value, just as in the case of the cylinder [3.1].

The model tests [2.53], [3.2] gave considerably lower buckling loads than predicted by the linear theory, again as in the case of the cylinders. The rate of decrease in the critical load was of about the same magnitude as in the case of the cylinders, except for the range of greater R/t ratios: from about $R/t \geqq 1000$ on, the conical shells carried more load than the corresponding cylindrical ones (Fig. 3.2).
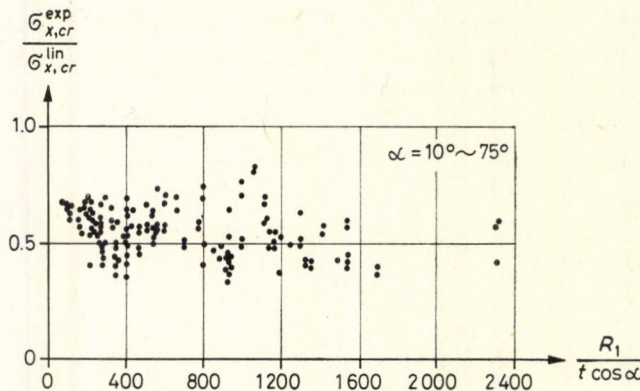
Fig. 3.2. Experimental results on conical shells compressed along the generatrices

However, if we neglect this excess strength to the benefit of safety, the computation of conical shells becomes completely identical to that of cylinders.

The experimental shells generally buckled near their larger ends in circumferential short waves arranged in several tiers. The buckling deformation was less in the region where the radius was smaller, and it was largest along the edge with maximum radius R_2. These results comply with the theoretical predictions.

3.2. Hydrostatic Pressure

In the case of hydrostatic pressure (Fig. 3.3) the following stresses arise in the conical shell:
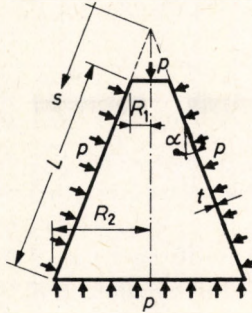
Fig. 3.3. Conical shell subjected to hydrostatic pressure

$$\sigma_{\text{hoop}} = -\frac{ps \tan \alpha}{t},$$
(3.2)

$$\sigma_{\text{gen}} = \frac{\sigma_{\text{hoop}}}{2}.$$
(3.3)

The results of the various theoretical investigations differ slightly from each other. According to Niordson [3.3], the critical pressure of the (truncated) cone is equal to that of a cylinder with the radius

$$R = \frac{R_1 + R_2}{2}$$
(3.4)

and with the length L equal to the (skew) generatrix length of the cone (see Fig. 3.3). The critical pressure of this equivalent cylinder is given by the Batdorf formula (2.28).

According to Seide [3.5], the critical pressure of the equivalent cylinder is to be multiplied by a factor γ depending on $(1 - R_1/R_2)$ to be taken from Fig. 3.4.

Seide also showed that the truncated conical shell buckles, like the cylindrical one, in one half wave in the axial direction, provided the inequality $0 \leq (1 - R_1/R_2) \leq 0.64$ is fulfilled (cones with small vertex angles). In the case of $(1 - R_1/R_2) > 0.64$ a second, shorter half wave also develops near the apex. This may obviously be explained by observing that in this case the section near the apex is considerably stiffer than the other parts, so that the equivalent cylinder will be, so to say, shorter. Possibly this fact causes the value of factor γ (Fig. 3.4) to be greater than one in this range.
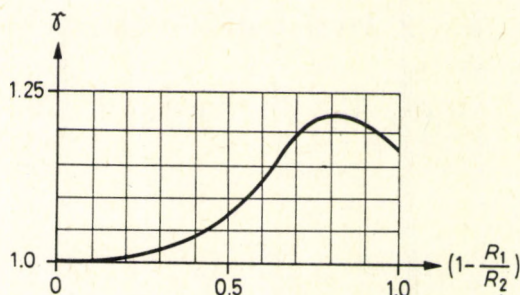
Fig. 3.4. Multiplication factor for the critical stress of the
equivalent cylinder in the case of hydrostatic pressure

The experiments [2.54], [3.5] mostly gave values around these theoretical results.
As with the cylinder subjected to circumferential compression, the experimental
buckling pressures were not less than 60% of the theoretical ones. Figure 3.5 shows
the test results published in [2.54] compared with the linear critical pressure of the
equivalent cylinder. It can be seen that most of them differ by, at most, 20%
from the theoretical value of Niordson. Greater discrepancy (40%) occurs only
in the case of the complete cone with $(1 - R_1/R_2) = 0$, i.e. just in the range where
Seide's factor γ is greater than one. On the other hand, experiments with "near-
perfect" conical shells [3.7] confirmed the validity of Seide's factor γ (Fig. 3.4)
by yielding buckling pressures always greater than that of the equivalent cylinder
multiplied by γ. Still, the experimental results of Fig. 3.5 suggest that conical
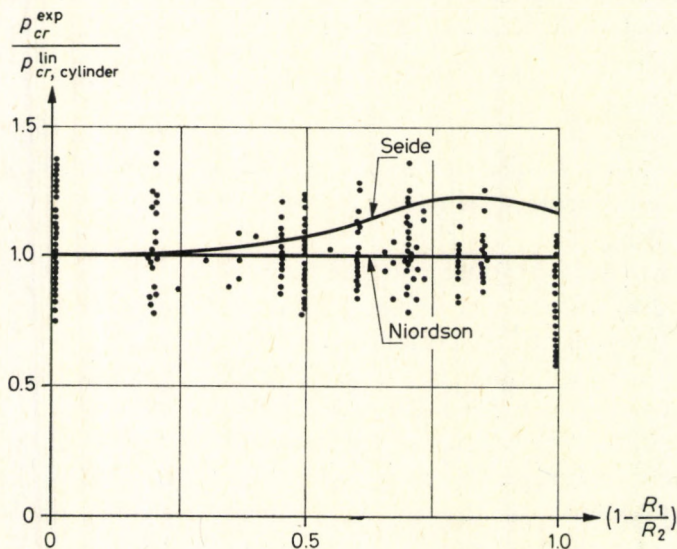
Fig. 3.5. Experimental results on conical shells subjected to hydrostatic pressure

shells, in the range where γ is appreciably greater than one, are more sensitive to initial imperfections than those with a lower geometric parameter $(1 - R_1/R_2)$. For this reason, and also for the sake of simplicity, we propose that for design purposes Niordson's results should be accepted, i.e. practical computations should be made simply on the equivalent cylinder.

3.3. Simultaneous Action of Axial Compression and Hydrostatic Pressure

The problem of the simultaneous action of axial compression and hydrostatic pressure was investigated theoretically by Seide [3.6]. Experimental results to be found in [2.54] show that the straight line of Dunkerley, representing the interaction between the critical loads of the cylinders equivalent as to axial compression and hydrostatic pressure respectively, gives critical stresses lying slightly on the safe side (see Figs 2.18–2.19 and the pertaining remarks).

4. Stability of Spherical Shells and Domes of Other Forms

4.1. Buckling of Spherical Shells Subjected to Uniform Overall Radial Pressure

Among the doubly-curved surfaces with positive Gaussian curvature it is the spherical shell that is simplest to treat mathematically, due to its constant curvature. In fact, its buckling problems are treated very thoroughly in the literature. We begin with the buckling investigation based on the linear theory using the so-called "equilibrium method" (as that presented in Section 2.1.).

The exact derivation of the equations does not make use of the fact that one buckle extends over only a comparatively small area of the shell surface, which, consequently, can be regarded as *shallow* in the region of one buckle. The exact theory requires lengthy and intricate computations leading to Legendre (spherical) functions [2.17], [2.17a], [2.51].

However, we know from the exact theory and from experiments that the diameter of one buckle is small as compared to that of the sphere, so that the shell can be regarded as shallow in the region of one buckle. Consequently, we may start with the shallow-shell equations, thus greatly facilitating the derivation. In the following we shall develop the linear critical load in this way, see [2.6], [2.12] or [2.57].

We substitute the geometric expressions corresponding to the sphere into the general shallow-shell equations (2.4). In the case of the z-axis pointing toward the centre of the sphere, the latter assume the following forms, with the approximations allowed by the shallow-shell theory (Fig. 4.1):

$$\frac{\partial^2 z}{\partial x^2} = \frac{\partial^2 z}{\partial y^2} = \frac{1}{R}, \tag{4.1a}$$

$$\frac{\partial^2 z}{\partial x \partial y} = 0, \tag{4.1b}$$

$$L_P = \frac{1}{R}\left(\frac{\partial^2}{\partial x^2} + \frac{\partial^2}{\partial y^2}\right) = \frac{1}{R}\varDelta. \tag{4.1c}$$

The internal forces of the pre-buckling state are as follows:

$$n_{xy} = 0, \tag{4.2a}$$

$$n_x = n_y = -\frac{pR}{2}. \tag{4.2b}$$

The incremental radial load $\bar{p}$ arising during buckling is the product of the com-
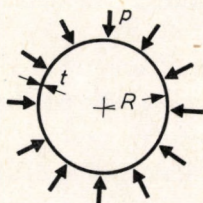
Fig. 4.1. Radically compressed spherical shell

pressive forces (4.2a) and of the change in curvature due to the buckling deformation w:

$$\bar{p} = -\frac{pR}{2}\left(\frac{\partial^2 w}{\partial x^2} + \frac{\partial^2 w}{\partial y^2}\right) = -\frac{pR}{2}\Delta w. \tag{4.2c}$$

Substituting all these expressions into Eq. (2.4) we obtain:

$$B\Delta^4 w + \frac{T(1-v^2)}{R^2}\Delta^2 w = -\frac{pR}{2}\Delta^3 w. \tag{4.3}$$

Assuming for w a "*reticulated*" (chessboard) pattern, similar to that of the cylinder,

$$w = w_1 \sin\frac{\pi}{l_x}x \sin\frac{\pi}{l_y}y \tag{4.4}$$

furnishes the following equation for the critical pressure p_{cr}:

$$p_{cr}\frac{R}{2} = B\pi^2\left(\frac{1}{l_x^2} + \frac{1}{l_y^2}\right) + \frac{T(1-v^2)}{R^2\pi^2\left(\dfrac{1}{l_x^2} + \dfrac{1}{l_y^2}\right)}. \tag{4.5}$$

By differentiating p_{cr} with respect to $\left(\dfrac{1}{l_x^2} + \dfrac{1}{l_y^2}\right)$ and equating the derivative to zero, we obtain:

$$\left(\frac{1}{l_x^2} + \frac{1}{l_y^2}\right) = \frac{1}{\pi^2}\sqrt{\frac{T(1-v^2)}{BR^2}}. \tag{4.6}$$

Hence, the buckling shape (i.e. the ratio of the two buckling half-wave lengths) is again indeterminate, as in the case of the axially compressed cylinder [Eq. (2.10)].

Substituting Eq. (4.6) into Eq. (4.5) we arrive at the critical value of the radial pressure:

$$p_{cr}^{lin} = \frac{2}{\sqrt{3(1-v^2)}} E \frac{t^2}{R^2} = \frac{1.16}{\sqrt{1-v^2}} E \frac{t^2}{R^2}. \tag{4.7}$$

Assuming an *axisymmetric* buckling pattern on the shallow shell yields the same result.

Since, as in the case of the axially compressed cylinder, we have several buckling modes associated with the same linear critical load, the spherical shell also exhibits the "compound-buckling" behaviour.

This linear, also called "classical", value of the critical pressure was derived first in 1915 by Zoelly [4.43], who used the exact equations (i. e. he did not make use of the shallowness of the shell), and assumed an axisymmetric buckling pattern. Later van der Neut [4.27] showed that assuming an asymmetric buckling pattern yields the same results.

Nevertheless, experiments gave substantially lower values than this linear critical load. In Figs 4.2 and 4.3 we compiled the results of some test series plotted against the ratio R/t and the geometric parameter λ respectively. (The parameter λ, a characteristic of the spherical cap, is defined by Eq. (4.11); see also Fig. 4.9.)
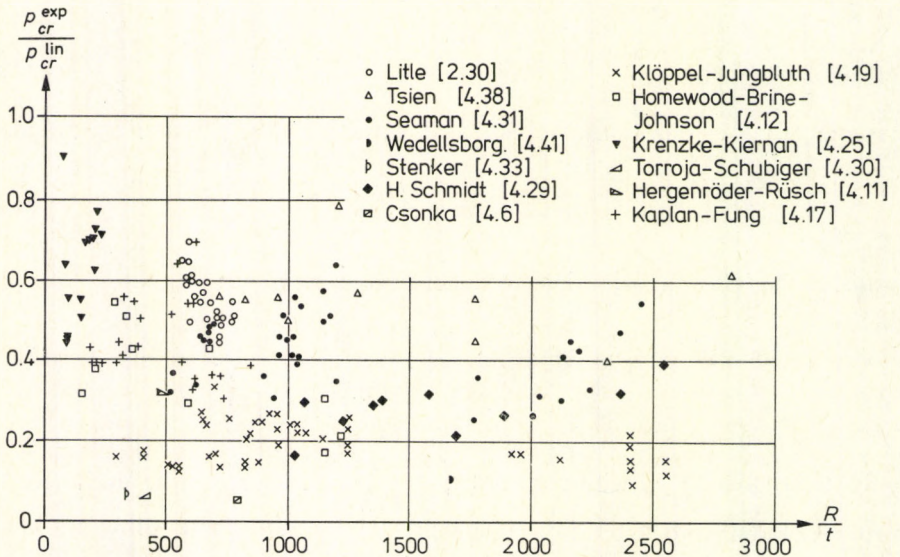
Fig. 4.2. Exeprimental results on spherical shells versus R/t
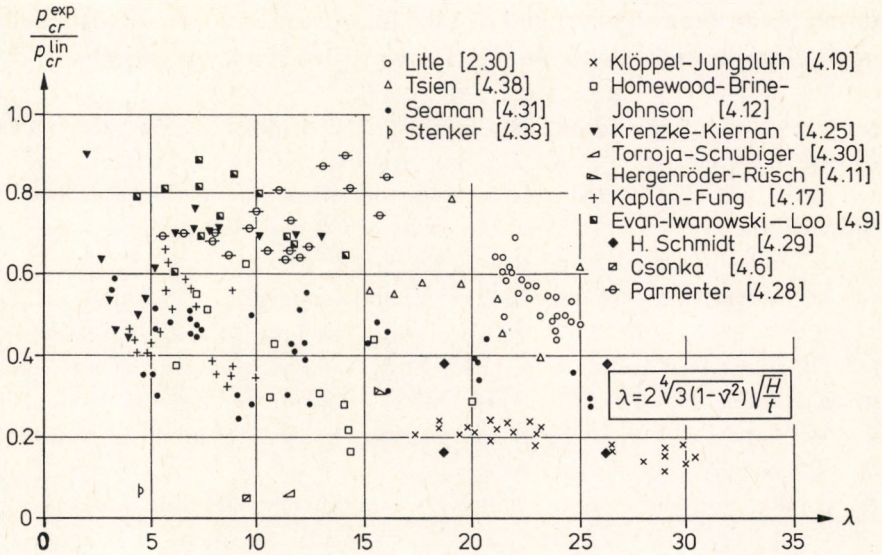
Fig. 4.3. Experimental results on spherical shells versus the geometric parameter λ

From the results of Schmidt [4.29] we plotted in Fig. 4.3 only those representing the four extreme cases; the others lie in between. For the sake of simplicity, the results for non-spherical shells were also plotted in these figures (see item (d) below).

To these seemingly completely irregular results some sense can be given by the following viewpoints:

(a) For some experiments *"near-perfect" shells* with practically no initial imperfections were manufactured by special methods. These were the specimens of Parmerter [4.28], Krenzke and Kiernan [4.25], Evan–Iwanowski and Loo [4.9]. Their results are, in fact, higher than those for the other, less perfect, shells. The models of Adam and King [4.1] and of Carlson, Sendelbeck and Hoff [4.5], not shown in the figures, also belong to this group; they reached 80% or sometimes even 86% of the p_{cr}^{lin}.

(b) In some experiments the *supports of the shell's edges were not stiff enough*: either the base ring was too weak or — in the case of polygonal shells — the edges were supported by vertical diaphragms having no rigidity perpendicular to their planes. To this group belong the shells of Csonka [4.6], Torroja and Schubiger [4.30], Schmidt [4.29], Hergenröder and Rüsch [4.11], Stenker [4.33], as well as some of the experiments of Klöppel and Jungbluth [4.19] (these will be discussed later).

The supports of the models of Kaplan and Fung [4.17], Homewood, Brine and

5*

Johnson [4.12], Seaman [4.31] and of Litle [2.30] were also weaker than a rigid clamping (see the evaluation in [4.39]). These buckled at a lower critical load than the others.

(c) In the following cases the experimental shells had *noncircular ground plans*. This caused deviations from the axisymmetric distribution of the internal forces resulting in not exactly definable local disturbances, in addition to the effect mentioned under (b). Here belong the shells of Csonka, Torroja and Schubiger, Schmidt, and Hergenröder and Rüsch.

(d) In the experiments of Csonka, Torroja and Schubiger, and Schmidt, the shell surfaces were *not spherical*. We shall deal with this kind of shell in Section 4.3.

(e) The lowest test results were yielded by *reinforced concrete* shells (Csonka, Torroja and Schubiger, and Stenker). One can account for these by recognizing that concrete has cracks, it creeps and probably has greater initial imperfections than metallic shells (see Section 9.8).

(f) Finally, it should be noted that every experimental shell was *shallow* except for those of Tsien [4.38] and Litle, as well as some of the shells of Klöppel and Jungbluth, Homewood, Brine and Johnson, Seaman, and Krenzke. In his study, which evaluates a great number of experiments, Wang [4.39] points to the fact that only the critical loads of the shallow shells depend on the parameter λ (see Eq. (4.11)), while those of deep ones do not.

The kind of loading (whether it maintains its direction like gravity loading, or whether it remains perpendicular to the buckled surface like fluid pressure) is, according to [4.32], practically irrelevant for the magnitude of the critical stress of the complete sphere, as contrasted with the case of the cylinder under lateral pressure. This is most probably due to the fact that spherical shells always buckle in small, local, shallow waves. Therefore, we will not deal with the kind of loading here any more.

The discrepancy between the linear critical load and the test results necessitated the development of a buckling theory for spherical shells which takes *large deformations* into account ("nonlinear" theory). Its essential feature, as with what was said on cylinders, is that — maintaining the assumption concerning the shallowness of the shell surface — in the expressions for the deformations the second powers of the first derivatives of the displacement w, perpendicular to the shell surface, are also taken into account. This makes possible the description of the buckling process beyond the equilibrium position close to the underformed state, up to displacements several times the wall thickness. For geometrically *perfect, complete spherical shells* this calculation was first made by Kármán and Tsien [4.18]. They assumed the shape of the buckling pattern, characterizing its extension by a free parameter, with respect to which they minimized the load at

every loading step. Thus, they determined the lowest point of the post-critical load-displacement curve, obtaining (for $v=0$) the result

$$p_{cr}^{lower} = 0.365 \frac{Et^2}{R^2} \tag{4.8}$$

(Fig. 4.4.). They used as the abscissa the ratio of the average displacement f of the load to the displacement f_{cr}^{lin} pertaining to the linear critical load. Since the average displacement f gives the change in volume ΔV of the sphere, we may write $f/f_{cr}^{lin} = \Delta V / \Delta V_{cr}^{lin}$, where ΔV_{cr}^{lin} denotes the change in volume pertaining to the linear critical load. As ordinates we plotted the ratio p/p_{cr}^{lin}, which, for Eq. (4.8), assumes the value 0.315.
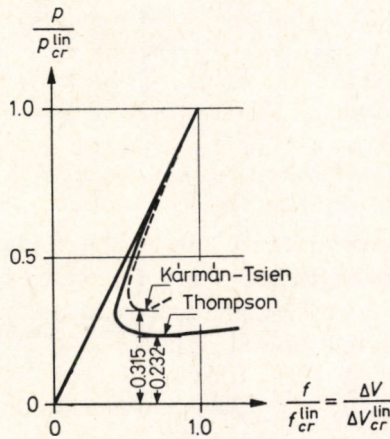
Fig. 4.4. Post-critical behaviour of the perfect spherical shell

Later, improving the accuracy of the calculation, Tsien [4.38] arrived at the value of

$$p_{cr}^{lower} = 0.312 \frac{Et^2}{R^2}, \tag{4.9}$$

i.e. 0.27 times the linear critical load.

In their comments on the derivation of Kármán and Tsien [4.18], Friedrichs [4.10] and Mushtari and Surkin [4.26] cite two errors of principle, which nevertheless roughly compensate for each other. On the one hand, they neglected the tangential displacements of the shell surface; on the other hand, they minimized the load instead of the total potential energy (cf. the description of the nonlinear method in Section 2.1).

Thompson [4.34] assumed four free parameters in the expression for the buckling pattern. Thus, he was able to show that both the shape and the extension of the
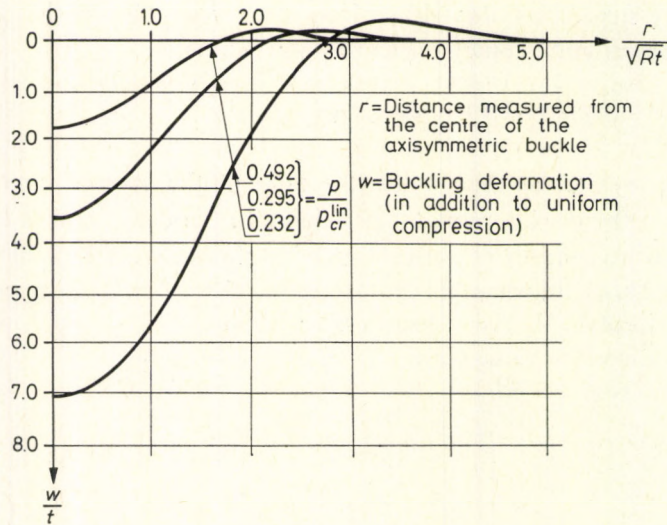
Fig. 4.5. Variation of the buckling shape during the buckling process

buckling pattern greatly vary durint snapping, that is, the buckling half-wavelength increases with the decreasing load (Fig. 4.5). He assumed the deformation to be axisymmetric during the entire buckling process. Thus, he obtained with $v=1/3$ the second curve of Fig. 4.4. Its lowest point is

$$p_{cr}^{lower} = 0.283 \frac{Et^2}{R^2},$$

i.e. 0.232 times the linear critical load.

Other scientists performed further calculations on a similar basis in order to find the "true" value of the numerical factor appearing in the expression for p_{cr}^{lower}. Thus Pozo Frutos and Pozo Vindel [4.28a] got (with $v=0$) 0.23, Mushtari [4.26a] 0.22, Gabril'iants and Feodos'ev [4.10a] 0.13, and Dostanova and Raĭzer [4.7a] obtained (with $v=0$) the value

$$p_{cr}^{lower} = 0.126 \frac{Et^2}{R^2}, \tag{4.10}$$

i.e. 0.108 times the linear critical load.

Rauch, Jacobs and Marz [4.28b] found that, using Reissner's equations of small finite deflections [4.28c], p_{cr}^{lower} depends to some extend on the R/t ratio as well. They got 0.07 and 0.05 times the linear (classical) critical pressure for $R/t=100$ and 200 respectively.

All these results show that, although a perfect sphere theoretically buckles at the linear critical load, the shell is very sensitive to initial imperfections, as is

indicated by the shape of the curve, and as was to be expected because of the "compound buckling" mentioned earlier.

Further investigations on *complete shells* are mostly based on Koiter's method. This takes — according to what was said in Chapter 2 — every possible buckling mode of the linear theory into account. These are orthogonal in the frame of the linear theory. Koiter chose from these shapes those groups that, due to the nonlinearity, interact with each other and yield the minimum critical load. Hutchinson [4.14] investigated the perfect sphere in this way, starting from the shallow-shell equations, and also taking asymmetric buckling modes into account. He obtained a curve starting with a steeper initial tangent than that of Thompson in Fig. 4.4, but did not calculate its lowest point. On the other hand, for the sphere with initial imperfections he found a behaviour corresponding essentially to Fig. 1.1 (e). The snapping load p_{cr}^{bifurc} (or p_{cr}^{upper}) is given by the two upper curves in Fig. 4.6, plotted against the ratio of the initial imperfection amplitude
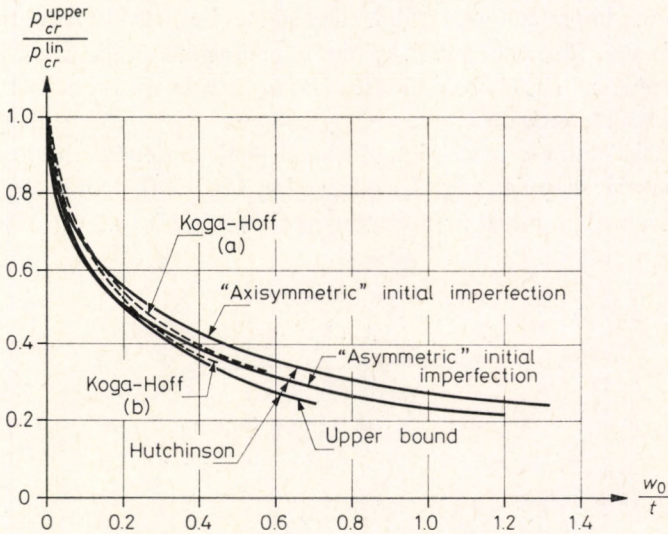
Fig. 4.6. Influence of the initial imperfection amplitude on the snapping load of the spherical shell

to the wall thickness (calculated for $v=1/3$). The two curves differ according to whether the shape of the initial imperfection is assumed to be actually similar to the first or to the second of the buckling modes, $w_1=a_1 \cos(bx)$ and $w_2=u_2 \sin(cx) \sin(\sqrt{3}cy)$, coupling with each other and yielding the most onerous combination. The upper curve is for a "symmetrical" initial imperfection similar in shape to w_1, while the initial imperfection assumed for the lower curve has the "asymmetric" shape of w_2. The phenomena correspond in both cases to

the compund "multimode buckling" described in Section 1.2. The investigation of Hutchinson can be considered as being completely general, since it is not confined to axisymmetric imperfections. It becomes inaccurate only for large imperfection amplitudes due to the approximations inherent to Koiter's theory. This is illustrated by the lowest curve of Fig. 4.6, which represents — according to the special theory of Koiter — an exact solution (i.e. also correct for larger imperfection amplitudes) taking a chosen imperfection shape as a basis. Since this does not represent the most onerous case, the truly exact curve has to lie somewhat lower.

Koiter [4.22] did not make use of the approximations of the shallow-shell theory, but he confined his investigation to axisymmetric imperfections and buckling shapes. His results are very close to those of Hutchinson.

Since the accuracy of Koiter's method — at least in its original form — becomes less and less with increasing imperfection amplitudes, due to omission of the higher terms, other investigators chose a different approach: they confined themselves to axisymmetric imperfections and buckling shapes but tried to solve this problem exactly. This was also motivated by the experimental observation (see e.g. in [4.21]) that spherical shells always deform — at least at the onset of the buckling process — axisymmetrically.

On the basis of these principles, Bushnell [4.4] computed the load intensity causing symmetric snapping (p_{cr}^{upper}, as defined by Fig. 1.1 (d)) for several geometric ratios. He assumed an initial imperfection as shown in Fig. 4.7 (b). When plotting
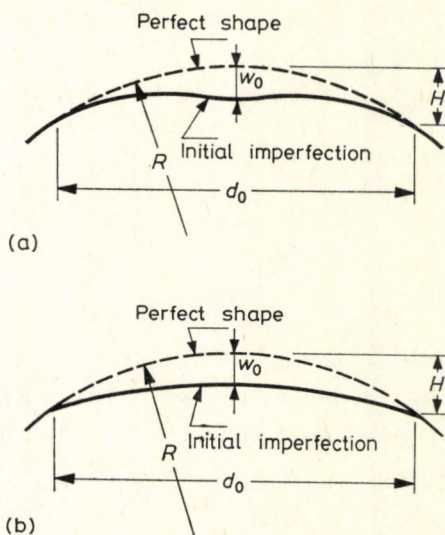
Fig. 4.7. The assumed initial imperfections

these p_{cr}^{upper}-values against the ratio of the imperfection amplitude to the wall thickness (w_0/t), he obtained different curves for different diameters d_0 of the initial imperfection. These curves can be combined to give a "festoon curve" (Fig. 4.8). In this figure the diameter d_0 of the imperfection was characterized by the geometric parameter λ, defined by Eq. (4.11), in which H denotes the height of the original (perfect) sphere over the imperfection circumference (Fig. 4.7 (b)). The envelope of this festoon curve, indicated by the dashed line, can be used for design.

The development of the festoon curve can be explained by two factors. On the one hand, spherical shells with initial imperfections of different λ-s may behave differently because of the nonlinear character of the whole phenomenon, which means that, depending on the extent to which the diameter d_0 of the initial imperfection differs from the "natural" half buckling wavelength (given by the linear theory), the shell exhibits different behaviour patterns during buckling. On the other hand, that part of the spherical shell which is inside the initial imperfection behaves in a similar way to a spherical cap clamped along a circle with the diameter d_0 [4.4], and for that reason it is quite natural to obtain a festoon curve (see below).

Figure 4.8 shows that for a given ratio of w_0/t the minimum value of p_{cr}^{upper} is given by the curves with λ between 2 and 4. This approximately corresponds to $\lambda_{lin} = 2.35$ [1.2], which characterizes the half buckling wavelength of the axisymmetric mode given by the linear theory.

Koga and Hoff [4.21] solved the axisymmetric buckling problem of the complete sphere by a numerical method different from Bushnell's. They considered the two
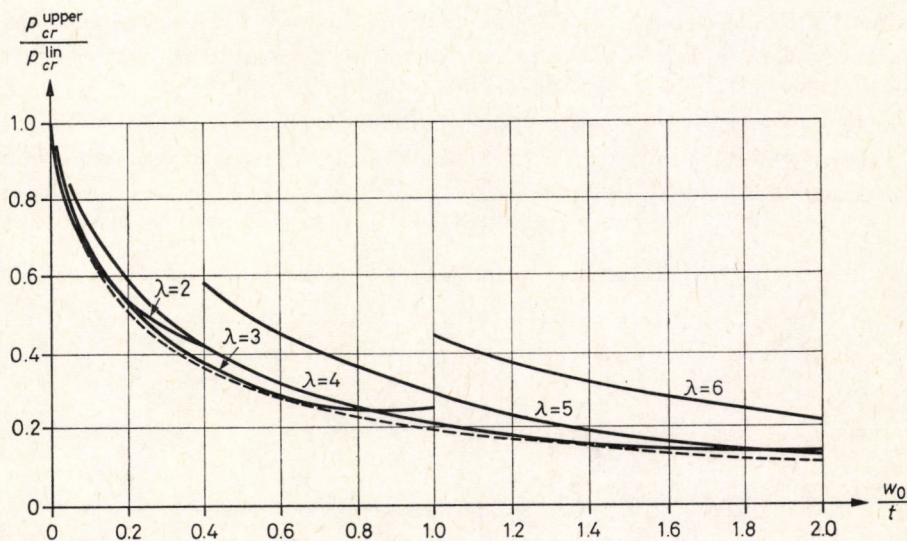
Fig. 4.8. Influence of the initial imperfection according to Bushnell

imperfection shapes of Fig. 4.7 and found that, for the imperfection shapes (a) and (b), the minimum values of p_{cr}^{upper} were obtained for $\lambda \approx 4$ and $\lambda \approx 3$, respectively. This latter result approximately corresponds to that of Bushnell (see Fig. 4.8).

These minimum values of p_{cr}^{upper} of Koga and Hoff are plotted by dashed lines marked with (a) and (b), versus w_0/t in Fig. 4.6. The curve marked with (b) practically coincides with the envelope of Bushnell in Fig. 4.8, providing a good control.

It is worth noting that the two curves of Koga and Hoff hardly deviate from each other. Consequently, for practical purposes, it is sufficient to characterize the initial imperfection by its amplitude w_0 only, independent of its shape.

It seems that the close agreement of these curves with those of Hutchinson, who also took asymmetric imperfections and buckling shapes into account, is due to two factors compensating for each other. On the one hand, Koga and Hoff [4.21] — as contrasted to Hutchinson — did not make use of the approximations of Koiter's theory, so that they obtained somewhat lower curves. On the other hand, as mentioned before, the buckling shape is, in fact, — at least in the initial stage of the buckling process — axisymmetric, so this assumption might increase the calculated p_{cr}^{upper} only to a small degree. In summary, we may conclude that for the critical load of a spherical shell — as contrasted to the cylindrical one — practically the same result is obtained whether only symmetric imperfection and buckling deformation, or also asymmetric imperfection and deformation, are considered; see also in [4.22].

Another series of theoretical investigations refers to the *spherical cap* with a clamped (or hinged) edge. The notations to be used are indicated in Fig. 4.9. For the understanding of the behaviour of the clamped spherical cap, we first consider the cap supported as shown in Fig. 4.10: its contour points may roll freely on a conical surface but cannot rotate. Hence, it is in a situation similar to a partial sphere: when subjected to external pressure it can undergo compression without bending. The linear theory furnishes a festoon curve for the critical load
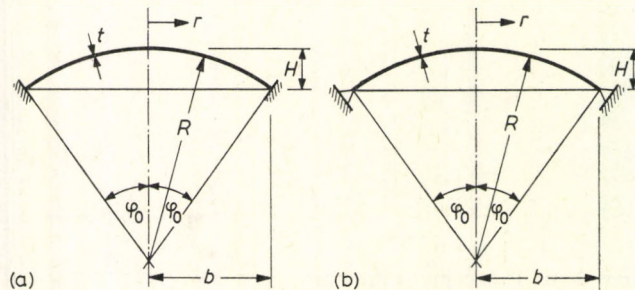
Fig. 4.9. Spherical cap.
(a) – Clamped, (b) – hinged

of this cap with a horizontal lower tangent, which coincides with the linear critical load (4.7) of the perfect complete sphere [4.3], [4.13]. Hence, the spherical cap supported in this way tends to buckle almost exactly like the complete sphere.
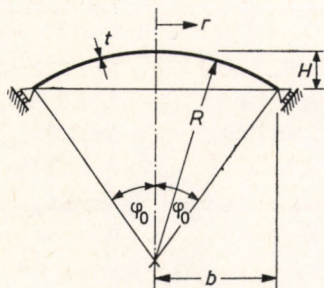
Fig. 4.10. Spherical cap supported by rollers

However, if the edge of the spherical cap is clamped or hinged (see Fig. 4.9), the shell — even if it was geometrically perfect — undergoes bending under the load before buckling, since the spherical cap gets compressed, while the support, being considered as infinitely rigid, does not. In certain cases this bending deformation has a shape of the same character as the buckling deformation, while in other cases it has the opposite character. Computations show that this behaviour depends on the geometric parameter

$$\lambda = 2\sqrt[4]{3(1-v^2)}\sqrt{\frac{H}{t}} = 2.63\sqrt[4]{1-v^2}\sqrt{\frac{H}{t}} \tag{4.11}$$

with H being the height of the cap (see Fig. 4.9). (The diameter of the cap, i.e. the radius of the sphere, does not appear in λ.)

The diagrams of Fig. 4.11 (a) show, on the basis of [4.3], the change in the slope of the *clamped* cap (see Fig. 4.9 (a)) due to bending for some values of λ. On the other hand, Fig. 4.11 (b) represents the diagrams for the change in the slope of the cap, supported as in Fig. 4.10, due to axisymmetric buckling deformation. (The cap is "most willing" to buckle in this latter way.) It can be seen that the two diagrams have similar forms for $\lambda=4$ and 10, while for $\lambda=7$ and 13 they have opposite characters.

Due to these bending deformations even the geometrically perfect spherical cap behaves as if it had an initial imperfection. Thus, its deformation corresponds to the "eccentric" curves of Fig. 1.1 (d). Using the results of [4.3], [4.35] and [4.42], in Fig. 4.12 we plotted with full lines the p_{cr}^{upper}- and p_{cr}^{lower}-values of these curves against λ. The curve of p_{cr}^{upper} has the peculiarity of oscillating about the line $p_{cr}/p_{cr}^{lin}=1$. The comparison with Fig. 4.11 shows that at λ-values, where bending
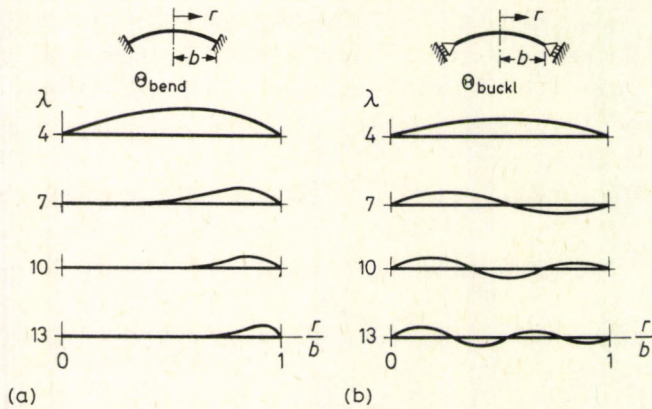
Fig. 4.11. Change in slope of the bending and buckling deformations
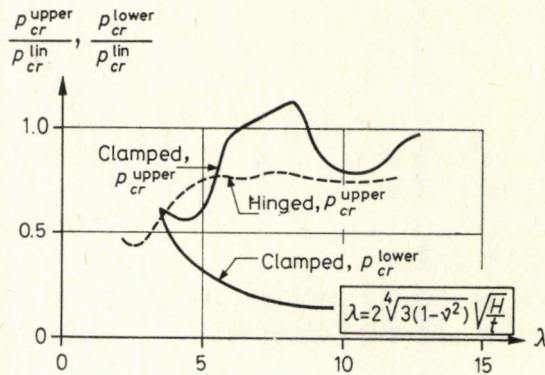
Fig. 4.12. Snapping load of the perfect spherical cap
(assuming axisymmetric buckling shape)

deformations due to the load are similar to the buckling deformation, the shell buckles at a load lower than the linear critical value, while where they are of an opposite character, the buckling load is greater than the linear one [4.3].

On the basis of [4.42], we plotted in Fig. 4.12 with a dashed line the p_{cr}^{upper}-curve of the *hinged* spherical cap (see Fig. 4.9 (b)) as well. This lies lower than that of the clamped cap, but has a similar character.

However, the p_{cr}^{upper}-curve of the clamped spherical cap according to Fig. 4.12 gives considerably higher values for the critical load than the experimental ones (see Fig. 4.3). Consequently, in order to explain this discrepancy, the *initial imperfections* of the cap have also to be taken into account. First Budiansky [4.3], then, refining the calculation, Thurston and Penning [4.37] developed a method for the investigation of the stability of clamped spherical caps with an *axisymmetric*

initial imperfection. They described the deformation of the shell by the nonlinear theory and determined the p_{cr}^{upper} according to Fig. 1.1 (d), assuming an axisymmetric buckling mode. The last-mentioned authors investigated experimentally and theoretically forty shell models which were manufactured with great care in order to produce predetermined initial imperfections. Theory and experiments corresponded fairly well except for the very thin and the "near-perfect" shells (about half of the models). Later Thurston [4.36], further improving the calculation, obtained somewhat lower p_{cr}^{upper}-values.

However, all these investigations had the shortcoming of disregarding the possibility of asymmetric buckling modes, although high-speed motion-picture recordings of the buckling process of spherical caps (e.g. [4.19]) showed that they often buckle asymmetrically, at least in one phase of the process. Thus, the phenomenon should correspond to Fig. 1.1 (e). Consequently, further theoretical investigations aimed at finding out the load intensity at which the axisymmetric deformation of the perfect spherical cap, described by the large-deflection (nonlinear) theory, bifurcates into an asymmetric mode. This bifurcation itself can be treated by the linear theory, so that a linear eigenvalue problem has to be combined with the nonlinear axisymmetric deformation. This problem was solved independently by Huang [4.13] and Weinitschke [4.42], both arriving at the same result: p_{cr}^{bifurc} is represented by a festoon curve when plotted against λ. Figures 4.13 and 4.14 show the curves for the clamped and the hinged spherical caps respectively, according to Weinitschke (n denotes the circumferential full-wave number of the asymmetric mode). The characteristic feature of these curves as contrasted to those describing the axisymmetric buckling of perfect spherical caps (see Fig. 4.12)
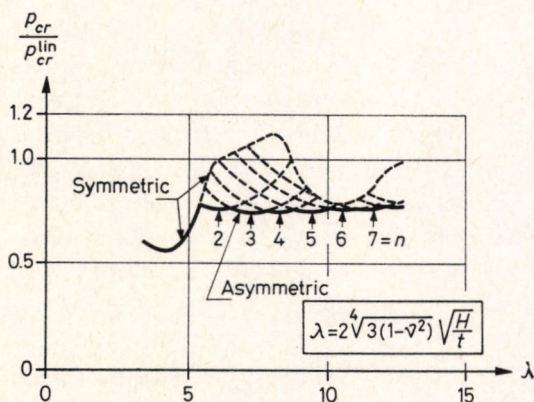
Fig. 4.13. Critical load pertaining to the asymmetric buckling which bifurcates from the axisymmetric deformation of the clamped perfect spherical cap
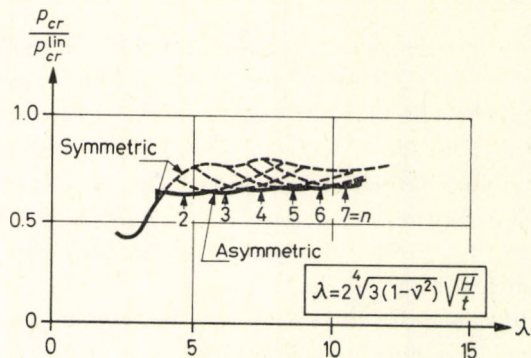
Fig. 4.14. Critical load pertaining to the asymmetric buckling
which bifurcates from the axisymmetric deformation
of the hinged perfect spherical cap

is that they do not oscillate, being rather constant and practically independent
of λ.

Archer and Famili [4.2] obtained the same curve when investigating the asymmetric vibrations of axisymmetrically deformed, clamped, spherical caps. The critical load intensity was reached when the eigenfrequency became zero.

Figure 4.13 shows that the clamped spherical cap is prone to bifurcation into asymmetric buckling for $\lambda > 5.5$ only. At smaller values of λ it buckles axisymmetrically.

This theory, considering also asymmetric buckling, agrees fairly well with the experiments made on "nearly-perfect" shells (the results of Krenzke and Kiernan, of Evan–Iwanowsky and Loo, and of Parmerter in Fig. 4.3). Still, there remained a considerable discrepancy with respect to the experiments on "less perfect" shells, suggesting that asymmetric initial imperfections should also be taken into account. These calculations, involving great mathematical difficulties, were first performed by Kao and Perrone [4.16]. Later Kao [4.16a] improved on the results using a more exact method. They assumed an initial imperfection with the section similar to Fig. 4.7 (a), extending to one quarter of the clamped cap (Fig. 4.15), and they described the deformation by the nonlinear theory of shallow shells. The maximum value of the load gave p_{cr}^{upper}. The ratio $p_{cr}^{upper}/p_{cr}^{lin}$ as a function of w_0/t was calculated for two values of λ (Fig. 4.16). These curves apparently yield the critical loads corresponding to the test results, so that they can be regarded as the final solution of the problem. (The curve pertaining to $\lambda = 8$ starts at $w_0 = 0$ from a value of $p_{cr}^{upper}/p_{cr}^{lin}$ greater than 1, corresponding to Fig. 4.12.)

Kao and Perrone also investigated the influence of the shape in the ground plan of the initial imperfection. They found that when the central angle of the imperfection in Fig. 4.15 is decreased from $90°$ to $45°$, this hardly influences the snapping load.

It seems from the foregoing that the buckling problem of spherical caps has been completely solved. There are, however, some experimental results which give higher critical loads than the theoretical curve of Fig. 4.13 [4.10b], [4.33a], [4.33b]. Since this phenomenon has not been rationally explained yet, it shows that there are still some problems to be clarified.

If we compare the theoretical results on the *complete sphere* and on the *clamped* (or hinged) *spherical caps* we arrive at the following conclusions:

When investigating the buckling of a complete sphere, the shell may be divided into two parts [4.21]: a shallow cap that buckles, and the remaining part that undergoes only slight deformation due to the joining conditions. Hence, the clamped cap differs from the complete sphere only in being supported against displacement and rotation along the edge somewhat more rigidly, which results in a critical load greater than (or at least equal to) that of the complete sphere. The critical load of the hinged cap may possibly be lower than that of the complete sphere. This explains why the curves for the snapping loads of the complete sphere and of the spherical cap are nearly identical. A detectable discrepancy is to be
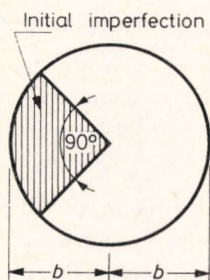
Fig. 4.15. Ground plan of the assumed asymmetric initial imperfection
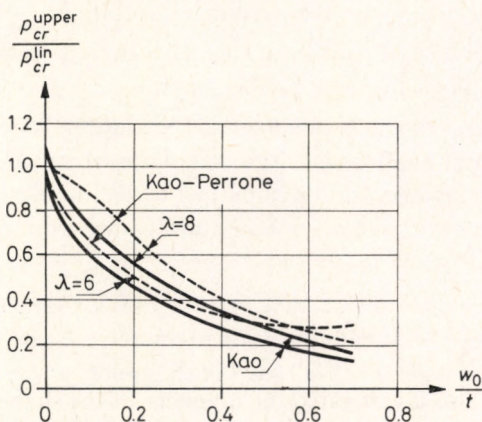
Fig. 4.16. Influence of the asymmetric imperfection on
the snapping load of the clamped spherical cap

expected only if the extension of the cap is less than the buckle which develops on the complete sphere, i.e. for small λ-values.

The similarity between the behaviour of the complete sphere and that of the cap also explains why complete spherical shells buckle axisymmetrically, or why the results of the axisymmetric buckling investigations on complete shells can be used for design (see Fig. 4.6). It was shown that the complete sphere is most sensitive to imperfections with λ-values around 3. These spherical shells behave in a similar way to caps with approximately the same λ-s. As Fig. 4.13 shows, caps are not prone to buckle asymmetrically if $\lambda < 5.5$. Bushnell [7.4] found, in fact, that complete spherical shells are inclined to buckle asymmetrically if λ is greater than about 6 [1.2].

It is also obvious from the foregoing that if the support of the spherical cap is weaker than that provided by the adjacent part of the shell (when imagining that the cap is part of a complete sphere), then the critical load of the cap is less than that of the complete sphere. Shells with a polygonal ground plan and supported by diaphragms with no bending rigidity belong to this group.

Figures 4.6 and 4.16 enable us to design spherical shells against buckling. We only have to assume in our computation the imperfection amplitudes to be expected. However, these diagrams do not contain the circumstances mentioned under (b,) (c), (d) and (e), in the description of the model tests (Figs 4.2, 4.3), i.e. the weakness of the supports, the non-circular ground plan, the non-spherical shape, and the material properties of the reinforced concrete. Nevertheless, the test results of Figs 4.2 and 4.3 could sufficiently be explained only by taking all these circumstances into account. These effects cannot be analysed exactly yet, so we try to make allowance for them by half-empirical methods based on model tests and approximate calculations, to be surveyed in what follows.

The material properties of *reinforced concrete* can approximately be taken into consideration as outlined in Section 9.8.

Since local *plastic yielding* may also explain the low critical load of some models, some recent theoretical analyses give the maximum stress value that arises in the vicinity of the buckle. However, this cannot be taken into account in a practically usable way yet, so that we have to content ourselves with the approximate method described in Section 9.4.

Of the approximate methods we first present the *half-empirical formula* established on the basis of the already mentioned test series by Klöppel and Jungbluth [4.19]. For the critical uniform radial load of the spherical cap they write (see Fig. 4.9):

$$p_{cr} = k(\varphi_0) k\left(\frac{R}{t}\right) 0.3 E \frac{t^2}{R^2}, \qquad (4.12)$$

where

$$k(\varphi_0) = 1 - 0.175 \frac{\varphi_0 - 20°}{20°}, \tag{4.13a}$$

and

$$k\left(\frac{R}{t}\right) = 1 - 0.07 \frac{R}{400t}. \tag{4.13b}$$

This formula is valid between the limits

$$20° \leq \varphi_0 \leq 60°, \tag{4.14a}$$

$$400 \leq R/t \leq 2000. \tag{4.14b}$$

Formula (4.12) actually completes that of Kármán and Tsien (4.8), and that improved by Tsien (4.9), by the factors $k(\varphi_0)$ and $k(R/t)$. For the sake of lucidity we compiled their extreme values in Table 4.1

Table 4.1

Values of the factors $k(\varphi_0)$ and $k(R/t)$
appearing in Eq. (4.12)

$\varphi_0 =$	20°	60°
$k(\varphi_0) =$	1.0	0.65

$R/t =$	400	2000
$k\left(\dfrac{R}{t}\right) =$	0.93	0.65

Equation (4.12) gives theoretically p_{cr}^{lower} of the perfect spherical cap (see Figs 1.4 (c), 4.4). In fact, we may regard it as the p_{cr}^{upper} of the imperfect shell, since this latter value was measured in the experiments. The imperfection amplitude corresponding to the factor 0.3 is, according to Fig. 4.16, $w_0/t \approx 0.4$.

The scatter of the test results around the value of Eq. (4.12) was at maximum $\pm 20\%$. The metal shells were supported by squeezing their plane edges between two rings to be regarded as infinitely rigid.

In order to assess the influence of the support stiffness on the critical load, Klöppel and Roos [4.20] performed a series of experiments in which the spherical caps — like the reservoirs — are connected to cylinders welded at the joints without edge rings (Fig. 4.17). The pressure acted only on the spherical cap. Varying the ratio of the wall thicknesses t_s of the sphere and t_c of the cylinder, they found that

the critical load (4.12) still has to be multiplied by the factor

$$\lambda_1 = 0.65\left(1 + \frac{R/t_s}{400 + R/t_s}\right)(\Phi_M + 0.5)\cos\varphi_0, \tag{4.15}$$

where

$$\Phi_M = \frac{\varkappa}{1+\varkappa}, \tag{4.16a}$$

$$\varkappa = \sqrt{\frac{b}{R}}\sqrt{\left(\frac{t_c}{t_s}\right)^3}, \tag{4.16b}$$

and

$$t_c/t_s \leq 2.5. \tag{4.17}$$
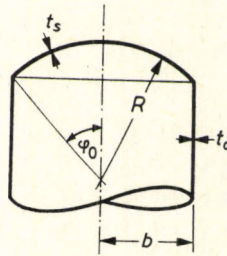
Fig. 4.17. Spherical cap joining a cylindrical shell

The values of λ_1 valid for $b/R = 1/3$ and $R/t_s = 1000\sim2000$ are indicated in Table 4.2.

Table 4.2

Values of the factor λ_1 appearing in Eq. (4.15)

If $t_c/t_s =$	0	1	2.5
then $\lambda_1 =$ (depending on R/t_s)	0.53~0.57	0.9~1.0	1.25~1.35

The deviation of the experimental results from Eq. (4.12) multiplied by Eq. (4.15) was at maximum $+23\% \sim -11\%$.

These data give valuable information on the influence of the supporting edge: if the edge has no rigidity against rotation at all ($t_c/t_s = 0$), then this reduces the critical load of the cap supported as in the experiments of Klöppel and Jungbluth [4.19] to about half its value. The clamping effect of the cylindrical wall reaches that of the support used by Klöppel and Jungbluth at about $t_c/t_s = 1$, while thicker cylinder walls obviously further increase p_{cr}. This effect is, in fact, obvious when

we consider that shell models in most cases started to buckle asymmetrically near the edges.

As far as we know, the test series of Klöppel and Roos was the first systematic attempt to investigate the influence of support stiffness on the critical load of spherical caps. The same problem was treated theoretically by van Koten and Haas in an approximate way [4.23], [4.24]. They tried to compare the rigidity of the circular edge ring of the spherical cap with that of the "missing" part of the shell. They considered the rigidity of the ring effective against rotation caused by uniformly distributed twisting moments, but they disregarded the elongation of the ring. The derivation followed that of Kármán and Tsien [4.18] and of Tsien [4.38] — see Eqs (4.8)–(4.9) and the remark to Eq. (4.12). Their results can be summed up as follows:

When we know the stiffness s_{shell} of the spherical cap against uniformly distributed bending moments acting on its edge

$$s_{shell} \approx \frac{Et^3}{4\sqrt{Rt}}, \tag{4.18}$$

and the stiffness of the edge ring s_{ring} against the same moments (appearing now as twisting ones):

$$s_{ring} = \frac{EI_{ring}}{(R \sin \varphi_0)^2}, \tag{4.19}$$

(where I_{ring} is the moment of inertia of the edge ring referred to the axis lying in the plane of the ring), we have to compute the parameter

$$\alpha_1 = \frac{2}{1 + \dfrac{s_{shell}}{s_{ring}}} \leqq 2. \tag{4.20}$$

The critical load can be determined from the "generalized" Eqs (4.8)–(4.9)

$$p_{cr} = cE \frac{t^2}{R^2}. \tag{4.21a}$$

The value of the factor c can be closely approximated by the simple formula:

$$c = 0.010 + 0.155\alpha_1. \tag{4.21b}$$

According to van Koten and Haas, $\alpha_1 = 2.0$ corresponds to the case of the complete spherical shell.

From the results of van Koten and Haas it can be seen that p_{cr} depends on both the half central angle φ_0 and the stiffness of the edge ring, but in a different way than that given by the formulas of Klöppel and Roos [4.20]. Accordingly,

this problem cannot be considered as definitely solved yet. Be that as it may, the formula of van Koten and Haas yielded a result for the test shell of Torroja and Schubiger [4.30] very close to that obtained in the experiment, although this latter was exceptionally low (see Figs 4.2 and 4.3).

A more exact analysis was performed by Bushnell [4.4a] who took into account the extensional rigidity of the ring as well. He followed the (initially) axisymmetric deformation of the spherical cap by the nonlinear theory and determined the load intensity at which asymmetric bifurcation occurs. For the cases of built-in, hinged and roller-supported edges (i.e. zero displacement and rotation, zero displacement and unprevented rotation, and unprevented displacement and rotation of the edge) he obtained upper critical load intensities of $0.790 p_{cr}^{\text{lin}}$, $0.690 p_{cr}^{\text{lin}}$ and $0.160 p_{cr}^{\text{lin}}$ respectively. Here p_{cr}^{lin} again means the value defined by Eq. (4.7).

Wang, Rodriquez–Agrait and Litle [4.40] investigated experimentally the influence of the stiffnesses of these three kinds of support on the critical load on fifty-two spherical PVC caps. They obtained $0.635 p_{cr}^{\text{lin}}$, $0.530 p_{cr}^{\text{lin}}$ and $0.190 p_{cr}^{\text{lin}}$ as average values for the clamped, hinged and roller-supported edges respectively, these being in acceptable agreement with the results of Bushnell. The discrepancy between the experimental and theoretical values might be accounted for by the fact that Bushnell did not take initial imperfections into account. The imperfections affected the experimental critical loads considerably in the first two cases, but much less in the third case because of the much greater bending deformation.

The above results show that the edge rigidity against rotation has far less influence on the critical load than its extensional rigidity, effective against displacement.

4.2. Spherical Caps under Partial Loads

4.2.1. Buckling of Spherical Caps under One-Sided Load

The buckling of spherical caps under one-sided uniform load was investigated experimentally by Klöppel and Roos [4.20]. We shall not be dealing here with this problem in detail, but only state that the intensity of the one-sided load causing buckling is close to that of the uniform load. A similar conclusion can be drawn from the calculation of Famili and Archer [4.9a].

However, we may remark that according to [9.2.3] the load intensity causing symmetric snapping of a flat arch becomes lower if it is arranged partially instead of over the whole arch; i.e. if we leave the two extreme sections of the arch that displace upwards unloaded. This reduction of the critical load intensity of the arch, if it is loaded by a single concentrated load applied at the centre, can even

be 30%. (In this case the concentrated load distributed over the central portion of the arch, displacing downwards during buckling, is to be regarded as load intensity.) Since we shall not deal with the most onerous arrangement of the partial load acting on a spherical cap in detail, the above information may be used for assessing this effect.

4.2.2. Buckling of Spherical Caps under a Centrally Applied Concentrated Load

The buckling problem of a clamped spherical cap under a centrally applied *concentrated load* was solved by Fitch [4.9b]. The critical load P_{cr} was made dimensionless as follows (Fig. 4.18):

$$Q_{cr} = \frac{P_{cr} R}{2\pi B},\qquad(4.22)$$
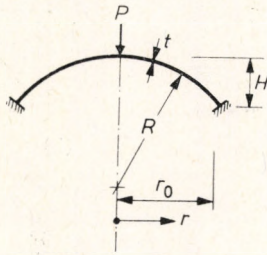
Fig. 4.18. Spherical cap under a concentrated load

R again being the radius of the sphere and B the bending rigidity of the shell:

$$B = \frac{Et^3}{12(1-v^2)}.\qquad(4.23)$$

The value of Q_{cr} as plotted against the geometric parameter λ of the shell (4.11) is given (for $v=1/3$) by the diagram of Fig. 4.19 (a) where n denotes the wave number of the buckle mode in the circumferential direction. (The dashed lines are theoretical values, the full lines are relevant.) Accordingly, $n=0$ denotes axisymmetric, and $n\geq1$ asymmetric, buckling modes. In the case of $\lambda<7.8$ neither snapping nor bifurcation develop: the load-deflection curve has the shape of Fig. 4.20 (a). In the range $7.8\leq\lambda\leq9.2$ the curve has a maximum (Fig. 4.20 (c)), i.e. snapping occurs, but these maxima are quite gentle and approach a point of inflexion, as λ tends to 7.8 (Fig. 4.20 (b)). For $\lambda>9.2$ asymmetric bifurcation occurs before the snapping load intensity is reached (Fig. 4.20 (d)). These bifurcation points are
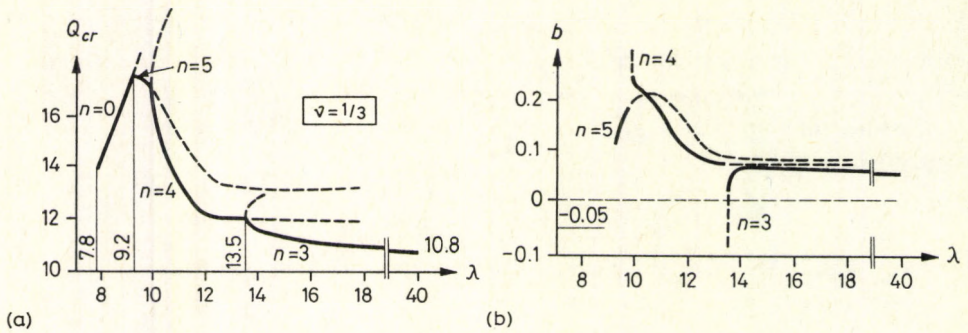
Fig. 4.19. Critical concentrated load and initial post-buckling behaviour of the spherical cap
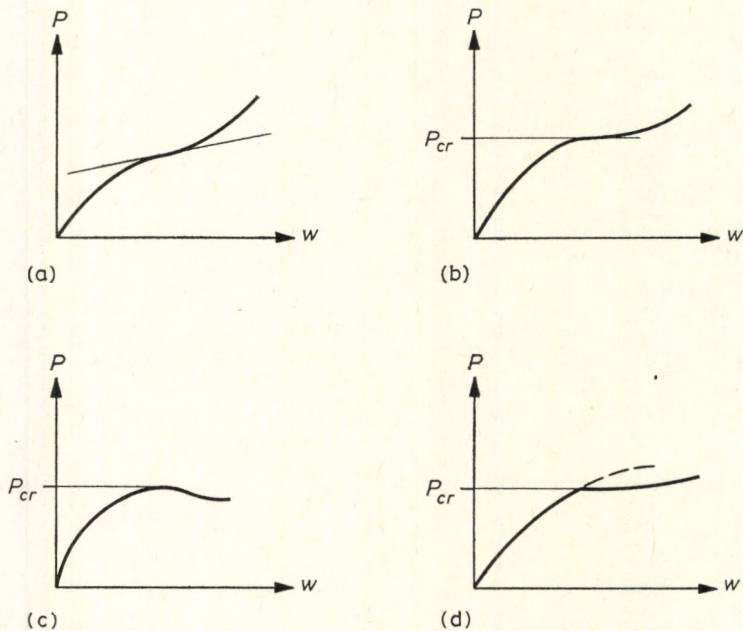
Fig. 4.20. Possible load-deflection paths of the spherical cap

indicated as critical loads at $\lambda > 9.2$ in Fig. 4.19 (a). Finally, if $\lambda \rightarrow \infty$, then $Q_{cr} \rightarrow \rightarrow 10.8$. For such large λ-s the buckling deformation is confined to the environment of the apex, so that this asymptotic value can be taken as the critical load of a complete spherical shell under two diametrically opposite concentrated loads.

The quantity b, which is characteristic of the initial tangent to the post-buckling load-deflection curve, is plotted in Fig. 4.19 (b) against λ. It can be seen that at $\lambda > 9.2$, b is always positive.

We show — according to the calculations of Fitch — the axisymmetric defor-
mation shape valid at the bifurcation critical load intensity $Q_{cr}=13.28$ for $\lambda=11$
in Fig. 4.21 (a), and in Fig. 4.21 (b) the asymmetric mode that bifurcates from the
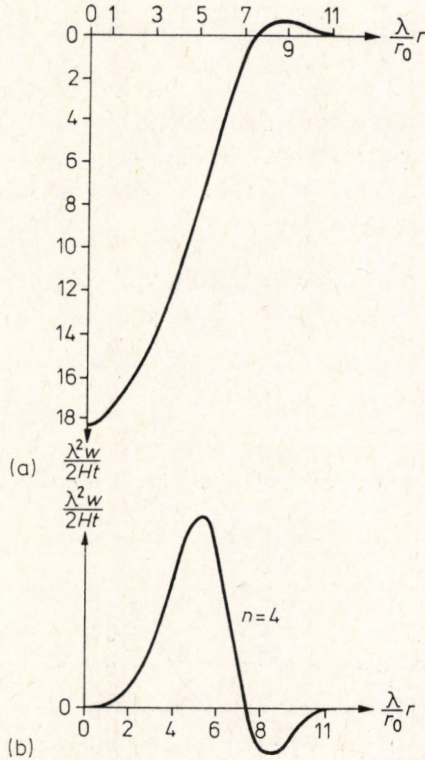
Fig. 4.21. Shapes of the axisymmetric deformation
and of the bifurcating asymmetric buckling mode for $\lambda=11$

former one. The diagrams show that at $\lambda=11$ the buckling mode extends to the
whole surface of the shell.

Fitch found that his results qualitatively agree with those of the model tests
reported on in the literature.

When *uniformly distributing the load over a circular area of radius* $\bar{r}$ (Fig. 4.22),
Fitch and Budiansky [4.9c] obtained for a built-in spherical cap with $\lambda=12$ (and
$v=1/3$) the results shown in Fig. 4.23. They introduced the notations:

$$\bar{p}_{cr} = \frac{p_{cr}}{p_{cr}^{lin}}, \qquad (4.24)$$

the ratio of p_{cr}, which acts over an area of radius $\bar{r}$, to the linear (classical) critical load p_{cr}^{lin} of a complete sphere loaded by overall radial pressure (4.7); further the geometric parameter, characteristic of the loaded surface:

$$\bar{\lambda} = \sqrt[4]{12(1-v^2)}\,\frac{\bar{r}}{\sqrt{Rt}}. \tag{4.25}$$

Figure 4.23 shows that up to $\bar{\lambda} \leq 2$, the buckling phenomenon does not differ essentially from that under a concentrated load ($\bar{\lambda}=0$). That is, from the axisymmetric deformation shape an asymmetric buckling mode bifurcates, and the post-buckling load-deflection curve has a positive initial slope ($b>0$ in Fig. 4.23 (b)).
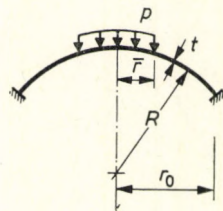
Fig. 4.22. Spherical cap under a load distributed over a small circular area

(a)

(b)
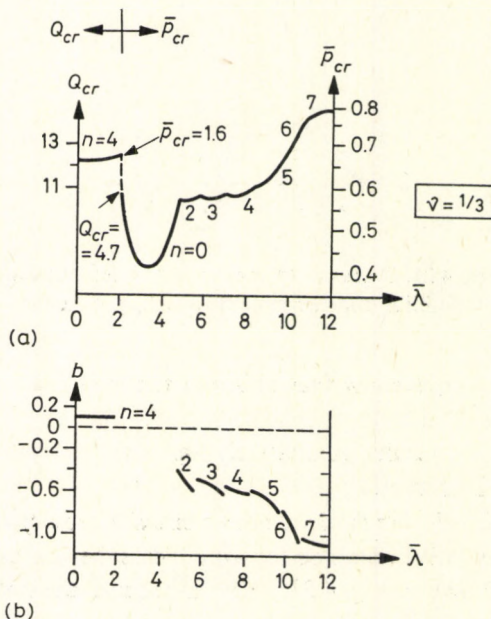
Fig. 4.23. Critical load intensity and initial post-buckling behaviour
of the spherical cap of Fig. 4.22 with $\lambda=12$

If the radius $\bar{r}$ of the loaded area is increased $(2<\bar{\lambda}<4.8)$, the axysimmetric load-deflection curve will have a peak, i.e. the shell will snap through before any bifurcation occurs. Hence, the sudden drop of the critical load intensity at $\bar{\lambda}=2$ is not due only to the change in the critical load parameter from Q_{cr} to $\bar{p}_{cr}$.

If $\bar{\lambda}>4.8$, bifurcation occurs before snapping, and at the same time the quantity b characteristic of the initial tangent of the post-buckling load-deflection curve becomes negative: the load bearing capacity becomes decreasing and the critical load will depend on the initial imperfections.

The limit $\bar{\lambda}<2$ for a positive b can be written (with $v=1/3$), by expressing $\bar{\lambda}$ with the help of (4.25) by the radius $\bar{r}$ of the loaded area, as

$$\bar{r} < \sqrt{Rt}. \tag{4.26}$$

In Fig. 4.24 we show the results of similar calculations by Fitch and Budiansky for the limiting case $\lambda \to \infty$. Since in the range $2<\bar{\lambda}<8$ these results are very close to those for $\lambda=12$, we may consider the critical loads computed for $\lambda=\infty$ as valid
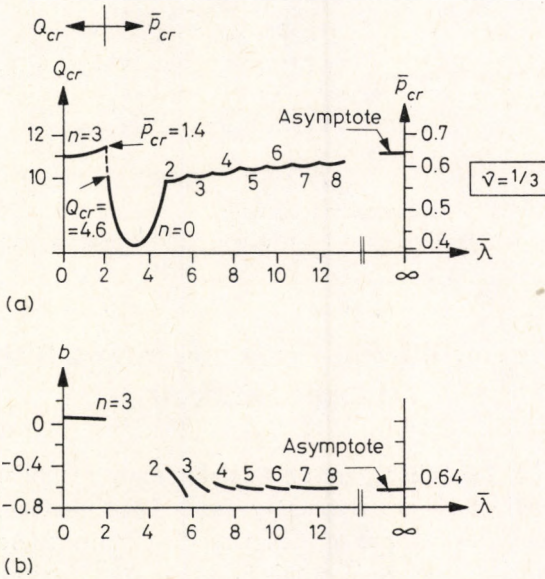
Fig. 4.24. Critical load intensity and initial post-buckling behaviour of the spherical cap of Fig. 4.22 with $\lambda \to \infty$

for $\lambda>12$ also, provided $2<\bar{\lambda}<(\lambda-4)$. In other words, in the range $\lambda>12$ the boundary conditions practically do not affect the buckling process, provided the distance between the edge of the loaded area and the shell edge is not less than 4λ.

The simultaneous action of overall uniform load p and a centrally applied concentrated load P on a clamped spherical cap was investigated by Loo and Evan-

Iwanowski [4.25a]. Their results, also confirmed by experiments, are shown (for $v=1/3$) in Fig. 4.25. The interaction curves, pertaining to different values of the geometric parameter λ (4.11), represent those intensities of the concentrated and distributed loads that cause buckling when acting together.

The left end points of the curves indicate the lower bounds for the uniform load intensity p below which no concentrated load intensity can produce buckling when acting simultaneously (i.e., the load-deformation curve will have no peak, cf. Figs 4.20 (a) and (b)).
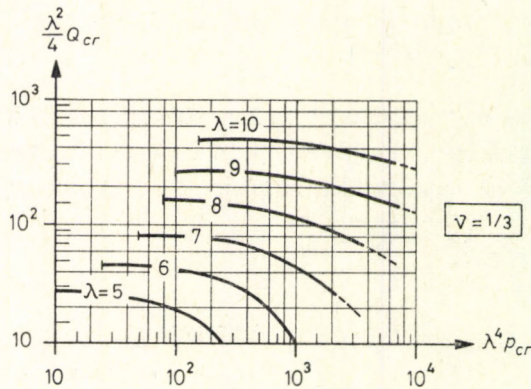
Fig. 4.25. Interaction curves of concentrated and
uniformly distributed loads acting on the spherical cap

4.3. Domes of Different Curvatures in Two Directions (Elliptic Surfaces)

In engineering practice other than spherical domes over circular, elliptic, rectangular, or polygonal plans are frequently used. Their mathematical treatment involves great difficulties because of their variable curvature. Accordingly, many less investigations have been made in this field than on spherical shells. In design the formula

$$p_{cr} = cE\frac{t^2}{R_1 R_2} \tag{4.27}$$

is frequently used. It may be considered as the generalization of that derived for spherical shells, substituting the product of the two main radiuses of curvatures $R_1 R_2$ for the square of the radius of the sphere, while the numerical value of the constant c is assumed according to the explanation given for the sphere or on

the basis of experiments [4.6], [4.29]. The experimental results of non-spherical shells were plotted in Figs 4.2 and 4.3 accordingly.

In the following we investigate the validity of Eq. (4.27). The buckling of shells with different principal curvatures was investigated by Dulácska [4.8] using the linear shallow-shell theory. In addition to the ratio of the two radiuses of curvature, he also varied the ratio of the compressive forces (n_1 and n_2) acting in the directions of the principal curvatures. As a result, he obtained (with $v=0.27$) the surface shown in Fig. 4.26, representing the critical load p_{cr} perpendicular to
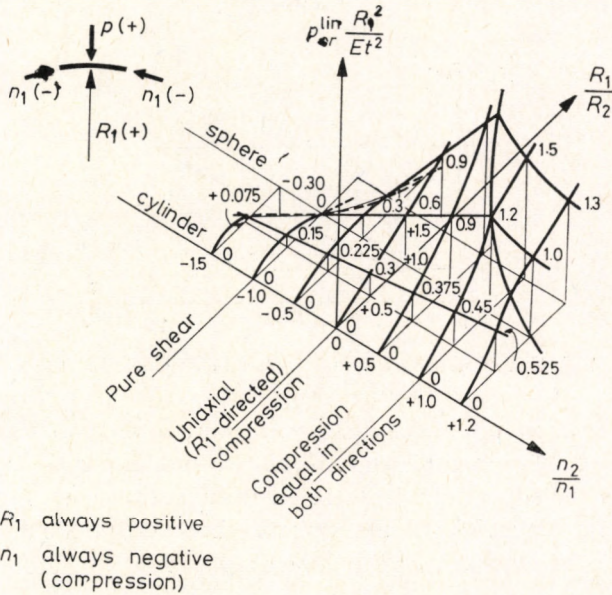
Fig. 4.26. Linear critical loads of doubly curved shells versus the ratios of the two radiuses of principal curvatures and of the compressive stresses arising in these directions

the shell surface. The derivation disregarded the stiffening effect of the edges, so that the results are valid only for shells which buckle in several waves, that is, when the boundary conditions have little influence. Consequently, the shell can also be regarded as shallow in the region of one buckle.

Figure 4.26 shows that the linear critical load of the sphere in the case of $n_1=n_2$ assumes an extreme peak value as compared to other cases of $n_1 \neq n_2$. This also explains the great imperfection sensitivity of the radially compressed sphere, i.e. its rapidly decreasing post-buckling load bearing capacity.

Figure 4.26 also shows that in using Eq. (4.27) we commit a slight error to the detriment of safety with respect to the linear critical load. That is, Eq. (4.27) may be represented by the straight line of Fig. 4.27. When keeping R_1 constant

and increasing R_2 from R_1 to infinity, the (linear) critical load decreases from that of the sphere to the value zero of the hydrostatically compressed (infinitely long) cylinder. (The reason, why a zero value for p_{cr} was obtained, in contradistinction to the finite values given by Eqs (2.29), is that in the frame of the shallow-shell theory an open cylindrical segment, having no edge stiffeners, was investigated.) This corresponds to some section of Fig. 4.26 starting from the point characterized by $R_1/R_2=1.0$ and $n_2/n_1=1.0$. The direction of this section depends on the ratio n_2/n_1 valid for the cases $R_1 < R_2$. In any case, it will be a curve bulging downwards as contrasted to the straight line of Fig. 4.27.
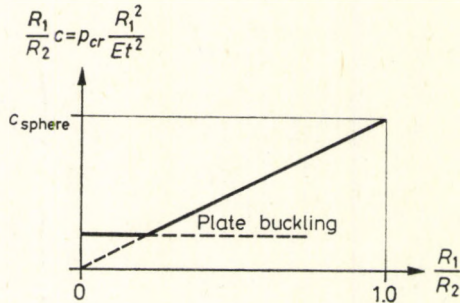
Fig. 4.27. Graphical representation of the approximate formula (4.27)

Figure 4.26 loses its validity at $R_1/R_2 \to 0$ because in this case the buckle ceases to be "local", i.e. of limited dimensions, but expands as far as possible and will be confined by the edges only. In these cases the critical load, in fact, does not become zero, but it remains at least as great as that corresponding to the buckling stress of a plain plate which has the same dimensions as the ground plan of the
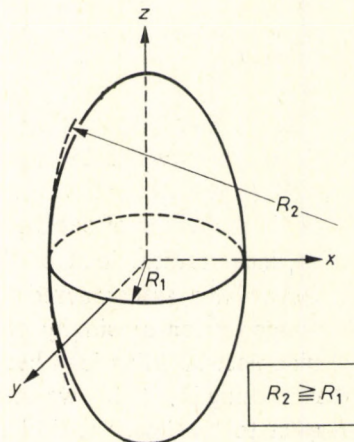
Fig. 4.28. The investigated ellipsoid of revolution

shell. The straight line of Fig. 4.27 will also not be valid as far as to zero. Its lower limit of validity is rather given by the horizontal straight line of the plate buckling.

On the basis of the linear theory, Hyman and Healey [4.15] computed the critical hydrostatic pressure of the ellipsoid of revolution shown in Fig. 4.28, assuming $v=0.3$. (They used the energy method requiring, in the framework of the linear theory, the consideration of the second power terms of the displacement components.) On the basis of experimental evidence they assumed that the buckling occurs in the vicinity of the plane xy, so that they considered the shell as shallow along the osculating circle with the radius R_2, but they did not use this assumption along the circle with radius R_1. Consequently, their derivation remained sufficiently accurate in the case of $R_2 \to 0$ as well, despite the small circumferential wave number along the circle R_1 (as contrasted to the Donnell equations, cf. what was said in Section 2.3). They confined their investigation only to n_2/n_1 values arising in the closed surface of revolution (Fig. 4.28) under hydrostatic pressure. These compressive forces are in the vicinity of plane xy:

$$n_1 = -\frac{pR_1}{2}\left(2 - \frac{R_1}{R_2}\right), \tag{4.28a}$$

$$n_2 = -\frac{pR_1}{2}, \tag{4.28b}$$

their ratio being:

$$\frac{n_2}{n_1} = \frac{1}{2 - \dfrac{R_1}{R_2}}, \tag{4.29}$$

while their shares in carrying the load are:

$$p_1 = \alpha p = -\frac{n_1}{R_1} = \left(1 - \frac{R_1}{2R_2}\right) p, \tag{4.30a}$$

$$p_2 = (1-\alpha)p = -\frac{n_2}{R_2} = \frac{R_1}{2R_2} p. \tag{4.30b}$$

Here α denotes the ratio of the load parts carried by internal forces in the two principal directions.

The result of Hyman and Healey is very close to that of Dulácska computed for ratio (4.29), see Fig. 4.26. The small difference is due to the afore-mentioned circumstance that they did not consider the shell as shallow in the plane xy. Hence, they obtained also in the case $R_2 \to \infty$ (hydrostatically compressed cylinder) a finite critical load. Moreover, their critical load depends on the ratio t/R_1 as well (when $R_1 \neq R_2$).

Nonlinear buckling investigations of shells with different principal curvatures were first carried out by van Koten and Haas [4.24]. They calculated the p_{cr}^{lower} of

the geometrically perfect shell, as interpreted in Fig. 1.4 (c), by using the Kármán–Tsien method (cf. also Fig. 4.4). For the value 1/2 of the load distribution factor α, as defined by Eqs (4.30), they obtained the full line upper curve of Fig. 4.29. Assuming $R_1/R_2 = 0.25$ they calculated p_{cr}^{lower} for other α-values too and found them to be practically independent of α.

The Eq. (4.27), p_{cr} considered as p_{cr}^{lower} (with a constant factor c), is represented by the slanting dashed line in Fig. 4.29.

To evaluate the results of van Koten and Haas we have to consider that, due to calculation difficulties, they assumed the edge of the buckle to lie on a plane ellipse. Thus, the geometry of the shell determines the ratio of minor and major axes, so that only two free parameters remain: the extension and the amplitude of the buckle. Due to these constraints it was not possible to allow for the distortion of the buckle in the case of other α-values (other n_2/n_1 ratios). Moreover, we do not even know for which α-value the assumed buckle shape best approximates to reality. Besides, for small ratios R_1/R_2 (with the limiting case of the hydrostatically compressed cylinder), the antisymmetric buckling mode may also be onerous, which was not considered in this procedure. Due to all these circumstances the method yields a greater critical load than the actual one.
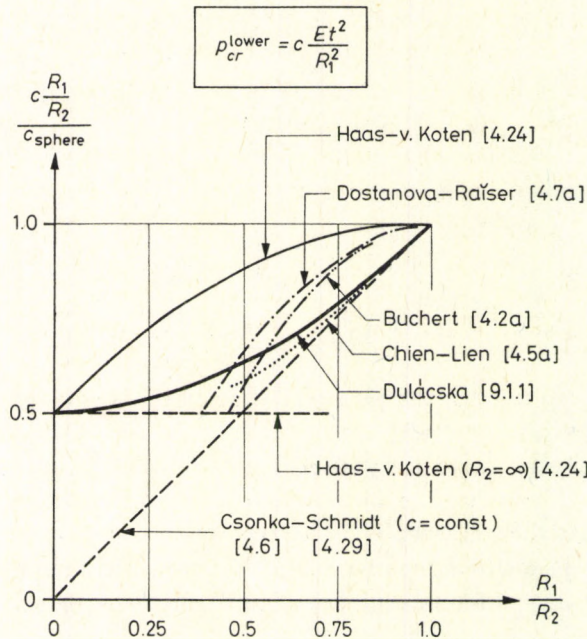

Fig. 4.29. Results of approximate post-critical analyses of shells having different curvatures in the two principal directions

Several other authors investigated the buckling problem of a geometrically perfect elliptic paraboloid shell having different curvatures in two directions. Buchert [4.2a] and, moreover, Dostanova and Raĭzer [4.7a], obtained results that lie in the range $0.5 < R_1/R_2 < 1.0$, between Eq. (4.27) and those of van Koten and Haas. Chien and Lien [4.5a] assumed an ellipse-shaped buckle, and in addition, complete preventing of displacement and rotation along the boundary of the buckle. Using the Galerkin method, they obtained, in the range $0.5 < R_1/R_2 < 1.0$, results which osculate that given by Eq. (4.27). Dulácska [9.1.1] approximated the buckling surface by two arches crossing each other and, using the energy method, arrived at the following expression for the critical load:

$$p_{cr}^{lower} = \frac{c_{sphere}}{2} E t^2 \left(\frac{1}{R_1^2} + \frac{1}{R_2^2} \right). \tag{4.31}$$

All these results are plotted in Fig. 4.29.

The investigation showed that the curve describing the post-buckling behaviour lies higher than the slanting straight line of constant c. This contradicts the explanation given to Fig. 4.26. This apparent contradiction was eliminated by the more detailed investigation of the post-buckling behaviour of the hydrostatically loaded ellipsoid of revolution shown in Fig. 4.28, carried out by Danielson [4.7] by the method of Koiter. In this case, the values of α corresponding to different R_1/R_2 ratios are defined by Eqs (4.30), yielding $\alpha = 1/2$ for $R_1 = R_2$. Danielson found the sphere $(R_1/R_2 = 1)$ to be most sensitive to initial imperfections: its post-buckling load bearing curve drops most abruptly (see Fig. 4.4). This sensitivity to imperfections decreases when the ratio R_1/R_2 differs from unity, and it soon approaches the behaviour of the hydrostatically compressed infinitely long cylinder $(R_2 \to \infty)$ characterized by Fig. 1.1 (a). This phenomenon is in accordance with Fig. 4.26 too: the peak value of the linear critical load in the case of $R_1 = R_2$ (and $n_1 = n_2$) explains the great sensitivity to imperfections. (The phenomenon is similar to the behaviour of the axially compressed cylinder as outlined in connection with Fig. 2.9.)

In summary, we may consider Eq. (4.27) applicable for practical purposes in the range $0.5 < R_1/R_2 < 1.0$. However, in the range $0 < R_1/R_2 < 0.5$ we may use Eq. (4.27) with the value corresponding to $R_1/R_2 = 0.5$. Due to the approximations in the methods presented, along with the fact that the computation of Danielson refers to a single value α for every R_1/R_2 ratio, it seems expedient to assume a safety factor somewhat greater than usual if the parameters of the shell in question differ from those assumed in the above mentioned investigations. This increased safety factor may be reduced in the future if more exact investigations determine p_{cr}^{upper} for every R_1/R_2 and α.

5. Stability Problems of Shells with Negative Gaussian Curvature (Hyperbolic Shells)

Hyperbolic paraboloid ("hypar") shells are frequently used as roofs supported either along its generatrices (see Fig. 5.4) or along its lines of principal curvatures ("saddle-shaped" shell, Fig. 5.1). Hyperbolic shells of revolution are mostly used as cooling towers (see Fig. 5.14). Since this kind of shell is prone to develop inextensional deformation, which may influence its stability, we have to deal briefly with this phenomenon as well.

5.1. Inextensional Deformation of Hyperbolic Shells

Certain hyperbolic shells are able to develop inextensional deformation under boundary conditions that would ensure rigidity in the case of other kinds of shells. (The inextensional deformation consists of bending and twist only, so that merely the bending and twisting rigidities of the shell play a part, the extensional ones are of no importance.) Vlaszov [5.32] showed interesting examples of this phenomenon. The theory of inextensional deformations was developed for the saddle-shaped hypar by Geyling [5.7], [5.8]. His results can be summed up as follows:

If a saddle-shaped hypar is supported by diaphragms which are rigid only in their own plane while perpendicularly to it they are entirely soft (Fig. 5.1), then the shell is capable of developing inextensional deformation in every case when, starting from an edge point, we can return to the same point after proceeding along a finite number of straight generatrices joining each other (Fig. 5.2). The
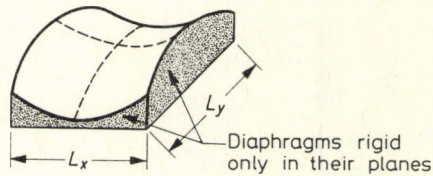
Fig. 5.1. Saddle-shaped hyperbolic paraboloid
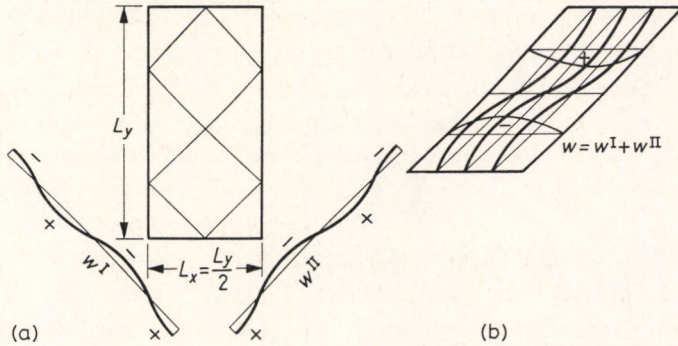
Fig. 5.2. Inextensional deformation of the saddle-shaped hypar

more times we have to go round before returning, the smaller are the wavelengths with which the shell has to develop the inextensional deformation. With decreasing wavelengths, on the one hand the bending rigidities of the shell hinder this deformation more and more, and, on the other hand, the wavelengths become much smaller than those of the buckling shape, and consequently they become less and less onerous.

However, if the shell has the shape shown in Fig. 5.2, where a hypar with two rows of straight generatrices perpendicular in ground plan is depicted, then the inextensional deformation comes about with large wavelengths, i.e. the shell becomes very "soft". Since it is this type of hypar that is able to carry uniform load with membrane forces only, without exerting horizontal thrust at the supports [2.17], [2.35], and that is readily used in engineering practice, the significance of the problem is not purely theoretical.

The inextensional deformation consists theoretically of the sum of two cylindrical deformation surfaces parallel to the straight generatrices (Fig. 5.2 (a)). The curves w^I and w^{II} hence represent two surfaces that have constant ordinates along one row of generatrices. Their sum produces the total inextensional deformation shown in Fig. 5.2 (b). As can be seen, this is a "reticulated" deformation pattern with ordinates $w=0$ along the edges.

Now, if such an inextensional deformation coincides with the buckling mode of the shell, its critical load — or more exactly the system of internal forces caused by this load — corresponds to that of a flat plate of the same ground plan buckling in the same mode.

This inextensional deformation requires horizontal displacements along the edges of the saddle-shaped hypar (see Fig. 5.1). These displacements are compatible with the diaphragms described earlier.

The hypar confined as shown in Fig. 5.4 behaves quite differently. It can be considered as the internal part of the shell in Fig. 5.2, bounded by straight

7 Buckling of Shells

generatrices. It can be seen that the inextensional deformation of Fig. 5.2 (b) does not furnish $w=0$ along the edge-generatrices. Hence, if the supports do not permit any displacement w, no inextensional deformation can develop. This reasoning is in agreement with the theoretical and experimental results to be presented in Section 5.2 that disregard inextensional deformation completely.

The hyperboloid of revolution [5.18], [5.27], [5.32] shows essentially the same behaviour as the saddle-shaped shell. If only the radial displacements of both edges are prevented, i.e. the shell is connected to upper and lower horizontal diaphragms, rigid only in their own planes, by hinges, then the shell is capable of performing inextensional deformation in every case when, starting from an edge point, we can return to the same point after travelling along a sequence of straight generatrices of finite number.

The condition for the possibility of inextensional deformation can be expressed, according to Vlaszov [5.32], by the following equation:

$$\frac{(\xi_u+\xi_l)R_0 b}{\sqrt{(b^2+\xi_u^2 R_0^2)(b^2+\xi_l^2 R_0^2)}} = \sin\frac{m\pi}{n}, \tag{5.1a}$$

where

$$b = \xi_l R_0^2 \sqrt{\frac{1}{R_l^2 - R_0^2}}. \tag{5.1b}$$

Here m is the number of the half buckling waves in the meridional direction, while n denotes the number of the circumferential full buckling waves. Obviously, $m\geqq 1$ and $n\geqq 2$, and both of them can only be whole numbers. The other notations are explained in Fig. 5.14.

If we support the hyperboloid of revolution at one of its edges only, but here prevent two displacement components, then no inexetensional deformation can occur [5.27]. However, a "nearly-inextensional" deformation (i.e., large deformation of the entire shell connected with small specific elongations and distortions) may develop, which renders the shell more sensitive to the small deformations of the not entirely rigid supporting structure [5.18].

Finally we should remark that, due to the possibility of inextensional deformation, the rigidity of the shell is provided mainly by the bending stiffness of the shell wall, while the role of the tensile (membrane) stiffnesses is negligible. In shell structures with no inextensional deformation, the decreasing post-buckling load bearing capacity is mostly caused by the decrease of the membrane stiffnesses due to the change in curvatures. However, if there is no active membrane stiffness, there is nothing to decrease, so that the load-bearing capacity of the structure will remain constant or will even be increasing.

This phenomenon is illustrated in Fig. 5.3, which shows the results obtained by Hutchinson for toroidal shells [5.12]. The factor α, which depends on the geometric
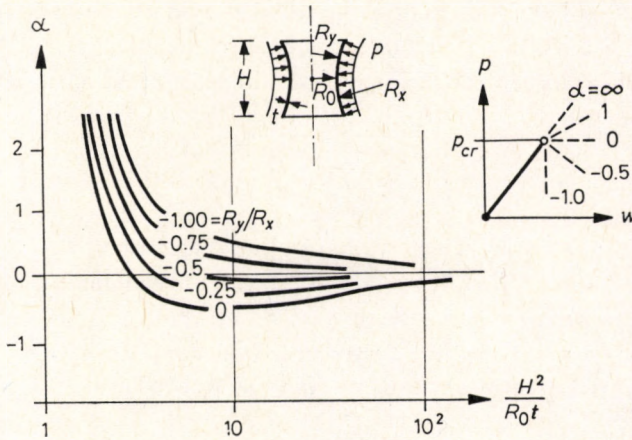
Fig. 5.3. Post-critical behaviour of a hyperbolic shell of revolution

ratios, characterizes the increasing or decreasing character of the post-buckling behaviour. The results shown in Fig. 5.3 suggest that in the range $H^2/R_0t > 100$ such shells practically do not exhibit a decreasing post-buckling load bearing capacity.

5.2. Buckling Caused by Uniform Load of a Hyperbolic Paraboloid Supported along the Generatrices

If a hyperbolic paraboloid (hypar) supported along its four generatrices (Fig. 5.4) is subjected to a vertical load p uniformly distributed in ground plan, there arise, according to the membrane theory, only shearing forces of constant magnitude over the whole shell surface. The buckling of such a shell was investigated on the
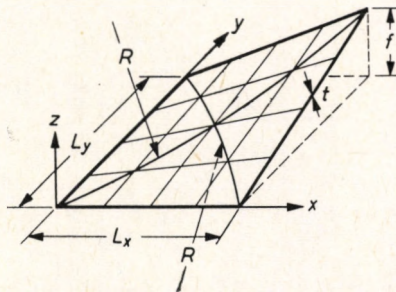
Fig. 5.4. Hypar shell over a rectangular ground plan supported along its generatrices

basis of the linear theory, assuming hinged edges and *shallowness* of the surface. Ralston [5.28] considered a hypar over a square ground plan ($L_x = L_y$) and, assuming a series of seventeen terms for the buckling deformation w, arrived at the following result:

$$p_{cr} = \varrho \frac{f^2}{L_x^4} \frac{2Et^2}{\sqrt{3(1-v^2)}}. \tag{5.2}$$

Here ϱ is a festoon curve, which we have plotted against f/t (for $v=0.3$) in Fig. 5.5 (a), omitting some rather dense "slings". It can be seen that the lower envelope (tangent) of the festoon curve gives $\varrho=1$ from about $f/t \geqq 25$ on. This lower tangent can be obtained also in a very simple way, see [2.12].

La Tegola [5.22] arrived at the same result as Ralston.
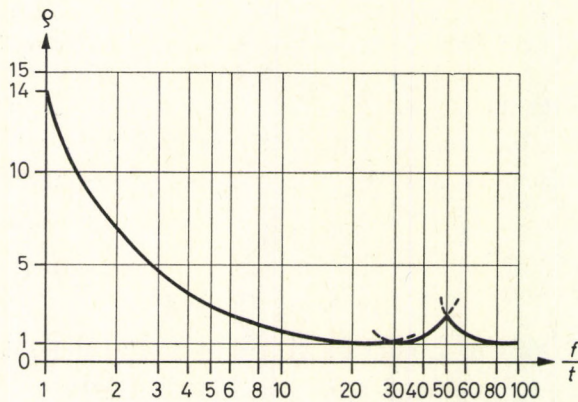
(a)
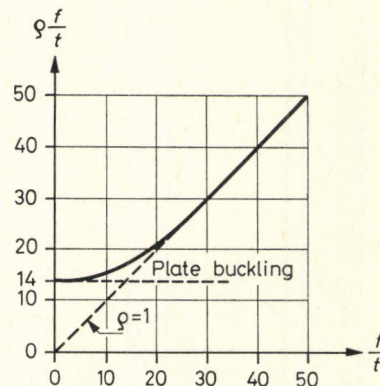
(b)

Fig. 5.5. (a) – Coefficient of the critical load of the hypar shell shown in Fig. 5.4, (b) – Changeover of the critical shearing stress of the hypar into that of a flat plate

The transition into a plane plate ($f \to 0$) can be represented clearly if we plot the critical shearing stress τ_{cr} instead of the critical load against f/t. The membrane theory of shells yields (see, e.g., [2.17a]):

$$n_{xy} = p \frac{L_x L_y}{2f}.$$ (5.3a)

Thus ($L_x = L_y$):

$$\tau_{cr} = p_{cr} \frac{L_x^2}{2ft} = \left(\varrho \frac{f}{t} \right) \frac{Et^2}{L_x^2 \sqrt{3(1-v^2)}}.$$ (5.3b)

The product factor $\varrho f/t$ was plotted in Fig. 5.5 (b) (substituting the lower tangent for the festoon curve of ϱ from $f/t = 25$ on). The value $\varrho f/t = 14$ at $f = 0$ corresponds to the critical shearing stress of a square plate with hinged edges [2.51]. With increasing curvature of the shell (i.e. with increasing f) τ_{cr} first slowly, then more and more rapidly, augments until at $f/t = 25$ it osculates the straight line pertaining to $\varrho = 1$. This may be interpreted as indicating that the critical stress is provided by the bending stiffness alone if the shell is very shallow, while with increasing curvature the tensile stiffness plays a greater and greater role, raising τ_{cr} to the value given by the straight line $\varrho = 1$.

The quantity L_x^2/f in Eq. (5.3b) is equal to the main radius of curvature R of the hypar over a square ground plan (see Fig. 5.4). When considering that in our case of pure shear the shearing stress τ is equal to the principal compressive stress σ_1 acting along the principal curvature line, in the case of $\varrho = 1$, Eq. (5.3b) turns into the expression

$$\sigma_{1cr} = \frac{Et}{\sqrt{3(1-v^2)}R}.$$ (5.4)

This formula is identical with Eq. (2.13), valid for the axially compressed cylinder.

Leone and Wang [5.23b] took into consideration that due to bending and edge effects the shearing force is not exactly uniform all over the shell and that in the edge zones other internal forces also arise. They obtained slightly greater critical loads than Eq. (5.2). Consequently, in using Ralston's result we remain on the safe side.

Experiments on hypars supported along the generatrices [5.23], [5.23b] showed that while the buckles are short in the direction of the principal compressive stress, they extend to the edges parallel to the principal tensile stress (Fig. 5.6). The shell models generally buckled at about 70% of the computed linear critical load (5.2). Lower buckling loads were observed only on shells with weak edge beams. All this is similar to the cylinders subjected to lateral pressure or to torsion: they also have similar ratios of experimental to theoretical linear critical loads.

The experimental shells generally showed an increasing post-buckling load bearing capacity. This can be explained physically by considering the tensioned
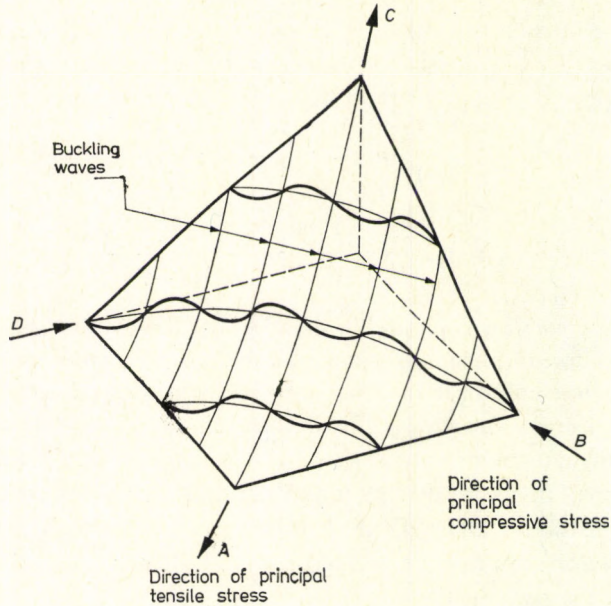
Fig. 5.6. Buckling shape of the hypar shown in Fig. 5.4
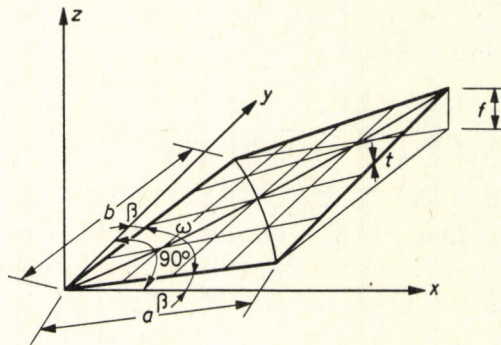
Fig. 5.7. Hypar over a skew ground plan supported along its generatrices

strip connecting the corner points A and C (see Fig. 5.6) as suspending the buckling compressed strips. This effect obviously depends on the extent to which the corner points may be considered as rigidly supported against horizontal displacement. It also depends on the horizontal bending stiffness of the edge beams since it is more favourable for the shell if it is suspended by the other tensioned strips in addition to AC.

Hauptenbuchner [5.10a] generalized Ralston's result (5.2) for hypars with unequal side lengths and for skew ground plan (Fig. 5.7). She obtained for the

linear critical load:

$$p_{cr} = \bar{\varrho} \, \frac{f^2}{a^2 b^2} \, \frac{2 E t^2}{\sqrt{3(1-v^2)}} \, (1 + \cot^2 \omega) \tag{5.5}$$

where $\bar{\varrho}$ means a festoon curve again, which has for greater f/t ratios the lower tangent 1.0, while the shape of the curve and its starting point at $f=0$ (see Fig. 5.5 (a)) depend on the ratio b/a and on the angle ω (see Fig. 5.7). Since $ab/\sqrt{1+\cot^2\omega}$ is equal to the ground plan area of the shell, Eq. (5.5) states that p_{cr} is inversely proportional to the square of the shell ground plan area.

Hauptenbuchner's model tests [5.10a] showed the same trends as those of Leet [5.23], described earlier: they buckled mostly at load values between 60% and 70% of the linear critical load intensity (5.5). The experimental load-deflection curves of Hauptenbuchner exhibited an ascending post-buckling load bearing capacity, and were similar to the dashed lines of Fig. 1.1 (b). Hence, the values of the experimental buckling loads could only be determined with some uncertainty. This statement also holds for the experimental results of Leet [5.23].

One additional remark seems to be necessary here. Hyperbolic paraboloid shells on skew parallelogram ground plans are free from normal forces along their straight generatrices only if their edges are free to move horizontally (perpendicularly to their directions). Since in most cases this condition is not fulfilled, in the case $\omega < 90°$ compressive forces, and in the case $\omega > 90°$ tensile forces, develop along the generatrices, which may influence the onset of buckling. This phenomenon needs further investigation.

5.3. Buckling of Saddle-Shaped Hyperbolic Paraboloid Shells under Uniform Load

The equation for the linear critical load of the saddle-shaped hypar shell (Fig. 5.8) was first derived by Apeland [5.1a], who applied Reissner's general solution for shallow shells [5.29] to this particular case. He assumed in his solution a membrane stress state that exerts lateral thrust in two directions and complies with the compatibility requirements. Gioncu and Ivan [5.9] determined minimum critical loads from Apeland's equation, assuming that the shell buckles in many short waves along the x direction shown in Fig. 5.8. He thus found that the critical load of the saddle-shaped shell is equal to that of a hypar supported along its generatrices and having the same principal curvatures as the saddle-shaped shell.

However, the saddle-shaped hypar is used in practice mostly as a shell without lateral thrust, and, moreover the buckling shape may not have many waves in the x direction either.
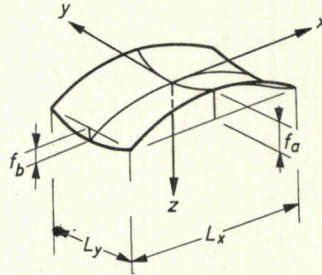
Fig. 5.8. Notations for the saddle-shaped hypar

Let us first suppose that the saddle-shaped shell carries the uniform load p as an arch in the x direction, i.e. by forces n_x only. The corresponding support conditions are: vertical diaphragms rigid only in their planes along the edges $y = \pm L_y/2$, and rigid support along the edges $x = \pm L_x/2$. (Strictly speaking, the membrane stress state associated with these boundary conditions is statically indeterminate. However, numerical investigations with the aid of the bending theory showed that the shell carries at least 98 % of the uniform load by membrane forces n_x, so that the arch-like action can be considered as a good approximation.) For this case the linear critical load was determined in [5.5a]. The result is:

$$p_{cr}^{lin} = c_1 \frac{Et^2}{R_x R_y} = c_1 \frac{64 E t^2 f_a f_b}{L_x^2 L_y^2}. \tag{5.6}$$

The values of the factor c_1 are compiled in Table 5.1 for various geometric ratios. They yield critical loads that are about one third of those obtained by Gioncu.

The stability problem of the saddle-shaped hypar supported by diaphragms which cannot withstand lateral forces was first clarified for the range $1 \leqq f_a/f_b \leqq 4$ by Jankó in four papers [5.13], [5.14], [5.15], [5.15a]. In the first paper [5.13] he found that the shell carries the load up to $f_a/f_b = 1.5$ predominantly by bending, so that there is no question of buckling. The range $1.5 < f_a/f_b < 2.0$ is a transitory zone, and, from $f_a/f_b \geqq 2.0$ on, the shell is capable of carrying the load predominantly by membrane forces without exerting lateral thrust on the edges. Hence the stability problem has to be investigated in the range $2.0 \leqq f_a/f_b \leqq 4.0$

In his second paper Jankó [5.14] determined the linear critical load of the geometrically perfect shell which does not exert lateral thrust on the edges. He took into consideration in the x direction at most nine terms, in the y direction at most three terms, of the series for the buckling shape and used the Galerkin method.

In Fig. 5.9 we show the variation of the critical load as a function of the ratio f_a/f_b for a chosen set of geometric parameters.

Jankó [5.14], [15.5a] compiled tables and diagrams for the easy computation of the critical loads of shells with geometric ratios occurring in practice. We present his results in an abridged form in Table 5.2. For the so-called "normal" shell

Table 5.1

Values of the factor c_1 appearing in Eq. (5.6) valid for arch-like saddle-shaped hypar shells

$8f_b/t$	100						200						300					
$L_x/L_y =$	0.5	1.0	1.5	2.0	2.5	3.0	0.5	1.0	1.5	2.0	2.5	3.0	0.5	1.0	1.5	2.0	2.5	3.0
$f_a/f_b = 0.5$	0.564	0.344	0.282	0.195	0.166	0.182	0.481	0.294	0.200	0.188	0.129	0.113	0.459	0.259	0.182	0.141	0.137	0.094
1.0	0.580	0.412	0.266	0.246	0.191	0.141	0.516	0.339	0.227	0.157	0.159	0.133	0.497	0.282	0.180	0.143	0.126	0.158
1.5	0.585	0.421	0.276	0.233	0.233	0.163	0.535	0.355	0.231	0.175	0.141	0.150	0.519	0.310	0.202	0.158	0.120	0.112
2.0	0.586	0.444	0.318	0.224	0.215	0.192	0.546	0.390	0.234	0.194	0.139	0.135	0.533	0.344	0.220	0.161	0.127	0.105
2.5	0.585	0.464	0.331	0.228	0.202	0.211	0.552	0.395	0.262	0.202	0.144	0.129	0.543	0.353	0.230	0.163	0.144	0.113
3.0	0.585	0.479	0.345	0.237	0.199	0.198	0.557	0.409	0.266	0.198	0.163	0.130	0.549	0.374	0.251	0.165	0.141	0.121
3.5	0.585	0.492	0.369	0.261	0.201	0.196	0.560	0.423	0.276	0.210	0.167	0.130	0.554	0.395	0.248	0.184	0.139	0.121
4.0	0.584	0.501	0.379	0.260	0.205	0.186	0.563	0.437	0.295	0.207	0.186	0.129	0.558	0.416	0.259	0.184	0.147	0.126

$$p_{cr}^{lin} = c_1 \frac{Et^2}{R_x|R_y|} = c_1 Et^2 \frac{64 f_a f_b}{L_x^2 L_y^2}$$

Table 5.2

Values of the factor c_2 of the linear critical load of saddle-shaped hypar shells according to Jankó [5.15a]

$8f_b/t$	80				160				240				320			
$L_x/L_y =$	1.0	2.0	2.5	3.0	1.0	2.0	2.5	3.0	1.0	2.0	2.5	3.0	1.0	2.0	2.5	3.0
$f_a/f_b = 1.50$	0.081	0.084	0.082	0.090	0.062	0.065	0.069	0.077	0.066	0.071	0.068	0.069	0.076	0.074	0.076	0.071
1.75	0.090	0.090	0.110	0.140	0.058	0.059	0.064	0.074	0.054	0.055	0.056	0.060	0.056	0.058	0.056	0.057
2.00	0.096	0.093	0.112	0.140	0.054	0.052	0.060	0.072	0.041	0.040	0.044	0.051	0.036	0.035	0.038	0.042
2.25	0.103	0.098	0.117	0.142	0.054	0.051	0.062	0.075	0.037	0.035	0.041	0.050	0.028	0.026	0.031	0.038
2.50	0.114	0.106	0.123	0.146	0.065	0.061	0.071	0.085	0.050	0.048	0.054	0.062	0.044	0.043	0.046	0.051
2.75	0.119	0.114	0.131	0.149	0.087	0.085	0.091	0.101	0.080	0.083	0.084	0.087	0.084	0.089	0.086	0.085
3.00	0.099	0.119	0.119	0.115	0.113	0.105	0.106	0.109	0.105	0.111	0.109	0.107	0.105	0.125	0.122	0.117
3.25	0.081	0.087	0.087	0.087	0.093	0.092	0.093	0.098	0.092	0.086	0.087	0.088	0.086	0.090	0.090	0.088
3.50	0.067	0.061	0.062	0.065	0.060	0.071	0.070	0.066	0.070	0.067	0.069	0.072	0.071	0.063	0.064	0.065
3.75	0.058	0.045	0.046	0.050	0.038	0.034	0.034	0.035	0.034	0.035	0.034	0.034	0.033	0.039	0.038	0.036
4.00	0.057	0.040	0.042	0.047	0.031	0.021	0.022	0.024	0.022	0.014	0.015	0.017	0.016	0.011	0.011	0.012

$$p_{cr}^{lin} = c_2 \frac{Et^2}{R_x|R_y|} = c_2 Et^2 \frac{64 f_a f_b}{L_x^2 L_y^2}.$$
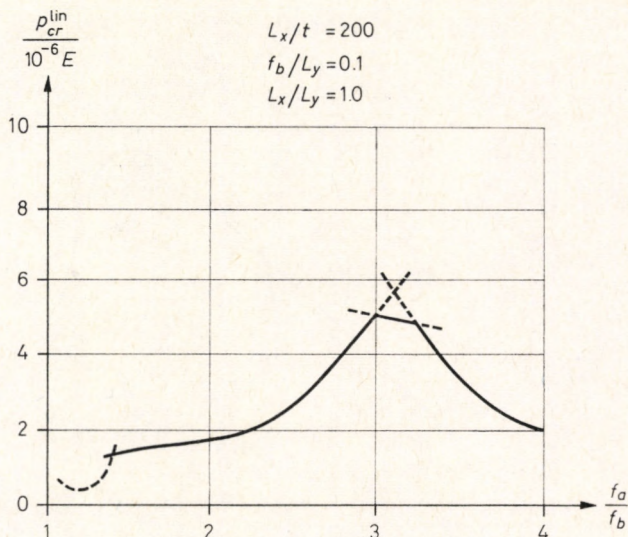
Fig. 5.9. Linear critical load of a saddle-shaped hypar exerting no lateral thrust

with the geometric ratio $f_a/f_b=4$ [5.1] we set up, on the basis of the diagrams of Jankó, an approximate formula suitable for preliminary calculations:

$$p^{lin}_{cr(f_a/f_b=4)} \approx \frac{32}{\sqrt{3}} E \frac{t^3}{L_x^3} \frac{f_b}{L_y} \left(7 + \frac{L_x^2}{L_y^2}\right). \tag{5.7}$$

The investigations of Jankó also showed that the shell does not buckle exactly in the form of an inextensional deformation: this latter is rather completed by some additional extensional terms. However, the dominant term of the buckling shape is always an inextensional one pertaining to some adjacent ratio f_a/f_b, i.e. to $f_a/f_b=9/4$ or $f_a/f_b=4$.

As can be seen from Fig. 5.9, in the range $2.5 \le f_a/f_b \le 4$ the critical load is always greater than or equal to that of the "normal" shell with the ratio $f_a/f_b=4$. Since the buckling shape of this latter is almost exactly inextensional, its critical load represents a "lower critical load" for other shells with different f_a/f_b ratios, as defined in Fig. 1.4 (c), and may thus be regarded as a lower bound for the critical loads of shells of other geometric parameters and with initial imperfections as well as for the critical loads bifurcating from the deformed shape.

Figure 5.9 also shows that the critical load has a peak value at about $f_a/f_b=3$. Hence these shells have a high critical load but they also are rather sensitive to initial imperfections, since a small deviation in the geometric data of the surface results in a sharp drop in the critical load.

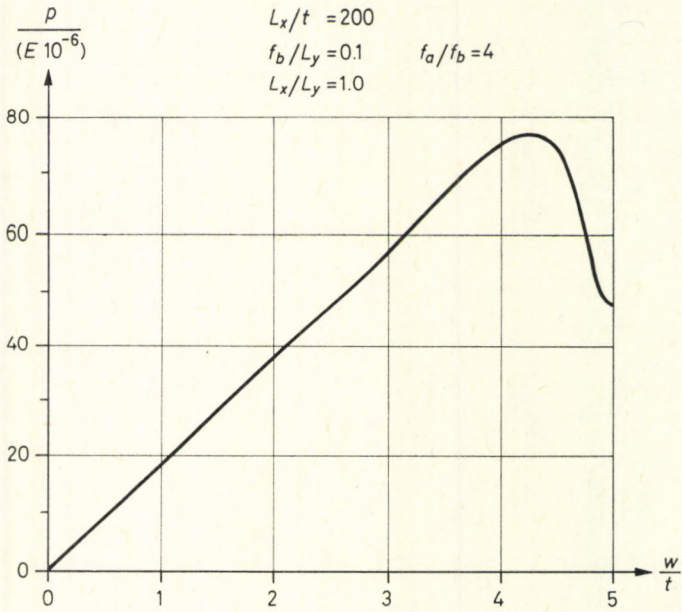In his third paper Jankó [5.15], investigated the behaviour of the perfect shell,

Fig. 5.10. Load-deflection curve of a saddle-shaped hypar in the case of snapping
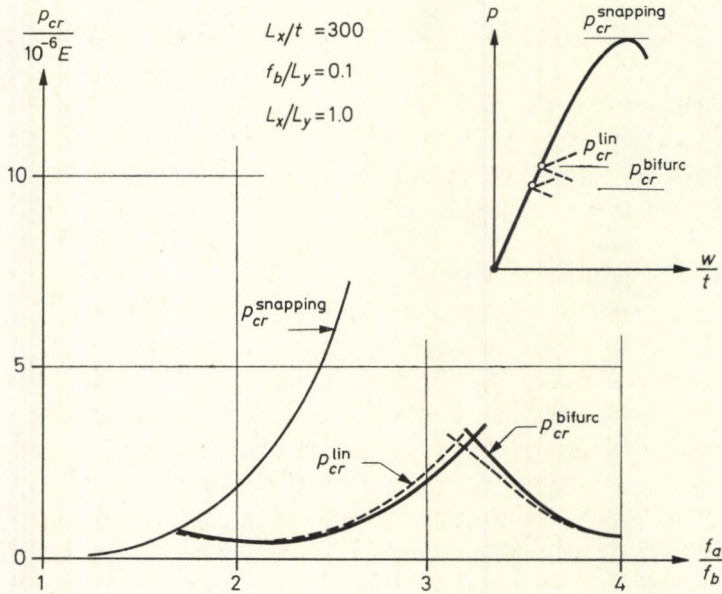

Fig. 5.11. Comparison of the linear critical load, the snapping load, and the critical load causing bifurcation from the deformation leading to snapping of a saddle-shaped hypar

and of the shell deformed by a uniform load, with the nonlinear theory, assuming a buckling shape with two free parameters. According to his findings, the saddle-shaped shell is also prone to snapping but the pertaining critical load is in most cases several times greater than the linear critical load (causing bifurcation). The snapping diagram of the "normal" shell with the geometric ratios as indicated in Fig. 5.9 is shown in Fig. 5.10.

It is also possible that bifurcation occurs from the deformed shape. In the range investigated ($1.5 \leq f_a/f_b \leq 4$), this bifurcating critical load p_{cr}^{bifurc} is mostly lower than the linear critical load (calculated with an undeformed shape). The result of one of Jankó's examples is shown in Fig. 5.11. The difference between the two critical loads is, in this case, about 10%, but in other cases this may be more.

Jankó finally investigated whether the character of the load bearing capacity after bifurcation from the deformed shape is increasing or decreasing. He found in the cases $f_a/f_b > 3$ a slightly increasing character, and in the cases $f_a/f_b < 3$ a decreasing one. In his fourth paper [5.15a] he improved the accuracy of his previous results by using a more refined calculation.

Unfortunately, his method was not suitable to determine the lower critical load of the perfect shell, or the dependence of the upper critical load on the initial imperfection.

5.4. Buckling of Hyperbolic Shells of Revolution

Among the hyperbolic shells of revolution the simplest one is the hyperboloid of revolution. This surface can be generated by rotating a pair of hyperbolas around their axis of symmetry which does not intersect them. The inextensional deformation of this surface was treated in Section 5.1. However, hyperbolic surfaces of revolution may also be generated by rotating, e.g., a parabola or any other curve around the axis.

Hyperbolic shells are mostly used as cooling towers and are made, as a rule, of reinforced concrete. The dimensions of the cooling towers increased steadily increasing for years without their stability problem being thoroughly investigated. After the collapse of three cooling towers at Ferry-bridge in 1965, the research into the stability of hpyerbolic shells of revolution began. Due to the comparatively short time that has elapsed since then and to the intricacy of the problem, we cannot expect an exhaustive and easy-to-survey treatment of the subject, so that there is some uncertainty in the determination of the critical loads of such shells. For example the results of the research, due to difficulties in the investigations, are exactly valid only for certain simplified boundary conditions (e.g. rigidly supported hinged lower edge). There are hardly any results to be found for an elastically

supported bottom edge, which is the actual boundary condition of the cooling towers.

Because of the more intricate nature of the elastic support, it seems feasible to use the two simple extreme cases as upper and lower bounds: entirely prevented and totally free displacements in meridian direction. However, some caution in necessary here. If the geometric ratio makes an inextensional deformation possible, and we apply hinged top and bottom diaphragms rigid only in their planes (i.e. allowing totally free displacements in meridian direction), these will not hinder the inextensional deformation and we obtain an unrealistically low critical load. By hindering the displacement of such shells in the meridional direction we may markedly increase the critical load, because by so doing we hinder the inextensional deformation.

Several older papers on model tests did not mention the support conditions applied in the experiments. Their results often differ considerably from each other. It thus seems probable that the discrepancy could be explained by the differences in the kinds of support. Another possible explanation is that when investigating experimentally the compression in the meridian direction, the results concerning the general and the local buckling were not separated, so that these results could have appeared mixed.

In recent years rather accurate computer calculations have been developed for the determination of the critical load. Lehmkämper [5.23a] calculated the critical loads of cooling tower shells with various dimensions and stiffening ribs for several loading cases. Veronda and Weingarten performed computer calculations on shells previously tested experimentally, taking the actual boundary conditions into account, and they found a rather close agreement [5.31]. These investigations included several loading cases and different boundary conditions. For the ratio of the experimental to the calculated critical load the following mean values and variational coefficients (i.e. standard deviations divided by the mean values) were obtained:

— vertical load: 0.96 (0.10),
— lateral pressure: 1.04 (0.12).

Unfortunately, not every engineer has access to the afore-mentioned computer calculations. Moreover, it will take a long time before, on the basis of numerical examples calculated by the exact computer programmes, practical recommendations can be set up. Hence, it seems necessary to present some less accurate but easy-to-use results and methods obtained by more simple means.

Since the buckling problems of hyperbolic shells of revolution can by no means be regarded as definitely solved — indeed for certain cases there are no theoretical results at all — the experiments are even more important for the design than usual.

5.4.1. Loads, Boundary Conditions and Buckling Modes of Hyperbolic Shells of Revolution

There are two dominant kinds of *loads* acting on hyperbolic cooling towers: their own weight and wind pressure. Both loads cause both meridian-directed and hoop stresses, as contrasted to cylinders with vertical axis where their own weight does not cause any hoop stresses. Hence, the influence of both stresses on buckling should be investigated simultaneously. Since, however, it is much simpler to deal separately with the two kinds of stresses, following Krätzig [5.20] we shall deal separately with the two basic loading cases shown in Fig. 5.12. In case (a) no stress arises in the meridian direction, while in case (b) there are no hoop stresses. We shall denote the critical hoop force pertaining to case (a) with $n^0_{y,cr}$, while the critical meridian force of case (b) will be called $n^0_{x,cr}$. The superscript "zero" refers in each case to the zero value of the other normal force.

The theoretical and experimental investigations [5.26], [5.31] definitely showed that in the case of simultaneous action of both normal forces the condition of stability can be expressed (slightly to the benefit of safety) by the Dunkerley theorem:

$$\frac{n_x}{n^0_{x,cr}} + \frac{n_y}{n^0_{y,cr}} = 1. \tag{5.8}$$

The *boundary conditions* at the upper and lower edges of the hyperbolic shell, to be used in stability investigations, depend on the structural solution of the cooling tower, and are as follows:

$$n_x = 0$$
$$n_{xy} = 0$$
$$n_y = pR_y$$
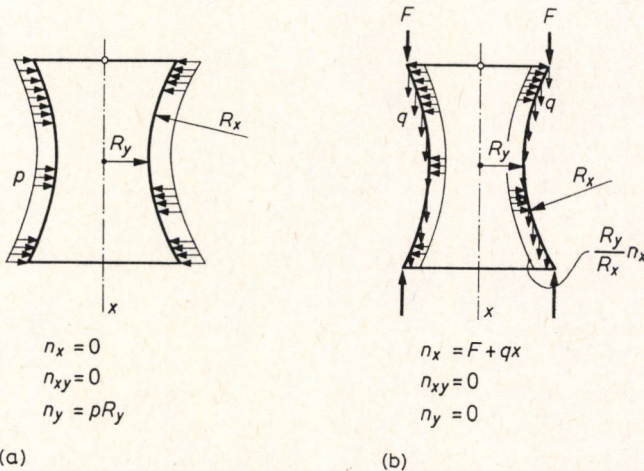
(a)

$$n_x = F + qx$$
$$n_{xy} = 0$$
$$n_y = 0$$

(b)

Fig. 5.12. The "pure" circumferential compression and the "pure" meridian-directed compression of a hyperbolic shell of revolution

At the *upper edge* mostly a stiffening ring is applied, due to which the following boundary conditions apply for the buckling of the shell: $w = \partial^2 w/\partial x^2 = v = n_x = 0$. During erection (and also in the case of smaller towers) there is no stiffening ring, so that the boundary conditions become:

$$\partial^2 w/\partial x^2 = \partial^3 w/\partial x^3 = n_x = n_{xy} = 0.$$

At the *lower edge*, in most cases, also a stiffening ring is applied, sometimes realized by the thickening of the shell wall. The ring or the lower edge is mostly supported by a truss resting on the soil, through which the cooling air can stream into the tower. The compression of this truss and the subsidence of the foundation act as elastic support for the shell. Moreover, if the foundation is light, it may also lift from the soil along a certain section.

If we assume a hinged joint, the boundary conditions of the lower edge can be written as follows:

$$w = v = 0, \quad \partial^2 w/\partial x^2 = 0,$$

and

$$u_{\text{shell}} = u_{\text{support}}.$$

(It should be noted that, due to the lower stiffening ring, it is irrelevant whether we denote by u the displacement in the vertical or in the meridional direction.)

If the vertical stiffness of the foundation and of the truss can be considered infinitely great, then $u_{\text{support}} = 0$. On the other hand, if the foundation may lift, then along this section we have to set $n_x = 0$ instead of the restriction for u.

Hyperbolic shells have four characteristic *buckling modes*.

In the case of a free upper edge, the specific distribution of the wind pressure

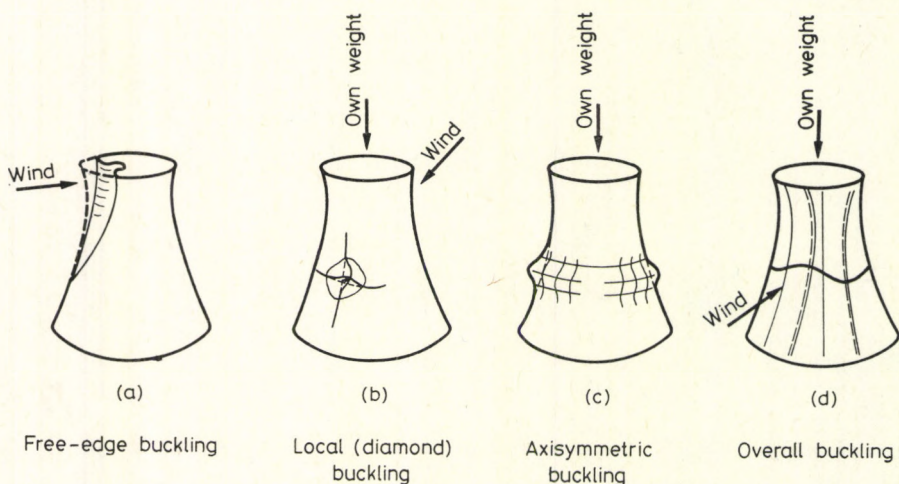| (a)	(b)	(c)	(d)
Free-edge buckling	Local (diamond) buckling	Axisymmetric buckling	Overall buckling

Fig. 5.13. The buckling modes of the hyperbolic shells of revolution

may cause a buckling pattern shown in Fig. 5.13 (a), which we shall call *free-edge buckling*.

The meridian-directed forces may cause *local buckling* in a diamond-shaped pattern shown in Fig. 5.13 (b). This phenomenon is similar to the buckling of cylinders under axial compression. The boundary conditions (even comparatively weak edge supports) do not influence this buckling mode, as a rule, since in the vicinity of the upper edge ring the meridian-directed forces are small so that they cause no local buckling here, while near the lower edge the usual thickening of the shell wall prevents local buckling.

The meridian-directed forces may also cause an *axisymmetric buckling* shown in Fig. 5.13 (c), which is again similar to the case of the axially compressed cylinder.

Finally, a reticulated buckling pattern, extending to the entire surface, has to be mentioned, which we call *overall buckling* (Fig. 5.13 (d)). This buckling mode is markedly influenced by the boundary conditions.

In the following we shall treat, in turn, the critical loads pertaining to each buckling mode. The notations are explained in Fig. 5.14.
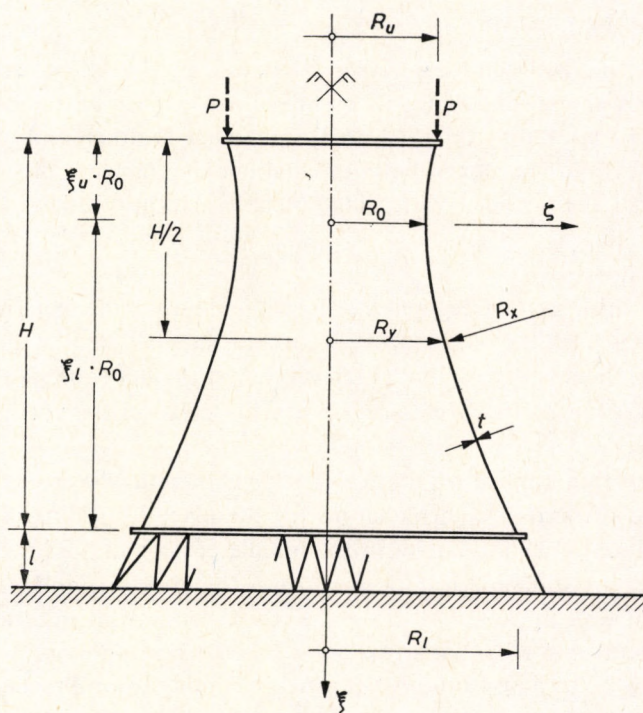

Fig. 5.14. Elevation of a hyperbolic shell of revolution. Notations

5.4.2. Free-Edge Buckling

The buckling of the free edge is caused by the lateral pressure of the wind. It may be onerous during erection when the strength of the concrete is still low and the upper stiffening ring is not yet built.

Most authors set up the following formula for the critical wind pressure (i.e. the maximum pressure value of the circumferential distribution of the wind load):

$$p_{cr} = CE\left(\frac{t}{R_0}\right)^{7/3} = C\sqrt{12}\,\frac{\sqrt{BT}}{R_0^2}\sqrt[3]{\frac{t}{R_0}}, \tag{5.9}$$

where R_0 is the throat radius, B and T are the bending and tensile stiffnesses of the shell wall, respectively. For the factor C they suggest values on the basis of model tests, depending on the geometric ratios (principal curvatures and height to throat radius) of the shell:

Der and Fidler [5.4]: $\qquad\qquad\qquad C = 0.060 \sim 0.077$;
Walther and Wölfel [5.33]:
— taking extreme cases into account: $C = 0.048 \sim 0.309$;
— considering practical cases only: $\quad C = 0.072 \sim 0.220$.

The discrepancies between these values are caused by the various support conditions of the lower edge and by the different geometric ratios of the shell.

Cole, Abel and Billington [5.2], [5.3], and also Walther and Wölfel [5.33], investigated by more exact computer calculations the influence of various factors and compared their results with those of several other authors [5.21], [5.31], [5.36].

Their findings are:

(a) If the shell has a free upper edge without any stiffening ring, the wind pressure causes buckling on the upper section of the shell. Besides the weakness of the free edge, there is the additional reason that in the upper section of the tower an increased local internal wind suction develops, due to the vortices caused by the free edge.

A stiffening ring applied on the upper edge eliminates the free-edge buckling, and the wind pressure becomes onerous for the overall buckling. In such cases the wind-induced buckling bulges in the middle part or in the lower half of the tower. The upper stiffening ring thus increases the critical wind load of the shell with constant wall thickness by about $10 \sim 20\%$. If the wall thickness of a shell with upper stiffening ring is increased towards the bottom along the lower half of the shell by up to 3 or 4 times, as is usual in cooling tower practice, the critical wind pressure augments by about $50 \sim 100\%$ as compared to the shell with constant wall thickness.

(b) As compared with the uniform lateral pressure, the actual wind pressure distribution causes an increase of $20 \sim 30\%$ in the critical load (referred to the peak value of the wind pressure).

(c) Constant wind profile along the height reduces the critical pressure by about 20% as compared with the maximum intensity of the actual wind profile, increasing upwards.

(d) The interaction of the horizontal wind pressure p and of the vertical own weight q can be closely approximated by the straight line of Dunkerley:

$$\frac{p}{p_{cr}} + \frac{q}{q_{cr}} = 1. \tag{5.10}$$

(e) The factor C in Eq. (5.9) depends on the ratio of the two radiuses of curvature of the shell. In the case of a rigid lower support ($u=0$), the value of C may be computed from the relation:

$$C = \frac{1}{3} \sqrt{\frac{R_y}{R_x}}, \tag{5.11}$$

which was obtained by approximating the results of numerical examples in the range $0.05 < R_y/R_x < 0.25$. Here R_x denotes the radius of curvature of the meridian line at the halfway height of the shell according to Eq. (5.19), while R_y is the horizontal radius of the shell at the same height (see Fig. 5.14).

If the support is elastic ($u_{shell} = u_{support}$), the value of C yielded by Eq. (5.11) has to be multiplied by a factor $\varkappa$ depending on the elasticity of the foundation. This latter is characterized by the expression $k_s R_0/(Et)$, with k_s as the spring constant of the support of the lower shell edge in vertical direction and E as the modulus of elasticity of the shell material. The factor $\varkappa$ is given by the diagram of Fig. 5.15, obtained by fitting a curve on the $\varkappa$ values of numerical examples. In these latter the ratio of p_{cr} for $k_s = 0$ (no hindering of vertical displacement) to that for $k_s = \infty$ (rigid support) was equal to 1/6. Taking this value into account, the curve of Fig. 5.15 can be approximated by the relation:

$$\varkappa = 1 - \left[1 - \frac{p_{cr}(k_s = 0)}{p_{cr}(k_s = \infty)} \right] \frac{1}{1 - 3k_s \dfrac{R_0}{Et}}. \tag{5.12}$$

(f) Evaluation of some experimental results [5.33] showed a dependence of the critical load on the ratio of the shell height H to the throat radius R_0. When the ratio H/R_0 is decreased from 4 to 2 or 1, the critical load increases to two or three times its value. However, the experiments which were in good agreement with the exact computer calculations [5.31] did not show such a dependence. The explana-
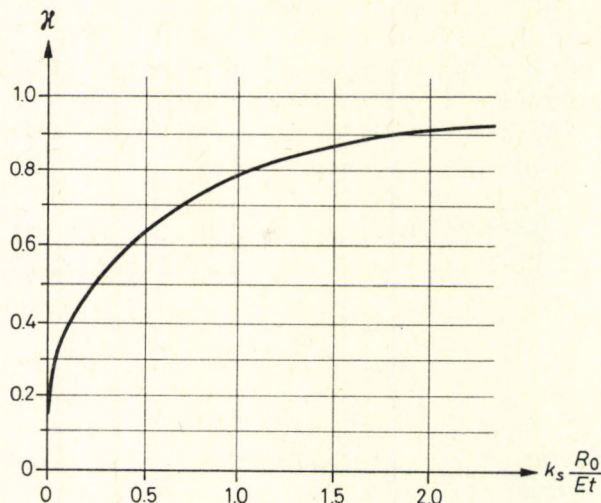
Fig. 5.15. The diminishing effect of the elastic foundation on
the linear critical load of the hyperbolic shell of revolution

tion of this phenomenon is that H/R_0 can also be expressed by R_x/R_y, so that
Eq. (5.11) automatically contains this dependence, too.

(g) Hyperbolic surfaces are much less sensitive to initial imperfections than
elliptic ones. This follows from the fact that the lower critical load of the geometri-
cally perfect shell (computed by the nonlinear theory) is only slightly less than the
linear critical load.

As an explanation for this phenomenon we have to consider that the nonlinear
theory may cause a considerable deviation from the linear critical load only if the
membrane stiffnesses constitute a great part of the buckling resistance. Due to the
propensity of hyperbolic shells to inextensional deformation, their membrane
stiffnesses play only a minor role and their critical load is comparatively low, but
— as with what has been said in connection with Fig. 2.9 — their imperfection-
sensitivity is also small (or even absent in some cases).

5.4.3. Local Buckling

The compressive forces acting in meridian direction also cause hoop forces
in a hyperbolic shell of revolution, so that its critical load is less than that of a
substituting cylinder with the radius R equal to R_y of the hyperbolic shell (see
Fig. 5.14), see [5.24].

According to the investigations of Rosemeier [5.30], the critical loads computed on the replacement cylinder can be used for the hyperbolic shell of revolution provided they are multiplied by the reduction factor:

$$\frac{1}{1+R_y/R_x},$$ (5.13)

R_x and R_y being defined in Fig. 5.14.

Thus, we arrive at the following results:

$$n_{x,cr}^{lin} = \frac{0.6}{1+R_y/R_x}\frac{Et^2}{R_y},$$ (5.14)

$$n_{x,cr}^{lower} = \frac{1}{1+R_y/R_x}\,n_{x,cr}^{lower}\,(\text{cylinder}),$$ (5.15)

$$n_{x,cr}^{upper} = \frac{1}{1+R_y/R_x}\,n_{x,cr}^{upper}\,(\text{cylinder}).$$ (5.16)

In practical cases, the local buckling analysis has to be carried out at various heights, since the wall thickness as well as the stresses vary along the height.

5.4.4. Axisymmetric Buckling

Axisymmetric buckling was investigated by Kohli [5.17]. He derived for the critical value of the meridian force the expression:

$$n_{x,cr} = \lambda\,\frac{Et^2}{R_y}.$$ (5.17)

For R_y see Fig. 5.14. The factor λ has the value $0.96\sim0.93$ for shells with an upper stiffening ring and $0.46\sim0.43$ for unstiffened shells. The higher λ-values were obtained for the linear critical load while the lower values give the lower critical load (of the geometrically perfect shell) obtained by the nonlinear theory.

Since these values exceed those of the other buckling modes, axisymmetric buckling, as a rule, need not be investigated.

5.4.5. Overall Buckling

The linear critical load of the overall buckling, which extends to the entire surface, is usually described by the following formula, similar to Eq. (5.17):

$$n_{x,cr} = \lambda \frac{Et^2}{R_y},\qquad(5.18)$$

R_y being shown in Fig. 5.14.

For the factor λ, various researchers obtained different results from the evaluation of model tests:

Krätzig [5.19]: $\lambda = 0.079$
Rosemeier [5.30]: $\lambda = 0.07 \sim 0.10$
Der and Fidler [5.4]: $\lambda = 0.18$
Wianeczki [5.34]: $\lambda = 0.12$
Mateja [5.25]: $\lambda = 0.24 \sim 0.27$

The lowest value among the above results is only one fourth of the highest one.

As possible reasons for these discrepancies we may mention the different geometric ratios and boundary conditions occurring in the model tests and computations of the various authors.

Krätzig [5.20] calculated numerical tables, from which we can establish the following expression for λ:

$$\lambda = (1.13 \sim 1.85) \sqrt[3]{\frac{t}{4R_0}}.$$

His tables make it possible to compute the values of $n_{x,cr}^{\mathrm{lin},0}$ and $n_{y,cr}^{\mathrm{lin},0}$ separately, as functions of the ratio throat to lower radii R_0/R_l and of the dimensionless height factor ξ_l, see Fig. 5.14. (The definitions of $n_{x,cr}^{\mathrm{lin},0}$ and $n_{y,cr}^{\mathrm{lin},0}$ are to be found in Section 5.4.1.) Unfortunately, these tables do not allow the influence of the dimensions of the upper part of the tower (above the throat) and of the ratio R_y/t to be properly taken into account. The critical loads computed by these tables give results that are $30 \sim 50\%$ higher than those obtained by exact computations confirmed by model tests [5.31]. Due to all these circumstances, we now present, on the basis of [5.6], the results of an approximate method which takes into consideration the influence of the geometric parameters. The main point of the approximation is that the investigation is carried out on a hyperbolic paraboloid shell by which we replace the hyperbolic shell of revolution in question. Since the hypar is a translational surface and, therefore, has no twist, it is less rigid than the hyperbolic shell of revolution, and has a somewhat lower critical load, which is, however, much easier to determine.

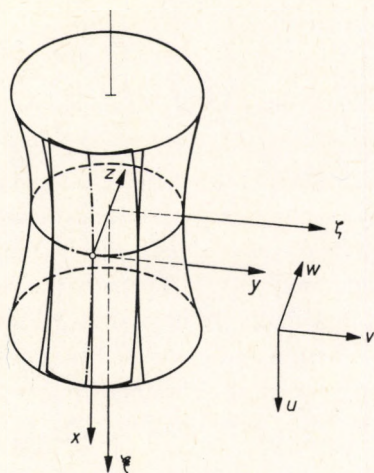The replacement hypar is shown in Fig. 5.16. Its radius of curvature in the y

Fig. 5.16. The substituting hyperbolic paraboloid

direction R_y is assumed to be equal to the horizontal radius R_y of the shell of revolution at its half way height, i.e. at the mid-distance between the two edges (see Fig. 5.14). For the other radius of the hypar R_x we have chosen, at the half-way height of the tower, the radius of curvature of the flat parabola arc which lies in common plane with the axis of revolution and passes through the end points of R_u, R_y and R_l (see Fig. 5.14), i.e.:

$$R_x = \frac{H^2}{8 \left(\frac{R_u + R_l}{2} - R_y \right)}. \tag{5.19}$$

By using these radiuses, the curvatures of the replacement hypar closely approximate the average curvatures of the hyperbolic shell of revolution in question.

We can write the equation of the replacement hypar surface as follows:

$$z = \frac{y^2}{2R_y} - \frac{x^2}{2R_x}. \tag{5.20}$$

The boundary conditions are:

— along the upper edge (stiffening ring): $w = \partial^2 w / \partial x^2 = v = n_x = 0$,
— along the lower edge (rigid support): $w = \partial^2 w / \partial x^2 = v = u = 0$.

The buckling shape was assumed to have the form:

$$w = \sin \frac{n\pi}{R_y} \sum_m A_m \sin \frac{m\pi}{H} x \tag{5.21}$$

with the pertaining stress function:

$$F = T \sin \frac{n\pi}{R_y} \sum_m A_m F_m \sin \frac{m\pi}{H} x. \tag{5.22}$$

Here T denotes the tensile stiffness of the shell wall. Introducing the above expressions for w and F into the compatibility equation, the coefficients F_m can be determined. The above expressions can satisfy the boundary condition $u=0$ by combining two terms with different m-s. The pairs of the m-values and n have to be chosen in such a way that they make the critical load a minimum.

We performed this computation and calculated the critical load in [5.6] according to the rules of the energy method. The following expressions for the critical meridian and hoop normal forces were obtained:

$$n_{x, cr}^{\mathrm{lin}, 0} = \lambda_x^0 \frac{Et^2}{R_y}, \tag{5.23}$$

$$n_{y, cr}^{\mathrm{lin}, 0} = \lambda_y^0 \frac{Et^2}{R_y}. \tag{5.24}$$

The numerical values of the factors λ_x^0 and λ_y^0 are compiled in Tables 5.3 and 5.4. Since by linear interpolation we would commit an error to the detriment of safety, we recommend a parabolic interpolation between the values of the tables.

Due to the variation of the meridian directed force, its value valid at the halfway height of the tower should be compared with that of the critical force.

The interaction of the meridian and hoop forces can be accounted for, according to the reasoning in Section 5.4.1, by the Dunkerley formula (5.8).

We compared the critical forces $n_{x, cr}^{\mathrm{lin}}$ given by the exact calculations and verified by model tests [5.31] with those computed with the λ-values of Tables 5.3 and 5.4, and found that the λ-values of the tables yield results about 10% lower than the more exact ones.

It seems probable that the effect of the support elasticity along the lower edge is similar in the cases of all the loading and buckling types. Consequently, we may use $\varkappa$ (5.12), introduced in the case of the free-edge buckling, as a multiplicator for assessing the influence of the support elasticity on the critical load in our case too.

It was found by several nonlinear investigations on the overall buckling [5.2], [5.31] that the lower critical load (of the perfect shell) is only a few per cent (maximum 5%) lower than the linear critical one. Hence, knowledge of the latter seems to be sufficient to perform the stability investigation of hyperbolic shells of revolution.

Table 5.3

Values of the factor λ_x^0, appearing in Eq. (5.23)

R_y/t	100				200				300			
H/R_y	2	4	6	8	2	4	6	8	2	4	6	8
$R_x/R_y=2$	0.224	0.137	—	—	0.180	0.133	—	—	0.157	0.160	—	—
4	0.289	0.188	0.183	—	0.240	0.159	0.155	—	0.209	0.133	0.174	—
6	0.344	0.255	0.192	0.153	0.276	0.193	0.170	0.159	0.249	0.172	0.146	0.197
8	0.392	0.264	0.238	0.199	0.333	0.228	0.170	0.146	0.286	0.192	0.161	0.130
10	0.424	0.294	0.246	0.199	0.364	0.257	0.208	0.170	0.329	0.234	0.183	0.165

$$n_{x,\,cr}^{0,\,lin} = \lambda_x^0 \frac{Et^2}{R_y}.$$

Table 5.4

Values of the factor λ_y^0, appearing in Eq. (5.24)

R_y/t	100				200				300			
H/R_y	2	4	6	8	2	4	6	8	2	4	6	8
$R_x/R_y = 2$	0.115	0.070	—	—	0.087	0.067	—	—	0.080	0.081	—	—
4	0.092	0.055	0.040	—	0.060	0.040	0.034	—	0.056	0.034	0.038	—
6	0.062	0.040	0.036	0.030	0.057	0.034	0.026	0.031	0.046	0.028	0.022	0.035
8	0.057	0.039	0.029	0.023	0.044	0.029	0.022	0.018	0.045	0.026	0.024	0.016
10	0.057	0.035	0.025	0.023	0.040	0.026	0.022	0.021	0.035	0.024	0.018	0.016

$$n_{x,\,cr}^{0,\,\text{lin}} = \lambda_y^0 \, \frac{E t^2}{R_y}.$$

6. Stability Problems of Shells with Free Edges

6.1. General Remarks on the Stability of Shells with Free Edges

All the kinds of shells discussed in the foregoing were supported all along their boundaries. In modern architecture, however, shells with unsupported edges are gaining ground, their appearance being much more graceful than that of the edge-supported ones.

Due to their free edges, these shells generally do not buckle locally (like, e.g. the axially compressed cylinder or the radially compressed sphere), but the structure *buckles as a whole*. Thus, the local shell-like buckling merges into the "arch-like" buckling of the whole structure.

The stability of shells with free edges is a rather unexplored field. Hence we report on a model test here which allows us to draw conclusions of a fairly general nature.
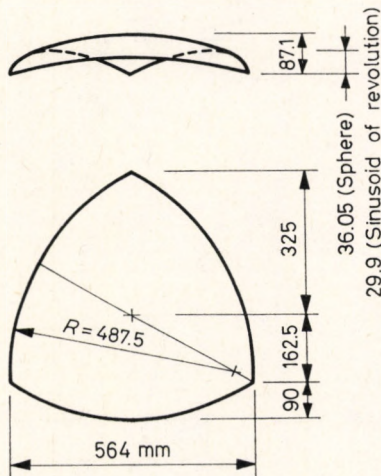
Fig. 6.1. Dimensions of
the investigated shell model with free edges

The experiment was performed on two shells of slightly different surfaces (sphere and sinusoid of revolution), made of 3 mm thick plexiglass [6.6]. Their dimensions are shown in Fig. 6.1. The structure was supported only at its three corner points, their edges were unstiffened. Under uniform load they closely approximated the funicular surface of the load, i.e. only small bending moments arose in the shells.

The edges of the models began to wrinkle at a considerably lower load intensity than necessary to cause local buckling of an edge-supported shell (Section 4.1), i.e. the structure started to buckle as an arch. With the aid of the generalized Southwell-plot (Section 9.9) we established that the structure has an increasing post-buckling load bearing capacity, see Fig. 1.1 (b) [9.9.2], [9.9.3]. In fact, both structures failed, not because of instability, but due to bending in the vicinity of the supports.

This increasing post-buckling load bearing behaviour can clearly be explained by Fig. 6.2. The structure first carries the load according to Fig. 6.2 (a), i.e. it behaves as if it consisted of three arches. After wrinkling of the edges, the internal
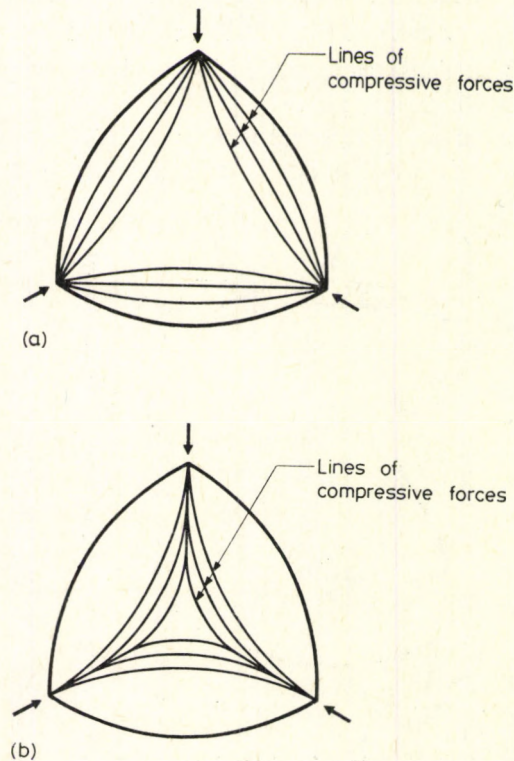
Fig. 6.2. Rearrangement of the internal forces

forces rearrange themselves: the lines of compression "retreat" to the internal part of the shell, which is less exposed to buckling (Fig. 6.2 (b)). Thus the outer parts are relieved, preventing increased buckling deformations of the edges, while the inner parts are able to carry much greater compression.

This model test allows us to draw the following conclusion for shells with free edges: We may reckon with increasing load bearing capacity after buckling of the whole structure, provided that the internal forces can rearrange themselves by shifting to the interior of the shell, and if this inner part alone is able to carry more load than the complete original structure with free edges working in compression [9.9.2].

When designing an actual shell structure with free edges, it is advisable to make a model test, except if its stability problems can be considered as solved, like e.g. the shell-arches to be discussed in Section 6.2.

6.2. Stability of Shell-Arches and Shell-Beams

Among shells with free edges only the stability problems of the shell-arches (and shell-beams) are solved in detail [6.5]. We report on them briefly in this section.

Shell-arches are, essentially, curved bars with thin-walled open cross sections (Fig. 6.3). The cross section of the bar has to have an axis of symmetry, which lies in the plane of the arch; otherwise the cross section may be optional. If the bar axis is straight, we are dealing with a shell-beam.

Owing to the symmetry of the cross section, instability phenomena in the arch plane and perpendicular to it can be treated separately.

6.2.1. Stability Investigations in the Plane of the Arch

Instability phenomena occurring in the plane of the arch cannot be treated by the classical methods of buckling analysis for arches with solid cross section, since the cross sections of the shell-arch undergo a transverse bending deformation. This is shown in Fig. 6.4. Compressive and tensile stresses parallel to the arch axis, which arise from bending, produce resultants due to the curvature of the arch axis, causing transverse bending of the cross section. Thus, the thin cross section undergoes considerable deformation, resulting in a substantial reduction in the bending stiffness of the shell-arch as compared to the ordinary arch with undeformable cross section. This phenomenon was first analysed by Kármán [6.4]

Arch (elevation)

Beam (elevation)
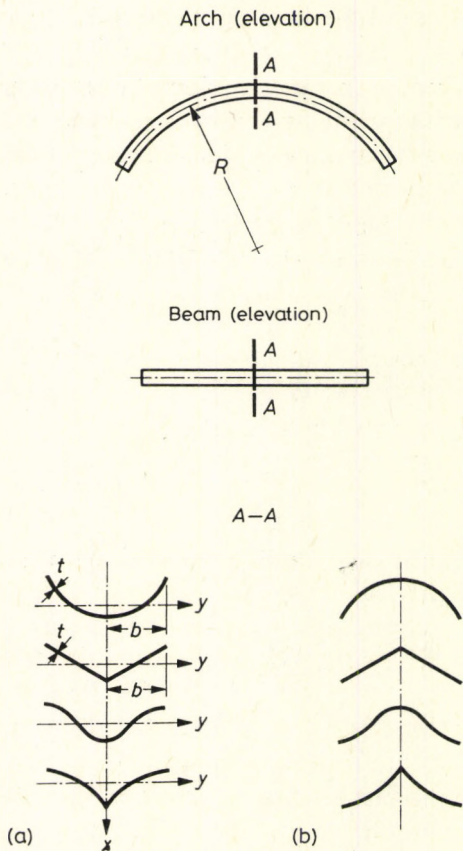

A—A

(a)   (b)

Fig. 6.3. Shell arches and shell beams with cross sections
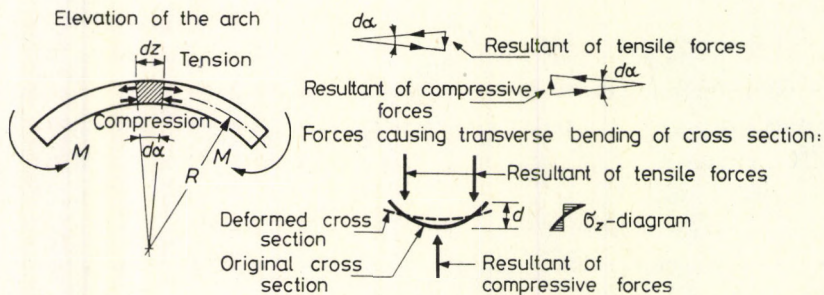(a) open upwards, (b) open downwards

Fig. 6.4. Flattening of the cross section

and Brazier [6.1] for closed tubes and by Weinel [6.7] for doubly curved open strips.

Owing to this deformation of the cross section, in the case of *pure bending* (Fig. 6.5 (a)) the behaviour of the shell arch is characterized by the diagram of Fig. 6.6, representing the bending moment M versus the change in the curvature
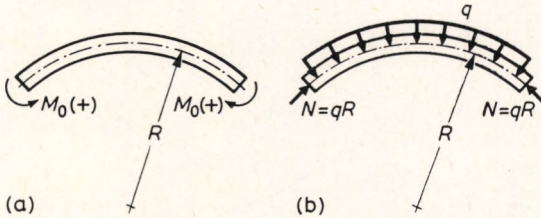
Fig. 6.5. The two basic loading cases.
(a) – Pure bending, (b) – central compression

χ. (I_y denotes the moment of inertia of the cross section calculated by the elementary theory, referred to the horizontal axis y.) This diagram shows that the arch not only undergoes much larger deformations than might be expected on the basis of the elementary theory, but at a certain value M_{cr} of the positive bending moment, as defined in Fig. 6.5 (a), it also *loses its stability in pure bending* by snapping through, due to the flattening of the cross section. In the case of a negative bending moment this does not happen, because the cross sections bulge and the arch becomes stiffer against bending, as shown by the lower part of the curve in Fig. 6.6. Hence, the shell-arch behaves "asymmetrically" with respect to $+M$ and $-M$ (see Fig. 1.1 (d)), as mentioned in Section 1.2.

The critical bending moments causing snapping (i.e. the peaks of the curves $M(\chi)$ in Fig. 6.6 for different geometric ratios) are given for the four cross sections
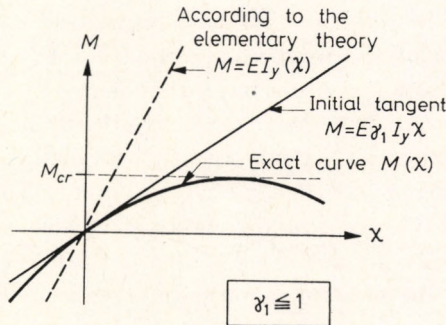

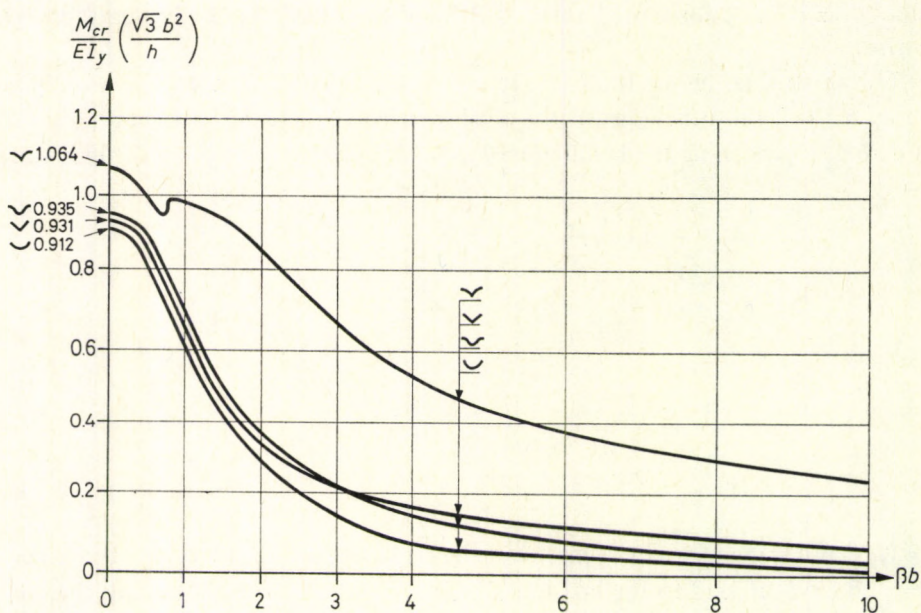Fig. 6.6. Behaviour of the shell arch under pure bending

Fig. 6.7. Critical bending moments causing snapping due to flattening of the cross sections

of Fig. 6.3 in Fig. 6.7, plotted against the geometric parameter

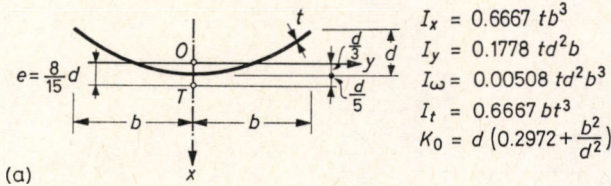$$\beta b = \frac{\sqrt[4]{3b}}{\sqrt{tR}} = \frac{1.316\,b}{\sqrt{tR}} \tag{6.1}$$

with the notations as shown in Fig. 6.3. The shell-beam is characterized by $\beta b = 0$. The discontinuity in the curve of the wing-shaped cross section at $\beta b = 0.75$ is due to the fact that the $M(\chi)$-curve itself contains two buckles, the one and the other giving M_{cr}^{max} below and above $\beta b = 0.75$ respectively.

The geometric data of the four cross sections of Fig. 6.3 are compiled in Fig. 6.8. The centroids and the shear centres are denoted by O and T respectively.
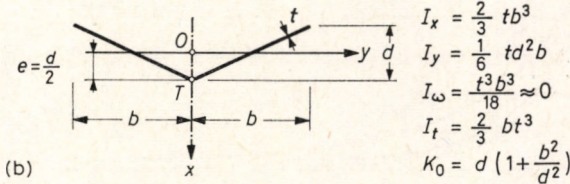
It should be mentioned that — due to the transverse bending — the arch-directed stresses in the cross section do not vary linearly with the height [6.5].

In the case of *central compression* caused by uniform radial load in an arch with a circular axis (Fig. 6.5 (b)), the bending rigidity of the arch, necessary for calculating buckling, is given by the initial tangent to the $M(\chi)$-curve in Fig. 6.6. The factor γ_1 determining the reduced moment of inertia $\gamma_1 I_y$ is plotted against βb in Fig. 6.9. for the four cross section types. A simple approximate expression for γ_1 is also given by the dashed line.
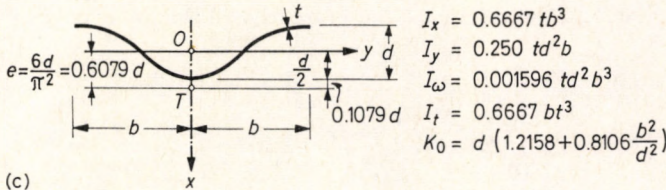
Flat parabola of the second degree:

$I_x = 0.6667\, tb^3$

$I_y = 0.1778\, td^2 b$

$I_\omega = 0.00508\, td^2 b^3$

$I_t = 0.6667\, bt^3$

$K_0 = d\left(0.2972 + \dfrac{b^2}{d^2}\right)$

$e = \dfrac{8}{15}d$

(a)

Flat $\vee$:

$I_x = \dfrac{2}{3}\, tb^3$

$I_y = \dfrac{1}{6}\, td^2 b$

$I_\omega = \dfrac{t^3 b^3}{18} \approx 0$

$I_t = \dfrac{2}{3}\, bt^3$

$K_0 = d\left(1 + \dfrac{b^2}{d^2}\right)$

$e = \dfrac{d}{2}$

(b)

Flat wave (cosine):

$I_x = 0.6667\, tb^3$

$I_y = 0.250\, td^2 b$

$I_\omega = 0.001596\, td^2 b^3$

$I_t = 0.6667\, bt^3$

$K_0 = d\left(1.2158 + 0.8106\dfrac{b^2}{d^2}\right)$

$e = \dfrac{6d}{\pi^2} = 0.6079\, d$

(c)

Flat wing (composed of two parabolas of the 2nd degree):

$I_x = 0.6667\, tb^3$

$I_y = 0.1778\, td^2 b$

$I_\omega = 0.00508\, td^2 b^3$

$I_t = 0.6667\, bt^3$

$K_0 = d\left(0.7428 + 0.875\dfrac{b^2}{d^2}\right)$

$e = \dfrac{7}{15}d$

(d)
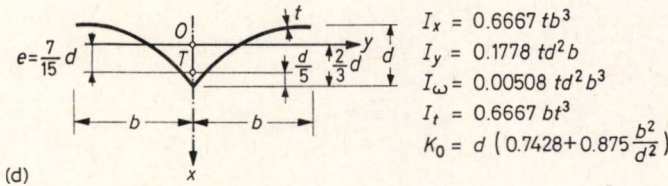
Fig. 6.8. Cross section characteristics

When knowing $\gamma_1 I_y$, the critical load of the shell arch can be determined by the usual arch analysis. However, this will yield only a theoretical critical load for the central compression N_{cr}^{lin}, as explained in Fig. 1.1 (c). (Since the arch buckles always antisymmetrically, its two halves developing bending deformations of opposite signs, its "asymmetric" behaviour with respect to the bending deformation mentioned above does not become manifest.) Nevertheless, the post-buckling behaviour of the whole arch has a decreasing character (Fig. 1.1 (c)), so that *eccentric compression* due to *one-sided load* has also to be considered.

Detailed investigations [6.3], [6.5] resulted in the curve shown in Fig. 6.10, describing the interaction between compressive force N from uniform load and
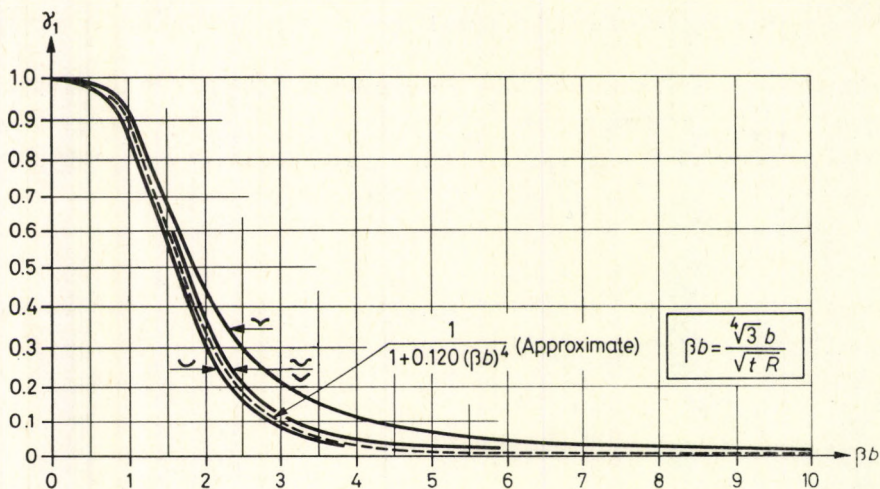
Fig. 6.9. Multiplication factor of the reduced moment of inertia

$$\frac{1}{1+0.120\,(\beta b)^4} \quad \text{(Approximate)} \qquad \beta b = \frac{\sqrt[4]{3}\,b}{\sqrt{t\,R}}$$

$$\frac{M}{M_{cr}} = \left(1 - \frac{N}{N_{cr}}\right)^m$$
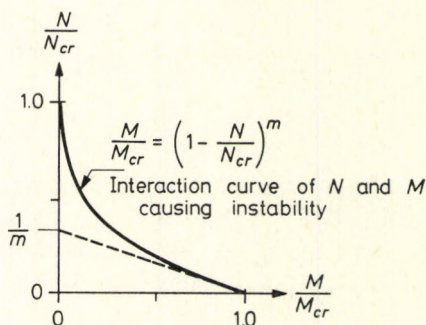
Interaction curve of N and M causing instability

Fig. 6.10. Interaction curve of central compression and
of bending moment causing snapping due to flattening of the cross section

bending moment M_2 arising at the quarter point of the arch due to antisymmetric load, which cause buckling when acting simultaneously. An approximate equation for the diagram is also given in Fig. 6.10. The curve is characterized by its convexity when seen from the origin and by its vertical tangent at $N/N_{cr}=1$. This defines a behaviour similar to that of the axially compressed cylinder (Figs 2.7, 2.8), or of the radially compressed sphere (Figs 4.6, 4.8). Consequently, the buckling of the compressed shell-arch belongs to the type described by Figs 1.4 (c) and 1.5, necessitating the assumption of a bending moment due to initial imperfection even in the case of central compression, and the reduction of the critical compressive force N_{cr}^{lin} accordingly.

6.2.2. Stability Investigations Perpendicularly to the Plane of the Arch

The buckling of shell-arches out of their plane may be treated as *lateral or torsional buckling of curved bars with open cross sections,* since their cross sections do not deform during these instability phenomena. Shell-arches differ from ordinary arches (with solid cross sections) in the following ways:

— their torsional to bending rigidity ratio is much smaller then unity;
— their shear centres do not coincide with their centroids;
— due to their thin walls, the compressive stresses, originally acting parallel to the arch axis, are bound to follow the distortion of the wall, and so exert a twisting effect on the structure.

These properties considerably reduce the critical load as compared with ordinary arches.

The theory of lateral (torsional) buckling of arches with open cross section was developed in [6.5]. Due to their small torsional rigidity, all the lateral stability problems of shell arches can be treated by considering their twisting deformations only. Thus, for most cases, closed formulas could be established. Nevertheless, the results are even so too lengthy to be reproduced here. We shall content ourselves with two remarks.

All the investigations mentioned were carried out on the basis of the linear theory. Accordingly, the interaction curve of bending and compression has the shape shown in Fig. 6.11, where M_2 again denotes the bending moment due to antisymmetric load arising in one fourth of the arch. This curve has exactly the opposite character of that in Fig. 6.10, the latter representing the combination of a nonlinear (snapping) phenomenon with a linear one. On the other hand, the lateral instability problems, being linear bifurcation phenomena, always yield an interaction curve bulging outwards, as required by the theorem of Dunkerley see in [2.27], [2.40].
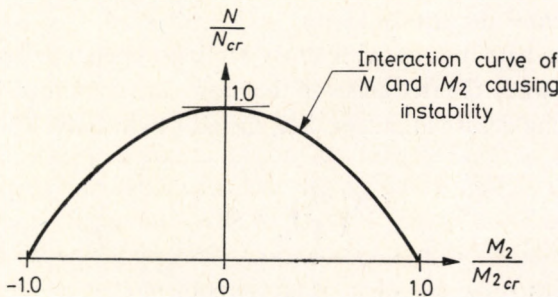

Fig. 6.11. Interaction curve of central compression
and of bending moment causing lateral (torsional) buckling

The model tests [6.5], performed to check the results of the linear theory, mostly showed an increasing (sometimes a constant) post-buckling load bearing capacity, corresponding to Fig. 1.1 (b) (or Fig. 1.1 (a) respectively). Therefore, the linear critical loads may be used for design purposes.

6.2.3. Lateral Buckling of Suspended Shell-Beams

The formulas for the critical load causing lateral buckling of shell-beams with cross sections shown in Fig. 6.3 will be presented on the basis of [6.2] and [6.5].

We assume that the beam is suspended at both ends, rigidly connected at points F to the end cross sections (Fig. 6.12), and loaded by uniformly distributed forces q acting at points P of the cross sections at a height m above the shear centres. (If the height f of the suspension point F is increased to infinity, we obtain the case of the usual "fork-like" support, i.e. when the ends of the beam are prevented from rotating about the beam axis, but are still free to rotate about the vertical axis.)
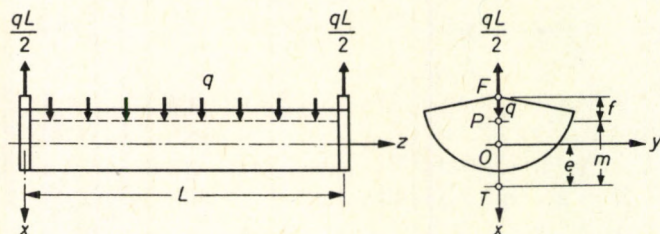
Fig. 6.12. Suspended shell-beam

Both ends of the beam are considered as free to warp. (Warping may be prevented by horizontal end diaphragms but, according to detailed investigations [6.5], this hardly increases the critical load.)

First we deal with beams with cross sections open upwards, as shown in Fig. 6.3 (a), i.e. when the free edges of the beams are compressed.

Lateral buckling deformation consists, then, of twist only. The critical bending moment

$$\left(\frac{ql^2}{8}\right)_{cr} = M_{cr} \tag{6.2}$$

is to be calculated from the quadratic equation

$$a_2 M_{cr}^2 + a_1 M_{cr} + a_0 = 0 \tag{6.3}$$

with the coefficients:

$$a_2 = 5.145K_0^2 + 12.36K_0 m + 10.17K_0 \frac{m^2}{f} + 1.6m^2 + 1.441 \frac{m^3}{f}, \qquad (6.4a)$$

$$a_1 = -\left[24.29K_0 GI_t + 1043K_0 \frac{EI_\omega}{l^2} + 19.74mGI_t + 1597m \frac{EI_\omega}{l^2} + \right.$$

$$\left. + 14.58 \frac{m^2}{f} GI_t + 1281 \frac{m^2}{f} \frac{(EI_\omega)^2}{l^2} \right], \qquad (6.4b)$$

$$a_0 = 21.9(GI_t)^2 + 2163GI_t \frac{EI_\omega}{l^2} + 19\,214 \frac{(EI_\omega)^2}{l^4}. \qquad (6.4c)$$

The cross section characteristics appearing in these expressions are compiled in Fig. 6.8.

In Fig. 6.13 we plotted the critical bending moment M_{cr} causing lateral buckling of a beam with V-shaped cross section (with $EI_\omega \approx 0$), loaded by its own weight acting in the centroid ($m=e$), against the inverse value of the suspension height f. It can be seen that, compared to the case of end cross sections with prevented twist ($f=\infty$; i.e. $m/f=0$), the suspension at a finite height up to $m/f=2$ (i.e. as low as three quarters of the cross section height) does not cause a substantial reduction in the critical bending moment.
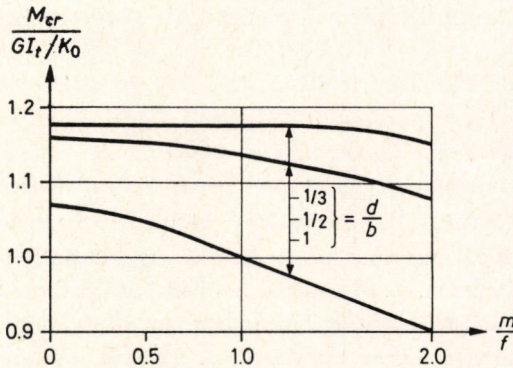
Fig. 6.13. Bending moment causing lateral buckling
of a suspended shell-beam with V-shaped cross section
(open upwards), the load acting on the centroid

However, if the cross section of the beam is open downwards (Fig. 6.3 (b)), i.e. the free edges are in tension, then the lateral bending deformation also has to be taken into consideration when calculating lateral buckling. The critical bending moment M_{cr} is to be computed also in this case from Eq. (6.3), but with the

coefficients derived on the basis of [6.2]:

$$a_2 = \frac{l^2}{EI_x}\left(-0.1650 - 0.1331\frac{m}{f} + 0.05657\frac{K_0}{f}\right), \tag{6.5a}$$

$$a_1 = -\left[K_0 + 1.747m + 1.416\frac{m^2}{f} + 0.1435\frac{l^2}{fEI_x}\left(GI_t + EI_\omega\frac{\pi^2}{l^2}\right)\right], \tag{6.5b}$$

$$a_0 = 2.155\left(GI_t + EI_\omega\frac{\pi^2}{l^2}\right). \tag{6.5c}$$

The definitions of the symbols are to be found in Figs 6.8 and 6.12. In Formulas (6.5a, b, c), m and K have to be taken with negative signs because of the inverse position of the cross sections as compared to Fig. 6.8.

The suspension height f influences M_{cr} in this case much more strongly than with cross sections open upwards (Fig. 6.3 (a)). On the other hand, the critical bending moment causing lateral buckling of beams with cross sections open downwards is generally much greater than either the snapping moment causing flattening (Fig. 6.7), or the bending moment causing local buckling of the compressed middle part of the cross sections. Thus, we also touch briefly upon this latter problem.

6.2.4. Local Buckling of Shell-Arches and Shell-Beams

If the free edges of the shell-arch (beam) are in compression (central compression, or bending that causes compression in the free edges), the local buckling would begin at the free edge. The buckling half wavelength extends over the entire length of the arch (beam), so that the local buckling merges with the instability of the whole structure. (This was shown for straight bars with angle cross section in [2.51].) Hence, the local buckling has to be investigated only if the free edges of the structure are in tension, as in the case of shell-beams with cross sections open downwards (Fig. 6.3 (b)). The stability analysis of the middle part of the cross sections has to be carried out as for a shell, as shown in the previous chapters. Some special points to be considered for its implementation are to be found in [6.5].

7. Buckling of Orthotropic Shells

7.1. Orthotropic Shells in General

The elastic properties of isotropic shells, dealt with in the foregoing, are the same in every direction. However, this static model is only suitable to describe the behaviour of shells which consist of one solid layer made of a unique, isotropic material.

Due to their static and structural advantages, composite (reticulated, ribbed, corrugated, sandwich, etc.) shells are frequently used in the engineering practice. Since their properties differ markedly from those of isotropic shells, we have to use the theory of anisotropic shells to describe their behaviour with sufficient accuracy.

It is rather intricate to take general anisotropy into account, so we will deal here only with a special case of anisotropy called orthotropy. Moreover, we stipulate that the cross section of the shell be symmetric with respect to the middle surface of the shell.

An orthotropic shell has in every point of the middle surface two particular planes perpendicular to each other and to the middle surface, which are characterized by the fact that in every optional pair of planes symmetric to them the elastic properties of the shell are the same. The intersection lines of these two particular planes with the middle surface are called the principal directions of orthotropy.

Taking these principal directions as co-ordinates, the stiffness matrix of the shell can be set up as follows (neglecting the deformation due to transverse shear, to be considered in Section 8.1 on sandwich shells):

$$
\begin{bmatrix} n_x \\ n_y \\ n_{xy} \\ m_x \\ m_y \\ m_{xy} \end{bmatrix} = \begin{bmatrix} \bar{T}_x & \bar{T}' & 0 & 0 & 0 & 0 \\ \bar{T}' & \bar{T}_y & 0 & 0 & 0 & 0 \\ 0 & 0 & \bar{T}_{xy} & 0 & 0 & 0 \\ 0 & 0 & 0 & \bar{B}_x & \bar{B}' & 0 \\ 0 & 0 & 0 & \bar{B}' & \bar{B}_y & 0 \\ 0 & 0 & 0 & 0 & 0 & \bar{B}_{xy} \end{bmatrix} \begin{bmatrix} \varepsilon_x \\ \varepsilon_y \\ \gamma_{xy}/2 \\ w'' \\ w^{\cdot\cdot} \\ w'^{\cdot} \end{bmatrix} . \tag{7.1}
$$

Here the following notations have been used:

$\varepsilon_x, \varepsilon_y$	— specific elongations in the direction of x and y respectively;
γ_{xy}	— angular distortion of the directions x and y;
w	— displacement perpendicular to the shell surface;
$'$ and $\cdot$	— differentiation according to x and y respectively;
$\bar{B}_x, \bar{B}_y$	— bending stiffnesses in the directions x and y respectively,
$\bar{B}_{xy}$	— torsional rigidity;
$\bar{T}_x, \bar{T}_y$	— tensile stiffnesses in the directions of x and y respectively;
$\bar{T}_{xy}$	— shearing stiffness in the plane xy connecting *half* the distortion angle and the shearing force;
$\bar{B}'$ and $\bar{T}'$	— transversal bending and tensile stiffnesses respectively.

It should be remarked that in some references the shearing and torsional stiffnesses are differently defined and, accordingly, in these cases the stiffness matrix (7.1) also undergoes some modification.

The rigidity matrix of the orthotropic shell (7.1) is always symmetric with respect to the main diagonal [7.30], so that the elements denoted by dashes are identical in both directions.

In some cases, as e.g., in the case of the plate reinforced by ribs having different torsional stiffnesses in two directions, the torsional rigidity $\bar{B}_{xy}$ is composed of two parts, see in Chapter 8.

In the following we suppose that the lines traced according to the principal directions of orthotropy in the different points of the shell form a usable system of co-ordinates.

The investigation of such an orthotropic shell is still fairly complicated, so we shall examine the possibility of neglecting the terms $\bar{B}'$ and $\bar{T}'$, which represent the effect of the transversal contraction. That is, in this case the rigidity matrix will have elements only in its main diagonal.

In the case of isotropic shells, Poisson's ratio ν appears in factors which have the extreme values of

$$\frac{1}{1-\nu^2} \quad \text{or} \quad \frac{1}{\sqrt{1-\nu^2}} \quad \text{(see e.g. Eqs (2.11) and (4.7)).}$$

For $\nu=0.3$ these values become 1.125 or 1.06. Consequently, if we assume $\nu=0$, i.e. if we neglect the transversal contraction, this diminishes the computed critical load by $11\sim6\%$. (On the other hand, if we neglected only $\bar{B}'$ and $\bar{T}'$ in the rigidity matrix on the isotropic shell, while in the other rigidity characteristics we took ν into consideration, the aforementioned errors would increase to 1.5 times their values.)

The influence of v on several kinds of orthotropic shells is even less. For example, the critical load of a ribbed shell will be influenced only by the v of the plate but not by the v of the ribs. Hence, the error caused by the assumption of $v=0$ will be less than indicated above, and the result will be on the safe side. Consequently, the assumption of $v=0$ simplifies the stability analysis considerably, and many authors of the papers to be reported on also used this assumption.

In most cases of orthotropic shells it is not possible to neglect Poisson's ratio in the rigidity characteristics because it does not appear in them explicitly. Moreover, the influence of the transversal contraction is, in some cases, (e.g. reticulated shells) considerable. Hence, in these cases we propose the following procedure: We omit the elements $\bar{B}'$ and $\bar{T}'$ from the rigidity matrix, but assume values for the other elements which compensate for this omission. We denote these substituting rigidity characteristics by capital letters without overlining. (Of course, if $v=0$, the two kinds of rigidity characteristics become identical.)

The relations between the actual and the substituting rigidity characteristics can be obtained from the equilibrium and compatibility equations of shallow shells. We have to choose the substituting rigidities in such a way that they furnish the same equations as the actual ones. The substituting rigidity characteristics are as follows:

$$B_x = \bar{B}_x, \tag{7.2a}$$

$$B_y = \bar{B}_y, \tag{7.2b}$$

$$B_{xy} = \bar{B}_{xy} + \bar{B}', \tag{7.2c}$$

$$T_x = \bar{T}_x - \frac{\bar{T}'^2}{\bar{T}_y}, \tag{7.2d}$$

$$T_y = \bar{T}_y - \frac{\bar{T}'^2}{\bar{T}_x}, \tag{7.2e}$$

$$T_{xy} = \frac{\bar{T}_{xy}}{1 - \frac{\bar{T}'\bar{T}_{xy}}{\bar{T}_x\bar{T}_y - \bar{T}'^2}}. \tag{7.2f}$$

Hence, the rigidity properties of the orthotropic shell, symmetric to the middle surface, can be characterized by six data. The simplified stiffness matrix assumes the following form:

$$
\begin{bmatrix} n_x \\ n_y \\ n_{xy} \\ m_x \\ m_y \\ m_{xy} \end{bmatrix} =
\begin{bmatrix}
T_x & 0 & 0 & 0 & 0 & 0 \\
0 & T_y & 0 & 0 & 0 & 0 \\
0 & 0 & T_{xy} & 0 & 0 & 0 \\
0 & 0 & 0 & B_x & 0 & 0 \\
0 & 0 & 0 & 0 & B_y & 0 \\
0 & 0 & 0 & 0 & 0 & B_{xy}
\end{bmatrix}
\begin{bmatrix} \varepsilon_x \\ \varepsilon_y \\ \gamma_{xy}/2 \\ w'' \\ w^{..} \\ w^{/.} \end{bmatrix}. \tag{7.3}
$$

The rigidity characteristics will be determined for the different composite shells in Chapter 8, otherwise we refer to the literature [7.10], [7.31]. Thus, the equilibrium and compatibility equations of shallow orthotropic shells of constant stiffness can be developed in a rectangular system of co-ordinates as follows [2.13]:

$$
-(B_x w'''' + 2B_{xy} w''^{\cdot\cdot} + B_y w^{\cdots}) + F''(z_0^{\cdot\cdot} + w_0^{\cdot\cdot} + w^{\cdot\cdot}) -
$$

$$
-2F_0^{\cdot\prime}(z_0^{\cdot\prime} + w_0^{\cdot\prime} + w^{\prime\cdot}) + F^{\cdot\cdot}(z_0'' + w_0'' + w'') +
$$

$$
+ w^{\cdot\cdot} F_0'' - 2w'^{\cdot} F_0^{\cdot\prime} + w'' F_0^{\cdot\cdot} = 0, \tag{7.4a}
$$

$$
\frac{F''''}{T_y} + \frac{2F''^{\cdot\cdot}}{T_{xy}} + \frac{F^{\cdots}}{T_x} = -w^{\cdot\cdot}(z_0'' + w_0'') + 2w'^{\cdot}(z_0^{\cdot\prime} + w_0^{\cdot\prime}) -
$$

$$
- w''(z_0^{\cdot\cdot} + w_0^{\cdot\cdot}) - w^{\cdot\cdot} w'' + w'^{\cdot 2}. \tag{7.4b}
$$

Formulas (7.4a) and (7.4b) are the Donnell-type equations of the shallow orthotropic shell, which also take into account the second powers of the derivatives of the displacement w, perpendicular to the shell surface. In the equations z_0 denotes the height of the shell surface over the plane xy, w_0 the sum of the initial imperfection and the pre-buckling deformation due to static load, w the buckling deformation, and F_0 and F the stress functions belonging to the internal forces due to static load and to buckling respectively.

The method of solution and the considerations concerning the taking of linear and nonlinear terms into account applied in this chapter are essentially the same as in the previous chapters.

7.2. Linear Critical Load of the Orthotropic Shell

If we neglect the nonlinear terms in Eq. (7.4a, b), we obtain the differential equations which determine the linear critical load. Most shell shapes can be closely approximated by the shallow paraboloid

$$
z_0 = \frac{1}{2R_x} x^2 + \frac{1}{2R_y} y^2. \tag{7.5}
$$

The solution of the equilibrium and compatibility equations for this shell shape can be written in the form

$$
w = W \cos\left(\frac{\pi}{l_x} x\right) \cos\left(\frac{\pi}{l_y} y\right), \tag{7.6}
$$

if we assume a rectangular ground plan, hinged edges, the pre-buckling internal forces

$$\ddot{F}_0 = n_x = \text{constant},$$

$$F_0'' = n_y = \text{constant},$$

$$\dot{F}_0' = -n_{xy} = 0,$$

and geometrically perfect shape ($w_0=0$). In Eq. (7.6) W is an (undetermined) constant, while l_x and l_y denote the buckling lengths in the directions x and y respectively. The critical internal forces n_x, n_y, caused by the critical load intensity, can be determined, according to [2.13], from the characteristic equation

$$\frac{n_x}{l_x^2} + \frac{n_y}{l_y^2} = \pi^2 \left[\frac{1}{l_x^8} \left(\frac{B_x}{T_y} \right) + \frac{1}{l_x^6 l_y^2} \left(\frac{2B_{xy}}{T_y} + \frac{2B_x}{T_{xy}} \right) + \right.$$

$$+ \frac{1}{l_x^4 l_y^4} \left(\frac{B_x}{T_x} + \frac{4B_{xy}}{T_{xy}} + \frac{B_y}{T_y} \right) + \frac{1}{l_x^2 l_y^6} \left(\frac{2B_{xy}}{T_x} + \frac{2B_y}{T_{xy}} \right) +$$

$$\left. + \frac{1}{l_y^8} \left(\frac{B_y}{T_x} \right) + \left(\frac{1}{\pi^2 l_y^2 R_x} + \frac{1}{\pi^2 l_x^2 R_y} \right)^2 \right] \cdot \left(\frac{1}{l_x^4 T_y} + \frac{2}{l_x^2 l_y^2 T_{xy}} + \frac{1}{l_y^4 T_x} \right)^{-1}. \quad (7.7)$$

The critical force (or forces) in Eq. (7.7) have to be minimized with respect to l_x and l_y. However, we have to observe the geometric restictions for l_x and l_y set by the boundary conditions or by other requirements, e.g. that along the circumference of a cylinder only an integer number of buckling wavelengths can develop.

In the case of some isotropic shells under certain loadings, several buckling modes were associated with the linear critical load (e.g. axially compressed cylinder, radially compressed sphere). This does not hold true for orthotropic shells. As remarked in Section 2.1, orthotropy mostly does not allow multimode (compound) buckling [8.2.6a], [8.2.6b]. As a rule, uniquely determined buckling lengths, l_x and l_y, are associated with the minimum critical load [7.22], [7.30].

As with isotropic shells (see Eqs (2.5a) and (4.1)), the result obtained for the paraboloid (7.5) may be used as an approximation for orthotropic shells of other shapes. The only requirement is that the paraboloid should approximate fairly closely the actual shape inside one buckle. Consequently, in the case of a radially compressed spherical shell $R_x=R_y=R$ and $n_x=n_y=pR/2$. With these data, the critical load p_{cr}^{lin} can be computed from Eq. (7.7). Or, for the cylinder shown in Fig. 2.2, $R_y=R$, $R_x=\infty$ and $y=R\varphi$, and the critical load can again be determined from Eq. (7.7).

On the basis of what has been said above and of the exact and approximate methods to be found in the references, we shall now present the critical loads for several kinds of orthotropic shells.

7.3. Linear Critical Load of the Orthotropic Cylinder

In certain cases, it is expedient to form three parameters of the six rigidity char-
acteristics (7.2), becasue they describe the main properties of the orthotropic
cylinder fairly well [7.1], [7.22], [7.30]. These parameters are:

$$\vartheta_s = \frac{\sqrt{T_x T_y}}{T_{xy}},$$

$$\vartheta_p = \frac{B_{xy}}{\sqrt{B_x B_y}}, \tag{7.8}$$

$$\gamma = \frac{B_x T_y}{B_y T_x}.$$

The values $\vartheta_s = \vartheta_p = \gamma = 1$ correspond to the isotropic shell.

We call the cylinder ring-stiffened if $1/\gamma > 1$, and axially (or stringer)-stiffened
if $1/\gamma < 1$. It should be remarked that — except for short cylinders — if we use the
same amount of material, the critical loads of ring-stiffened cylinders are always
greater than those of stringer-stiffened ones, so that the former are more advan-
tageous.

The buckling mode of the cylinder of length L has several characteristic shapes.
One is the axially symmetric mode (with $l_y = \infty$ and $l_x = L/m$, $m = 1, 2, 3, ...$)
that yields the minimum critical load for some cases of axial compression. In
other cases of axial compression, and furthermore for circumferential compression,
the reticulated buckling pattern proves to be the most onerous (with $l_x = L/m$ and
$l_y = R\pi/n$ for a complete cylinder, while $l_y = L_y/n$ for a cylindrical panel, L_y being
the circumferential length of the panel and $n = 2, 3, ...$). In addition, the diamond
shape buckling pattern may also occur, see also in Section 7.7.1.

The buckling shape of the twisted cylinder has one half wave skew to the cylinder
axis with the length L in the x direction, while in circumferential direction several
waves develop [7.21].

7.3.1. Axially Compressed Orthotropic Cylinder
(with or without Internal Pressure)

In the case of axial compression (see Fig. 2.2), the buckling pattern is either
axisymmetric or reticulated. Gerard's investigations [7.9] clarified which of the
two will develop, i.e. which one is associated with a lower critical load. His results
are shown in Fig. 7.1, using the parameters defined by Eqs (7.8).

$$\vartheta_s = \frac{\sqrt{T_x\,T_y}}{T_{xy}}$$

$$\vartheta_p = \frac{B_{xy}}{\sqrt{B_x\,B_y}}$$

$$\frac{1}{\vartheta} = \frac{B_y\,T_x}{B_x\,T_y}$$

(a)

(b)
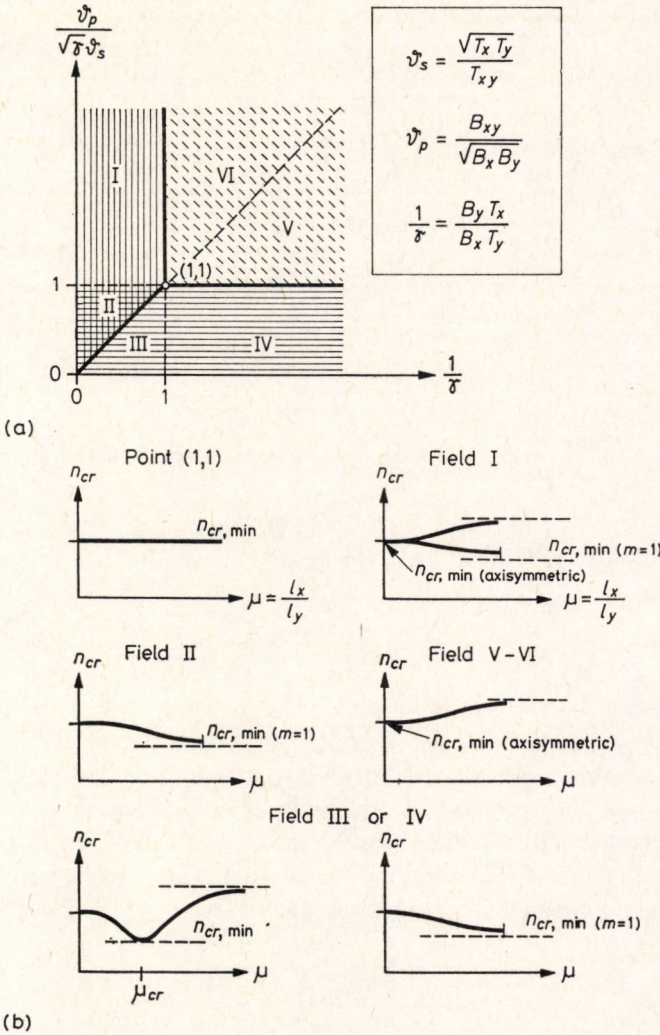
Fig. 7.1. Buckling patterns of axially compressed orthotropic cylindrical
shells as functions of the rigidity parameters

According to various values of the rigidity parameters of the shell, Fig. 7.1 (a) is subdivided into six fields. The diagrams of Fig. 7.1 (b) show the variations of the critical forces corresponding to each field. The parameters corresponding to point (1,1) characterize the isotropic cylinder, for which the same critical load is associated with any buckling length ratio $\mu = l_x/l_y$. In Field I, there are two possibilities: the minimum critical load is associated either with axisymmetric

buckling, or with a reticulated pattern, where the buckling length in the axial direction extends to the whole cylinder ($l_x=L$, i.e. $m=1$). In Field II, the minimum critical load is always associated with a reticulated pattern with a wavelength in the axial direction equal to the entire length of the cylinder ($l_x=L$). In Fields III and IV, the reticulated buckling pattern is the most onerous one, either with $m=1$ ($l_x=L$), or with $l_x=L/m$, where $m=2, 3...$ Finally, cylindrical shells falling into Fields V and VI always buckle axisymmetrically.

If Fig. 7.1 shows that the axisymmetric buckling pattern is the most onerous one, the critical axial compression can be calculated from the following formula (see [2.13], [7.9], [7.30]):

$$n_{x,cr}^{\mathrm{lin}} = \frac{2}{R}\sqrt{B_x T_y}. \tag{7.9}$$

As with isotropic shells, the axisymmetric buckling is not influenced by the internal pressure.

If the shell buckled in a reticulated pattern with an infinitely large buckling length in the x direction, its critical load would be given by the expression:

$$n_{x,cr}^{\mathrm{lin}} = \frac{2}{R}\sqrt{B_y T_x}. \tag{7.10}$$

This formula may serve for assessing the critical load of a cylinder that buckles with $l_x=L$.

If Fig. 7.1 yields a reticulated buckling pattern, the internal pressure may increase the critical load up to that pertaining to axisymmetric buckling.

In the general case, the critical axial load can be calculated from Eq. (7.7). Expressing $n_{x,cr}^{\mathrm{lin}}$ from this, considering that, in the case of an internal pressure p, $n_y=-pR$, and minimizing $n_{x,cr}^{\mathrm{lin}}$ with respect to l_x^2, we arrive at the following equation:

$$n_{x,cr}^{\mathrm{lin}} = \frac{2}{R}\sqrt{(B_x+2\mu^2 B_{xy}+\mu^4 B_y)\left(\frac{1}{T_y}+\frac{2\mu^2}{T_{xy}}+\frac{\mu^4}{T_x}\right)^{-1}} + pR\mu^2. \tag{7.11}$$

Here again $\mu=l_x/l_y$ is the ratio of the two buckling lengths. Equation (7.11) is in accordance with the relations to be found in the literature [7.22], [7.30].

The minimum critical load is to be determined by choosing an appropriate value for μ. As was mentioned in Section 7.2, in the case of orthotropic shells, only one buckling mode is associated with the minimum linear critical load, so that we will find the minimum value of $n_{x,cr}^{\mathrm{lin}}$ at a definite value of μ.

In the case of axisymmetric buckling, $\mu\to0$, and Eq. (7.11) turns into Eq. (7.9).

For the determination of the value of μ which makes the critical load a minimum, Fig. 7.2 may be of some help. Figure 7.2 (a) shows the additive term of the critical
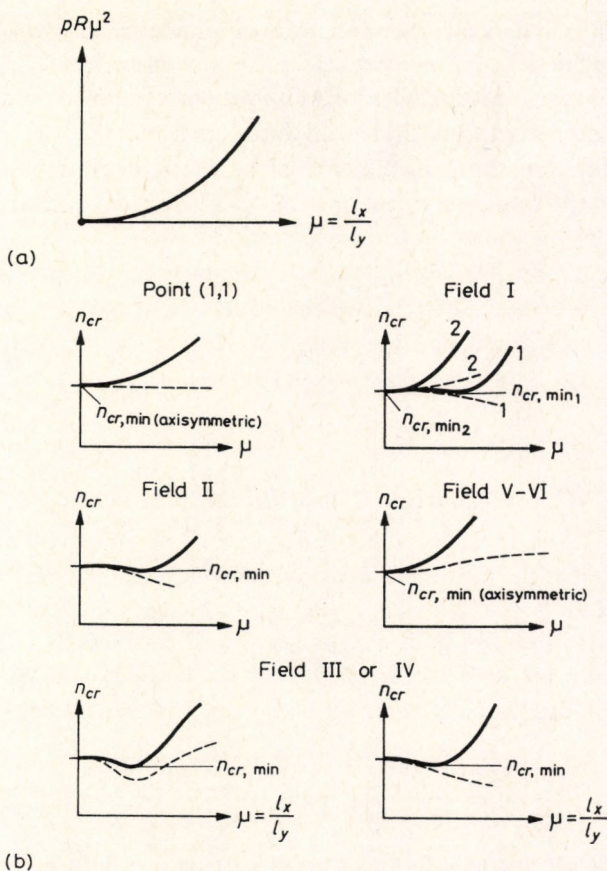
Fig. 7.2. The influence of the internal pressure p on
the linear critical loads of axially compressed orthotropic cylindrical shells

load due to the internal pressure p. This parabola has to be added to one of the curves plotted with dashed lines in Fig. 7.2 (b), representing the case of pure axial compression. The full line curves give the sum of both effects.

The diagrams show that, in the cases belonging to Fields V and VI in Fig. 7.1, when axisymmetric buckling occurs without internal pressure, the same buckling mode remains onerous with $p > 0$. In the other cases we have to minimize p_{cr} with respect to μ and, in addition, to check the case $l_x = L$, too. From these two values the actual critical load will be the one which belongs to a smaller l_x.

In engineering practice it is generally more expedient to compute $n_{x,cr}^{lin}$ from Eq. (7.7) for a series of μ values instead of performing the minimization analytically.

The internal pressure p influences the buckling of stringer- and ring-stiffened cylinders differently.

Ring-stiffened cylinders may develop, as mentioned earlier, two kinds of buckling pattern (see Fig. 7.1). If the shell buckles axisymmetrically, the internal pressure does not interfere, while it impedes buckling with a reticulated pattern. However, the difference between the critical axial forces pertaining to axisymmetric and reticulated buckling patterns in the absence of internal pressure is rather slight. This fact limits the influence of the internal pressure too, since the critical load cannot be greater than that of the axisymmetric buckling.

On the other hand, *stringer-stiffened* cylinders show, in the absence of internal pressure, a much greater difference in the critical axial forces pertaining to axisymmetric and reticulated buckling patterns. Hence, the internal pressure may increase the critical load to several times its value.

7.3.2. Orthotropic Cylindrical Shells in Bending

We have seen that the maximum axial compressive bending stress causing buckling of a closed, isotropic, cylindrical shell hardly exceeds it critical uniform compressive stress. Holston [7.12], as well as Reese and Bert [7.20a], showed that this statement is valid for orthotropic cylindrical shells too. Thus, buckling due to bending may be analysed by the formulas valid for the critical stress of axial compression.

7.3.3. The Orthotropic Cylinder under Circumferential Compression
Due to External Lateral Pressure

For the loading case shown in Fig. 2.11 (a), the critical load can be calculated from Eq. (7.7) with the membrane forces $n_x=0$, $n_y=pR$. The buckling length l_x in the direction x always extends to the whole cylinder length L, hence $l_x=L$. The buckling length l_y has to be chosen in such a way that the critical load be a minimum. An informative value of the circumferential wave number n which determines l_y on a closed cylinder may be read off the diagram of Fig. 7.3, recommended for hydrostatic compression [7.3].

In the case of very long closed cylinders, the end supports do not influence the magnitude of the critical load, so that this will be equal to that of a ring. Equation (7.7) yields:

$$p_{cr}^{ring} = \frac{4B_y}{R^3},$$

(7.12)
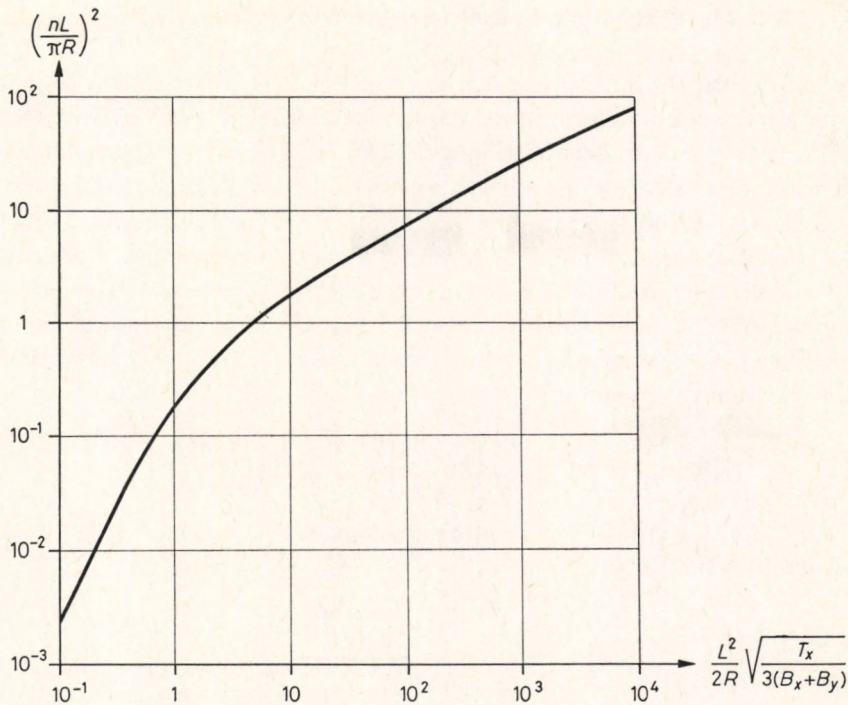
Fig. 7.3. Buckling full wave member in circumferential direction
of hydrostatically compressed orthotropical cylinders

which is the equivalent of Eq. (2.29c) for the orthotropic case, corresponding to
the constant directional pressure considered in the derivation of Eq. (7.7). For
fluid pressure the remarks made in connection with Eqs (2.29a, b, c) apply.

If the shell is a long but flat cylindrical panel, we may take $l_y \approx L_y/2$, so that we
obtain the critical load of a flat arch:

$$p_{cr}^{arch} = \frac{4\pi^2 B_y}{RL_y^2} . \tag{7.13}$$

The critical pressures p_{cr}^{ring} or p_{cr}^{arch} give a lower bound for the critical loads of
cylinders of medium lengths L.

In the case of long cylinders and those of medium length, the effect of ring-
stiffening is stronger. For short cylinders, however, the effect of stringer-stiffening
increases more and more, so that the critical load can reach a much higher value
than that given by Eq. (7.13).

10 Buckling of Shells

7.3.4. The Orthotropic Cylinder Subjected to Hydrostatic Pressure

The effect of hydrostatic pressure, shown in Fig. 2.11 (b), is similar to that of the lateral pressure dealt with in the previous section, with the difference that in the present case an axial compression with $n_x = pR/2$ also arises. The circumferential compression has the value $n_y = pR$. The buckling length in the axial direction again extends over the whole length of the cylinder, i.e. $l_x = L$. The critical pressure is to be computed from Eq. (7.7). For ring-stiffened closed cylinders Bodner [7.3] performed the minimization and obtained the diagram of Fig. 7.3. This gives the circumferential full wave number n, which yields the minimum critical pressure p_{cr}^{lin}. Knowing n, the critical hydrostatic pressure may be computed, according to [1.1], [7.3], from the equation:

$$ p_{cr} = \frac{2\pi^2 B_x}{RL^2} \left[1 + \frac{n^2 L^2}{\pi^2 R^2} \left(1 + \frac{B_y}{B_x} \right) - \frac{T_x L^4}{B_x R^2 \pi^4} \left(1 + \frac{n^2 L^2}{2R^2} \right)^3 \right]. \tag{7.14} $$

The value of the critical hydrostatic pressure can also be immediately read off the diagram of Bodner, Fig. 7.4.
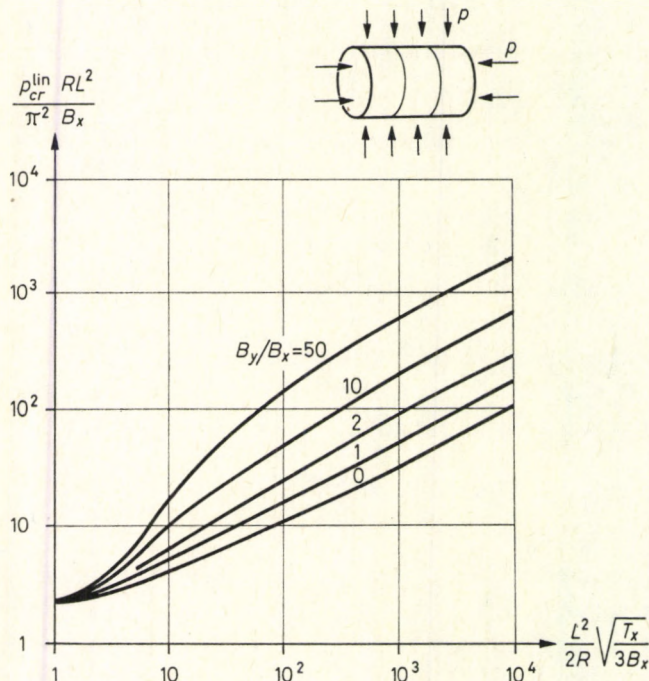
Fig. 7.4. Linear critical load of the ring-stiffened cylindrical shell subjected to hydrostatic pressure

7.3.5. Torsion of the Orthotropic Cylinder

Equation (7.7) is not suitable for the investigation of the buckling caused by torsion, since it does not contain the shearing force n_{xy}. In fact, up to now no exact solution has been found for buckling by torsion. Hence, instead of using the equilibrium equations, investigations were carried out by the energy method, assuming different buckling shapes.

Simitses [7.24] established the influence of each rigidity characteristic on the critical load. He found that the role of B_y is important in all cases, that of B_{xy} only for medium and short shells, while that of B_x only for short cylinders. The quantities T_x and T_{xy} hardly influence the critical twisting load.

Milligan and Gerard [7.20] developed the following expression for the critical shearing force $n_{xy, cr}$ or the twisted orthotropic cylinder of medium length:

$$n_{xy, cr} = 0.89 Z_t^{3/4} \frac{\pi^2 B_x}{L^2}, \qquad (7.15)$$

where Z_t is given by the equation:

$$Z_t = \frac{T_y L^4}{12 R^2 B_x} \sqrt{\frac{T_y}{T_x}} \left(\frac{B_y}{B_x}\right)^{5/6}. \qquad (7.16)$$

Hayashi [7.11], (and in [1.1]) also determined the critical load of medium and short twisteed cylinders. His results are presented in the diagram shown in Fig. 7.5.
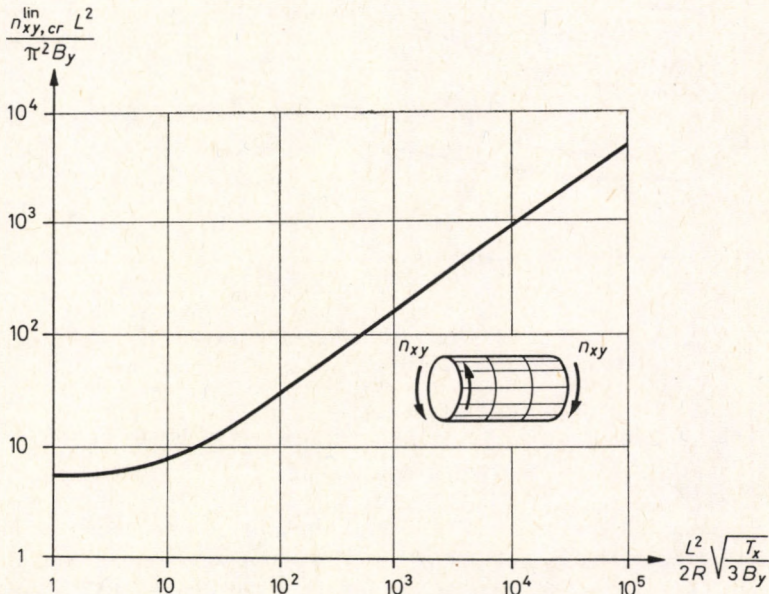
Fig. 7.5. Linear critical shearing force of the twisted orthotropic cylinder

The buckling mode of the twisted cylinder is always long-shaped, including an angle smaller to the axial than to the circumferential direction. Hence, the circumferential direction intersects the buckling wave nearly perpendicularly, resulting in a far greater role for the ring-stiffening.

Stein *et al.* [7.29], see also in [1.1], in their solution for the ring-stiffened twisted cylinder also took into consideration that the ring-stiffening consists of individual ribs, the number of which along the cylinder length sets an upper bound for the critical load, since the shell may also buckle between the ribs. (This limitation is, of course, not valid for cylinders made of orthotropic material.) Their results are represented by the diagram of Fig. 7.6. Using the parameter Z defined in the figure, the critical shearing force can be readily determined.
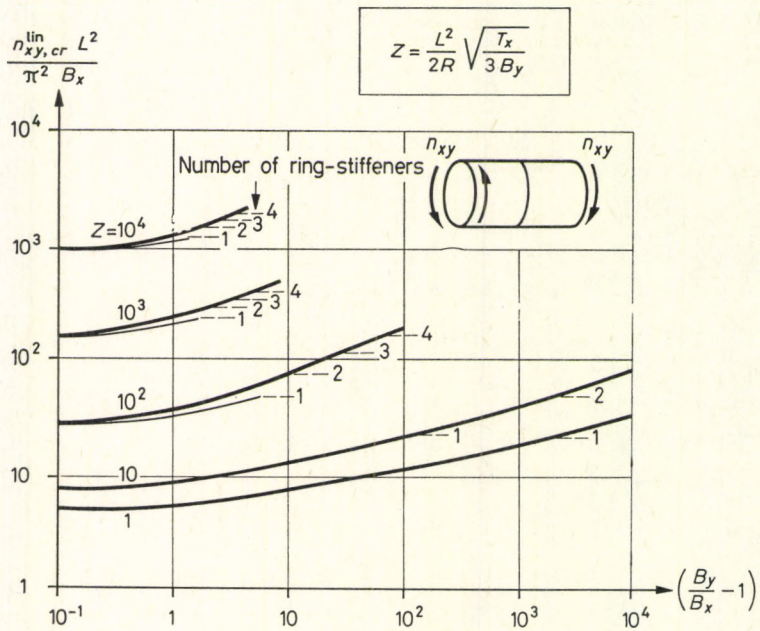
Fig. 7.6. Linear critical shearing force
of the twisted cylinder ring-stiffened by discrete stiffeners

7.3.6. Simultaneous Action of Several Kinds of Loads on the Orthotropic Cylinder

We may conclude on the effect of several kinds of simultaneously acting loads on the orthotropic cylinder only from numerical examples or experimental results.

According to the investigations of Holston [7.12], and further of Reese and Bert [7.20a] cited before, the critical compressive stresses caused by bending and by

central compression have practically the same value. We have also seen on the isotropic cylinder that the interaction of axial and lateral pressures may be safely approximated, according to Seide and Weingarten [2.45], by the expression:

$$\frac{n_x}{n_{x,cr}} + \frac{n_y}{n_{y,cr}} = 1.$$

The numerical examples of Mah, Almroth and Pittner [7.15] show the relation:

$$\left(\frac{n_x^{\text{bending}}}{n_{x,cr}}\right)^2 + \frac{n_y}{n_{y,cr}} = 1$$

to be valid for the interaction of axial compression due to bending and of circumferential compression.

Batdorf [2.3] established the relation:

$$\left(\frac{n_{xy}}{n_{xy,cr}}\right)^2 + \frac{n_x}{n_{x,cr}} = 1$$

for the interaction of shear and axial compression.

Finally, Stein *et al* [7.29] found for internal, and Simitses [7.24] for external, lateral pressure that the expression:

$$\left(\frac{n_{xy}}{n_{xy,cr}}\right)^2 + \frac{n_y}{n_{y,cr}} = 1$$

can be regarded as valid for the simultaneous action of shear and circumferential compression or tension due to lateral pressure.

For more than two loading cases no complex investigations have been made yet. On the basis of the foregoing, however, the following Dunkerley-type expression can be set up, which yields results corresponding to all the relations shown hitherto (or deviating on the safe side), provided n_y is compression:

$$\frac{n_x}{n_{x,cr}} + \frac{n_y}{n_{y,cr}} + \left(\frac{n_{xy}}{n_{xy,cr}}\right)^2 = 1. \tag{7.17}$$

Until more detailed investigations have been made, we recommend the approximate general formula (7.17) for use.

7.4. Linear Critical Load of Orthotropic Conical Shells

Most investigations referring to orthotropic conical shells were made by Singer *et al.* [7.2], [7.25], [7.26], [7.27]. They found that, as with isotropic shells (see Chapter 3), orthotropic conical shells may also be analyzed on a substituting cylinder with orthotropy and stiffness properties corresponding to the cone.

7.5. Linear Critical Load of Orthotropic Spherical Shells

The linear critical value of the uniform radial pressure acting on the orthotropic complete spherical shell was computed exactly by Crawford and Schwartz [7.5]. Their results coincide with those calculated for the substituting shallow elliptic paraboloid. Hence, we can calculate the critical load of the latter from Eq. (7.7), with $R_x = R_y = R$ and $n_x = n_y = pR/2$. Owing to the manifold symmetry of the spherical shell, the tensile and bending rigidity characteristics in the x and y directions are mostly equal with each other. Consequently, the minimum critical load is associated with $l_x = l_y$, so that only a minimization with respect to l_x is needed. The critical load becomes:

$$p_{cr}^{lin} = \frac{4}{R^2} \sqrt{(B_x + 2B_{xy} + B_y)\left(\frac{1}{T_x} + \frac{2}{T_{xy}} + \frac{1}{T_y}\right)^{-1}}.$$ (7.18)

If the rigidities in the x and y directions differ from each other, then $l_x \neq l_y$, and p_{cr}^{lin} has to be determined by a double minimization process.

7.6. Linear Critical Load of Orthotropic Hyperbolic Paraboloid Shells

The critical load of saddle-shaped hypar shells (see Fig. 5.8) can be determined from Eq. (7.7), provided that the two membrane forces n_x and n_y can be regarded as constant all over the shell surface. In the computation it should be observed that the two radiuses of principal curvatures (and possibly the two membrane forces) have opposite signs.

The hypar shell of Fig. 5.4, with the principal directions of orthotropy parallel to the supported generatrices, cannot be treated by Eq. (7.7). That is, the surface has a twist, but this does not appear in the equation; moreover, the uniform load is carried only by shearing forces n_{xy}, which are also not contained in Eq (7.7). Consequently, we have to resort to Eqs (7.4a, b) and to solve them for the surface $z_0 = fxy/L_xL_y$, the membrane forces $n_x = n_y = 0$, $n_{xy} = $const. and the pre-buckling deformation $w_0 = 0$.

From experiments and from the internal forces it follows that the solution of these differential equations, i.e. the buckling shape of the shell, extends over the whole width of the shell in one direction, while many half waves develop in the other (as with Fig 5.6). We keep the many half waves in the second direction, but for simplicity we assume no change in curvature in the first direction. The error committed in this is mostly negligible and always serves to the benefit of safety.

Since the principal directions of orthotropy are parallel to the generatrices rather than to the directions of principal curvatures, the direction of the waves has to be turned by an angle α with respect to the principal curvature [7.6]. Hence, the approximate solution for the deflection may be written as

$$w = W \sin a(y \tan \alpha - x).$$

Introducing this expression into the differential equations and eliminating F, we arrive at the characteristic equation:

$$\left(\frac{B_x}{T_y}\right) a^8 + \left(\frac{2B_{xy}}{T_y} + \frac{2B_x}{T_{xy}}\right) a^8 \tan^2 \alpha + \left(\frac{B_x}{T_x} + \frac{4B_{xy}}{T_{xy}} + \frac{B_y}{T_y}\right) a^8 \tan^4 \alpha +$$

$$+ \left(\frac{2B_{xy}}{T_x} + \frac{2B_y}{T_{xy}}\right) a^8 \tan^6 \alpha + \left(\frac{B_y}{T_x}\right) a^8 \tan^8 \alpha + 4 \frac{f^2}{L_x^2 L_y^2} a^4 \tan^2 \alpha = \qquad (7.19)$$

$$= 2n_{xy} \left(\frac{a^6 \tan \alpha}{T_y} + \frac{2a^6 \tan^3 \alpha}{T_{xy}} + \frac{a^6 \tan^5 \alpha}{T_x}\right).$$

In Eq. (7.19), the quantities a and α have to be chosen in such a way as to render n_{xy} a minimum.

The critical shearing force cannot be lower than that of the flat orthotropic plate with the same rigidity properties and ground plan, as with Figure 5.5 (b). The deviation from the case of the isotropic shell is that the critical shearing stress of plate buckling lies, as a rule, comparatively higher for orthotropic plates than for isotropic ones, so that even steeper orthotropic shells may fail by plate buckling rather than by shell buckling. The critical shearing force of an orthotropic plate is, according to Seydel (see in [2.40]):

$$n_{xy,cr} = \frac{\pi^2}{L_y^2} \sqrt[4]{B_x B_y^3} \left[2 + (0.6 + \vartheta_s)\left(2.1 + 2.5 \frac{L_y^2}{L_x^2}\sqrt{\frac{B_x}{B_y}}\right)\right], \qquad (7.20)$$

with L_y as the smaller side length.

The critical load can be computed from the minimum value of n_{xy}, which is to be determined from Eqs (7.19) or (7.20), as follows:

$$p_{cr} = \frac{2f}{L_x L_y} n_{xy,cr}. \qquad (7.21)$$

7.7. Nonlinear and Experimental Investigations
on Orthotropic Shells

Many fewer nonlinear investigations have been made in the range of large post-buckling deformations for orthotropic shells than for isotropic ones; moreover, these investigations mostly refer to geometrically perfect shells. This has several reasons, such as:

(a) it is necessary to get a clear picture of the behaviour of isotropic shells first, on the basis of which orthotropic shells may be studied;

(b) nonlinear buckling investigations on orthotropic shells are far more intricate than those on isotropic ones;

(c) ribbed shells, representing the bulk of orthotropic shells, show experimental buckling loads that are generally much closer to the linear critical ones than for isotropic shells; actually, orthotropic shells buckle in several cases at the linear critical loads.

Most nonlinear investigations refer to orthotropic cylinders. This is due to the fact that most vehicles with a shell body are of (nearly) cylindrical form (planes, ships, submarines, rockets). The number of orthotropic shells of other forms used in civil engineering practice is small as compared to the former.

7.7.1. Nonlinear and Experimental Investigations on Cylinders

The post-buckling behaviour of axially compressed, geometrically perfect cylinders was first treated by March [7.16], using a simplified nonlinear theory. The investigation was further developed by Schnell, Brühl and Thielemann [7.22], [7.30], assuming an enlarged buckling pattern, but they did not present a general solution. They showed on two numerical examples (one on a ring-stiffened, one on a stringer-stiffened cylinder), that the critical load pertaining to the reticulated buckling pattern of the stringer-stiffened cylinder is much lower than that pertaining to the axially symmetric pattern, and moreover that the load bearing capacity drops to an $n_{x,cr}^{lower}$ equal to about one third of the linear critical value, as with isotropic shells. A diamond-shaped buckling pattern is associated with $n_{x,cr}^{lower}$. The linear critical loads pertaining to the reticulated and axisymmetric patterns of the ring-stiffened cylinder respectively, were almost equal, $n_{x,cr}^{lower}$ being about two thirds of $n_{x,cr}^{lin}$. Again a diamond-shaped pattern was associated with $n_{x,cr}^{lower}$. The diamonds are longer in axial direction with stringer-stiffened cylinders, and longer in

ring direction with ring-stiffened ones. The linear critical load of the diamond-shaped buckling pattern is higher than that of the reticulated one. Hence, the buckling of an axially compressed orthotropic cylinder proceeds as follows:

Geometrically perfect orthotropic cylinders begin to buckle in a reticulated pattern when reaching $n_{x,cr}^{lin}$, while some ring-stiffened ones begin to buckle axi-symmetrically. At a comparatively small buckling amplitude, these patterns jump over into the diamond-shaped one, associated with a decreasing load bearing capacity, as with isotropic cylinders.

Hence, these investigations have shown that in some cases orthotropic cylinders behave similarly to isotropic ones, while in other cases they behave more favourably.

With knowledge of these results, Almroth [7.1] performed extensive computations for the determination of the lower critical load of axially compressed, geometrically perfect cylinders with the stiffness parameters $0 \leq \vartheta_p \leq 2$, $0.5 \leq \vartheta_s \leq 8.0$. His results obtained for long cylinders showed that the ratio $n_{x,cr}^{lower}/n_{x,cr}^{lin}$ depends only slightly on the parameters ϑ_s and ϑ_p, but varies strongly with the parameter γ, which indicates whether the cylinder is stringer- or ring-stiffened. The aforementioned ratio is the smallest for isotropic cylinders, it slightly increases for
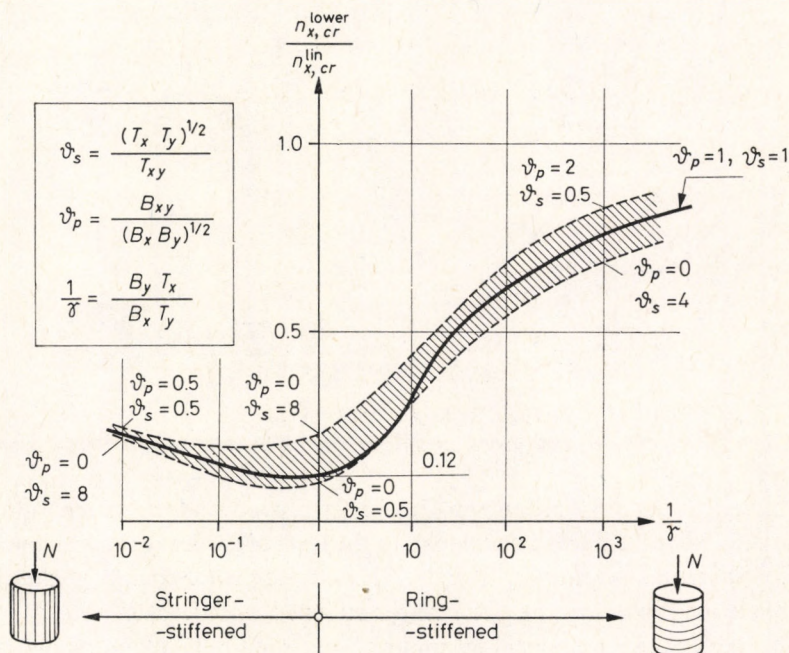
Fig. 7.7. Influence of ring- and of stringer-stiffening on the lower critical load of axially compressed long cylindrical shells

stringer-stiffening, and greatly increases for ring-stiffening. (It should be noted that the axially directed stiffeners also take some compression.) Almroth presented his results in the form of a series of diagrams. From these we constructed Fig. 7.7, where the investigated range of ϑ_s, ϑ_p is denoted by a dotted area. The dashed boundary curves of this area were obtained by selecting those ϑ_s- and ϑ_p-values which yield extreme ratios. Inside the dotted area, the ratio $n^{lower}_{x,cr}/n^{lin}_{x,cr}$ corresponding to the parameters $\vartheta_s=\vartheta_p=1$ is marked by a full line. The intersection point of this curve with the ordinate axis corresponds to the isotropic cylinder.

Almroth's calculations on short cylinders showed that stringer-stiffening becomes more effective, and the ratio $n^{lower}_{x,cr}/n^{lin}_{x,cr}$ increases considerably with decreasing shell length. His results are shown in Fig. 7.8 for the most characteristic cases.
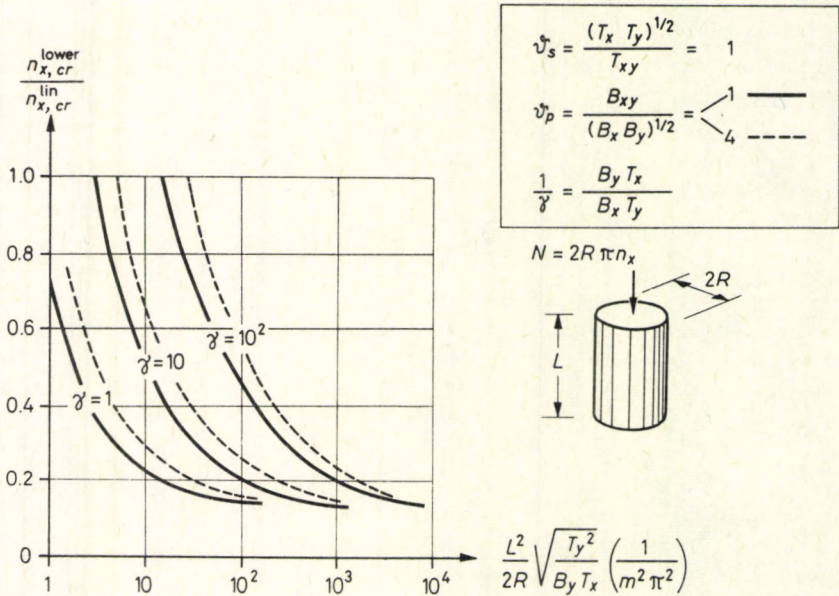
Fig. 7.8. Lower critical loads
of the stringer-stiffened orthotropic cylindrical shell subjected to axial compression

The investigations of Thielemann [7.30] also proved that the internal pressure may not only raise the linear critical load to the level of the axisymmetric buckling, but it also increases the ratio $n^{lower}_{x,cr}/n^{lin}_{x,cr}$. This increase is, of course, greater in the cases, where $n^{lower}_{x,cr}$ was low, i.e. for stringer-stiffened cylinders.

On the basis of two numerical examples to be found in [7.30], we show in Figs 7.9 (a) and (b) the variation due to the internal pressure of the load bearing capacity of a stringer-stiffened and of a ring-stiffened perfect cylinder.
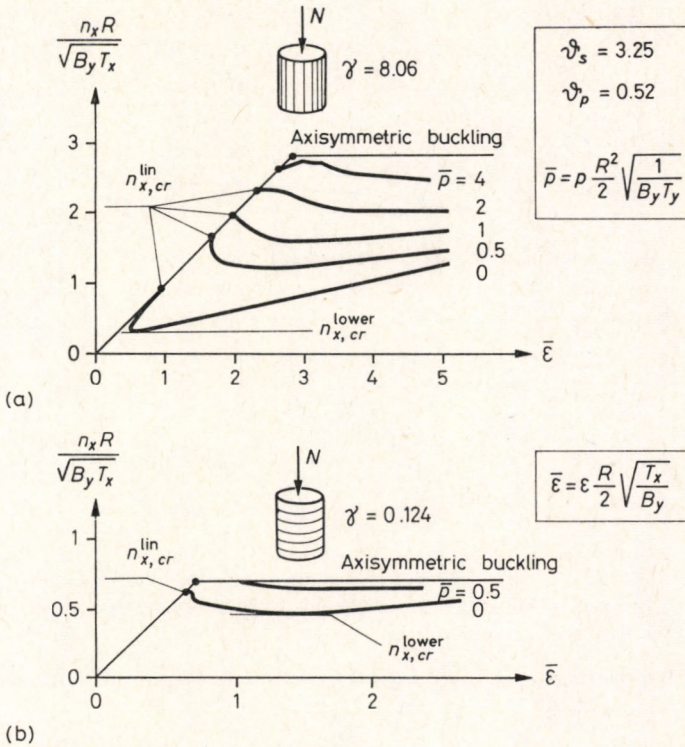
Fig. 7.9. Influence of the internal pressure p on the buckling
of the axially compressed orthotropic cylindrical shell.
(a) − Example for the stringer-stiffened cylinder,
(b) − example for the ringstiffened cylinder

Experimental results [7.9], [7.23], [7.28] showed that stringer-stiffened shells are more sensitive to initial imperfections than ring-stiffened ones. Among the ring-stiffened cylinders those with light stiffeners are more sensitive. Shells made of orthotropic materials [7.23] are found to be more sensitive than rib-stiffened ones. The investigations of Tennyson, Chan and Muggeridge [7.29a] showed that the upper critical loads of cylinders made of anisotropic materials depend on the initial imperfection in the same way as those of isotropic ones.

In Fig. 7.10 we show the results of some series of experiments performed on axially compressed ring-stiffened shells [7.28], [7.32]. The experimental buckling loads were plotted against the ratio of stiffener area to shell wall area, indicating in parenthesis the corresponding values $1/\gamma$ as well. The experimental results
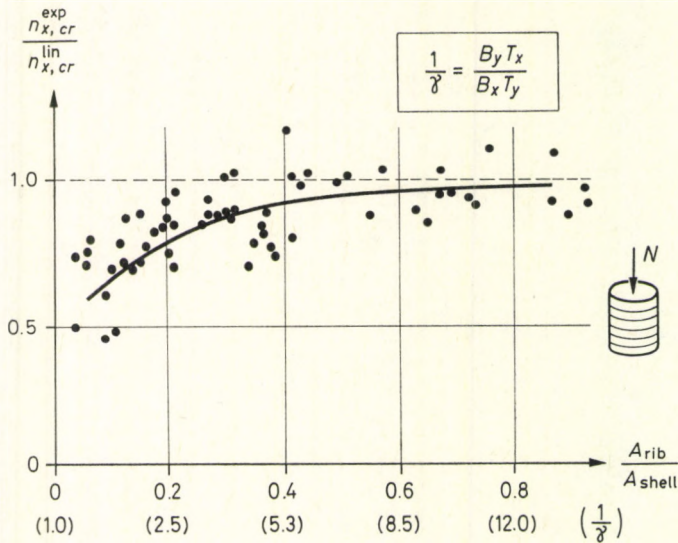
Fig. 7.10. Experimental results on ring-stiffened cylindrical shells subjected to axial compression, plotted against the ratio of rib area to skin area

approach the linear critical load with increasing rib rigidity. This fact may be explained as follows:

From experiments made on axially compressed isotropic cylinders it is known (cf. Fig. 2.3 (a), (b), (c)) that the experimental critical load, which is equal to the upper critical load, decreases with increasing R/t ratio. This diminution may be approximated fairly well by the expression:

$$n_{x,cr}^{upper} \approx \frac{n_{x,cr}^{lin}}{1+\dfrac{\sqrt{3}}{1000}\dfrac{R}{t}} \tag{7.22}$$

obtained from the average values of experimental results. For the ribbed cylinder, the effect of the ribs may be taken into account by establishing an "equivalent isotropic thickness" $\bar{t}$ to be determined from the equality:

$$\frac{E\bar{t}^3}{12} E\bar{t} = \sqrt{B_x B_y} \sqrt{T_x T_y}. \tag{7.23}$$

The ribs increase the actual shell thickness t to $\bar{t}$, so that the ratio $R/\bar{t}$ characterizing the ribbed shell will be comparatively low. Introducing this value into Eq. (7.22) we obtain the upper (i.e. epxerimental) critical forces near the linear critical one.

Introducing the value $\bar{\iota}$ computed from Eq. (7.23) into (7.22), we obtain the full line curve plotted in Fig. 7.10. It coincides practically with the average values of the experimental results, visually showing the described effect.

The higher critical loads (as compared to the linear critical ones) of ring-stiffened cylinders may be explained by considering that the circumferential ribs are used only for stiffening, whereas the longitudinal ribs — in the case of axially compressed cylinders — undergo compression too, thus also becoming prone to buckling themselves. One part of the rigidity of the axial ribs is necessary for preventing their own buckling, so that only their remaining rigidity is able to stiffen the shell. Besides, the circumferential buckling length — because of geometric reasons — cannot be larger than one fourth of the circumference, while the longitudinal buckling length is geometrically limited only by the cylinder length. Hence, ring-stiffening has a much more favourable effect for long cylinders than stringer-stiffening.

A third reason may be the finding of Singer et al. [7.28], who established by very careful measurements that among shell models manufactured with the same technology, the stringer-stiffened ones had much larger initial imperfections than the ring-stiffened ones. This also shows the great influence of manufacturing technology on the magnitude of initial imperfections and thereby on the actual critical load.

Summing up the results on orthotropic cylinders, we may state the following:

The actual critical loads of orthotropic shells are, according to the experiments, much closer to the linear critical values than those of isotropic shells. From the two possible kinds of stiffening, ring-stiffening is the more favourable.

These results may be explained by the following characteristics of the orthotropic shell:

(a) The lower critical loads of orthotropic shells compared to the linear ones are higher than those of the isotropic ones. This may be also related to the fact that a unique buckling mode is associated with the (minimum) linear critical load [8.2.6a], [8.2.6b], as contrasted to the multimode (compound) buckling of the isotropic cylinder. This results in a less steep drop in the post-buckling load-bearing capacity. Ring-stiffening raises the lower critical load even more than stringer-stiffening. Thus, instead of the ratio $n_{x, cr}^{lower}/n_{x, cr}^{lin} \approx 0.10 \sim 0.15$ valid for isotropic shells we obtain for the same ratio $0.25 \sim 0.70$ for orthotropic ones.

(b) The ratio of the radius to the equivalent (isotropic) thickness is, as a rule, much smaller for ribbed orthotropic shells than for unstiffend isotropic ones, and smaller $R/\bar{\iota}$ ratios result in higher $n_{x, cr}^{upper}$. Thus, instead of values $n_{x, cr}^{upper}/n_{x, cr}^{lin} \approx 0.3 \sim \sim 0.5$ valid for isotropic shells, ribbed ones yield values of $0.7 \sim 0.9$.

(c) The torsional stiffness B_{xy} is comparatively small for shells stiffened by ribs with small torsional rigidity. As can be seen from Eq. (7.7), B_{xy} has approximately

the same effect on the linear critical load as the sum of B_x and B_y, provided the buckle is rectangular. The lower critical load is associated with a diamond-shaped buckling pattern, since, in this case, the buckle has a shape closer to the circular or elliptic form on which the torsional rigidity has a much smaller effect. This further reduces the difference between $n_{x,cr}^{lin}$ and $n_{x,cr}^{lower}$.

(d) With short shell models stiffened by longitudinal ribs, the partial clamping effect exerted by the platens of the compression machine on the ribs, being in contact over their whole cross section, is greater, due to the greater equivalent thickness $\bar{t}$, than with unribbed or ring-stiffened shells.

Thus, due to all these effects, the ratio $n_{x,cr}^{experimental}/n_{x,cr}^{lin}$ increases from the values $0.15 \sim 0.60$, valid for isotropic shell, to $0.7 \sim 1.1$ for the test models of ribbed orthotropic ones.

The experimental critical loads of circumferentially compressed [7.23] and of twisted orthotropic cylinders [7.20] were found to be practically equal to the linear critical values. This was, in fact, to be expected since the isotropic cylinder subjected to these loadings was also less sensitive to initial imperfections than under axial compression. The effects mentioned under (a) to (d) for axially compressed orthotropic cylindres are mostly valid for circumferential compression and torsion too, so that the orthotropic cylinder is even less sensitive to imperfections than the isotropic one. Thus its upper critical load is also higher as compared to the linear critical one, resulting in the ratio $p_{x,cr}^{experimental}/p_{cr}^{lin}$ approaching or even reaching unity, and oscillating around this value.

7.7.2. Nonlinear and Experimental Results on Other Kinds of Shells

Nonlinear [7.13] and experimental [7.25], [7.26], [7.27] research on *orthotropic conical shells* showed that substitution by an equivalent cylinder is suitable not only for determining the linear critical load, but also for investigating the post-critical behaviour. This may be done according to Chapter 3, using the orthotropic cylinder characteristics described in Section 7.6.1.

To our knowledge no exact nonlinear investigations exist for *orthotropic spherical shells;* there are only half-empirical methods based on experiments [7.4], [7.5], [7.7], [7.18]. For example, Bushnell [7.4] modifies the geometry of the shell according to the initial imperfection and determines the critical load on this modified shell as an eigenvalue-problem. On the basis of his examples, made for homogeneous, isotropic shells, the curve of the critical load versus imperfection can be constructed. This is similar to that representing the decrease fo the upper critical load of the isotropic shell with increasing initial imperfection amplitude: we

obtain 0.55 and $0.35p_{cr}^{lin}$ for $w_0/t=0.25$ and 0.50, respectively (cf. e.g. Fig. 4.6). The curve constructed this way may be accepted as that of the upper critical load of the orthotropic spherical shell. The ribbed spherical caps tested in [7.18] had R/t values of about 50. Accordingly, in conformity with what has been said before, their critical loads did not deviate by more than 10% from the linear critical values. Their buckling patterns also corresponded to those of the linear theory.

Orthotropic hyperbolic paraboloid shells are manufactured mostly by distorting corrugated plates. For such shells no nonlinear investigations have been made; in fact, these are not even necessary, since the experiments [7.8], [7.17] showed that, as with the isotropic hypar, the orthotropic one also has an increasing post-buckling load bearing capacity. The test shells of [7.17] failed in the "shell buckling" range, while those of [7.8] failed in the "plate buckling" range. The critical loads deviated from the linear critical values determined according to Section 7.5 by less than 10%.

It can be seen from the foregoing that the buckling problems of orthotropic shells are still far from being solved. Much research is needed in the domain of nonlinear buckling and, above all, in the determination of the upper critical load.

8. Buckling of Composite Shells

In this chapter we shall deal with the stability problems of sandwich, rib-stiffened, reticulated and corrugated shells. All four types of shells have in common that they may fail not only by overall but also by local buckling. The critical load intensities of these two kinds of buckling generally differ from each other and, consequently, they practically do not interact. If, however, the proportions of a composite shell cause overall and local bucklings to occur at about the same load intensity, the interaction of the two kinds of buckling may considerably reduce the critical load ("erosion of the optimum design", "compound buckling", see in [1.7], briefly described in Section 1.2). This reduction of the critical load may generally be assessed at 10–15%, but in some cases this may be even more.

This interaction of the local and overall buckling may be computed approximately by the method for considering the effect of plasticity, described in Section 9.4. For this purpose we have to consider the critical load intensity causing local buckling as p_{pl}, which is uniquely related to the specific normal force n_{pl} appearing in Section 9.4. When dealing with the different types of composite shells in detail, we shall specify the details of this method.

As we shall see from the viewpoint of overall buckling these four composite shell structures may be considered orthotropic shells as described in Chapter 7, and in special cases even is isotropic ones. Hence the calculation methods of orthotropic or isotropic shells can be applied.

In what follows we investigate the special problems of sandwich, rib-stiffened, reticulated and corrugated shells, in turn. When necessary, the conditions for considering them as homogeneous orthotropic shells from the viewpoint of overall buckling will be established. The data needed to calculate the rigidity characteristics of these shells will be presented. Finally, the considerations to be taken into account in calculating the local buckling will be outlined.

8.1. Sandwich Shells

Sandwich structures mostly consist of three layers: of two thin faces with a comparatively high extensional rigidity and of a much thicker core with a small but finite shearing rigidity.

The faces are mostly continuous plates but they may also be reticulated surfaces (Fig. 8.3.2) or ribs (Fig. 8.4.4). The core may be made of light, homogeneous, possibly sponge-like, materials (balsa wood or expanded plastic), but also of plate-cell constructions. We show the two most characteristic ones of the latter (honeycomb and box-like cores) in Fig. 8.1.1.

(a)

(b)
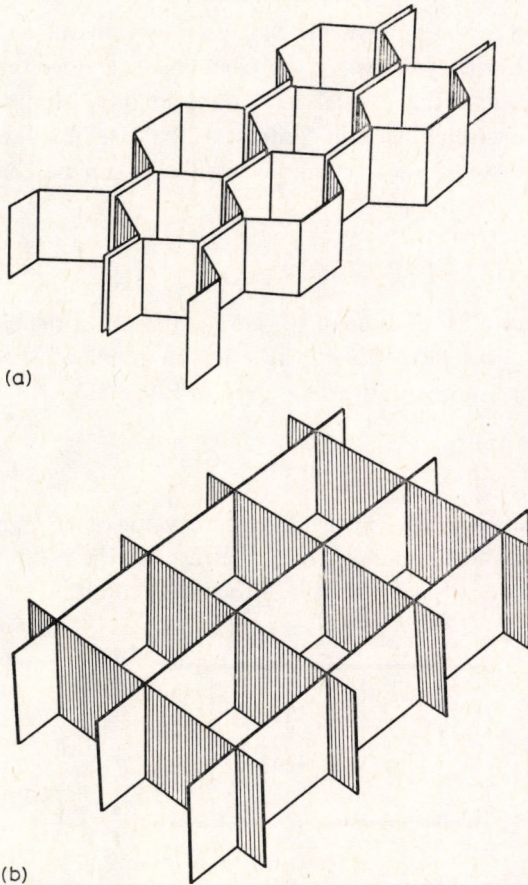
Fig. 8.1.1. Cell-like cores.
(a) – Honeycomb core, (b) – box-like core

The faces obviously have to be fastened to the core in such a way as to exclude a failure of these joints due to flexural and buckling shear before buckling.

Sandwich constructions are generally calculated by considering only the extensional stiffnesses of the faces and the transversal shearing stiffness of the core. Accordingly, the bending and tensile stiffnesses of the sandwich plate can be written as follows:

$$\left.\begin{aligned} B &= \frac{E_f t h^2}{2}, \\ T &= 2E_f t. \end{aligned}\right\} \tag{8.1.1}$$

Here E_f and t are the Young's modulus and the thickness of one face respectively, and h is the structural height of the entire sandwich plate, i.e. the distance between the middle surfaces of the faces.

The deformation of the sandwich shell caused by transverse shear is, due to the low transversal shearing stiffness of the core, much greater than that of a solid shell. This may reduce the critical load considerably. Hence, this ,,sandwich-effect'' cannot be neglected here, in contrast to the case of solid shells. The deformation due to transverse shear ("sandwich-effect") can be characterized by the factor

$$\varrho = \frac{1}{2G_c h}, \tag{8.1.2}$$

where G_c is the modulus of shear of the core material. In the case of the box-like core shown in Fig. 8.1.1 (b) the substituting modulus of shear can be calculated from the expression with the data given in Fig. 8.1.2:

$$G_{\text{substituting}} = G_c \frac{d}{s}. \tag{8.1.3}$$

For the honeycomb core (see Fig. 8.1.1. (a)), the value of $G_{\text{substituting}}$ as computed from Eq. (8.1.3) has to be multiplied by the ratio of the ratio of the diameter to the half circumference of one hexagon of the honeycomb.
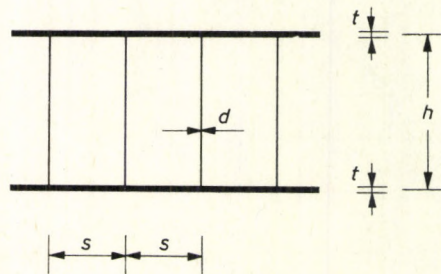
Fig. 8.1.2. Cross section of a sandwich plate with cell-like core

Sandwich constructions may be isotropic or orthotropic with respect to the faces and to the core as well. Since a survey of the theory of orthotropic shells would be rather lengthy, we confine ourselves in this section to isotropic sandwich shells only. For lack of a more exact calculation method, shells orthotropic with respect to the faces can be approximately analysed according to Chapter 7, while orthotropic cores can be made approximately isotropic by the relation:

$$\varrho = \frac{1}{2}(\varrho_x + \varrho_y). \tag{8.1.4}$$

Here, ϱ_x and ϱ_y are the values of the factor ϱ to be determined in the directions x and y respectively. More exact methods are outlined in [8.1.1], [8.1.6], [2.13]. An excellent survey of the theory of sandwich shells with a comprehensive list of references is to be found in [8.1.2].

8.1.1. Overall Buckling

The main difference between sandwich and solid shells with respect to buckling is that the deformation of the core due to transverse shear (the "sandwich-effect") considerably reduces the critical load of the shell.

The linear critical load of the axially compressed cylindrical sandwich shell with thin faces was first determined by Teichmann *et al.* [8.1.8]. Their results are shown in Fig. 8.1.3.
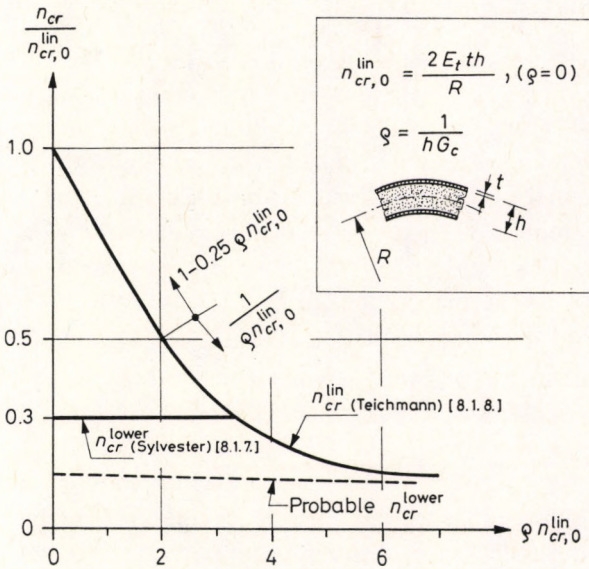
Fig. 8.1.3. Critical load of an axially compressed cylindrical sandwich shell

Hegedűs [8.1.3] considered the bending stiffnesses of the faces, too, when investigating the axially compressed cylinder. He found that if the bending stiffnesses of the faces are entirely neglected, the critical loads of the reticulated and axisymmetric bucklings are equal to each other. On the other hand, if any bending stiffness, no matter how small, is attributed to each face, the critical load of the axisymmetric buckling becomes smaller than that of the reticulated pattern. According to his results, the surplus critical load calculated with the bending rigidities of the faces and with the buckling wavelength of the axisymmetric buckling can be simply added to that computed for the same buckling mode with faces having no bending stiffnesses at all.

The experiments of Teichmann *et al.* showed that in the case of shear-soft cores ($\varrho n_{cr,0}^{lin} > 4$) the experimental critical loads agree well with those computed on the basis of the linear theory, so that for $\varrho n_{cr,0}^{lin} > 4$ the linear critical loads of the sandwich cylinders can be considered as the actual ones. On the other hand, experiments made with shear-rigid cores ($\varrho n_{cr,0}^{lin} < 4$) yielded much lower values than the linear critical loads. Here we have denoted by $n_{cr,0}^{lin}$ the axial linear critical load computed by disregarding the "sandwich-effect".

The lower critical load of the geometrically perfect cylindrical sandwich shell was first determined by March and Kuenzi [8.1.5], who used the nonlinear theory of Kármán and Tsien [2.21]. Later Sylvester, [8.1.7] by improving the calculation with the aid of Kempner's method, obtained about three quarter of this value.

In Fig. 8.1.3 we have shown the critical loads of the axially compressed cylindrical sandwich shell plotted against $\varrho n_{cr,0}^{lin}$.

To evaluate Sylvester's results we have to consider that the horizontal straight line of his n_{cr}^{lower} intersects the curve of the linear critical load; moreover that in the case of $\varrho = 0$, corresponding to the homogeneous solid shell, it yields $n_{cr}^{lower}/n_{cr}^{lin} = 0.3$. We know, however, that for the homogeneous solid shell more recent and more exact computations [2.1] furnished the value 0.108 instead of the earlier one of about 0.3. Thus, more exact computations for the sandwich shell would presumably shift the line of the lower critical load downward, and we would probably obtain the dashed line of Fig. 8.1.3 osculating the hyperbola of the linear critical load from underneath.

Yao [8.1.9] extended the investigations to the radially compressed spherical sandwich shell. His essential result is that the diagram of Fig. 8.1.3 is applicable in this case too.

Experiments performed on spherical caps [8.1.4] and on cylindrical shells quoted in [8.1.6] showed that the ratio of n_{cr}^{upper} (i.e. the experimental critical load) to n_{cr}^{lin} of shells with initial imperfections depends on the ratio R/h, as in the case of homogenous shells.

For design the uppper critical load n_{cr}^{upper} of the imperfect shell would be needed. No investigations have been made, however, for its determination. Experiments [8.1.1], [8.1.6] showed that the sensitivity of sandwich shells to imperfections decreases with increasing values of ϱ. In the case of $\varrho=0$, the upper critical load can evidently be determined by the results for the homogeneous solid shell.

Practically we may proceed as follows: For $\varrho=0$ we determine the upper critical load n_{cr}^{upper} of the imperfect homogeneous shell and connect this by a tangential straight line with the curve of the linear critical load of the sandwich shell, plotted against $\varrho n_{cr,0}^{lin}$. We thus obtain for n_{cr}^{upper} an approximate straight line which starts from the n_{cr}^{upper} of the corresponding homogeneous shell at $\varrho=0$ and osculates, according to the experiments, the curve of n_{cr}^{lin} for greater values of ϱ. In the case of zero initial imperfection, this straight line starts from the value of the linear critical load, and we may assume that its lowest position is the straight line of the lower critical load (n_{cr}^{lower}), marked in Fig. 8.1.3 with dashed line. This approximate determination of the straight line of n_{cr}^{upper} is hown in Fig. 8.1.4.

We shall not deal here with the problems of the twisted cylinder and of the cylinder under lateral pressure, we only refer the reader to the book by Plantema [8.1.6] which treats them extensively.

$$n_{cr,0}^{lin} = \frac{2\,E_t th}{R} \, , \, (\varrho=0)$$

$$\varrho = \frac{1}{hG_c}$$
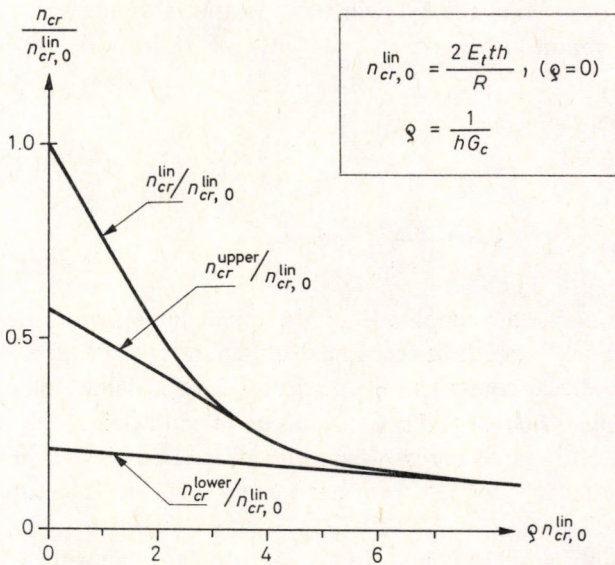
Fig. 8.1.4. Approximate determination of the upper critical load n_{cr}^{upper} of the axially compressed cylindrical sandwich shell

8.1.2. Local Buckling

Several kinds of local buckling may occur in sandwich shells.

The core supports the faces elastically, so that the buckling of the faces —
called wrinkling — occurs like that of a plate on elastic foundation.

The critical stress σ_{cr}^f of the face can be computed for $v_c = 0.3$ and up to the
limit $\dfrac{2t}{h} \sqrt[3]{\dfrac{E_f}{E_c}} \leq 1$ from the equation

$$\sigma_{cr}^f = \beta_1 \sqrt[3]{E_f E_c^2}, \qquad (8.1.5)$$

where $\beta_1 = 0.57$ [8.1.1]. Here v_c denotes Poisson's ratio of the core, while E_f and
E_c are the moduli of elasticity of the face and the core, respectively.

Another kind of local failure is the detachment of the initially imperfect face
from the core and its buckling with a greater wavelength. The corresponding critical
stress can be calculated, according to [8.1.1], from the expression

$$\sigma_{cr} = \beta_2 \sqrt[3]{E_f E_c^2}, \qquad (8.1.6)$$

where β_2 might be given by the following interpolation formula which approximates
the data to be found in [8.1.1]:

$$\beta_2 \approx \frac{0.75 - 0.25k}{1 + \dfrac{3}{2}\dfrac{k}{\varrho_f}}, \qquad (8.1.7)$$

where

$$k = \frac{w_0 E_c}{h \sigma_{adh}} \quad \text{and} \quad \varrho_f = \frac{t}{h}\sqrt[3]{\frac{E_f}{E_c}}.$$

Here w_0 is the maximum amplitude of the initial imperfection of the face and
σ_{adh} is the adhesive strength between face and core.

There are sandwich constructions in which the local failure has a third form,
namely, local plate buckling. This may occur in sandwich shells with box-like,
honeycomb or corrugated cores, where either the faces buckle in compression
between the core plates or the core plates buckle in shear. Therefore, they can be
analyzed accordingly.

We can certainly avoid local buckling if, according to what will be said in Section
8.2.1 on rib-stiffened shells, the critical load causing local buckling is at least
twice that pertaining to overall buckling.

On the other hand, if we want to take local buckling and its interaction with
overall buckling into account, we have to consider the load causing local buckling

as the plastic load p_{pl} (Section 9.4), depending on the amplitude of initial imperfection too. There are several other problems of detail concerning local buckling of sandwich shells that will be dealt with here. Their comprehensive treatment with diagrams usable for design is to be found in [8.1.1].

8.2. Rib-Stiffened Shells

The local buckling of rib-stiffened shells is represented by the buckling of the skin between the ribs. We analyze this first, because it determines the necessary density of the ribs. Following that we deal with the problems related to the replacement of the rib-stiffened shell as a whole by a continuous one; these include the effective width of the skin with respect to the bending of the ribs, problems of the one-sidedness (eccentricity) of the ribs, and the role of Poisson's ratio. After having clarified these questions, the rigidity characteristics of the equivalent orthotropic shell can be established and an overall buckling analysis can be performed.

Throughout this section, t denotes the actual thickness of the skin (without ribs).

8.2.1. Buckling of the Shell Panels between the Ribs.
Density and Rigidity of the Ribs Required to Prevent Skin Buckling

Rib-stiffening greatly increases the critical load of the whole shell structure. If, however, the distance between the ribs is greater than the buckling length of the unstiffened skin, this latter will buckle at the same stress as if the shell were unstiffened. Thus we may choose one of the two following ways. We may either permit the buckling of the skin between ribs but ensure that the whole load should be taken by the ribs (with the effective width of the buckled skin). This principle is generally used in aircraft design.

In common engineering structures, however, the buckling of the skin between ribs under service loads is generally not considered desirable. From this principle it follows that if the distance between the ribs is greater than or equal to the buckling length developing in the unstiffened shell, the ribs increase the load bearing capacity only by taking some part of the load themselves. However, in this case, the structure will be less economical than if we use the material of the ribs to increase the shell thickness. That is, in this latter case, the load bearing capacity increases not only proportionally to the material added, but also because of the increase in the critical stress due to the greater wall thickness. Hence, there is little sense in arranging the ribs that sparsely. Thus, the distances between the ribs have to be chosen inferior to the buckling lengths of the unstiffened shell.

Accordingly, we first have to know the dimensions of the buckle of the unstiffened shell, and secondly, how the critical stress of a shell panel, supported along the ribs, increases with decreasing rib distances as compared with the unstiffened shell. In the following we present the buckling lengths of some characteristic shells for several loading cases and the critical stresses of the shell panels smaller than these lengths.

We saw in the foregoing that perfect shells begin to buckle with buckling lengths determined by the linear theory, while imperfect ones begin to buckle with greater buckling lengths. In any case the buckling lengths increase during the buckling process (see Fig. 2.10). Thus, we commit an error to the benefit of safety if we choose the rib distance smaller than the buckling length of the linear theory. We may certainly consider the rib-stiffening as practically effective if the distance of the ribs is not greater than 0.7 times the buckling length of the unstiffened shell. In this case the critical load of the shell panel between the ribs is appoximately twice that of the unstiffened shell.

Critical load of axially compressed cylindrical shell panels. The unstiffened complete cylindrical shell buckles under this load in small, local waves. The relation between the two half wavelengths l_x and l_y according to the linear theory is given by Eq. (2.10), and can be written in the following form:

$$l_y = \frac{1}{\sqrt{\dfrac{\sqrt[4]{12(1-v^2)}}{\pi\sqrt{Rt}\,l_x} - \dfrac{1}{l_x^2}}}. \tag{8.2.1}$$

The ratio of the two buckling lengths is undetermined.

Accordingly, we plotted l_y against l_x in Fig. 8.2.1, assuming $v = 0.3$. The main conclusion to be drawn from the diagram is that l_x and l_y cannot be smaller than $1.73\sqrt{Rt}$ and $3.46\sqrt{Rt}$ respectively. Therefore, in the case of ribs running in one direction only, we have to arrange them closer than whichever of these two minimum lengths is perpendicular to the ribs. On the other hand, if we apply two-way rib-stiffening, the distances of the ribs in the two directions should be smaller than the buckling lengths proportional to the rib distances, determined by the diagram.

The critical stress of the shell panel stiffened by ribs closer than these values can be computed from Eq. (2.8) (assuming hinged supports along the ribs), substituting the rib distances b_x, b_y for the buckling lengths l_x, l_y (Fig. 8.2.2):

$$n_{x,cr}^{\text{lin}} = \frac{\pi^2 E t^3}{12(1-v^2)b_x^2}\left(\frac{b_x^2}{b_y^2}+1\right)^2 + \frac{E t b_x^2}{\pi^2 R^2}\frac{1}{\left(\dfrac{b_x^2}{b_y^2}+1\right)^2}. \tag{8.2.2}$$
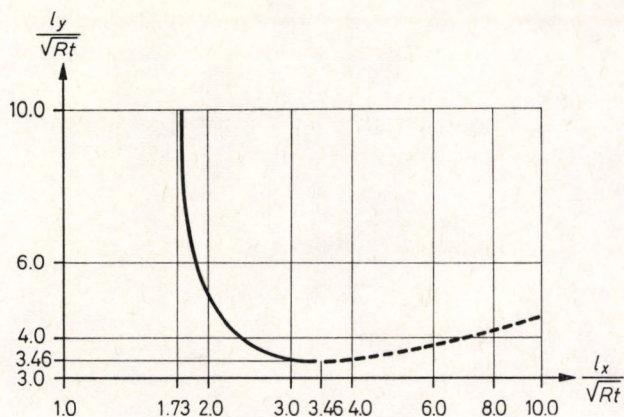
Fig. 8.2.1. Half buckling wavelengths of the axially compressed cylindrical shell according to the linear theory
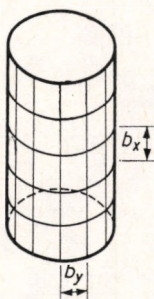
Fig. 8.2.2. Ribbed cylindrical shell

The derivation without assuming the shallowness of the shell yields the same result [2.51].

Equation (8.2.2) assumes buckling in one half wave in both axial and circumferential directions. This is true as long as $b_x \leqq b_y$. If, however, $b_x > b_y$, then — as with flat plates — the shell panel may buckle in several half waves in the axial direction, so that its critical load may be equal at most to that of a shell panel of the dimension b_y in both directions, i.e. to

$$n_{x,cr}^{\text{lin}} = \frac{\pi^2 E t^3}{3(1-v^2) b_y^2} + \frac{E t b_y^2}{4\pi^2 R^2}. \tag{8.2.3}$$

The first terms in Eqs (8.2.2) and (8.2.3) represent the bending stiffness of a flat plate with the same dimensions as the shell panel, while the second terms express the additional extensional (membrane) stiffness due to the curvature.
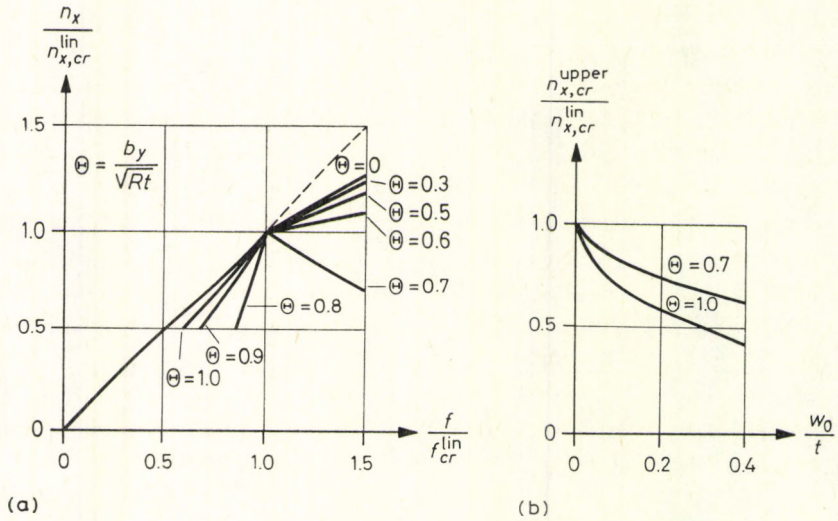
Fig. 8.2.3. Post-buckling behaviour of the axially compressed cylindrical panel

The post-buckling behaviour of the cylindrical shell panel was studied by Koiter [8.2.8]. He obtained initial tangents to the post-buckling load-deflection curves of the perfect panel as shown in Fig. 8.2.3 (a), where f denotes the compression in the axial direction, and $\Theta = b_y/\sqrt{Rt}$ is a geometric parameter, characteristic of the curvature of the shell panel. The value $\Theta = 0$ corresponds to flat plates. At small values of Θ, the post-critical load bearing capacity has an ascending character, so that the linear critical load can be considered as the actual critical load. From $\Theta > 0.64$ on, however, the initial tangent becomes negative. For this range, Fig. 8.2.3 (b) gives the magnitude of $n_{x, cr}^{upper}$ causing snapping, plotted against the amplitude w_0 of the initial imperfection for two Θ-values. So, as the central angle of the shell panel increases, its behaviour approaches that of the complete cylinder.

All these were confirmed by Tamate and Sekine [8.2.16], who analyzed the post-critical behaviour of cylindrical shell panels of the side length $b_x = b_y$.

The experiments [2.51], [2.57] yielded results in accordance with the theory outlined above.

From the theoretical analyses published in [2.57] we may draw a conclusion that can be useful in practical applications. That is, the (not completely exact) calculation yielded for the post-critical σ_{cr}^{lower} of the perfect shell panel a value equal to the critical stress of the flat plate of the same side lengths b_x, b_y. On the other hand, it is known that the flat plate exhibits an increasing post-buckling load bearing capacity. Hence, we may state that if we cannot determine the critical load of a shell panel exactly, then we may take instead the critical load of a flat

plate loaded and supported in the same way, committing an error generally to the benefit of safety.

Critical load of a cylindrical shell panel compressed in the circumferential direction. Since the unstiffened cylindrical shell under lateral pressure buckles in one half wave in the axial direction between the supports, but develops several half waves in the circumferential direction, we can compute the critical stress of shell panels of ring-stiffened cylinders from Eqs (2.25) if we substitute the distance b_x between the ring-directed ribs for the length L of the cylinder.

More exact investigations on the basis of the linear theory [8.2.14] showed that the shell panel may buckle at a load smaller than that of a complete cylinder, if the distance between the axial stiffeners allows a circumferential wave number that is prevented on the complete cylinder by the circumferential continuity. However, this reduction is less than 10%, and the critical load can by no means be smaller than that given by the envelope of the festoon curve.

Axial stiffeners increase the critical load practically only if they are arranged more densely than the circumferential half wavelength determined by Eq. (2.26). In these cases we may compute the critical stress from the more exact formulas to be found in [2.17a] or [2.51], which also contain the circumferential wave number, if we take the distance b_y of the axial stiffeners as the half wavelength.

Critical load of cylindrical shell panels subjected to pure shear. The linear theory yields the following critical shearing stress (see Fig. 8.2.2):
if $b_x \geqq b_y$:

$$\tau_{cr} = k_s E \left(\frac{t}{b_y}\right)^2, \tag{8.2.4a}$$

and if $b_x \leqq b_y$:

$$\tau_{cr} = k_s' E \left(\frac{t}{b_x}\right)^2. \tag{8.2.4b}$$

According to the investigations of Kromm and Schapitz (see in [7.21]), the factors k and k' can be read off Figs 8.2.4 (a) and 8.2.4 (b) respectively.

Critical load of spherical shell panels subjected to radial pressure. The half buckling wavelengths of an unstiffened spherical shell — assuming rectangular buckles — can be obtained from Eq. (4.6):

$$l_y = \sqrt{\frac{1}{\dfrac{\sqrt{12(1-v^2)}}{\pi^2 Rt} - \dfrac{1}{l_x^2}}}. \tag{8.2.5}$$

The interdependent half wavelengths (for $v=0.3$) are plotted in Fig. 8.2.5. As can be seen, the half wavelength cannot be shorter than $1.72 \sqrt{Rt}$ in either direction.
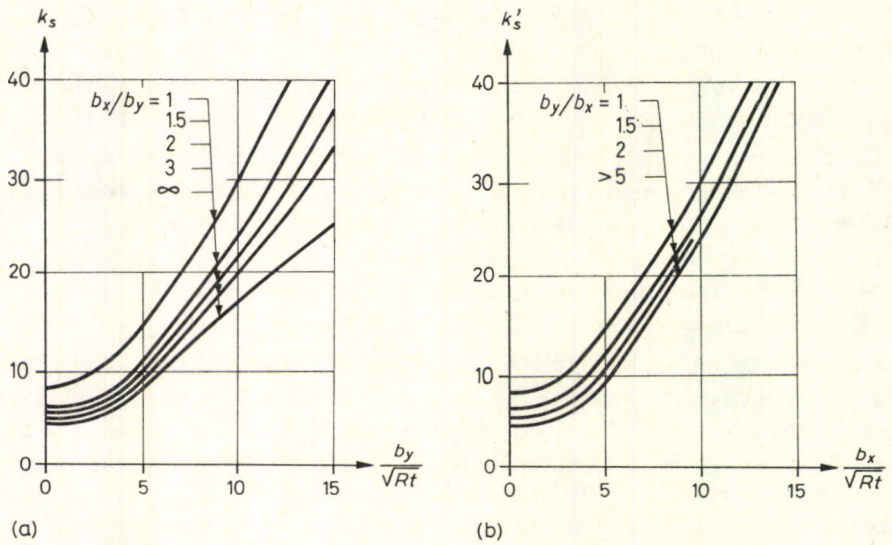
Fig. 8.2.4. Multiplication factors of the cylindrical panel subjected to pure shear
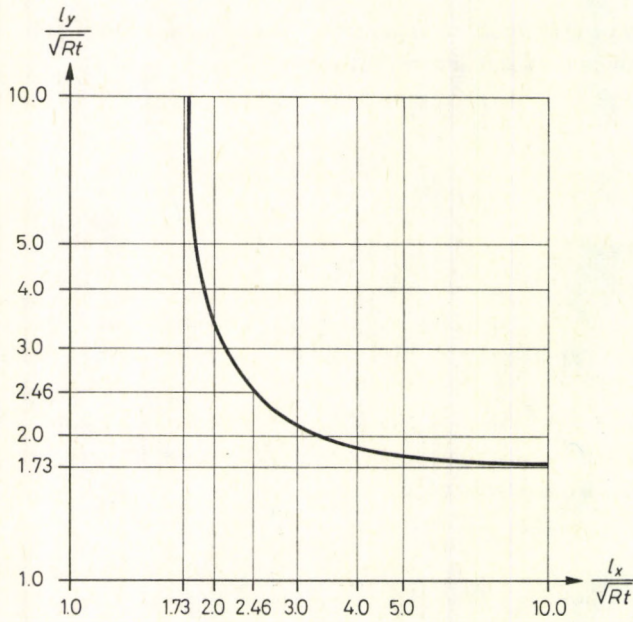
Fig. 8.2.5. Half buckling wavelengths of the radially compressed
spherical shell according to the linear theory

Hence, if we want to increase the critical load of the shell panel as compared to that of the unstiffened shell, we have to arrange the stiffeners so densely as to obtain rib distances b_x and b_y smaller than the related pairs of values in Fig. 8.2.5. In this case the critical compressive force is to be computed from Eq. (4.5), substituting b_x and b_y for l_x and l_y respectively:

$$n_{x,cr}^{\text{lin}} = n_{y,cr}^{\text{lin}} = p_{cr}\frac{R}{2} = \frac{\pi^2 E t^3}{12(1-v^2)}\left(\frac{1}{b_x^2}+\frac{1}{b_y^2}\right)+\frac{Et}{\pi^2 R^2}\frac{1}{\left(\dfrac{1}{b_x^2}+\dfrac{1}{b_y^2}\right)}. \qquad (8.2.6)$$

The first and second terms on the right-hand side of Eq. (8.2.6) represent the bending and extensional rigidities, corresponding to flat plate and curved (membrane) shell action respectively. In the case of $R \to \infty$, i.e. if we divide the spherical shell into smaller and smaller panels, we approach the flat plate more and more: the post-critical behaviour exhibits an ascending character. The considerable decrease of the critical load after buckling (see Fig. 4.4) will fully prevail only when the rib distances reach the half buckling wavelengths of the unstiffened shell. The phenomenon is similar to that depicted in Fig. 8.2.3 (a).

The following problem may also arise: what is the *necessary stiffness of the ribs* which prevents skin displacements perpendicular to the skin surface along the ribs during skin buckling sufficiently to allow us to consider the ribs as rigid supports of the skin?

To our knowledge, this question has not been generally answered as yet. However, it is possible to suggest a simple rule which in all likelihood ensures that the skin buckles as if the ribs were rigid supports.

We start from the analogy of a theorem established by Dulácska for simple bar structures [8.2.3a], [8.2.3b], which can be briefly stated as follows:

If we want to stiffen a comparatively weak simple frame in such a way that it only buckles with unmovable nodes, we have to apply a sufficiently rigid structure.
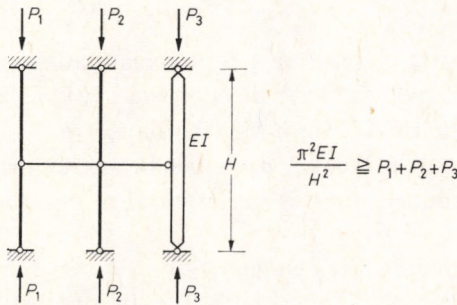
Fig. 8.2.6. The basic principle according to which we can establish
the necessary rigidity of the rib

Its rigidity can be taken as sufficient if its critical load, computed assuming infinitely elastic material, is not less that the sum of all the loads acting on the stiffened frame and on the stiffening structure (Fig. 8.2.6).

Applying this principle to our case, we have to stipulate that the ribs be capable of carrying all the load acting on the skin and on the ribs, assuming infinitely elastic behaviour.

In this computation an effective width of the skin, as valid before skin buckling (see Section 8.2.2), can be assumed as part of the rib. (According to what is said in Section 8.2.2 on the interaction of overall and skin buckling, this rule does not ensure that the ribs are, in fact, able to carry the load after the skin has buckled.)

8.2.2. Effective Width of the Skin with Respect to the Bending of the Ribs

In a plate connected with ribs, the bending causes stresses of varying magnitude (Fig. 8.2.7). As is known, we may define an "effective width" b_e of the plate, forming a T-section with the ribs, i.e. assuming constant bending stress all along its width. This effective width may be determined in such a way as to obtain either the same rigidity as that of the actual structure or the same bending stress as the
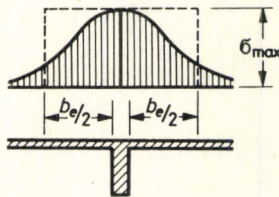
Fig. 8.2.7. Effective width of the ribbed plate

maximum bending stress in the actual ribbed plate at the junction of rib and skin. We thus arrive at two different effective widths. The difference results from computing the strain of the skin from the relation $\varepsilon_x = (\sigma_x - \nu\sigma_y)/E$, and that of the rib from $\varepsilon_x = \sigma_x/E$, so that different σ_x-values belong to the same ε_x in rib and plate. However, if Poisson's ratio is neglected, the two effective widths become identical.

For the buckling analysis the bending stiffness rather than the bending stress arising in the plate is relevant. Consequently, the effective width providing the same bending stiffness should be used. However, since the effective width yielding the same bending stress is at most only a few per cent greater, we may use this as well.

The effective width may also be different depending on whether we allow the buckling of the shell panels between the ribs or not. In common engineering practice we generally do not allow the buckling of the panels, so that we shall deal here mainly with unbuckled skins.

Effective width of the unbuckled skin. Chwalla [8.2.3] found for *flat plates* that the effective width b_e is constant along the length of the rib, provided the rib deflects in a sine wave shape (which corresponds to the buckling wave). The ratio of b_e to the half wavelength l of the sine wave is given in Table 8.2.1 for some values of Posison's ratio v.

Table 8.2.1

Values of the effective width b_e of a flat plate according
to Chwalla [8.2.3]

$v =$	0.3	0.2	0.1	0
$b_e/l =$	0.363	0.380	0.402	0.424

These values refer to a plate of infinite width, connected to one rib only. However, the effective width cannot be greater than the distance of the ribs, so that this latter sets an upper bound for the values of the table.

The problem becomes more intricate if the rib is connected to a curved shell instead of to a flat plate. The following value can be derived for the effective width of a *cylindrical shell connected to an axial rib* by Schorer's approximate theory valid for cylindrical shells [2.32], [7.10], on the basis of the identical maximum bending stress requirement and assumnig $v=0$ [8.2.7]:

$$\frac{b_e}{l_x} = 1.266 \sqrt[4]{\frac{Rt}{l_x^2}}, \qquad (8.2.7)$$

where l_x is the axial half wavelength.

Since the derivation assumed only one axial stiffener, the maximum value of b_e to be taken into account cannot be greater than the distance b_y of the stiffeners. In addition, we also have to check (because of the approximations inherent in Schorer's theory) whether b_e obtained from Eq. (8.2.7) is not greater than that valid for the flat plate (see Table 8.2.1), since the effective width of a cylindrical shell has to be smaller in any case than that of the flat plate.

The effective width b_e of a *cylindrical shell connected to circumferential ribs* was determined by Biezeno and Koch (see in [8.2.2]) on the basis of equal rigidities. They calculated b_e as a function of the rib distance b_x and the circumferential (full)

wave number n, for different ratios t/R. We present in Fig. 8.2.8 from their results the effective widths pertaining to $b_x = \infty$. When using these values we have to keep in mind that b_e cannot be greater than the actual distance b_x of the ribs.

The effective width given by Fig. 8.2.8 approaches with increasing R (or n) that of the flat plate (see Table 8.2.1), but it always remains smaller than that.
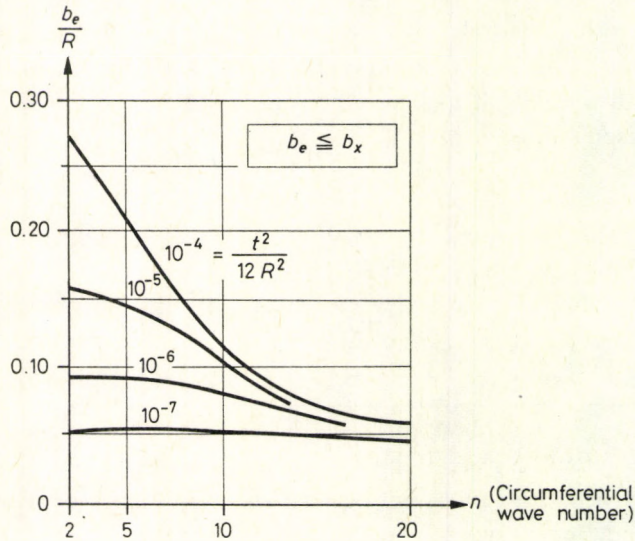
Fig. 8.2.8. Effective width of the ring-stiffened cylindrical shell

Lundgren [2.32], assuming

$$\frac{n^4 t^2}{12 R^2} \ll 1,$$ (8.2.8)

derived for $b_x = \infty$ the following formula for the effective width:

$$b_e = 1.52 \left(1 - 0.29 n^2 \frac{t}{R}\right) \sqrt{tR},$$ (8.2.9)

which shows, in the range given by Eq. (8.2.8), a rather close agreement with the curves of Fig. 8.2.8.

For the calculation of the effective width of the cylindrical shell as outlined above, we ought to know the axial half buckling wavelength of the composite shell. However, this depends on the rigidity of the ribbed shell, this being, in turn, dependent on the effective width. Thus, we can solve the problem by trial and error only, correcting the assumed effective width and half buckling wavelength step by step.

Bodner [7.3] proposed a correction to the effective width of Biezeno and Koch in order to obtain the distance of the ribs if the areas of the ribs tend to zero. This has significance only in the case of very weak stiffeners.

Behaviour of ribbed shells after buckling of the skin. According to both experiments and analysis, the load bearing capacity of the ribs considerably increases after the skin has buckled. This is exploited in airplane construction in such a way that for some short-term loads skin buckling is allowed, because it disappears after the load has decreased. In common engineering construction skin buckling is generally not allowed, although it would yield some economic advantages.

In the following we only outline briefly the phenomena of the skin buckling and the difficulties of design connected therewith.

A *flat plate* between stiffeners, subjected to uniform compression parallel to the stiffeners, buckles as shown in Fig. 8.2.9 (a). The plate is able to produce shortening in the direction of the ribs, in the section $c-c$ situated far from them, mostly by buckling deformation, undergoing only a small compression. As we examine the
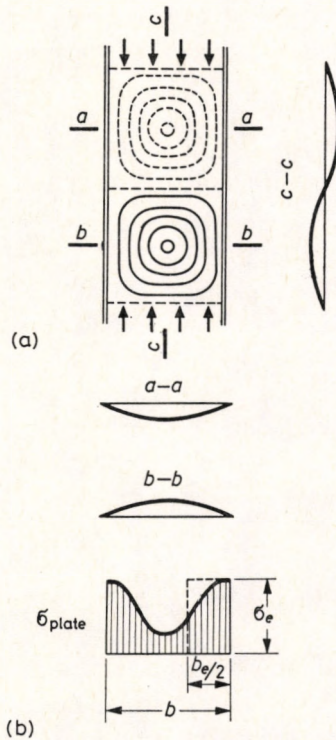
Fig. 8.2.9. Effective width of the buckled plate

sections closer and closer to the ribs, the buckling deformation decreases, so that the plate has to undergo greater and greater compressive strains. The stress σ in the plate, being proportional to the compressive strain, will vary according to the diagram shown in Fig. 8.2.9 (b). A stress σ_e corresponding to the entire compressive strain arises close to the stiffener, while farther away σ decreaes. The effective width b_e denotes the width of the plate with which it could carry a force equal to that of the actual structure if along this width b_e the stress σ_e arose everywhere.

This effective width may be computed, according to Marguerre [8.2.9], from a cubic equation. Very useful graphs are to be found for this purpose in [7.21]. However, the effective width decreases with the increase of the load acting on the structure and also with increasing rib deflection, since the skin becomes more and more buckled. (The phenomenon is to some extent similar to the decrease of stiffness of cracked reinforced concrete shells described in Section 9.8). Thus, we already encounter some difficulties if we want to design the rib as a simple compressed bar against buckling, since its bending stiffness depends on the load and on the magnitude of buckling deformation as well [7.21].

The phenomenon may also be described as an interaction between local and overall bucklings. That is, the buckling of the skin reduces the rigidity of the *whole* structure, rendering the character of the post-buckling load bearing capacity decreasing even in cases when both local and overall bucklings have, considered alone, increasing characters. This phenomenon is very clearly demonstrated in a simple example in the paper of Walker [8.2.18].

The problem becomes even more intricate in the case of *stiffened shells* with buckled skin. The effective width of the buckled skin may be computed on the basis of an approximate assumption of Ebner [8.2.4], see also in [7.21], but, to the best of our knowledge, no simple method exists for the buckling analysis of an orthotropic shell, whose rigidity properties depend on the deformation. Hence, we do not deal with this problem any more here, only mention that the interaction of local and overall bucklings was treated by Byskov and Hutchinson [8.2.2b]. This interaction reduces the actual critical load most if the critical loads of local and overall bucklings, considered separately, are equal.

8.2.3. Problems of Eccentric Stiffening

The skin can be stiffened in two ways: the ribs can be arranged on both sides of the skin, symmetrically to its midsurface, or only on one side of it (eccentric stiffening). In the first case, after "smearing out" the rigidities of the ribs, the equations of orthotropic shells presented in Chapter 7 correctly describe the

behaviour of the structure. However, this kind of stiffening is much more difficult to realize — no matter whether the shell is made of reinforced concrete or of metal — than the eccentric one. Moreover, it is also less economical than the latter, since eccentric stiffeners provide with the same cross sections a considerably greater bending rigidity.

The behaviour of the eccentrically stiffened shell can no longer be described by the equations of Chapter 7. To make the difference more easily understood, we first examine the role of eccentric stiffeners on the flat plate, including also the case when stiffeners running in two directions are arranged on opposite sides of the plate.

Eccentrically stiffened flat plates. If we arrange the stiffeners eccentrically, we obtain no unique "neutral plane", in which no stresses arise either from bending or from twisting. To put it more exactly: the twisting moments cause not only twist but, in the skin, also angular distortion, that is in-plane (membrane) shearing stresses too. Because of these latter, in order to maintain equilibrium, in-plane compressive and tensile stresses also arise in the skin. The phenomenon is essentially the same as the "warping" of twisted thin-walled bars with open cross section. Thus, it can be seen even without detailed analysis that the effective torsional resistance of an eccentrically stiffened flat plate is greater than its "torsion rigidity" proper. Due to this effect, the differential equation of the eccentrically stiffened plate is of the eight order [8.2.6], [8.2.17], as contrasted to the fourth-order differential equation of the symmetrically stiffened plate.

If we want to use the fourth-order differential equation of the orthotropic plate, we have to neglect the above described additional rigidity due to the eccentric arrangement of the stiffeners, and we have to take only the torsional rigidity proper of the ribbed plate into account. By so doing, in the stability analysis we always commit an error to the benefit of safety, since we consider the structure less rigid than it is in reality.

We may obtain useful information for the magnitude of this error from the paper of Trenks [8.2.17], in which he compared the exactly computed deflection (i.e. the rigidity) of the eccentrically stiffened plate with the approximate value obtained by taking only the torsional rigidity of the ribbed plate into account. He showed that the error is greater in proportion as

— the eccentricity of the centroid of the rib as related to the thickness of the plate is greater;
— the cross sectional area of the rib as related to the area of the plate between the ribs is larger;

— the moment of inertia of the ribbed plate as related to the cube of the plate thickness is smaller; and

— the role the twist plays in the deformation of the plate is greater.

Numerically he has obtained in the case of a square plate simply supported all along its boundary, with the eccentricity ratio $e/t \leqq 12$ (Fig. 8.2.10), subjected to a centrally applied line load distributed according to a half sine wave, so that the deflection becomes at most 30% or 6% larger in the cases of one or two directional ribs respectively. In these computations he neglected the effect of the rib eccentricity, as compared with the exact computation which takes the rib eccentricity into account.

(a)

(b)
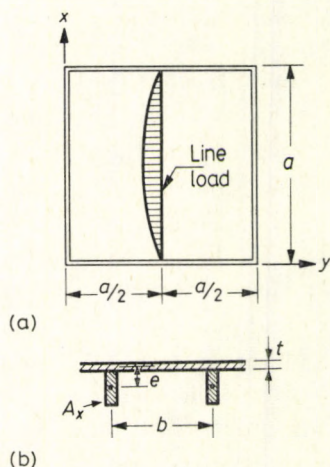
Fig. 8.2.10. The eccentrically stiffened flat plate investigated by Trenks [8.2.17]
(a) – Ground plan, (b) – cross section

Pflüger [8.2.11], [8.2.12] developed and solved the exact differential equations of the flat plate eccentrically stiffened by ribs without and with torsional rigidity (i.e. with open and close cross sections respectively). For one-directional stiffeners and compression in the same direction we compared the diagrams of Pflüger with the critical stresses of the orthotropic plate, i.e. taking only the torsional rigidity of the ribbed plate into consideration. The deviations showed close agreement with those given by Trenks.

As far as the critical load of a flat plate is concerned, it obviously makes no difference whether the stiffeners are arranged on one or on the other side of the plate. However, it does make a difference whether ribs running in two directions are arranged on the same side or on opposite sides of the plate [8.2.2a]. Let us

consider, e.g. ribs running in the x direction. Because of the eccentricity of these ribs, displacements develop in the plane of the plate, causing in-plane stresses. From the equilibrium and compatibility equations (see, e.g. [8.2.2a] or [8.2.13]) can be derived that the normal in-plane forces arising in the x and y directions have the same sign. If the y directional ribs are arranged on the same side of the plate as the x directional ones, they produce — due to curvatures of the same sign in the x and y directions — normal forces of the same sign as the x directional ribs. Hence, the influences of both rows of ribs combine, and the "warping rigidity" of the ribbed plate will be, so to say, doubled.

However, if the y directional ribs are arranged on the opposite side of the plate to the x directional ones, in-plane forces of opposite signs arise due to the x and y directional ribs respectively, so that they cancel out each others' influence.

Eccentrically stiffened shells. In the case of ribbed shells, the eccentric arrangement of the stiffeners causes — besides the increase in rigidity as explained in connection with flat plates — the following effect: it does make a difference whether the ribs are arranged on the outer (convex) or on the inner (concave) side of the skin. This phenomenon was discovered by van der Neut [8.2.10]. For a better understanding of it let us investigate, according to [8.2.5], a stringer- and ring-stiffened cylincrical shell. The results thus found will be valid for doubly-curved ribbed shells too.

First we have to define some notions. We call the inflexion points of the neutral fibre of ring-directional bending simply inflexion points, while by nodal points we denote those points which undergo no displacement either in radial or in tangential directions during buckling deformation. (The nodal points generally do not lie on the neutral fibre of bending.) The lines connecting the nodal points are called nodal lines.

If ring-directional waves develop during buckling, the arch length would have to increase along the half waves bulging outwards and decrease along those bulging inwards, if the inflexion points did not displace in the ring direction as shown in (Fig. 8.2.11 (a)). The shell obviously tries to eliminate these elongations, so that the inflexion points displace in the ring direction from the inward half waves to the outward ones. If the amplitude of the buckling half waves did not vary in the axial direction (i.e. if in the axial direction very long half waves developed), then these displacements of the inflexion points could completely eliminate the elongations in the ring direction. However, if the buckling amplitude in the axial direction varies, then the inflexion points have to shift to a varying degree, i.e. they have to displace by sections in opposite directions. This causes shearing deformation in the shell surface, according to Fig. 8.2.11 (b), which is hindered by its shearing rigidity. Hence, finally, the shell undergoes some elongation or compression in the ring
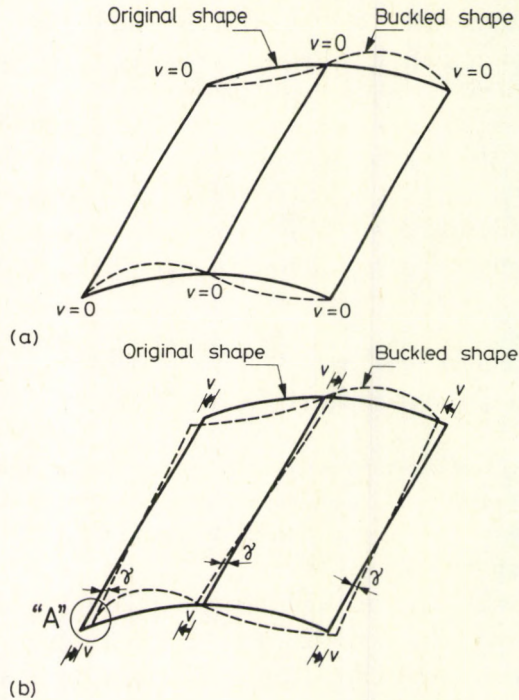
Fig. 8.2.11. Displacement of the inflexion point
of an eccentrically stiffened shell during buckling

direction (along the outward or inward bulging half waves), and also some shearing deformation. The corresponding normal and shearing forces are proportional to each other, and have the same order of magnitude.

The shearing deformation develops in the neutral surface of ring-directional bending of the shell, according to Fig. 8.2.11 (b). However, in the surface passing through the nodal lines, no such distortion arises, since — by definition — the nodal lines do not shift in the ring direction.

The nodal lines always lie outside the neutral surface of the ring-directional bending, since the inflexion points always shift towards the outside bulging half waves in the ring direction (see Fig. 8.2.12, representing the enlarged detail "A" of Fig. 8.2.11 (b).

The shearing deformation, arising in the surface of the shell which is capable of taking shearing forces, is the greater, the farther it lies from the surface passing through the nodal lines. In the case of unstiffened or symmetrically stiffened shells, the surface capable of taking shearing forces coincides with the neutral surface of bending. Hence, the excess buckling rigidity of such "common" shells, as
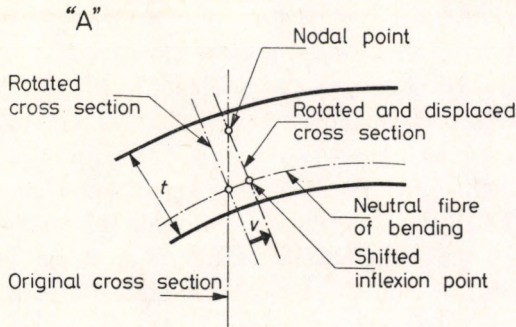
Fig. 8.2.12. Enlarged detail "A" of Fig. 8.2.11 (b)

compared with that of flat plates, is due to the shearing deformation arising in the surface capable of taking shearing forces. That is, this latter lies at a certain distance from the nodal lines, which lie outside the neutral surface.

The surface capable of taking shearing forces of a shell with outside stiffeners (i.e. the inside skin) is at a greater distance from the nodal lines than the neutral surface of bending of the "common" shells. Thus, these shells with outside stiffeners exhibit an excess rigidity in buckling.

Hence the curvature of the shell has the same stiffening influence as the outside ring-stiffeners: these two effects have to be added up. Thus, in accordance with what has been said about flat plates, outside stringer-stiffeners increase the stiffening effects both of the curvature in the ring direction and of the outside ring-stiffeners. To sum up, we may conclude that outside ring- and stringer-stiffeners alike give an (effective) excess buckling rigidity to the shell.

On the other hand, inside ring-stiffeners bring the skin capable of taking shearing forces nearer to the nodal lines, thereby decreasing the stiffening effect of the curvature, until the skin reaches the nodal lines. In this latter position the effective buckling rigidity of the shell becomes a minimum. (Until this position, the influence of the longitudinal stiffeners is the same as described before: outside ribs increase, inside ribs decrease the stiffening effects due to the ring-directional phenomena.) In this position, the effective buckling rigidity of the stiffened shell will be less than that of a symmetrically stiffened shell with the same (geometric) rigidity characteristics (but, of course, greater than that of the unstiffened skin). If the ring-stiffeners shifted the position of the skin beyond (i.e. inside) the nodal lines, the effective buckling rigidity of the structure would increase again. As a rule, however, this does not occur practically, or if it does, the effective buckling rigidity does not increase again to the level of that of the symmetrically stiffened shell. Hence, the effective buckling rigidity of shells with inside stiffeners will certainly be lower

than that of shells with outside stiffeners, and in some cases even lower than that of symmetrically stiffened shells with the same (geometric) rigidity characteristics.

It follows from the foregoing that the difference in effective rigidities of outside and inside stiffeners becomes manifest only if the buckling deformation contains some twist, i.e. if the buckling half-wave lengths in both directions do not differ very much from each other. We may also say that the ultimate cause of the difference in effective rigidities of outside and inside stiffeners is the same as that of the excess rigidity due to the eccentric stiffeners of the flat plate: the "warping stiffness". With shells, however, — due to the curvature — outside stiffeners increase while inside ones decrease this effect as compared to the flat plate.

The phenomenon described in the foregoing is called the "primary effect" of eccentric stiffeners of shells. There is a "secondary effect" too, due to the transverse contraction, which acts in the opposite sense.

Let us first consider the case of outside stiffeners. The outward bulging half waves in the longitudinal direction induce compression in the inside lying skin. Due to the transverse contraction (Poisson's ratio), this causes tension in the ring direction, reducing the ring-directed displacement of the inflexion points caused by the primary effect. On the other hand, along the inward bulging longitudinal half waves the skin undergoes tension in the axial direction, which, due to the transverse contraction, induces compression in the ring direction, again decreasing the displacements of the inflexion points. The reduction of the inflexion point displacements, however, diminishes the shearing deformation shown in Fig. 8.2.11, rendering the shell less stiff.

In the case of inside stiffeners the secondary effect has an inverse influence, since the skin lies outside. The shearing deformation shown in Fig. 8.2.11 increases, so that the shell becomes more rigid.

To sum up, the secondary effect makes the shell with outside stiffeners less rigid than that with inside ones. Hence, the secondary effect acts in a sense contrary to the primary effect.

The secondary effect appears even if the buckling deformation contains no twist, provided that the ribs are arranged in the direction of the buckling waves, as e.g. in the case of axisymmetric buckling of stringer-stiffened shells. That is, due to the transverse contraction, variable hoop elongations and shearing deformations develop in the skin. If Poisson's ratio of the skin is equal to zero, the secondary effect obviously also ceases to exist.

It cannot always be decided without a detailed analysis which of the primary or the secondary effects, acting in contrary senses, prevails, i.e. whether outside or inside stiffening results in providing a greater effective rigidity. According to the investigations of Geier [8.2.5] and Singer, Baruch and Harari [8.2.13], in the case

of cylindrical shells under lateral (or hydrostatic) pressure, inside stiffeners provide a greater stiffness for long cylinders, while outside stiffeners are more effective for short ones. In other cases, however, when the buckles are not long-shaped as in the aforementioned cases, but are (nearly) square, outside stiffeners provide a greater effective rigidity, as a rule. Thus, in the case of axially compressed cylinders, it is always outside stiffeners that provide a greater rigidity.

Numerical computations showed the following differences between the rigidities of outside and inside stiffeners of the same cross sections in favour of outside ones: For ring-stiffeners, mostly $10 \sim 15\%$ [8.2.1], in extreme cases (very heavy stiffeners) $30 \sim 40\%$ [8.2.6b]. For stringer-stiffeners the difference may reach 100% or, in the case of very heavy stiffeners, even more [8.2.2a], [8.2.6a], [8.2.6b].

However, this favourable effect of outside stiffeners is greatly counteracted by the increased sensitivity of outside stiffened shells to initial imperfections. In fact, from the basic paper of Hutchinson and Amazigo [8.2.6b], the conclusion can be drawn, taking it by and large, that — except for very long shells exhibiting more favourable behaviour — the stiffeners which provide a higher critical load (i.e. outside, in particular longitudinal ones) are rather sensitive to imperfections. This circumstance partially counterbalances their advantages described earlier.

In all probability this imperfection-sensitivity accounts for the fact that in several cases the experiments did not exhibit the difference between the critical loads of outside and inside stiffened shells [7.9], [8.2.15]. In other cases, however, the difference was well marked [8.2.2c], [8.2.6a].

The exact value of the linear critical load of eccentrically stiffened shells has been calculated for several cases. Closed solutions are to be found in [8.2.6a] for axially compressed stringer-stiffened shells, in [8.2.1] and in [8.2.13] for ring-stiffened and ring- and stringer-stiffened ones respectively, under hydrostatic pressure, and in [8.2.2a] for ring- and stringer-stiffened shells under the simultaneous action of axial compression and hydrostatic pressure. Ribbed shells of revolution are treated in [7.4].

The buckling analysis of ribbed shells — as with ribbed plates — can be reduced to that of simple orthotropic shells dealt with in Chapter 7 if we neglect the effect of the eccentricity of the stiffeners, i.e. if we neglect the excess torsional (or, to be more exact, warping) rigidity due to the eccentricity of the stiffeners together with their primary and secondary effects, and take only the torsional rigidity proper into account. Although it has not yet been proved that by so doing we remain on the safe side even in extreme cases, we may expect, as a rule, to obtain the critical load of the ribbed shell with an accuracy sufficient for practical purposes. We do not see any other way, at present, to perform the buckling analysis of these structures with a reasonable amount of work.

To sum up, we propose to neglect the warping rigidity and the primary and

secondary effects caused by the eccentricity of the stiffeners in the buckling analysis, to compute the rigidity characteristics with the well-known formulas of ribbed flat plates (see Section 8.2.6) and to consider the structure a simple orthotropic shell (Chapter 7).

8.2.4. Poisson's Ratio of the Stiffened Shell

Transverse contraction in the ribs is obviously of no interest.

Transverse contraction plays a role only in connection with the rigidity characteristics of the skin, so that, all things considered, its influence is much less than on unstiffened shells.

Neglecting transverse contraction always causes the rigidity characteristics to be considered less than their actual values, since v appears in their denominators in the form of $(1-v^2)$, see in Section 7.1. Hence, taking into account that the influence of Poisson's ratio is rather small, in order to simplify calculations it is expedient to set $v=0$. This also serves to the benefit of safety.

8.2.5. Density of Ribs Required for "Smearing out" their Rigidities

If we want to calculate ribbed shells as continuous orthotropic ones, in addition to what has been already said, the requirement has to be fulfilled also that there should be ribs not only on the nodal inflexion lines of the orthotropic shell, but also within the buckling half waves. As far as the necessary number of ribs within one half wave is concerned, we refer to some comparative analyses [7.14] and to results obtained for reticulated shells [8.3.1]. From these we may draw the conclusion that if the half buckling wavelength is equal to at least two times the rib distance, the "smearing out" of the rib rigidities furnishes results sufficiently accurate for practical applications.

As a rule, the buckling wavelength of ribbed (orthotropic) shells is considerably greater than that of the unstiffened skin (the half buckling wavelength being usually proportional to the square root of the effective thickness, which is many times greater for stiffened shells than for the unstiffened skin). Hence, if we choose, according to Section 8.2.1, a smaller rib distance than the half buckling wavelength of the unstiffened skin, we mostly also meet the requirement that the half wavelength of the stiffened shell should be equal to several rib distances. This was confirmed by the investigations carried out in [8.2.13a] showing that if we arrange the ribs so densely as to prevent skin buckling at a lower load intensity than necessary for overall buckling, then, in the case of stiffeners without torsional rigidity and for the value 10 of the geometric parameter Z (see Fig. 2.14), the "smearing out"

of the rib stiffenesses results in a critical load about 7% higher than that obtained with discrete stiffeners. This discrepancy rapidly decreases with increasing Z. For ring-stiffeners some results are to be found in [8.2.8a] which permit us to draw similar conclusions.

It should be noted that, according to [8.2.4a], the "smearing out" of the rib rigidities always results in a somewhat higher critical load than the computation with discrete stiffeners.

The method for taking individual stiffeners into account is to be found in [8.2.19] or [8.2.20].

It should be mentioned that individual stiffeners cause several disturbances not taken into account be the continuum approach. For example, if an axially compressed cylindrical shell is stiffened by ribs in the circumferential direction, the skin, due to Poisson's ratio, undergoes an elongation in the circumferential direction, while the ribs keep their original length. Consequently, the skin bulges outwards between the ribs, so that an appreciable initial imperfection comes about, which may reduce the critical load. Some aspects of this effect under pure bending are dealt with in [8.2.9a].

8.2.6. Rigidity Characteristics of the Orthotropic Shell Equivalent to the Stiffened One

Using the approximations mentioned above (neglecting the "warping rigidity", the primary and secondary effects due to the eccentricity of the stiffeners and the transverse contraction), the rigidity characteristics of the shell ribbed in x and y directions can be written as follows:

Extensional (membrane) rigidities:

$$T_x = E\left(t + \frac{A_x}{b_y}\right), \tag{8.2.10a}$$

$$T_y = E\left(t + \frac{A_y}{b_x}\right), \tag{8.2.10b}$$

$$T_{xy} = 2Gt. \tag{8.2.10c}$$

Bending (plate) rigidities:

$$B_x = \frac{EI_x}{b_y}, \tag{8.2.11a}$$

$$B_y = \frac{EI_y}{b_x}, \tag{8.2.11b}$$

$$B_{xy} = \frac{Gt^3}{6} + \frac{1}{2}\left(\frac{GI_{tx}}{b_y} + \frac{GI_{ty}}{b_x}\right). \tag{8.2.11c}$$

Here:

A_x, A_y — cross sectional area of one rib in the x and y directions respectively (without the skin);

b_x, b_y — rib distances (see Fig. 8.2.2);

I_x, I_y — moment of inertia of one rib in the x and y directions respectively, calculated with the effective width of the skin;

I_{xt}, I_{yt} — torsional constant of one rib in the x and y directions respectively, calculated without the skin;

$G = \dfrac{E}{2}$ — modulus of shear.

8.2.7. Suitable Stiffening of Cylindrical Shells

Regarding the question of which kind of stiffening is most effective for different loading cases, we may state that, as a rule, — in accordance with what has been said in Chapter 7 — stringer-stiffeners are more effective on short shells while ring-stiffeners are more expedient on long ones. Ring-stiffeners may also considerably increase the critical axial load of cylindrical shells when applied together with stringer-stiffeners [8.2.12a]. For the expedient design of the stiffening of axially compressed cylindrical shells we find instructions in [8.2.12a] and [8.2.12b].

8.3. Reticulated Shells

If the shell has to bridge a large span, we may expediently construct it of steel, covering the shell surface by a triangular network and arranging bars corresponding to its sides. We thus obtain a reticulated shell. The roofing layer plays no structural role in this case. The structural grid itself may be either single- or double-layered.

If the network of the structure has some regularity properties, it is generally possible to find a statically equivalent continuum and to reduce the overall stability analysis of the reticulated structure to that of a continuous shell as treated in the previous chapters.

8.3.1. Single-Layer Reticulated Shells

If the network consist of equilateral triangles, all bars have equal cross sections and they are rigidly connected at the joints (Fig. 8.3.1), then the equivalent continuum of the structure is a solid isotropic shell [8.3.3], [8.3.5] with the thickness:

$$t' = 2\sqrt{\frac{3EI+GI_t}{EA}}. \tag{8.3.1}$$

and with the modulus of elasticity:

$$E' = \frac{2A}{\sqrt{3}\,at'}\,E. \tag{8.3.2}$$
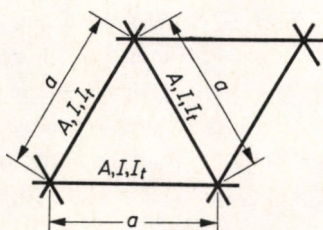
Fig. 8.3.1. The single-layer reticulated shell
that has an isotropic shell as equivalent continuum

Here the following notations have been used:

a — centre-line length of one bar;

A — cross sectional area of one bar;

I — moment of inertia of one bar (referred to the axis tangential to the shell surface);

I_t — torsional constant of one bar;

E — modulus of elasticity of the bar material;

G — modulus of shear of the bar material.

Poisson's ratio for tension of the equivalent shell is (independent of the bar material):

$$v' = 1/3. \tag{8.3.3}$$

In the case of bending a somewhat smaller v'' is obtained if $GI_t > 0$, so that the structure is not perfectly isotropic. This difference has, however, no practical significance since, according to what has been said in Chapter 7, the transverse contraction may be neglected in most cases anyway.

As with ribbed shells, here also the question arises of how dense the net should be in order to obtain a satisfactory accuracy when using the replacement homo-

geneous shell. Forman and Hutchinson [8.3.1] computed the linear critical load of a radially compressed reticulated (shallow) spherical cap and of an axially compressed reticulated cylinder, both with the net described above, exactly (considering the actual reticulated structure) and by using the replacement homogeneous isotropic shell. They assumed the torsional rigidities of the bars to be $GI_t = 0.769EI$, corresponding to circular solid or tube sections. They found for $a/\sqrt{Ri} \leq 2$ (with $i = \sqrt{I/A}$ as the radius of gyration of the bar cross section and R as the radius of the shell surface), or — substituting for i the equivalent wall thickness $t' \approx 3.88i$ valid for the assumed ratio GI_t/EI — for $a/\sqrt{Rt'} \leq 1$, that the continuum method yields (linear) critical loads less than 10% higher than the exact values.

With the aid of Figs 8.2.1 and 8.2.5, this result can easily be converted into a ratio of bar length to half buckling wavelength of the replacement shell. Since the linear theory does not determine uniquely the two lengths of the buckle, we took, for the benefit of safety, the minimum possible lengths in every case, and we obtained approximately that the 10% limit of error can be assured if the half buckling length of the reticulated shell, according to the linear theory, is equal to at least two bar lengths.

According to [8.3.1], the 10% limit of error can also be guaranteed by requiring that under the action of the (linear) critical load of the replacement shell the compressive force in no bar should exceed 70% of its Euler buckling load (assuming hinged ends).

If the grid consists of triangles other than equilateral, or the cross sections of bars in the different directions are not identical, the replacement shell will be anisotropic, see [8.3.2] or [8.3.3].

Single-layer shells have two kinds of buckling that might be considered as "local". One is the buckling of individual bars between the joints. This can be eliminated by designing the bars for buckling in the usual way, taking the clamping effect of the joining bars into account (or neglecting it for the benefit of safety, assuming hinged ends). The other phenomenon is the snapping of a part of the structure under a concentrated load, acting e.g. during erection. This may be treated with the aid of the replacement continuous shell, using the results presented in Section 4.2.2, since the phenomenon represents an "overall" rather than a "local" buckling problem, provided the network is "dense enough" to allow the continuum treatment. As an alternative, a special "local" method for the analysis of the snapping is to be found in [8.3.4].

8.3.2. Double-Layer Reticulated Shells

With respect to bending (and twist) the double-layer reticulated shell is equivalent to a homogeneous isotropic solid shell [8.3.3], [8.3.6] if both layers are identical and they consist of bars of identical cross-sectional areas forming nets of equilateral triangles (Fig. 8.3.2). The replacement shell has the thickness:

$$t' = \sqrt{3}\,h \qquad (8.3.4)$$

and the modulus of elasticity:

$$E' = \frac{4}{3}\frac{A}{ah}E. \qquad (8.3.5)$$

Here h denotes the distance between the two layers, while the other symbols are defined after Eqs (8.3.1)–(8.3.2).
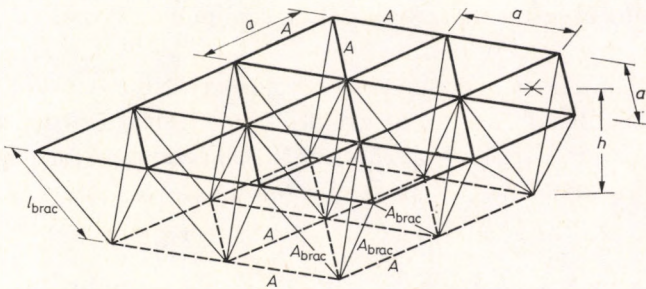
Fig. 8.3.2. The double-layer reticulated shell
that has an isotropic sandwich shell as equivalent continuum

Poisson's ratio is given by Eq. (8.3.3) in this case too.

With double-layer reticulated shells it makes practically no difference whether the joints are hinged or ensure a rigid connection between the bars, because the stiffness of the structure is provided by the extensional rigidities of the bars rather than by the rigid joint connections, as contrasted to single-layer shells.

The accuracy of the continuum buckling analysis of double-layer reticulated shells has not yet been investigated in detail. However, it seems to be logical to consider the results of Forman and Hutchinson [8.3.1], outlined in the previous section, for double-layer shells too.

Double-layer reticulated shells are much less stiff in transverse shear than their replacement solid shells defined by Eqs (8.3.4)–(8.3.5). In fact, they are equivalent to sandwich shells (see Section 8.1), rather than to solid ones. If every bracing member connecting the two layers has the same length and the same cross-sectional area, the structure is isotropic with respect to transverse shear, and it has the factor

ϱ characterizing the "sandwich-effect":

$$\varrho = \frac{\sqrt{3}\, l_{brac}^3}{E A_{brac}\, h^2},\qquad (8.3.6)$$

where (see Fig. 8.3.2):

l_{brac} — length of the bracing members;

A_{brac} — cross-sectional area of the same.

In buckling analysis the "sandwich-effect" should be taken into account as outlined in Section 8.1.

If the networks of the two layers consist of triangles other than equilateral, or the cross-sectional areas of the bars running in different directions are not equal to each other, the replacement continuum becomes anisotropic [8.3.3]. If the network of the two layers differ or if the rigidity properties of the two layers are not proportional to each other, the equivalent continuum becomes a ribbed shell [8.3.3].

The "local" instability of double-layer reticulated shells consists of the buckling of the individual bars. This can be avoided by designing the bars for buckling, taking into account the clamping effect of the adjacent bars (or neglecting it to the benefit of safety).

8.3.3. Interaction Between Local and Overall Buckling

When investigating the necessary net density of single-layer reticulated shells which allows the replacement continuum to be used, Forman and Hutchinson [8.3.1] considered this interaction, too. Their rule, given in Section 8.3.1, thus indicates the real, total deviation of the (linear) critical load of the replacement continuum from that of the actual reticulated structure.

On the other hand, if we consider the load intensity which causes local buckling (also taking, if necessary, the plasticity of the individual members into account) as n_{pl} (Section 9.4), and apply Eq. (9.4.2) for the "limit" case of Forman and Hutchinson ($0.7\, n_{pl} = n_{cr,\,el}$), we obtain a "combined" critical load 18% less than the elastic one, as compared with the 10% deviation given by Forman and Hutchinson, i.e. we remain one the safe side. This presumably applies to double-layer reticulated shells, too. Hence, we may also use this procedure in those cases when the condition given by Forman and Hutchinson (Section 8.3.1) is not fulfilled. (It should be remarked that although Eq. (9.4.2) is written for the upper elastic critical load, it may be applied to the linear critical load as well, because the former turns into the latter for $w_0 \to 0$.)

8.4. Corrugated Shells

Corrugated shells are mostly produced by twisting or bending corrugated (Fig. 8.4.2) or folded (Fig. 8.4.3) plates. Consequently, corrugated shells mostly have the shape of cylinders or hyperbolic paraboloids [8.4.1], [8.4.3], [8.4.4]. In [2.35] we also find an application in the form of an elliptic paraboloid.

The special feature of such corrugated or folded plates is that they have a great bending rigidity in the direction y perpendicularly to the waves, while in the direction x of the waves they have a small extensional rigidity. Due to this speciality of the rigidities, in the cases of the critical loads appearing as the product of these two rigidities ("shell-like" buckling), the critical load of the corrugated shell is the same as if it were made of the same sheet without corrugation [7.6]. The corrugation increases the critical load substantially only when it is determined mainly by the bending rigidity ("plate-like" buckling).

In order to understand this phenomenon better, we have to consider that the critical load appears as the product of extensional and bending rigidities, when the boundary conditions do not influence the buckling wavelength and the critical load is obtained by minimization, e.g. in the cases of the axially compressed cylinder, the radially compressed sphere or the (not too shallow) hyperbolic paraboloid supported along the generatrices. These cases represent "shell-like buckling". Plotting the critical load against the curvature ($1/R$) of the shell, we obtain a slanting straight line (Fig. 8.4.1).
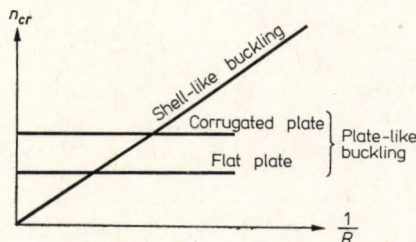
Fig. 8.4.1. Shell-like and plate-like critical loads

On the other hand, if the buckling wavelength is limited by the boundary conditions, then — in an extreme case — the curvature of the shell (i.e. its extensional rigidities) play no role, and the critical load is determined by the bending rigidities only ("plate-like" buckling); see the horizontal straight lines of Fig. 8.4.1. In these cases we may compute the critical compressive force as that of a flat plate with the same ground plan and the same boundary conditions. The corrugation increases the combinations of the bending rigidities in any case. Thus, only the

rigidity-increasing influence of the corrugation remains effective, shifting the horizontal line pertaining to the "plate-like" buckling of the corrugated plate (see Fig. 8.4.1) higher than that of the flat plate. This occurs e.g. in the case of the buckling of corrugated shallow hyperbolic paraboloid shells supported along the generatrices.

The exact curve of the actual critical load of the shell osculates the straight lines of shell-like and plate-like buckling, as in the case of the hyperbolic paraboloid shell, shown in Fig. 5.5 (b).

Accordingly, in the vicinity of the interaction point of the two straight lines, the buckling behaviour of the shell shows some intermediate behaviour between pure "shell-like" and "plate-like" buckling.

However, this transitory section is not very long; moreover, the critical load is not much higher than that given by the straight lines. Thus, the behaviour of the shell can be well characterized by the straight lines pertaining to shell-like and plate-like buckling.

It should be remarked that if a complete cylinder is corrugated in the axial direction (i.e. its straight generatrices are parallel to the axis x in Figs 8.4.2 or 8.4.3),
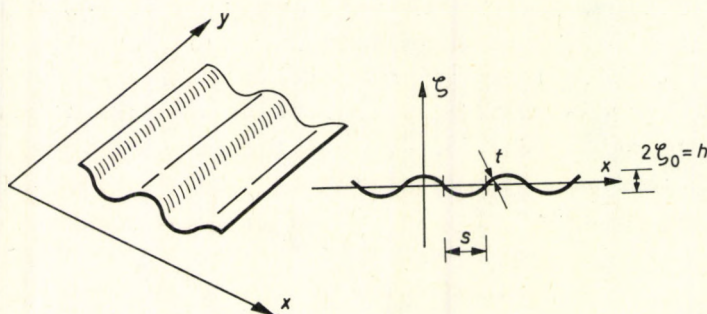
Fig. 8.4.2. Corrugated plate and its cross section
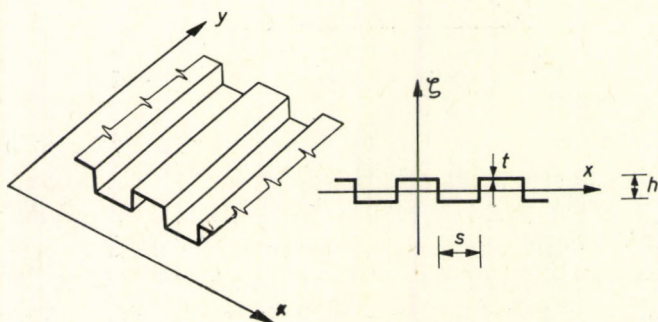
Fig. 8.4.3. Folded plate and its cross section

the bar-like buckling of the whole cylinder may also be onerous. That is, this kind of corrugation provides a rather low axial tensile stiffness which may reduce the rigidity against bar buckling more than that against shell buckling.

The rigidity of the corrugated shell may be increased by applying stiffening ribs or plates in the direction of the waves [2.35], as shown in Fig. 8.4.4. These
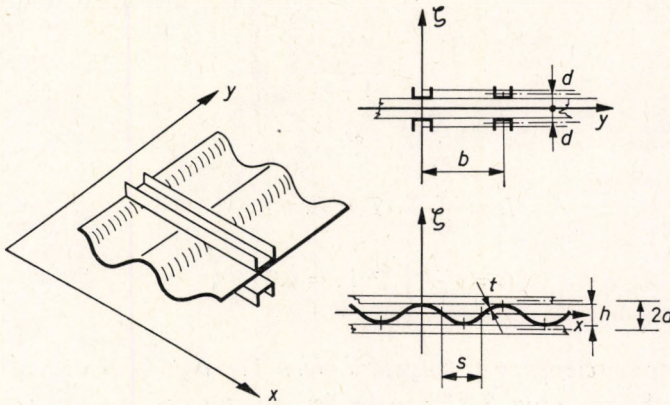
Fig. 8.4.4. Stiffened corrugated plate and its cross section (The stiffeners may also be bars of other cross sections, even flat plates)

increase the bending and extensional rigidities in the direction parallel to the waves, thereby raising the critical load of the corrugated shell too. In this structure the corrugated plate acts as a bracing. On the other hand, since this bracing consists of "curved members", rather than of straight ones, the transverse shear also causes bending in the corrugated "members". Consequently, the transversal shearing deformation can no longer be neglected. Thus, when calculating the critical load, the "sandwich-effect" (Section 8.1) also has to be taken into account.

In corrugated or folded shells, local buckling of the corrugations or of the folded plate elements can only occur if the structure as a whole buckles in a "plate-like" manner. That is, the critical load of the "shell-like" overall buckling is in any case lower than that of the local buckling occurring in very short buckling waves. On the other hand, in the case of stiffened corrugated (or folded) shells (see Fig. 8.4.4) local buckling also has to be investigated in the case of shell-like overall buckling. In order to use the procedure outlined in Section 9.4 for taking into account the interaction of overall and local buckling, we have to regard the load intensity of the appropriate local buckling as p_{pl}.

The rigidity characteristics of corrugated or folded shells described above, which are necessary for designing them like orthotropic ones for buckling, are given in the following.

Rigidity characteristics of the corrugated plate. The cross section of the corrugated plate is shown in Fig. 8.4.2. With $v=0$, assuming the sine arcs to be flat, and neglecting the warping rigidity (as in the case of ribbed shells), we may write the rigidity characteristics on the basis of [7.6] as follows:

$$\left.\begin{array}{l} B_x = B_{xy} = B, \\ B_y = B(1+\Theta), \\ T_x = \dfrac{T}{1+\Theta}, \\ T_y = T_{xy} = T. \end{array}\right\} \tag{8.4.1}$$

Here:

$$\left.\begin{array}{l} B = \dfrac{Et^3}{12}, \quad T = Et, \\[2mm] \Theta = \dfrac{12}{st^2}\int_0^s \zeta^2\,dx = 6.0\left(\dfrac{\zeta_0}{t}\right)^2. \end{array}\right\} \tag{8.4.2}$$

and

Rigidity characteristics of the folded plate. The rigidity characteristics of the folded plate shown in Fig. 8.4.3 may be derived in a similar way to those of the corrugated plate. However, the flatness of the cross section can no longer be assumed, since the influence of the plate sections in the direction ζ may be considerable. In the following we present the rigidity characteristics assuming $v=0$ and neglecting the warping rigidity:

$$\left.\begin{array}{l} B_x = B\dfrac{1}{1+h/s}, \\[2mm] B_y = B\left[1+3\left(\dfrac{h}{t}\right)^2+\dfrac{h}{s}\left(\dfrac{h}{t}\right)^2\right], \\[2mm] B_{xy} = B(1+h/s). \end{array}\right\} \tag{8.4.3}$$

$$\left.\begin{array}{l} T_x = T\dfrac{1}{1+3\left(\dfrac{h}{t}\right)^2+\dfrac{h}{s}\left(\dfrac{h}{t}\right)^2}, \\[2mm] T_y = T(1+hs), \\[2mm] T_{xy} = T\dfrac{1}{1+h/s}. \end{array}\right\} \tag{8.4.4}$$

In these formulas $B=Et^3/12$ and $T=Et$.

If the corrugated or folded shell has a curvature in the y direction with the radius of curvature R_y, its tensile stiffness in the x direction, T_x, increases, because the outward or inward bulging parts of the shell are forced onto circles of larger or smaller radiuses of curvature, and the hoop forces which arise hinder this deformation.

The modified values of the tensile stiffness T_x are [8.4.2]:

— for the corrugated shell:

$$T_x = \frac{T}{1 + \dfrac{6.0}{\dfrac{t^2}{\zeta_0^2} + 0.123 \dfrac{s^4}{\zeta_0^2 R_y^2}}}; \qquad (8.4.5)$$

— for the folded shell:

$$T_x = \frac{T}{1 + 3\dfrac{h^2}{t^2}\psi + \dfrac{h^3}{st^2}}, \qquad (8.4.6)$$

with ψ plotted in Fig. 8.4.5.
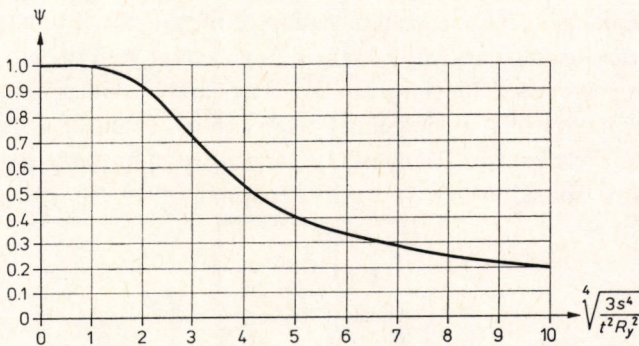
Fig. 8.4.5. Factor ψ representing the influence of curvature on the tensile stiffness T_x of folded shells

These modified T_x-values were derived for axisymmetric deformation. In the case of asymmetric deformation these values may be somewhat less [8.4.2].

Rigidity characteristics of the stiffened corrugated plate. The rigidity characteristics in the direction y of the stiffened corrugated plate shown in Fig. 8.4.4 are equal to those of the unstiffened one. In the direction x the rigidities of the corrugated plate can be neglected in comparison to those of the stiffeners, so that only these latter appear in the expressions. On the other hand, the "in-plane" shearing rigidity is hardly increased by the stiffeners, so that this will be provided by that of the corrugated plate. Finally, the torsional rigidity can be approximately obtained by taking that of the plate, neglecting those of the stiffeners.

Hence, the rigidities of the stiffened corrugated shell are:

$$
\left.\begin{aligned}
B_x &= \frac{2E}{b}(Ad^2 + I),\\
B_y &= B(1 + \Theta),\\
B_{xy} &= B,\\
T_x &= \frac{2E}{b}A,\\
T_y &= T_{xy} = T.
\end{aligned}\right\}
\tag{8.4.7}
$$

In these formulas, B, T, Θ are as defined by Eq. (8.4.2), A and I are, respectively, the cross-sectional area of one stiffening element and the element's moment of inertia referred to its own centroid.

It should be remarked that the upper and lower stiffeners may be shifted with respect to each other in the y direction.

The "sandwich-effect", i.e. the deformation of the corrugated plate, acting as a web, due to transverse shear, may be taken into account with the aid of the factor ϱ explained in Section 8.1. Its value can be determined by equating the transversal shearing deformation of the corrugated plate-web with that of a sandwich plate and expressing therefrom ϱ. The factors ϱ_x and ϱ_y valid in the x and y directions respectively, determined in this way, are as follows:

$$
\left.\begin{aligned}
\varrho_x &= \frac{1}{Et}\left(\frac{s}{h}\right)^2 (1 + 0.25\Theta),\\
\varrho_y &= \frac{1}{Et}\frac{2s}{t}.
\end{aligned}\right\}
\tag{8.4.8}
$$

To assess the critical load as that of an isotropic sandwich shell we may use the approximate expression (8.1.4). In cases demanding greater accuracy we may compute the structure as an orthotropic sandwich shell according to the procedures outlined in [2.13], [8.1.6].

9. Practical Application of the Results of the Stability Theory

In the previous chapters we presented the results of the theory of elastic stability. The knowledge of these results is, however, not sufficient to design an actual shell against buckling. We have to know, in addition, which are the values to be assumed for the basic data of the elastic stability analysis; furthermore we have to consider that the properties of the shell material generally differ from the linearly elastic ones. Thus, in the case of most structural materials the plasticity and, in the cases of concrete, synthetics, wood and metals (at high temperatures), the creep may reduce the elastic critical load considerably. Finally, for concrete and reinforced concrete shells, in addition to the aforementioned effects, the influence of cracks and reinforcement has to be clarified.

In the following we intend to deal with each of these aspects, in turn.

9.1. Factors Influencing the Critical Loads of Shells

The factors influencing the critical loads of shells may be classified as follows:

The critical load depends

— on the material properties of the shell that can be characterized by the modulus of deformation E (i.e. the modulus of elasticity of the material model, see Sections 9.4, 9.6, 9.8);

— on the extensional and bending rigidities, T and B respectively, of the shell; in the cases of "shell-like" buckling, these can be taken coupled as a unique "shell-buckling rigidity characteristic"

$$K = \sqrt{BT} \qquad (9.1.1)$$

into account, as is shown in [9.1.1];

— on the curvatures of the shell, characterized by the radiuses of principal curvatures.

These factors again depend on the following data or effects:

The modulus of deformation E depends on the

— quality (strength);
— creep;
— actual stress

of the material. (The effect of the plastic properties of the material is incorporated into the last item.)

The shell buckling rigidity characteristic K depends on the

— ratio of thicknesses of the erected and the designed shells;

and furthermore, in the case of reinforced concrete shells, on the

— cracks of the concrete;
— eccentricities of the normal forces;
— quantity, quality, and position inside the cross section of the reinforcing bars.

The radiuses of curvature of the shell depend on the initial imperfections caused by the

— inaccuracies of erection;
— bending moments,

taken into account by the initial eccentricity of the in-surface (membrane) forces, and by the amplitude w_0 of the initial imperfection.

First, we deal with the assumption of the proper initial eccentricity w_0 necessary for the determination of the critical loads of elastic shells (Sections 9.2–9.3). Next we investigate the influence of plasticity (Section 9.4) and of creep (Section 9.5) of the shell material. Then we deal with the special problems of shells made of metals, synthetics or timber and (reinforced) concrete (Sections 9.6, 9.7 and 9.8). The problems connected with the experimental determination of the critical load will be treated in Section 9.9. Finally, the necessary value of the safety factor will be examined (Section 9.10).

9.2 The Initial Imperfection and the Eccentricity of the Normal Force to be Taken into Account

We have seen in the previous chapters that the upper critical loads of most homogeneous elastic shells sharply decrease with increasing initial imperfection amplitude w_0. This decrease is due partly to the magnitude of the imperfection itself, partly to the eccentricity e_0 of the compressive force belonging to this imperfection. In the case of homogeneous shells the rigidity characteristics of the shell cross section were independent of the magnitude of the eccentricity, so that it was sufficient to investigate the decrease of the critical force dependent on the imperfection alone. However, the plastic deformation and load bearing capacity of the shell wall, and the rigidity of the cracked reinforced concrete cross section depend decisively on the eccentricity of the normal force. Consequently, in the following we have to deal separately with the influence of the imperfection w_0 and with that of the eccentricity e_0 of the normal force.

9.2.1. Relation between Imperfection and Eccentricity

One part of the imperfection causes bending moment, i.e. eccentricity, while the other part changes the distribution of the membrane forces, thus not giving rise to eccentricity. Hence our problem is to find the relation between the imperfection amplitude and the eccentricity resulting from the imperfection in the cases of various shell types.

If we impose a small deformation w onto a shell with a given geometry and state of stresses, we can determine the pertaining bending moment and the change in the membrane force at any point and in any direction with the aid of the classical bending theory. Dividing the bending moment by the modified value of the membrane force we arrive at the magnitude of the eccentricity. Performing this investigation for several shell surfaces and for various states of stresses we obtained the following results for the ratio $c = e_0/w_0$.

— in the vicinity of stiffened edges the value of c may become greater than unity; however, since the edge stiffener impedes buckling, the shell does not fail here;

— in regions where buckling may occur, the value of c always becomes smaller than unity;

— the value of c depends on the geometry, on the state of membrane stresses, and on the value of the imperfection amplitude w_0 as well; nevertheless, we may consider the following values, in the range $0.167 < w_0/t < 0.50$, as safe, good approximations:

— cylindrical shells: $c = 1.00$;
— domes: $c = 0.67$;
— hyperbolic shells: $c = 0.50$.

The value of c decreases with increasing w_0, so that in the range $w_0/t > 0.50$ the above values yield a wider margin of safety when computing e_0 from w_0.

Since we established the above c-values on the basis of the classical (small-deformation) bending theory, these values are independent of the buckling deformation w. Our qualitative investigations with the aid of the large-deflection theory showed that this can, in fact, be considered as a permissible approximation. So, with the above values of c we can convert imperfection to eccentricity and vice versa, according to which value is given and which is needed.

9.2.2. The Magnitude of the Imperfection

We described in Chapters 2 and 4 how the initial imperfection reduces the critical load. The greatest reduction was obtained by Kao [4.16a] for the spherical cap. However, he assumed an extremely onerous imperfection, one rather unlikely to occur in practice, i.e. an asymmetric one extending only over one quarter of the spherical cap. We may reasonably assume that only a part of the initial imperfections to be expected have these properties. Hence, we should take Kao's results only partially into account. If we evaluate the theoretical results, considering these viewpoints, we obtain the curves of Fig. 9.2.1, of which those of the radially compressed sphere and of the axially compressed cylinder coincide. These curves can be applied to calculate reliably the upper critical loads of cylindrical and spherical shells with known initial imperfections.

In the following, ϱ stands for the ratio of the upper critical load to the linear one, $(\varrho = p_{cr}^{\text{upper}}/p_{cr}^{\text{lin}})$, while the kind of upper critical load is indicated by subscripts. (Thus the values related to homogeneous, concrete, and reinforced concrete shells are denoted by ϱ_{hom}, ϱ_c, and ϱ_{rc}, respectively). The curves of Fig. 9.2.1 can be closely approximated in the range $w_0/t < 1$ by the expression:

$$\varrho_{\text{hom}} = \frac{1}{1 + A\dfrac{w_0}{t}}. \tag{9.2.1}$$

The value of A is different for the various shell types. Knowing the value of ϱ_{hom} valid for $w_0/t = 0.5$, $\varrho_{\text{hom}}(0.5)$, the constant A can be computed from the formula:

$$A = 2\left[\frac{1}{\varrho_{\text{hom}}(0.5)} - 1\right]. \tag{9.2.2}$$
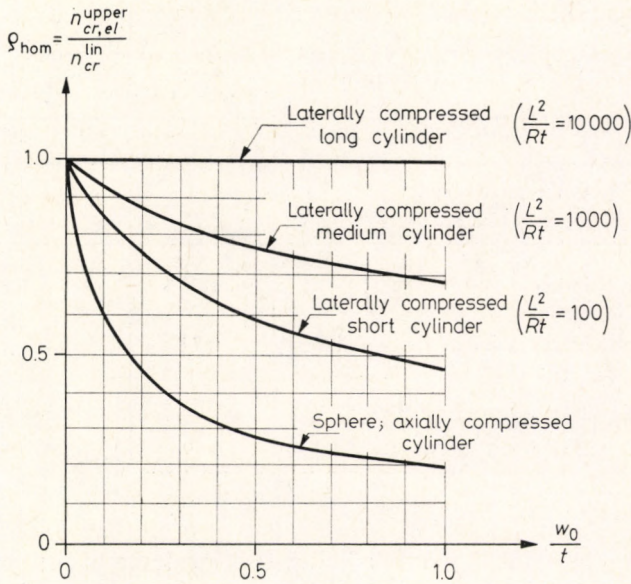
Fig. 9.2.1. Decrease of the upper critical loads of cylindrical and spherical shells with increasing initial imperfection amplitude w_0

The value of ϱ_{hom} (0.5) is to be assessed from the expression:

$$\varrho_{\text{hom}}(0.5) \approx \frac{1}{6}\left(1 + 5\,\frac{n_{cr}^{\text{lower}}}{n_{cr}^{\text{lin}}}\right). \tag{9.2.3}$$

The values of ϱ_{hom} (0.5) and A for various shell types are compiled in Table 9.2.1.

We still have to investigate the magnitude of w_0 to be assumed. Since, as Fig. 9.2.1 shows, the initial inperfection markedly reduces the critical load, we have to deal with this problem in detail.

The initial imperfection consists of two parts. One is the accidental imperfection due to inaccuracies of erection, the amplitude of which we denote by $w_{0,\,\text{accid}}$.

The other part is the calculable imperfection to be computed by the bending theory of shells. Its amplitude will be denoted by $w_{0,\,\text{calc}}$.

The coincidence of the maximum values of both imperfections is rather improbable. Thus, according to the rules of the probability theory, we may take the greater of the following values for design imperfection:

$$w_{0,\text{design}} \geqq \begin{cases} w_{0,\,\text{calc}} + 0.8 w_{0,\,\text{accid}} \\ w_{0,\,\text{accid}} \end{cases}. \tag{9.2.4}$$

Table 9.2.1

Values of ϱ_{hom} (0.5) and A (Eqs (9.2.3) and (9.2.2)) for various shell types

Shell types	ϱ_{hom} (0.5)	A
Axially compressed cylinder, radially compressed sphere	0.25	6.0
Long cylinders, $\left(\dfrac{L^2}{Rh} \geqq 10000\right)$,	1.00	0.0
Medium length cylinders $\left(\dfrac{L^2}{Rh} = 1000\right)$,	0.77	0.6
Short cilinders $\left(\dfrac{L^2}{Rh} = 100\right)$, subjected to lateral pressure	0.59	1.4

By so doing we have taken the probability of coincidence of the mean values of imperfection amplitudes into account. The standard deviations of the eccentricities from their mean values will be considered in the safety factor.

Accidental imperfection. When we compare the decrease of the theoretical critical load, as plotted against the initial imperfection (Fig. 9.2.1), with the decrease of the mean values of the experimental critical loads obtained for the axially compressed cylinder and the sphere, as plotted against the ratio R/t (see Figs 2.3 (a), (b), (c) and 4.2), we find that they show the same tendency. The reason for this phenomenon is that the thinner the shell is as compared to its radius of curvature, the less accurately it can be built.

For both the cylinder and the sphere, the upper and lower bounds at $R/t = 1000$ are 0.7 and 0.1, respectively. The average value of both is 0.4. According to [9.2.2], however, the distribution of the experimental values is not symmetric: for the experiments on cylinders, the mean value is 10% lower than the average value. A detailed evaluation of the experimental results on spheres furnishes a similar result. Thus, the mean value may be assumed to be 0.36.

The decrease of the critical load with increasing initial imperfection amplitude w_0 in the cases of axially compressed cylinders and of spheres can be expressed from Eq. (9.2.1) and Table 9.1.1, yielding the hyperbola:

$$\varrho_{\text{hom}} = \frac{p_{cr}^{\text{upper}}}{p_{cr}^{\text{lin}}} = \frac{1}{1 + 6\dfrac{w_0}{t}}, \qquad (9.2.5)$$

(Fig. 9.2.2 (a)). On the other hand, the mean value of the experimental critical loads as a function of the ratio R/t is approximately represented by the relation:

$$\frac{p_{cr}^{upper}}{p_{cr}^{lin}} = \frac{1}{1+\sqrt{3}\dfrac{R}{1000t}}, \qquad (9.2.6)$$

(a)   (b)
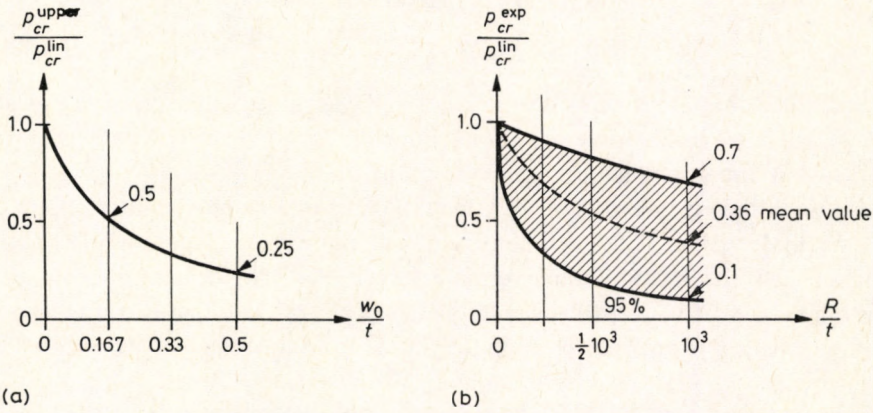
Fig. 9.2.2. (a) – Upper critical load of the axially compressed cylindrical and of the radially compressed spherical shell as a function of the maximum amplitude w_0 of the initial imperfection; (b) – scatter range of experiments on cylindrical and spherical shells plotted against the ratio of radius of curvature to wall thickness R/t

(Fig. 9.2.2 (b)). Equating the two left sides we obtain the following value for the accidental imperfection amplitude to be taken into account:

$$w_{0,accid} = \frac{R}{3500}. \qquad (9.2.7a)$$

The accidental imperfection was also checked by measurements [9.2.1]. On cylinders with the ratio $R/t=1000$ the amplitudes of the accidental imperfection half waves in the axial direction measured at points where it later buckled were around $R/3000$. Hence, the value given by Eq. (9.2.7a) seems to be acceptable for carefully fabricated shells.

In the case of erection methods which result in greater imperfections (e.g. assembling from parts by welding; reinforced concrete shells erected with a sliding formwork, etc.), it is reasonable to assume greater initial imperfection amplitudes than that given by Eq. (9.2.7a).

A further shortcoming of Eq. (9.2.7a) is that it disregards the fact that the accidental imperfection depends on the thickness of the shell as well, and that the accidental imperfection cannot become infinitely large if $R \to \infty$, i.e. in the case of the plane plate. Thus, evaluating measurements on erected cooling towers, we propose the following empirical formula for the accidental imperfection:

$$w_{0,\text{accid}} = 0.05\,t + \frac{R}{2000} \frac{a}{\dfrac{R/t}{1000} + \dfrac{1000}{R/t}}. \qquad (9.2.7b)$$

Here the factor a represents the influence of the accuracy of the erection method. For example we can assume $a=1$ for reinforced concrete shells with rigid formwork, while for sliding shuttering we can take $a=6$.

(It should be remarked that w_0 is not the maximum imperfection amplitude, but the mean value of the absolute values of the maximum amplitudes, i.e. in practice half the maximum measurable amplitude. The deviation from w_0 is covered by the safety factor, since the scatter of the critical load is mostly caused by the deviation of the imperfection amplitude from w_0.)

Calculable imperfection. This can be determined by the bending theory of shells. Some simple formulas for the initial eccentricities caused by the edge disturbances of membrane shells are to be found in [9.2.4] from which we can compute imperfection amplitudes outlined in Section 9.2.1.

Imperfections caused by vibrations due to dynamic influences also have to be included in the values of initial imperfection, if their magnitude is comparable with w_0, because, in the case of intensive dynamic excitation, the initial imperfection increased by the amplitude of vibration may cause the structure to buckle. Such vibrations arise, e.g. in the hulls of ships and in aeroplanes caused by the motors, or in some industrial buildings due to unbalanced machines.

In shell roofs, the deformation caused by the concentrated loads of workers during erection may also cause an increase in imperfection whose magnitude is comparable with w_0. This effect can be taken into account approximately by means of the snapping theory of flat arches [9.2.3], or according to the results for spherical shells [9.2.5].

9.3. Approximate Determination of the Upper Critical Loads of Eccentrically Compressed Elastic Shells

For the determination of the upper critical loads of eccentrically compressed shells of plastic material or of concrete or reinforced concrete, the load-deflection curves $p(w)$ of the homogeneous elastic shell (see Fig. 1.1) are needed. These can be found, however, for some cases only (e.g. in the example of the cylindrical panel dealt with in [2.57] and in the example of the spherical shell to be found in [4.21]), since the load is mostly plotted against the compression f measured in the load direction (see Fig. 1.4) rather than against the buckling deformation w.

Hence, we need a procedure to approximate the load-deflection diagram $p(w)$ of the eccentrically compressed shell. In what follows, such a method, outlined in [9.3.1], will be presented.

The load-deflection diagram $p(w)$ for the perfect shell is known for several cases. In the approximate procedure, we distort the relation:

$$p = p_{cr}\left(1 - \frac{w_0}{w}\right),\qquad(9.3.1)$$

valid for the eccentrically compressed straight bar (see Fig. 1.1 (a)), by proportional reduction in such a way that it osculates the $p(w)$ curve representing the post-buckling behaviour of the perfect shell instead of osculating the horizontal straight line p_{cr} of the bar.

If the $p(w)$-diagram of the perfect shell is not available, but the values p_{cr}^{lin} and p_{cr}^{lower} as well as w_{cr} pertaining to p_{cr}^{lower} are known, then the $p(w)$ diagram of the perfect shell with asymmetric post-buckling behaviour (Fig. 1.1 (d)) may be approximated by a parabola of the second degree which starts from the point $p/p_{cr}^{lin} = 1$ and has a horizontal tangent at the bottom point w_{cr} pertaining to p_{cr}^{lower}. The $p(w)$-diagrams of perfect shells of symmetric post-buckling behaviour (Fig. 1.1 (c)) start with a horizontal tangent, so that the approximation with the parabola starting with a falling tangent serves to the benefit of safety.

If even the w_{cr} value pertaining to the lower critical load of the shell is not known, then, maintaining the parabola approximation, we have to choose the smallest w_{cr} from those given for similar cases, because this yields the smallest critical load. Since w_{cr} is always greater than double the wall thickness, the value

$$w_{cr} \approx 2t\qquad(9.3.2)$$

may be used safely in any case.

We show this approximate procedure in Fig. 9.3.1, using the example of the complete sphere to be found in [4.21]. In Fig. 9.3.2 the approximate and exact values of the upper critical load p_{cr}^{upper} are compared with each other as plotted against the initial imperfection amplitude w_0.
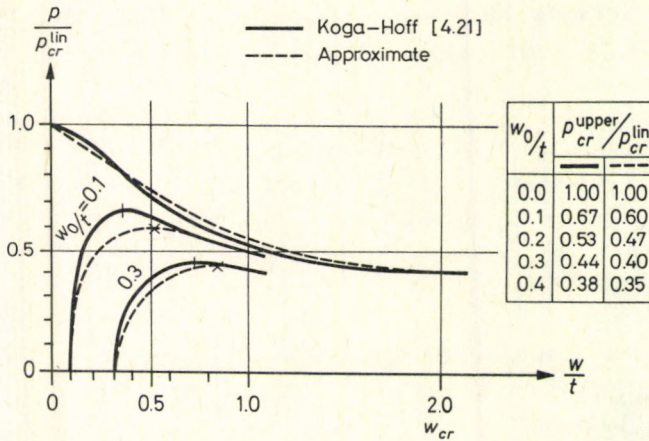
Fig. 9.3.1. Post-critical behaviour of the complete spherical shell and the approximate
construction of the load-deflection curve
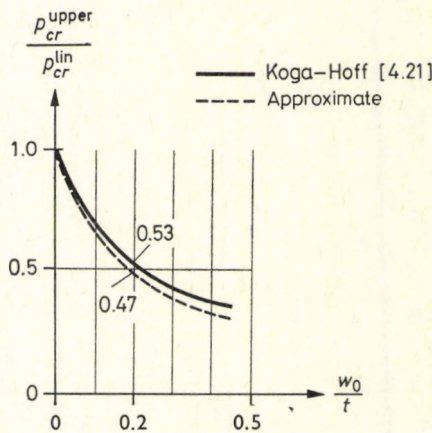
Fig. 9.3.2. Exact and approximate values of the upper critical
load of the spherical shell plotted against the amplitude
w_0 of the initial imperfection

From the diagrams to be found in the references we may draw the conclusion
that the lower critical load p_{cr}^{lower} of the perfect shell sets a lower bound to the upper
critical loads of the imperfect shell. That is, in the case of an imperfection amplitude
w_0 greater than that pertaining to a p_{cr}^{upper} equal to this p_{cr}^{lower}, the load-deflection
curve has, as a rule, no peak point, because increasing deformation implies a
steadily increasing load bearing capacity. Thus, in these cases, no upper critical
load can be defined any more — see the lowest dashed line in Fig. 1.4 (c).

9.4. Effect of Plasticity

Shells are mostly built of materials with plastic properties. If during shell buckling the deformations exceed the elastic limit and they become plastic, the critical load will be less than that given by the elastic theory. Hence it is necessary to take the influence of plasticity into consideration.

In stability analyses, the nonlinear or plastic behaviour of the shell material can be taken into account with the aid of simplified structural models, of approximate calculations based on logical considerations, or of more exact computer calculations using the plastic material model.

Unfortunately, there are not yet enough results of computer calculations available to establish definite simple rules for design. However, they allow us to draw the conclusion that the stability of elastic–plastic shells depends on the same factors as that of elastic shells. Besides, the critical load certainly has to be lower than the (fictitious) load causing plastic flow of the structure (without buckling). For guidance we shall mention some papers presenting such computer calculations.

Kaganov and Manevich [9.4.8] investigated the axisymmetric buckling of the geometrically perfect cylindrical shell of elastic–plastic material on the basis of the linear theory and also took internal pressure and variation of temperature into account. Grimaldi [9.4.4] treated a similar shell with the aid of the nonlinear theory. (His results are in close agreement with those to be found in [9.4.1], valid for the special case of eccentric buckling of plastic structures.) Zielnica [9.4.11] analyzed the buckling behaviour of plastic conical shells. Hutchinson [9.4.6] investigated the stability of structures made of plastic material, in particular that of a spherical dome, with the aid of a simplified structural model, taking geometric nonlinearity into account. Sureshwara et al. [9.4.10] analyzed shallow shells of revolution with clamped edges. They took four layers in the wall thickness into consideration. Assuming an axisymmetric deformation, they solved the snapping problem step by step, taking the elastic and plastic parts of deformation into account. By so doing they could also follow the spreading of the plastic zone. The relation of plasticity and shell buckling theories is clearly shown in their paper.

The first method suitable for practical application was given by Herber [9.4.5]. He established a substituting "slenderness ratio" from the lower critical load of the shell, and with this he computed the critical load according to the rules valid for bars made of plastic materials. By so doint he took the plasticity into account, but neglected the fact that the shell is more sensitive to imperfections than the straight bar. Pflüger [9.4.9], by plotting the curve representing the variation of σ_{cr}^{upper} of the cylinder as a function of R/t, determined the straight lines correspond-
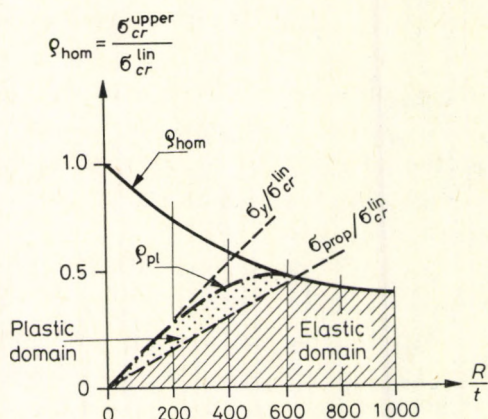
Fig. 9.4.1. The plastic critical load of the axially compressed geometrically perfect cylindrical shell according to Pflüger [9.4.9]
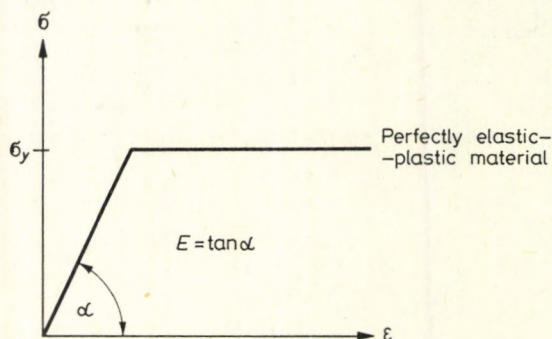
Fig. 9.4.2. Stress–strain diagram of perfectly elastic–plastic material

ing to the proportionality limit σ_{prop} and to the yield limit σ_y respectively, see Fig. 9.4.1. He constructed a parabola that has the line of σ_y as the initial tangent and touches the curve of σ_{cr}^{upper} at the point corresponding to σ_{prop}. This parabola forms an upper bound for the critical load of the shell with accidental initial imperfection (Fig. 9.4.1).

In [9.4.2] we developed a method which takes the imperfection sensitivity and the plasticity of the shells into account, and which can be generalized comparatively easily. Our results are in close agreement with the experiments. The basic assumption of the method is that during buckling plastic flow develops simultaneously in both directions. If this condition is not fulfilled, then we commit a slight error to the benefit of safety. In the following this method will be outlined.

In the analysis we assume a perfectly elastic–plastic material, whose stress–strain diagram is shown in Fig. 9.4.2. This corresponds fairly well to the properties of

metal shells, and moreover, by proper choice of the deformation characteristics, even to those of reinforced concrete ones.

The procedure is based on the principle of Ježek [9.4.7], which is valid for compressed bars. It states that the elastic and the ultimate values (n_{el} and n_{ult}) of the load intensity set lower and upper bounds to the upper critical load of an eccentrically compressed structure. Since these two bounds lie fairly close to each other, the upper critical load can be determined between these bounds with sufficient accuracy by an approximate graphical method. In fact, even the arithmetic mean of both bounds yields an acceptable result.

Here n_{el} denotes the internal specific force causing *yield stress* σ_y in one of the extreme fibres of the critical cross section (which is at the maximum amplitude of the buckling deformation), while n_{ult} causes *entire plastification* of the same cross section. For the case $e = w$ these notations are also defined in Fig. 9.4.3. Hence, the quantities n_{el} and n_{ult} are related to a cross section, and depend on the actual eccentricity $e = w$ of the specific compressive force acting on the
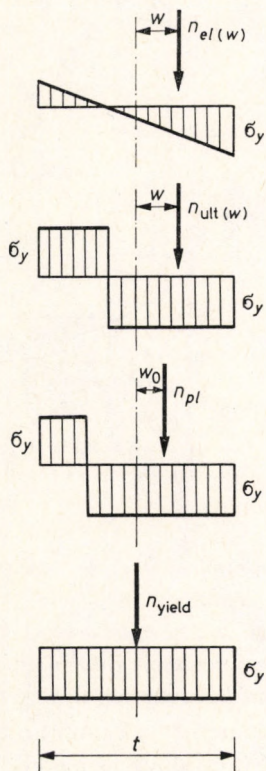
Fig. 9.4.3. Definitions of the elastic limit state
and of various plastic states of the cross section

same. Since we define n_{el} and n_{ult} as related to the cross section of the maximum buckling deformation, they may be approximately considered as characteristic of the state of the whole structure.

In the following we shall use two more quantities: n_{pl} and n_{yield} (see Fig. 9.4.3). By n_{pl} we denote that value of n_{ult}, which belongs to the given *initial eccentricity* $e_0 = w_0$, while n_{yield} is the *central* compressive force causing yield stress σ_y in the entire cross section.

For the analysis we use the approximate force-buckling deformation diagram described in Section 9.3, assuming $w_{cr} = 2t$. (Obviously, if there is a more exact diagram available, this has to be used.) We show the principle of the procedure in Fig. 9.4.4, using as an example a cylindrical shell with an initial imperfection amplitude $w_0 = 0.1t$ and the ratio $n_{yield}/n_{cr}^{lin} = 1$.
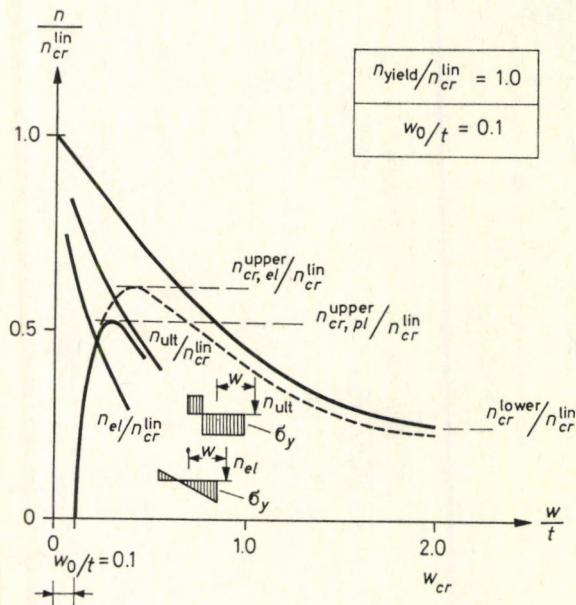
Fig. 9.4.4. Determination of the upper critical load

When the load intensity reaches the elastic limit n_{el}, i.e. when the curve of the load versus elastic deformation intersects that of n_{el}, the deformation curve does not continue along the dashed line corresponding to the elastic behaviour, but deviates, and, after having reached a peak point, osculates the curve of n_{ult}. This peak gives the plastic upper critical force or load ($n_{cr, pl}^{upper}$ or $p_{cr, pl}^{upper}$).

Plasticity changes the post-critical load bearing behaviour of shells, turning even their increasing characters into decreasing ones. This is shown in Fig. 9.4.5,

where we substituted, for simplicity, two sections of straight dashed lines for the load-deflection curve of the elastic shell. Figure 9.4.5 (a) corresponds to a comparatively high value of the elastic critical load. In this case the curves n_{el} and n_{ult} intersect that of the elastic deformation, resulting in a decreasing load bearing capacity in every case. On the other hand, Fig. 9.4.5 (b) shows an elastic critical load much lower than the central ultimate load n_{yield}. In that case a decreasing elastic load bearing capacity of a shell remains decreasing, while the behaviour of shell with increasing elastic load bearing capacity remains unchanged prior to buckling, but its post-critical load bearing capacity remains increasing only up to a certain level, after which it also becomes decreasing.

In a given case, the critical load of a shell is to be determined using the construction shown in Fig. 9.4.6. This can be performed, according to [9.4.2], in the following steps:

First, we draw the axes I and II. In point 1.0 of the axis II we erect a perpendicular axis III with the same scale as the axis I. We connect the point H_0 of the axis III (to be determined later) and the origin by a straight line IV. We draw the horizontal line V from the point $n_{cr,el}^{upper}/n_{cr}^{lin}$ of the axis I, intersecting the straight line IV at the point A. Here we construct a parabola with a vertical axis, starting with a horizontal tangent at A, intersecting the axis II at the point n_{pl}/n_{yield}. This parabola has to be intersected by a straight line VII connecting the origin with the point n_{yield}/n_{cr}^{lin} of the axis III. Projecting this point of intersection B onto the axis I, we obtain the sought value $n_{cr,pl}^{upper}/n_{cr}^{lin}$.
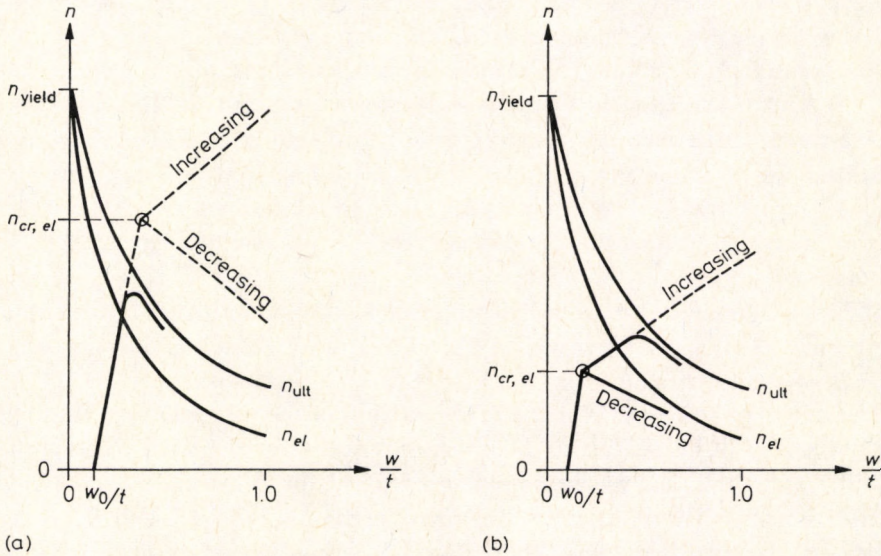
Fig. 9.4.5. Influence of plasticity on the post-critical behaviour of shells
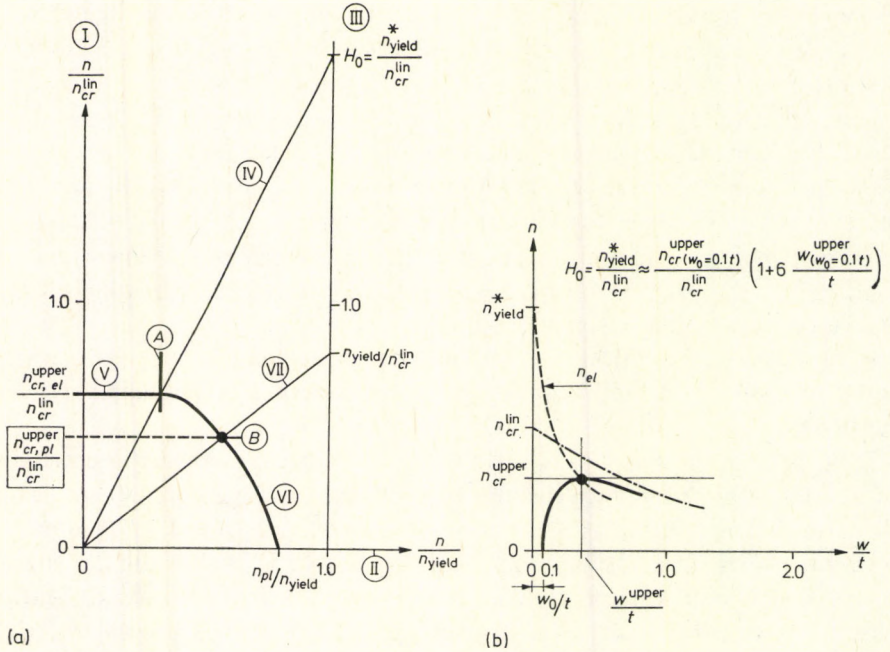
Fig. 9.4.6. (a) – Construction for the determination of the plastic critical load, (b) – definition of n_{yield}^{*} and determination of H_0

Here, $n_{cr,el}^{\text{upper}}$ and $n_{cr,pl}^{\text{upper}}$ denote the elastic and plastic upper critical loads respectively, while the other notations are to be found in Fig. 9.4.3.

The value H_0 to be plotted on the axis III is equal to the ratio $n_{\text{yield}}^{*}/n_{\text{lin}}^{cr}$, where n_{yield}^{*} is a fictitious central ("plastic") compressive force that has to be chosen in such a way that the curve n_{el} starting from n_{yield}^{*} should intersect the elastic load deflection curve of the shell pertaining to $w_0/t=0.1$ just at its peak point $n_{cr,el}^{\text{upper}}$ (Fig. 9.4.6 (b)). Namely, the curve n_{el} separates the elastic and the plastic ranges. The quantity n_{yield}^{*} thus belongs to a fictitious yield stress σ_y^{*}, independent of the actual yield stress σ_y of the material.

We may assume for the laterally compressed isotropic cylinder $H_0=4$, and for the axially compressed isotropic cylinder and the radially compressed sphere $H_0=2$, as good approximations.

The diagrams to be used for the determination of the plastic critical load were constructed in [9.4.2], assuming homogeneous shells for the axially compressed cylinder and the radially compressed sphere, and for the cylinder subjected to lateral pressure. These diagrams are reproduced in Figs 9.4.7 and 9.4.8. The plastic critical load is obtained by projecting the intersection point of the curve w_0/t and the straight line $n_{\text{yield}}/n_{cr}^{\text{lin}}$ onto the vertical axis.
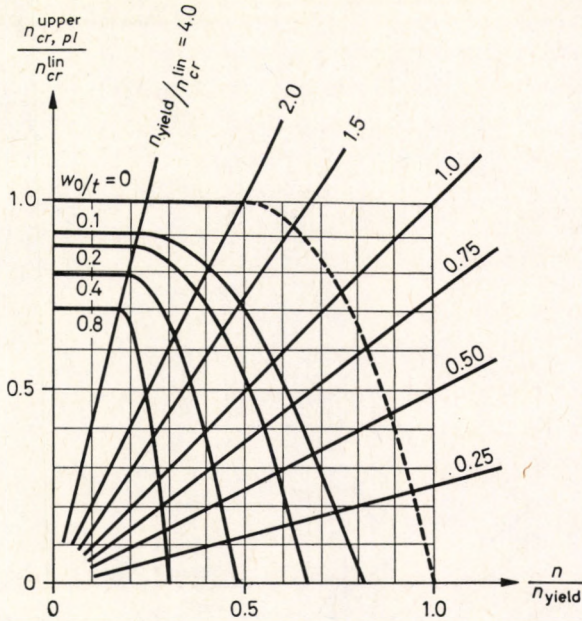
Fig. 9.4.7. Diagrams for the determination of the plastic critical load of long cylindrical shells compressed in the circumferential direction
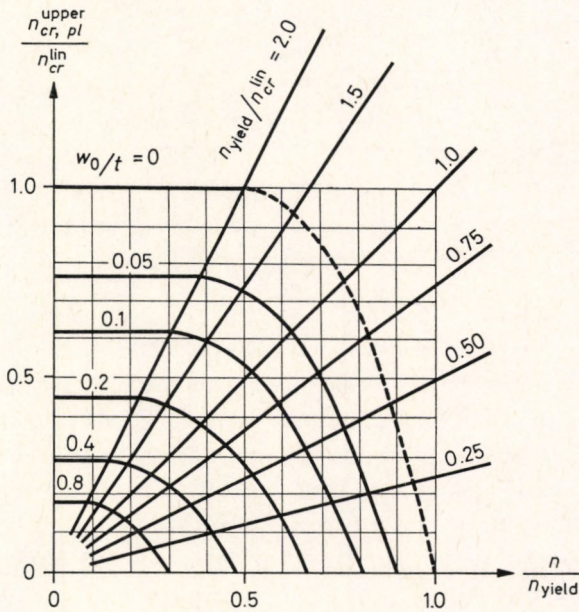
Fig. 9.4.8. Diagrams for the determination of the plastic critical loads of axially compressed cylindrical and radially compressed spherical shells

The perfectly elastic–plastic diagram of Fig. 9.4.2 may also be used in the cases of materials which have a curvilinear elastic stress–strain curve. This provides a good approximation in the case of any small eccentricity, but for central compression it results in a considerable error to the detriment of safety [9.4.7].

In [9.4.1] we proposed a more exact procedure for the determination of the critical force of centrally compressed structures. In order to avoid the error mentioned before, we constructed the dashed lines for the case of $w_0/t=0$ (central compression) in Figs 9.4.7, 9.4.8, 9.4.9 on the basis of [9.4.1].
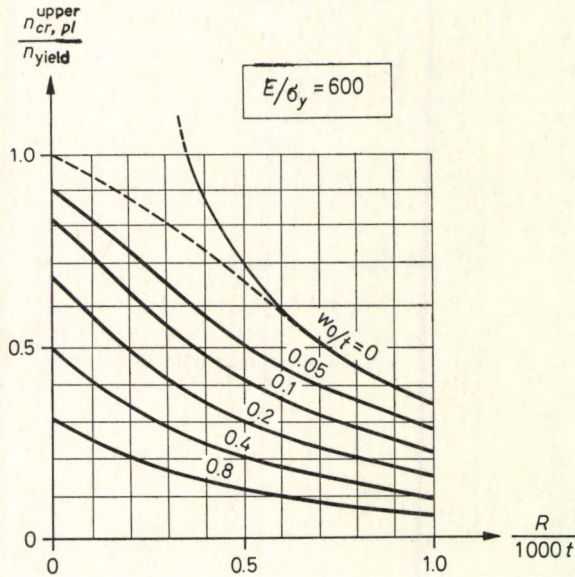
Fig. 9.4.9. Plastic critical forces of shells made of high-strength steel, pure aluminium or concrete as functions of R/t

If the structure is homogeneous, n_{pl} is the force which causes yielding, and then the structure is no longer able to carry any additional load. On the other hand, if the structure is not homogeneous but composite, the local buckling of one element (e.g. wrinkling of the faces of a sandwich shell, or buckling of the individual bars of a reticulated shell, etc.) also causes the structure to be no longer able to carry any additional load. Hence, in these cases, the value of n which causes local buckling should be considered n_{pl}, as mentioned in Chapter 8.

Assuming the ratio $E/\sigma_y=600$, approximately valid for structural steel with tensile and yield strengths of 500 and 350 N/mm² respectively, for mild (unalloyed) aluminium and also for usual concrete, we determined the plastic critical loads for shells and plotted them against the ratio R/t. We thus obtained the curves

of Fig. 9.4.9, similar to those of compressed bars plotted against their slenderness ratio.

As can be seen, the curves for shells lie lower than those valid for bars.

The plastic critical load can also be calculated in accordance with the graphical construction shown in Fig. 9.4.6. Of course, we have to assume $n_{\text{yield}}/n_{cr}^{\text{lin}} < H_0$, since otherwise elastic buckling would occur.

Introducing the abbreviations $\gamma = n_{\text{yield}}/n_{cr}^{\text{lin}}$ and $\alpha = n_{pl}/n_{\text{yield}}$, the calculation according to the graphical construction yields:

$$\frac{n_{cr,pl}^{\text{upper}}}{n_{cr,el}^{\text{upper}}} = \sqrt{\left[\frac{\gamma}{2\varrho_{\text{hom}}}\left(\alpha - \frac{\varrho_{\text{hom}}}{H_0}\right)^2 - \frac{\varrho_{\text{hom}}}{H_0}\right]^2 - \left[\left(\frac{\varrho_{\text{hom}}}{H_0}\right)^2 - \left(\alpha - \frac{\varrho_{\text{hom}}}{H_0}\right)^2\right]} -$$

$$- \left[\frac{\gamma}{2\varrho_{\text{hom}}}\left(\alpha - \frac{\varrho_{\text{hom}}}{H_0}\right)^2 - \frac{\varrho_{\text{hom}}}{H_0}\right]. \tag{9.4.1}$$

In the case of a homogeneous shell wall, α can be closely approximated up to $e_0/t \leq 1$ by the expression:

$$\alpha \approx \frac{1}{1 + 3\dfrac{e_0}{t}}.$$

Making use of this relation, we computed the values of ϱ_{pl} from Eq. (9.4.1) for $w_0/t = 0; 0.1; 1.0$, and plotted them against γ/H_0 in Figs 9.4.10 and 9.4.11 for the
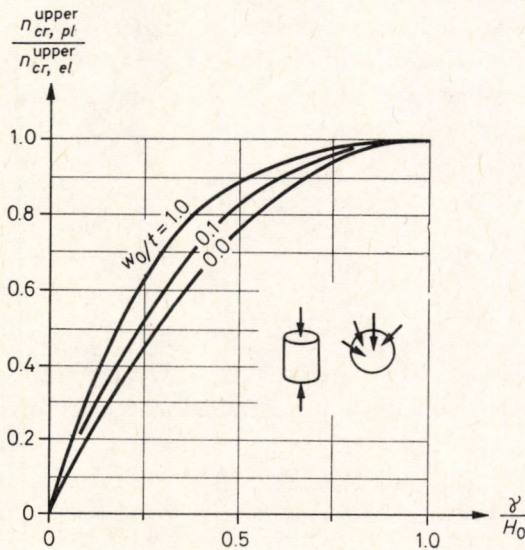
Fig. 9.4.10. The plastic critical loads of axially compressed cylindrical and of radially compressed spherical shells
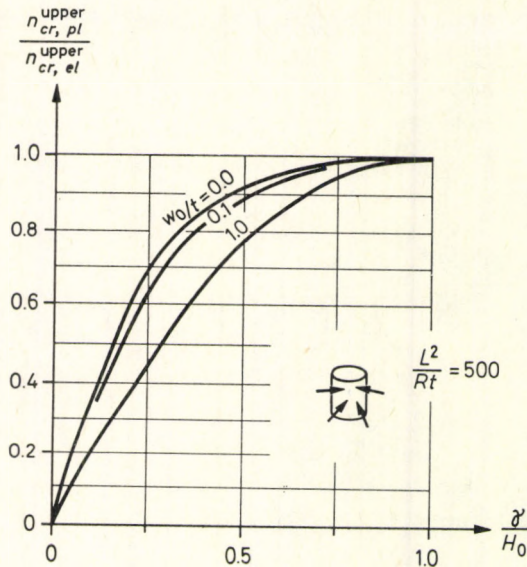
Fig. 9.4.11. The plastic critical load of the cylindrical shell under lateral pressure

axially compressed cylinder and the radially compressed sphere, and in addition for a cylinder of medium length under lateral pressure.

The reference [9.4.3] publishes simulated computer results performed on aluminium models. It contains all the data which are necessary to make a comparison with Eq. (9.4.1). For these shells, $\varrho_{hom} \approx 0.8$, and thus $w_0/t \approx 0.04$. We compared the results with the values computed for $w_0/t = 0$ and 0.05. The comparison is to be seen in Fig. 9.4.12.

All these diagrams can be approximated within an error limit of $\pm 10\%$ by the relation

$$\left(\frac{n_{cr,pl}^{upper}}{n_{cr,el}^{upper}}\right)^2 + \left(\frac{n_{cr,pl}^{upper}}{n_{pl}}\right)^2 = 1, \tag{9.4.2}$$

that may also be called the "quadratic Dunkerley formula". Transcribing the forces n into loads and expressing the plastic upper critical force from Eq. (9.4.2) we obtain

$$p_{cr,pl}^{upper} = \zeta p_{cr,el}^{upper} \tag{9.4.3}$$

with the factor

$$\zeta = \sqrt{\frac{1}{1 + \left(\frac{p_{cr,el}^{upper}}{p_{pl}}\right)^2}}. \tag{9.4.4}$$
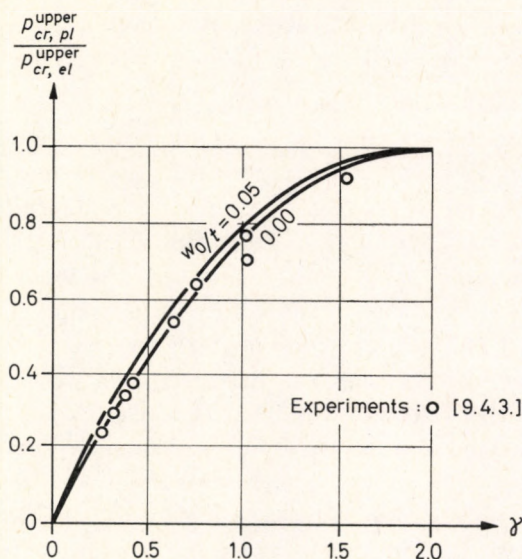
Fig. 9.4.12. Comparison of experimental critical loads of plastic
aluminium dome models with computed values

According to [9.4.2] we certainly commit an error to the benefit of safety if,
instead of (9.4.2), we use the semi-quadratic Dunkerley formula

$$\frac{n_{cr,\,pl}^{upper}}{n_{cr,\,el}^{upper}} + \left(\frac{n_{cr,\,pl}^{upper}}{n_{pl}}\right)^2 = 1. \tag{9.4.5}$$

Transcribing Eq. (9.4.5) into loads, and again using Eq. (9.4.3), ζ assumes the
following form:

$$\zeta = \frac{p_{pl}}{p_{cr,\,el}^{upper}} \sqrt{\frac{1}{4}\left(\frac{p_{pl}}{p_{cr,\,el}^{upper}}\right)^2 + 1} - \frac{1}{2}\left(\frac{p_{pl}}{p_{cr,\,el}^{upper}}\right)^2. \tag{9.4.6}$$

In practice, Eq. (9.4.4) can be advantageously used in evaluating experimental
results, and Eq. (9.4.6) is suitable for design.

The plastic behaviour probably caused a reduction in p_{cr}^{upper} in some model tests
reported on in the literature (Fig. 2.3 (a), (b), (c), Fig. 4.2), mainly in the range
of smaller R/t ratios. However, it would be rather difficult to assess this effect
subsequently, because there were not sufficient measured data.

For the idealized elastic–plastic diagram (Fig. 9.4.2), the deformation moduli
of the various materials are to be chosen differently. We treat this problem in
detail in the following sections.

9.5. Influence of Creep

Most materials used in shell structures develop, under certain conditions, deformations, that depend not only on the acting stresses but also on the time. Accordingly, the initial elastic deformation increases in time even if the stress applied remains constant. In the case of stresses increasing with time this increase of deformation becomes even more marked. This time-dependent deformation is called creep. Its influence on the stability of shells is unfavourable, since the increased deformation, as a rule, reduces the critical load.

The first research on creep can be probably attributed to Vicat [9.5.20]. Since then the theory of viscoelasticity has developed. An excellent survey of this field is given in Flügge's book [9.5.7]. Many viscoelastic models were proposed, but the pertaining material constants are only incompletely established.

The main features of the influence of creep on stability phenomena can be studied on very simple viscoelastic models, so that in the following these will be presented first. Then, the influence of creep on buckling will be analysed on a simple structural model, using various viscoelastic models. Finally, we show a practical method by which we can approximately consider the influence of creep in a very simple way.

9.5.1. The Basic Viscoelastic Models

The viscoelastic models are built up of two elements: the spring and the dashpot. Figure 9.5.1 (a) shows the *linear spring,* whose specific elongation ε is obtained by dividing the acting stress σ by the spring constant E:

$$\varepsilon_{\text{spring}} = \frac{\sigma}{E}.$$
(9.5.1)

The second element, the *dashpot* is to be seen in Fig. 9.5.1 (b). Its elongation ε is to be determined from the relation

$$\frac{d\varepsilon_{\text{dashp}}}{dt} = \frac{\sigma}{\eta},$$
(9.5.2)

where $d\varepsilon/dt$ is the creep rate and η is the viscosity coefficient. Connecting a spring and a dashpot in series, we obtain the Maxwell model (Fig. 9.5.2). It is also called *Maxwell fluid* since its deformation due to a constant stress tends to infinity for $t \to \infty$. The differential equation of its deformation can be built up from
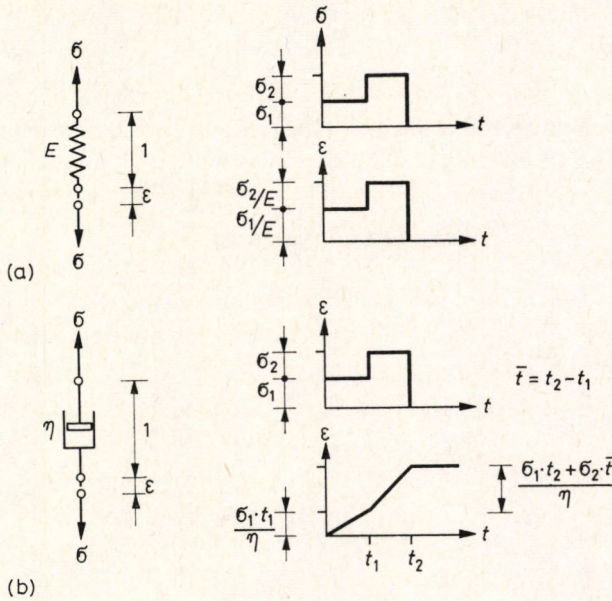
Fig. 9.5.1. Basic elements of the viscoelastic models:
(a) Spring, (b) dashpot
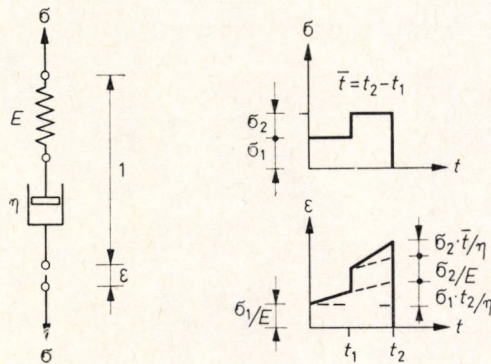
Fig. 9.5.2. The linear Maxwell fluid

Eqs (9.5.1) and (9.5.2):

$$\frac{d\varepsilon_{M}}{dt} = \frac{d\varepsilon_{spring}}{dt} + \frac{d\varepsilon_{dashp}}{dt} = \frac{1}{E}\frac{d\sigma}{dt} + \frac{\sigma}{\eta}. \qquad (9.5.3)$$

For some materials which also exhibit plastic behaviour, a better agreement can be obtained if the Maxwell model is completed by a nonlinear term. Thus, we

arrive at the equation

$$\frac{d\varepsilon}{dt} = \frac{1}{E}\frac{d\sigma}{dt} + \frac{\sigma}{\eta} + A\sigma^n, \tag{9.5.4}$$

where A and n are material constants. The last term on the right-hand side is called Odquist's [9.5.19], Norton's [9.5.17] or Bailey's [9.5.1] law.

Connecting a spring and a dashpot in parallel, we obtain the Kelvin (–Voigt) model (Fig. 9.5.3), also called *Kelvin solid,* since its deformation due to a constant stress tends to a finite value for $t \to \infty$. Since the elongation of the spring has to be equal to that of the dashpot, and also the sum of the stresses of both elements have to counterbalance the acting stress, the differential equation of the Kelvin model becomes:

$$\sigma = E\varepsilon + \eta\frac{d\varepsilon}{dt}. \tag{9.5.5}$$

Completing the Kelvin model by a spring, we arrive at the so-called *standard linear three-parameter solid* shown in Fig. 9.5.4, with the differential equation:

$$\left(\frac{1}{E_1} + \frac{1}{E_2}\right)\sigma = \varepsilon + \frac{\eta_2}{E_2}\frac{d\varepsilon}{dt}. \tag{9.5.6}$$

To describe qualitatively the behaviour of real materials, we can make advantageous use of the *Burger model,* which consists of a Maxwell and a Kelvin model, connected in series (Fig. 9.5.5). It contains all the properties of the models dealt with hitherto, and has the differential equation:

$$\sigma + \left(\frac{\eta_1}{E_1} + \frac{\eta_1+\eta_2}{E_2}\right)\frac{d\sigma}{dt} + \frac{\eta_1\eta_2}{E_1 E_2}\frac{d^2\sigma}{dt^2} = \eta_1\frac{d\varepsilon}{dt} +$$

$$+ \frac{\eta_1\eta_2}{E_2}\frac{d^2\varepsilon}{dt^2}. \tag{9.5.7}$$
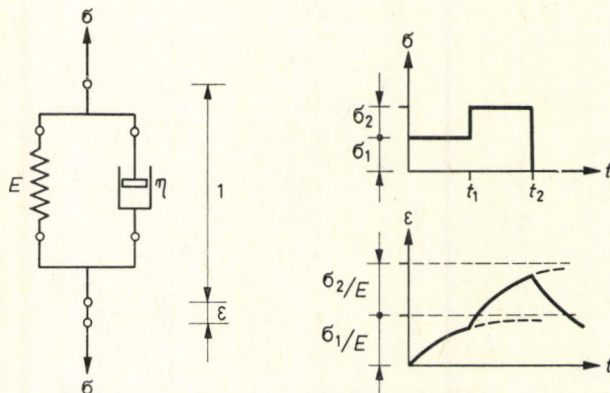
Fig. 9.5.3. The Kelvin solid
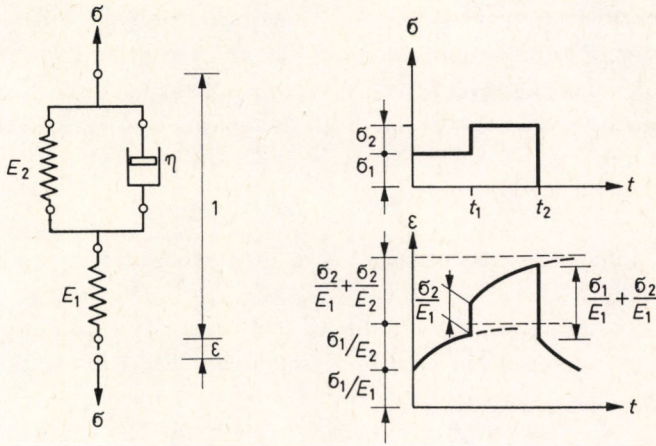
Fig. 9.5.4. The standard linear three-parameter solid
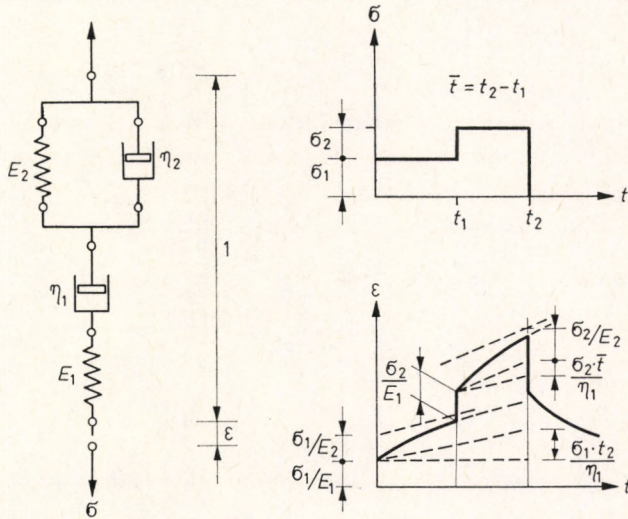
Fig. 9.5.5. The four-parameter Burger model

Integrating Eq. (9.5.7) between $t=0$ and $t=t$ for $\sigma=\sigma_1=$const., we obtain the following expression for the elongation:

$$\varepsilon = \frac{\sigma_1}{E_1} + \frac{\sigma_1}{\eta_1} t + \frac{\sigma_1}{E_2} \left(1 - e^{-\frac{E_2}{\eta_2} t}\right). \tag{9.5.8}$$

Setting the suitable parameters in the Burger model equal to infinity, we can obtain anyone of the models dealt with hitherto.

The Burger model is suitable for describing qualitatively the behaviour of every material, but may be quantitatively inaccurate in some cases. Its accuracy can be improved by connecting several Kelvin models either in series or in parallel. By so doing, the model will be more and more complicated, so we shall omit detailed treatment of it.

9.5.2. Influence of the Various Viscoelastic Models on the Stability

The influence of creep on the stability of structures with constant post-buckling load bearing capacity was analysed by Kempner [9.5.15]. His results, extended to various cases of post-buckling behaviour, can be shown visually on the structural model of Fig. 9.5.6, where a viscoelastic support hinders the bar from tilting under the force F [9.5.3a].
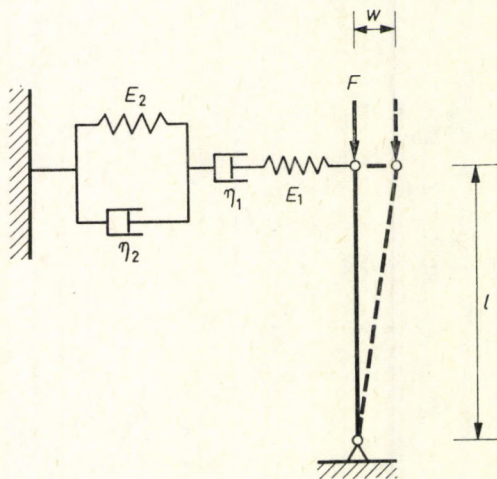
Fig. 9.5.6. A simple structural model for demonstrating the effect of creep

Setting $\eta_1=\eta_2=E_2=\infty$, the system becomes elastic with an Euler-type critical load:

$$F_E = E_1 l.$$

In the case of $F > F_E$, the system is unstable and buckles instantaneously according to the dashed line marked by 1 in Fig. 9.5.7 (a).

If the structure has an initial imperfection w_0, then the deformation follows the path denoted by 2 in Fig. 9.5.7 (a), approaching line 1 asymptotically.

Let us modify the previously described elastic model (that of Fig. 9.5.6 with $\eta_1=\eta_2=E_2=\infty$) by making the spring characteristic E_1 decrease with increasing
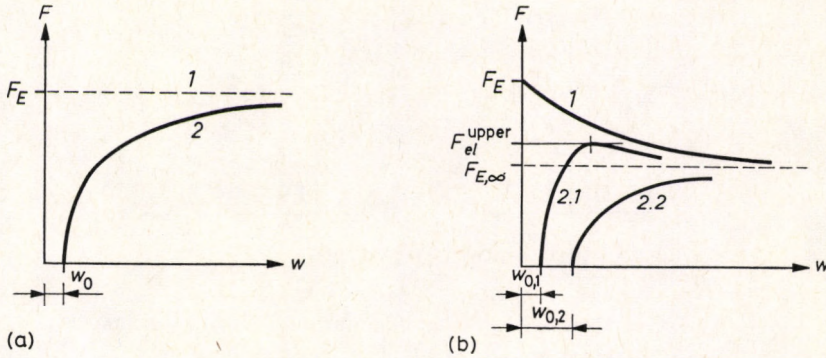
Fig. 9.5.7. (a) Buckling behaviour of the elastic structure with constant post-buckling load bearing capacity, (b) buckling behaviour of the elastic structure with decreasing post-buckling load bearing capacity

deflection q, i.e. let $E_1=E_1(w)$. Let us stipulate further that $E_1(w)$ approaches a finite nonzero value $E_{1,\infty}$ for $w\to\infty$. This modified model is then able to describe the behaviour of structures with descreasing post-buckling load-bearing capacity such as axially compressed cylinders and radially compressed spheres, but also other shells made of plastic materials and even of reinforced concrete, the rigidity of which is reduced by the cracks developing during deformation. If this model is loaded up to a load intensity F_E, the load bearing capacity decreases to the value $F_{E,\infty}=E_{1,\infty}l$. This phenomenon is plotted as Curve *1* in Fig. 9.5.7 (b). (In the case of shells, the value $F_{E,\infty}$ corresponds to the lower critical load.)

If there is an initial imperfection w_0 present, this structure may behave in two different ways. If w_0 exceeds a certain limit value, the deformation increases with steadily increasing load, following the Curve *2.2* which osculates the horizontal line of $F_{E,\infty}$. The behaviour is similar to that described by the Curve *2* in Fig. 9.5.7 (a). On the other hand, if w_0 is smaller than the above-mentione limit value, then the load bearing capacity exceeds $F_{E,\infty}$, and it increases to a certain extent until, after reaching a maximum value F_{el}^{upper}, the structure snaps through and follow with decreasing load bearing capacity the Path *2.1* of Fig. 9.5.7 (b) osculating the horizontal line of $F_{E,\infty}$. As we shall see later, the influence of creep is different in the cases of the two types of deformation Paths *2.1* and *2.2*.

Returning to the linearly elastic spring *1* we now choose a Maxwell fluid as supporting element, i.e. set $\eta_2=E_2=\infty$. The system is loaded by a force F with initial eccentricity w_0. The bar performs displacements increasing with time (see Fig. 9.5.8 (a)). As we see from Fig. 9.5.8 (b), the force-displacement path, valid at any fixed value of t, approaches asymptotically the line of the elastic critical force F_E.

15 Buckling of Shells
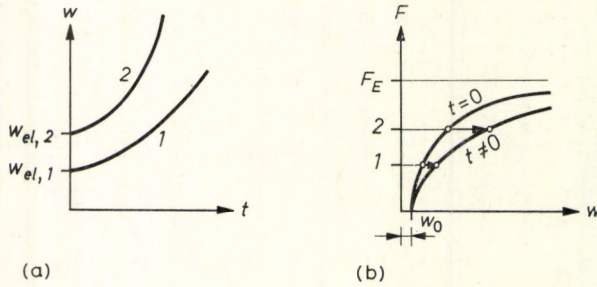
Fig. 9.5.8. Creep buckling behaviour of a Maxwell-fluid-type structure (a) as a function of time, (b) as a function of the deformation w.
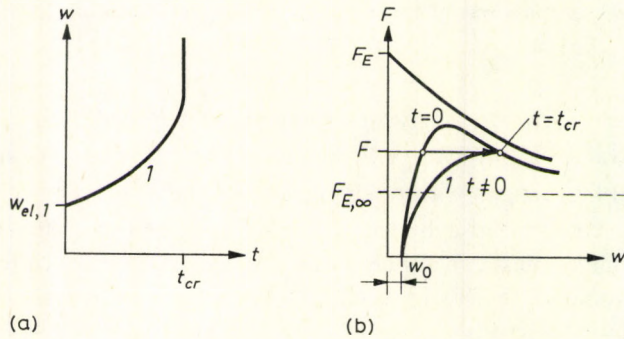
Fig. 9.5.9. Creep buckling behaviour of a Maxwell-fluid-type structure with a spring characteristic decreasing with deformation (a) as a function of time, (b) as a function of the deformation w.

This means that the critical load remains the same as the elastic one F_E valid for instantaneous loading, which was not reduced by the creep. On the other hand, the deformation w is increased by the creep. When the structure is unloaded, it does not return to its initial position w_0, but to a larger value. However, if $t \to \infty$, then the deformation w tends, at any small but finite value of F, to infinity.

Looking back upon the elastic case with a spring characteristic $E_1(w)$ which decreases with increasing w, it can be seen that the structure treated in the foregoing behaves according to the Curve *2.2* of Fig. 9.5.7 (b), i.e. its critical load is equal to $F_{E, \infty}$. Hence, in this case the creep of the Maxwell model increases the deformation of the structure, but leaves its critical load unchanged, see Fig. 9.5.8 (b). If the initial imperfection is smaller than the limit eccentricity, and the applied load exceeds $F_{E, \infty}$, then the elastic deformation develops according to the Curve *2.1* of Fig. 9.5.7. In this case the creep may increase the deformation after a certain time to such an extent that the structure arrives at the descending branch of the

curve (Fig. 9.5.9), becomes unstable and undergoes an infinitely large deformation. The corresponding time is called the critical time (t_{cr}). It can also be seen that a shorter critical time corresponds to a higher load.

Investigations made on the nonlinear Norton model (9.5.4) show that infinitely large deformations occur during a finite critical time in any of the hitherto treated cases. However, the nonlinear creep law is mostly needed only in the stress range close to the yield point, while in the case of lower stresses — as usual in the stability investigations of shells — the linear creep law yields, as a rule, a sufficient accuracy. Hence, we will no longer deal with the nonlinear creep law.

The aforementioned infinitely large deformation can be regarded in two different ways as a limit. Either we consider the critical time pertaining to a given load, or we seek the critical load which, at the end of the given period, causes an infinitely large deformation.

Let our next model be supported laterally by a standard linear three-parameter solid. First, we suppose $F \geqq F_E = E_1 l$. The bar obviously tilts at once.

We now form the resultant characteristic of both springs:

$\bar{E} = \dfrac{E_1 E_2}{E_1 + E_2}$. If we apply the force $\bar{F}_E = \bar{E}l$, the bar would just tilt abruptly if

no dashpot were present. The dashpot hinders the buckling, but the displacement w increases at a constant rate without bond. If $F < \bar{F}_E$, the displacement w approaches a finite limit value asymptotically. Finally, $F > \bar{F}_E$ causes the displacement to increase at an increasing rate. All this is shown in Fig. 9.5.10.
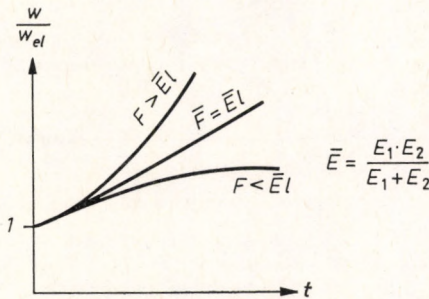
Fig. 9.5.10. Creep buckling behaviour of a standard
linear three-parameter-solid-type structure as a function of time

If we characterize the creep with the ratio of the full (elastic + creep) final displacement w_∞ to the elastic displacement w_{el}, i.e. with the final value of the creep factor $\varphi_\infty = w_\infty / w_{el}$, we may express $\bar{F}_E$ with the aid of $\varphi_\infty = E_1 / E_2$ as follows:

$$\bar{F}_E = \frac{F_E}{1 + \varphi_\infty}.$$

We can also formulate the phenomenon this way: in the case of instantaeouso loading ($t=0$) the load-deflection curve approaches F_E, while for long-termn lading ($t=\infty$) it osculates $\bar{F}_E = F_E/(1+\varphi_\infty)$, see Fig. 9.5.11.
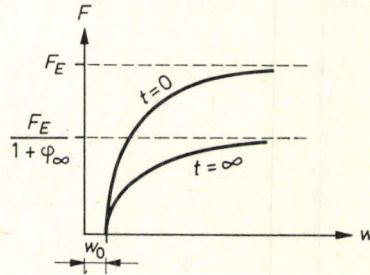
Fig. 9.5.11. Buckling behaviour of a three-parameter-solid-type structure (with constant post- buckling load-bearing capacity) as a function of the deformation w
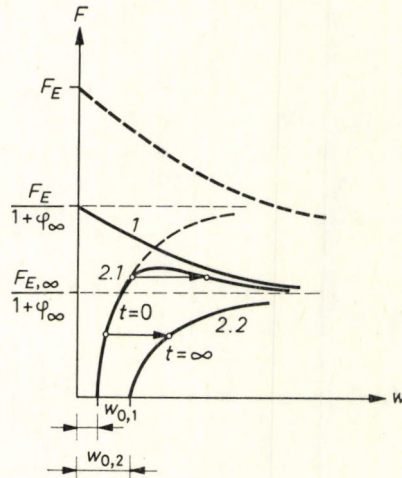
Fig. 9.5.12. Creep buckling behaviour of a structure with decreasing post-buckling load bearing capacity as a function of the deformation w

Let us investigate the same system with a spring characteristic $E_1(w)$ decreasing with increasing w, i.e. a structure with decreasing post-buckling behaviour. Its load-deflection curve is similar to the Curve *1* in Fig. 9.5.7, but starts from $F_E/(1+\varphi_\infty)$, instead of F_E. The curve of the imperfect structure *2.1*, which corresponds to that marked with $t=0$ in Fig. 9.5.11, osculates this Curve *1*. It deviates from the original, dashed curve (Fig. 9.5.12) valid for constant post-buckling load bearing capacity, and, after reaching a maximum, approaches the Curve *1*. The Curve

2.2, which corresponds to $t=\infty$, osculate the straight line $F_E/(1+\varphi_\infty)$ from underneath again, without reaching a maximum point.

We still have to mention briefly the case of an $E_1(w)$ which increases with increasing w, corresponding to the structures with increasing post-buckling load bearing capacity. The pertaining load-deflection curves have a monotonically ascending character, without maximum points. In Figs 9.5.13 (a) and (b) we show the curves valid for the Maxwell fluid type and for the three-parameter solid type support, respectively.

In the literature, numerous solutions are to be found for various cases of instability and post-buckling behaviour, considering creep laws more complicated than treated here. We do not intend to present them in detail but, for orientation, we list some of them as the following references: [9.5.2], [9.5.3], [9.5.4], [9.5.5], [9.5.6], [9.5.8], [9.5.9], [9.5.10], [9.5.12], [9.5.13], [9.5.14], [9.5.18].

(a)   (b)
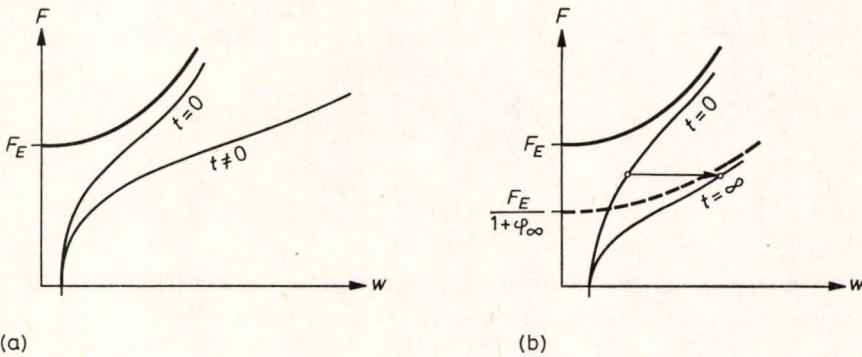
Fig. 9.5.13. Creep buckling behaviour in the case of an increasing post-buckling load bearing capacity as a function of the deformation w.
(a) of a Maxwell-fluid-like structure (b) of a threeparameter-solid-like structure

9.5.3. Practical Consideration of the Effect of Creep

As was mentioned in the previous section, we may either speak about a critical time pertaining to a given load, or about a critical load corresponding to a given time. In the literature, the effect of creep is mostly taken into consideration with the critical time t_{cr}. This can be explained by the fact that it is easier to express the critical time than the critical load from the formulas.

It was shown in the previous section that structures with certain kinds of creep have no critical time, while every structure has a critical load. Consequently, in the following we shall take the effect of creep into consideration by means of a critical load pertaining to a given creep period.

Our task is easier in the case of materials which behave according to the standard three-parameter solid (concrete, wood), since their creep tends to a finite final value. For design, it is sufficient to know the final value $\varphi_\infty = E_1/E_2$ of the creep factor $\varphi(t)$, pertaining to $t = \infty$. By dividing the modulus of elasticity by $(1 + \varphi_\infty)$, we consider every deformation as being increased to $(1 + \varphi_\infty)$ times its value and the load-deformation curves assume the shapes shown in Figs 9.5.11 and 9.5.12. The critical loads obtained this way will be, as a rule, slightly lower than the real ones, since the stress increments which develop in the final phase of the deformation prior to buckling have less time to induce creep than the stress parts which developed earlier. Theoretical computations [9.5.11], [9.5.16] as well as experiments on concrete dome models [9.8.15] fully confirmed the validity of the approximate calculation mentioned above, which consists of dividing the modulus of elasticity by $(1 + \varphi_\infty)$. Hence, in the case of structures which behave like the *standard linear three-parameter solid* with an increasing, constant or decreasing post-buckling load bearing capacity, the influence of creep can be allowed for by reducing the modulus of elasticity:

$$E = \frac{E_0'}{1 + \varphi_\infty}, \qquad (9.5.9)$$

where $E_0 = E_1$ is the initial modulus of elasticity measured under short-time loading (e.g. vibration).

If the planned lifetime of the structure is limited, we can take the value φ_l corresponding to the expected lifetime t_l of the structure, and reduce the modulus of elasticity accordingly:

$$E_1 = \frac{E_0}{1 + \varphi_l}. \qquad (9.5.10)$$

Structures whose creep response can be described by the *Maxwell fluid* (synthetics, ice) may behave in two different ways.

If the post-critical load bearing capacity of the elastic structure is constant or increasing, no creep stability analysis can be performed, since to infinite time infinite deformation corresponds under the action of any small but finite load. Consequently, the stability of such structures should be checked with E_0, as that of an elastic, geometrically perfect strcuture, but, in addition, a stress analysis should also be carried out for the increased deformation $w_{el}(1 + \varphi_l)$ corresponding to the expected lifetime t_l. On the other hand, if the post-critical load-bearing capacity of the structure decreases, i.e. the modulus of elasticity decreases with increasing deformation (see Fig. 9.5.7), then, as in the previous case, a stress analysis has to be performed for forces lower than $F_{E, \infty}$ (which corresponds to the p_{cr}^{lower} of shells), taking the deformation $w = w_{el}(1 + \varphi_l)$ into account. In both

cases w_{el} also contains the deformation increment caused by the compressive force acting on the structure with initial imperfection.

If the load is greater than the lower critical load $F_{E,\infty}$ of the structure, but is inferior to the linear critical load, then a more exact stability analysis is to be performed, applying a suitable creep buckling theory to be found in the literature. The phenomenon can be approximately analyzed by using the reduced modulus of elasticity according to Eq. (9.5.10) for the calculation of the upper critical load F_{el}^{upper} (see Fig. 9.5.7 (b)), but in this case we do not need to consider a critical load inferior to the lower critical load $F_{E,\infty}$. Hence, the approximate stability criteria for the Maxwell fluid type structures:

$$F_{cr} \approx \frac{F_{el}^{upper}}{1+\varphi_l},\tag{9.5.11}$$

but in any case:

$$F_{cr} \gtreqless F_{E,\infty}.\tag{9.5.12}$$

Finally, it should be remarked that all that has been said about creep in the foregoing is based on the uniaxial stress state. In shell structures, bi- (or tri-) axial stress states prevail, that are much more complicated. However, for the qualitative assessment of the behaviour of shell structures, the knowledge of the creep laws valid for the uniaxial stress state is sufficient.

9.6. Problems of Metal Shells

As outlined in Section 9.4, in order to assess the influence of plastic behaviour we assume the material to be perfectly elastic–plastic (see Fig. 9.4.2). We have now to investigate how this perfectly elastic–plastic model has to be chosen for real materials used in metal shell construction.

Metal shells are mostly built of steel or aluminium. Hence we deal with these two materials only.

9.6.1. Moduli of Deformation of Metals

Modulus of deformation of steel. Steels with a yield plateau have a stress–strain diagram according to Fig. 9.6.1, becoming curved beyond the propertionality limit σ_{prop} and osculating the horizontal yield plateau. This curved section is comparatively short, so that we may assume the modulus of deformation E (i.e. the modulus of elasticity of the perfectly elastic–plastic material model) to be equal to the initial modulus of elasticity of steel: $E_0 = 200 \text{ kN/mm}^2$ (Fig. 9.6.1).
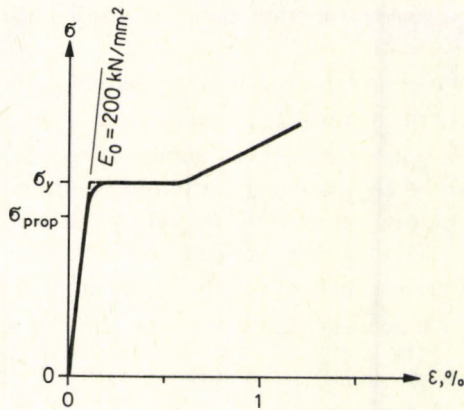
Fig. 9.6.1. Idealized stress–strain diagram of steel
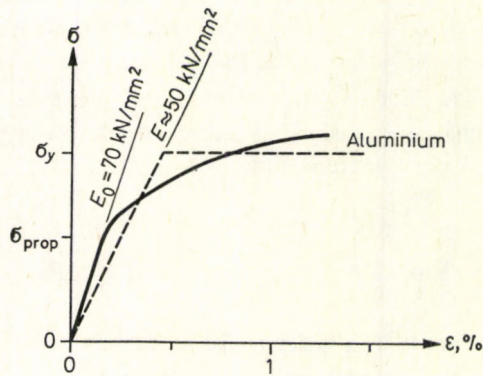
Fig. 9.6.2. Idealized stress–strain diagram of aluminium

For steels with no definite yield plateau, the perfectly elastic–plastic material model may be applied safely, provided that an appropriate value is chosen for σ_y, as is shown in Fig. 9.6.2 for aluminium.

Modulus of deformation of aluminium. The proportionality limit, σ_{prop}, for aluminium is lower as related to σ_y than for steel. The stress–strain diagram becomes curved and shows no definite yield plateau (Fig. 9.6.2). Nevertheless, it can be approximated by a "compensating" perfectly elastic–plastic material model, provided we chose the modulus of deformation appropriately. Thus we obtain for the modulus of deformation of the perfectly elastic–plastic aluminium model $E \approx 50 \text{ kN/mm}^2$, i.e. 0.7 times of the actual initial modulus of elasticity $E_0 = 70 \text{ kN/mm}^2$ (see Fig. 9.6.2).

9.6.2. Creep of Metals

Metals are prone to creep above a certain temperature. The curve characterizing creep deformation consists of three sections shown in Fig. 9.6.3. The behaviour in Section II can be approximated by the Maxwell fluid, while for Section III we may use Norton's law. If we replace Section I by the straight backward continua-
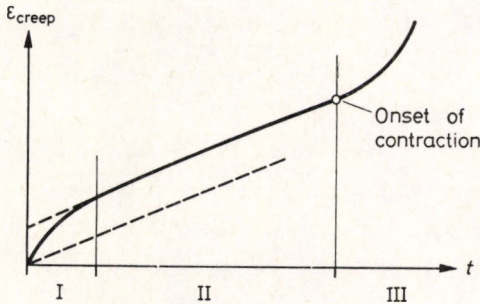
Fig. 9.6.3. Characteristic curve of the creep of steel at high temperatures

tion of Section II (dashed line), we may use the Maxwell fluid as a model throughout Section I and II. Its creep rate $d\varepsilon_{creep}/dt$ is constant, so that the creep factor $\varphi(t)$ can be computed from the relation:

$$\varphi(t) = \frac{t}{\varepsilon_{el}} \frac{d\varepsilon_{creep}}{dt}. \tag{9.6.1}$$

For information, we show in Figs 9.6.4 and 9.6.5 some diagrams representing the creep rates of a steel containing 0.15% carbon and of a chrome–nickel–steel
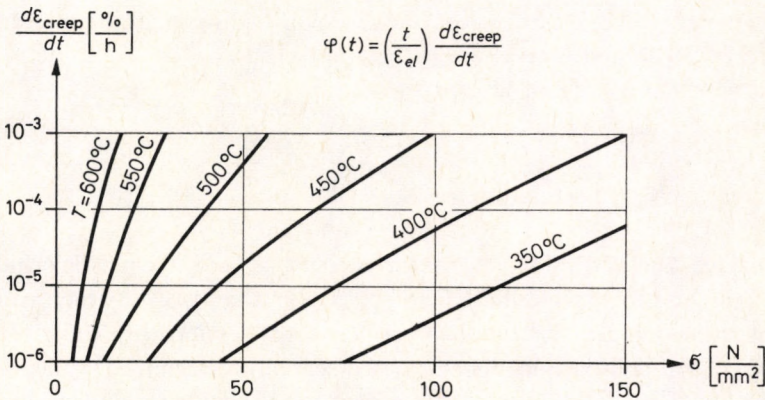
Fig. 9.6.4. Creep rate of steel containing 0.15% C
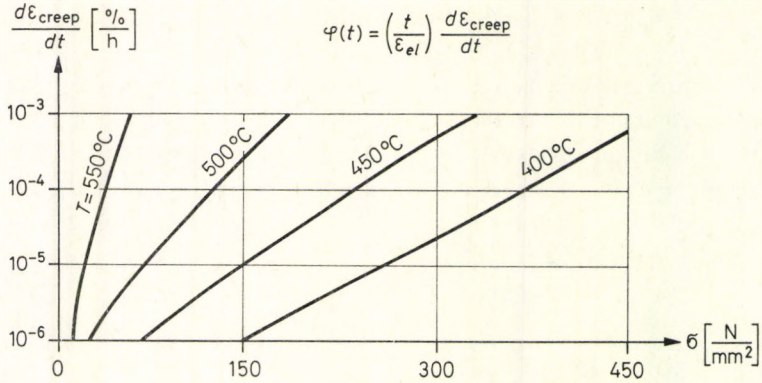
Fig. 9.6.5. Creep rate of a Cr—Ni steel
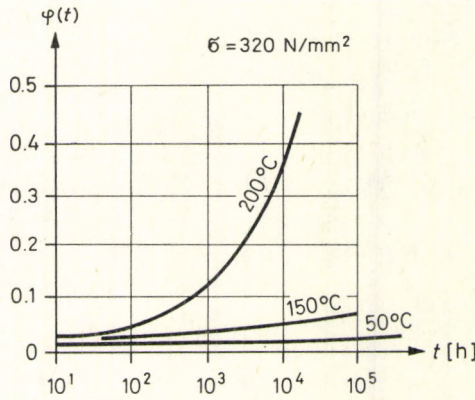
Fig. 9.6.6. Creep factor of a high-strength aluminium alloy

respectively. In Fig. 9.6.6 the creep factors of a high-strength aluminium alloy subjected to 320 N/mm² stress are to be seen, plotted against the duratoin t of the load which is measured in hours (h).

9.6.3. Dimensions of Metal Shells

As we have seen in Section 9.4, for the determination of the plastic critical load we need the elastic upper critical load $p_{cr, el}^{upper}$, and the load p_{pl} which causes the entire plastification and failure of the critical cross section with the given initial eccentricity. The elastic buckling load is essentially determined by the average cross sectional dimensions, so that we may take the design dimensions, to be considered as average ones, into consideration when computing $p_{cr, el}^{upper}$. On the

other hand, plastic failure may occur in one cross section only, so that for p_{pl} we have to take deviations in the dimensions of the individual cross sections into account. Consequently, when determining p_{pl}, we have to consider the dimensions reduced by the allowable tolerances.

9.6.4 Influence of Residual Stresses

Welding and straightening cause residual stresses in metal structures, due to which some parts of the cross sections become plastic at a lower load intensity than other parts. Experiments made on bars of welded I sections showed that the critical load of bars of medium slenderness is about 10–20% lower than that of rolled bars of the same cross sections. However, no such reduction could be observed on very slender bars, where buckling comes about without plastic deformation.

Applying these results to shells we find that reduction of the critical load due to residual stresses is to be expected in the range $R/t < 400$. In practice we can take this reduction into condiseration by computing the "plastic" critical load from the semi-quadratic Dunkerley formulas (9.4.5.) or (9.4.6), rather than from expression (9.4.1) or its approximate version (9.4.4). That is, the semi-quadratic Dunkerley formula deviates to the benefit of safety over about the same range and by about the same amount as the residual stresses reduce the critical load, and thus in practice it makes proper allowance for this effect.

9.7. Problems of Shells Made of Synthetics and of Timber

Homogeneous shells are built, besides of metals, either of synthetics or of timber. In this section we briefly deal with their specific problems.

9.7.1. Shells Made of Synthetics

Shell structures of synthetics have been built only in the last two decades, so that the relevant literature is much scarcer than that dealing with traditional materials. On the other hand, there are already many kinds of synthetics nowadays with considerably different characteristics. Consequently, it is not possible to give general recommendations. Thus, we shall only give a short informative description, based mainly on the work of Hintersdorf [9.7.4].

Synthetics can be divided into two main groups: thermoplastic and thermo-setting ones. If great mechanical strength is required, some suitable synthetics are reinforced by (glass or graphite) fibres.

In the following we present some data on the mechanical properties and their dependence on various factors. These data are to be regarded as rough informa-tion only, since they exhibit a considerable scatter even for the same material, and they differ even more for the various kinds of synthetics.

The moduli of elasticity of synthetics are considerably lower than those of metals. The ratio of the modulus of elasticity to the yield stress, E_0/σ_y, is about 30–50 in the case of thermosetting synthetics, and in the case of thermoplastics about 10–30, rather than 500–700 which is characteristic of metals. Hence, the stability analysis of structures made of synthetics is of primary importance. In addition, the modulus of elasticity of thermoplastic synthetics depends on the temperature too: at 40°C or 60°C it is only about one half or one fourth of that valid for 20°C.

The stress–strain diagrams of synthetics are, as a rule, straight over a long range, becoming slightly curved only at their end. Therefore synthetics can be considered as elastic materials. Only some special synthetics (e.g. cellulose acetate, synthetic foams) have notable plastic deformations.

Synthetics show a marked propensity to creep. The creep factor (i.e. the ratio of creep deformation to elastic deformation) referred to a ten-year period has the value of approximately one, but the creep deformation does not approach a finite value asymptotically. Consequently, for the creep model of synthetics the Burger model can be used (see Fig. 9.5.5). Besides, the creep factor of thermoplastic synthetics increases with increasing temperature: at 40°C it is about twice as great as at 20°C.

Long lasting loadings have an unfavourable effect on the strength of synthetics. Loading of one year's duration diminishes the strength of thermosetting synthetics by about 10%, and that of thermoplastic materials by about 50%.

The strength of thermoplastic synthetics is also diminished by heat. This decrease is approximately 1% for each degree centigrade of temperature over 20°C.

All these properties and uncertainties indicate the desirability of designing only shell structures of minor importance (i.e. whose failure does not cause any great damage) on the basis of the data on synthetics to be found in the literature; but even then it is advisable to use a higher safety factor than usual. For the design of structures of greater significance the material properties should be determined by experiments. The shorter duration of synthetics to be expected, as compared to conventional materials, should also be taken into consideration.

Theoretical and experimental investigations concerning the stability of cylindri-cal shells made of synthetics [9.7.6] showed that the imperfection sensitivity of

axially compressed cylinders made of fibre-reinforced synthetics corresponds to the theoretical value, but the experimental critical loads are $10\sim20\%$ lower than the computed ones. We may attribute this discrepancy to the fact that these computations neglected the small effect of plasticity and creep.

9.7.2. Shells Made of Timber

We give here some information about fir-(pine-)wood, which is the timber material most widely used for shell structures. Since the properties of wood scatter very much, the data presented here have to be considered only as rough infomation.

The properties of wood vary very greatly with its moisture-content u up to $u=30\%$, while over $u=30\%$ they are no longer influenced. The data to be given refer to $u=30\%$.

The compressive and tensile strengths of fir-wood are, parallel to its fibres, $20\sim30$ N/mm² and $40\sim50$ N/mm² respectively. The reduction of the moisture-content to 15% and to zero results in an increase in strength of about double and three or four times respectively.

The given strength values are valid only for short-term loading. A loading that lasts longer (for about one month) reduces the strength of wood by about 60% [9.7.3], see Fig. 9.7.1, where time is measured in hours (h).

The modulus of elasticity of fir-wood with $u=30\%$, parallel to its fibres, has the value of about $E_0=10$ N/mm². Reducing the moisture-content to 15% and zero results in an increase of E_0 of about 25% and 50% respectively.

The progress of creep in time depends on the moisture-content and on the ratio of actual stress to ultimate strength (σ_{ult}) of the wood. Some information is
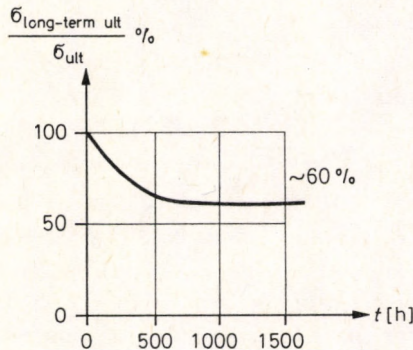
Fig. 9.7.1. Characteristic curve of
the long-term ultimate strength of fir-(pine-)wood

given in Fig. 9.7.2 on the basis of [9.7.1], [9.7.2] and [9.7.5]. If the actual stress is lower than the long-term ultimate strength, the creep tends to a finite end value and has to be modelled by the standard linear three-parameter solid. Accordingly, the creep curves for $\sigma_{actual}/\sigma_{ult}=0.25$ and $u=30\%$ or 10% have the forms of Fig. 9.7.2 (b).

On the other hand, if the actual stress exceeds the long-term ultimate strength, the rate of creep of the wood increases with time, resulting in failure without any additional load after a certain time.

The aforementioned characteristics of wood deteriorate markedly in temperatures higher than 100°C. Its ignition point lies at about $250 \sim 300$°C. Biological parasites (fungi, insects) may also markedly reduce the properties of the wood.
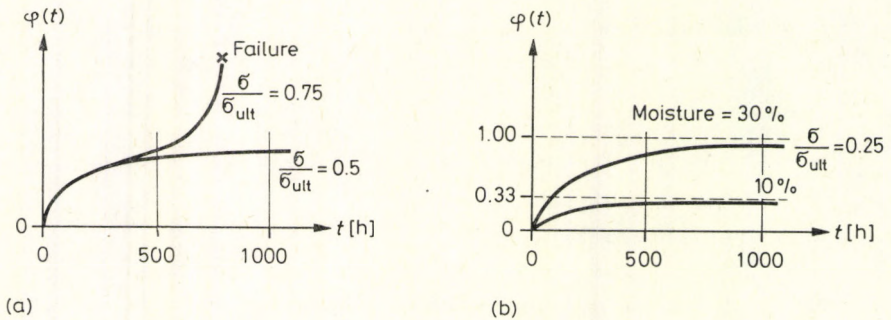
Fig. 9.7.2. (a) Characteristic creep curves of fir-wood for various ratios of the actual stress to the ultimate strength, (b) influence of the moisture content on the creep of fir-wood

9.8. Problems of Reinforced Concrete Shells

The deformation properties of the material of reinforced concrete shells which are necessary for buckling analysis cannot be defined as simply as for other materials, because the deformation depends on the cracks, the reinforcement, and the creep of the concrete as well, so that it becomes a nonlinear function of the load. Consequently, we have to deal with the deformation and rigidity characteristics of the reinforced concrete in detail.

The material model of the reinforcing bars can be assumed on the basis of Section 9.6.1.

The stress–strain diagram of the concrete is curved from the beginning on (Fig. 9.8.1). This curvature is, in fact, caused by a "nonlinear creep", i.e. a slowly developing deformation not proportional to the stress. We take this into account as the plasticity of the concrete. (In addition, the concrete has a "linear creep"
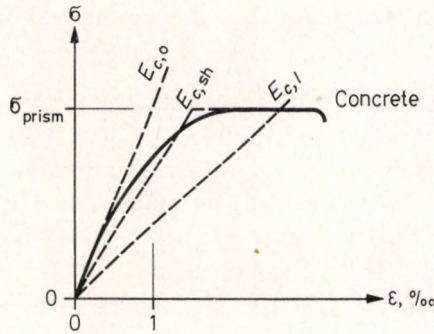
Fig. 9.8.1. Idealized stress–strain diagram of concrete

as well, i.e. a slowly developing deformation proportional to the stress, commonly called "creep".) Hence, we have to choose the modulus of deformation E_c of the perfectly elastic–plastic material model, approximating the real stress–strain diagram, depending on whether the load is acting for a long or for a short time. Namely, under a long-term load, the creep develops completely, while under a short-term (e.g. test) load only a fraction of it may come about. Thus, the perfectly elastic–plastic material model may be characterized by the modulus of deformation referred to long-term $(E_{c,l})$ or to short-term $(E_{c,sh})$ loading, according to the duration of the load. A load should be considered as long-term if it acts at least for one year during the lifetime of the structure. That is, practically the entire creep develops during this time.

In the case of loads acting for a very short time (e.g. vibrations), there is no creep at all, so that when analysing loads of this kind, the modulus of deformation E_c can be considered equal to the initial modulus of elasticity $E_{c,0}$ of the concrete.

In conclusion, we take into consideration the creep of the concrete by an appropriate choice of the modulus of deformation E_c.

The behaviour of the cracked reinforced concrete cross section is influenced by the geometric data and the material properties of both the concrete and the reinforcement. Assuming suitable moduli of deformation, and furthermore supposing that the behaviour of the whole cross section in bending can also be described by an ideally elastic–plastic material model, we obtain relations between bending moments and curvatures similar to that shown in Fig. 9.4.2 for stress and strain.

On the whole, reinforced concrete differs from elastic homogeneous material in the following ways:

— the compressed concrete zone creeps;
— the concrete and the reinforcement behave elasto-pastically,
— the tension zone of the concrete cracks, the stiffness of the cross section

drops, and the position, quantity and quality of the reinforcement plays an important role.

Several authors took the cracking of the concrete into consideration by diminishing the value of the modulus of elasticity [5.33], [9.8.11]. However, this method cannot follow the change in the stiffness due to the variation of the eccentricity of the compressive force. The method to be outlined in the following, based on [9.3.2], [9.8.4], takes this effect into account, so that there is a sufficient agreement between its results and those of the model tests.

In this section we shall use several subscripts that are explained below:

c	— concrete;
rc	— reinforced concrete;
st	— steel;
crack	— cracked (cross section);
uncr	— uncracked (cross section);
hom	— refers to the uncracked, unreinforced (homogeneous) concrete cross section considered as completely elastic, or to quantities computed with such a cross section;
0	— refers to the beginning of some process, e.g. to the initial value of the modulus of elasticity valid for the beginning of the loading process; or, in connection with ψ, it refers to the initial zero value of the eccentricity;
sh or l	— denotes whether the value of the deformation modulus is valid for short-term or long-term loading;
el	— computed with an elastic material model;
pl	— computed with a plastic material model; by the side of subscript cr it denotes the plastic critical load, while standing alone it denotes the compressive force causing plastification of the entire cross section when acting with the initial eccentricity.

9.8.1. Deformation Characteristics of the Concrete

Modulus of elasticity $(E_{c,0})$. The (initial) modulus of elasticity of the concrete, $E_{c,0}$, in fact, describes deformations caused by instantaneous effects (e.g. vibration).

The modulus of elasticity, $E_{c,0}$, depends on the strength of the concrete. Its mean value is, according to the generally accepted formula [9.8.13]:

$$E_{c,0} = 55\,000 \frac{\sigma_{\text{prism}}}{15 + \sigma_{\text{prism}}} \approx 6750 \sqrt{\sigma_{\text{prism}}} \quad [\text{N/mm}^2]. \tag{9.8.1}$$

Here σ_{prism} denotes the prism (or cylinder) strength of the concrete, related to the cube strength σ_{cube} as follows:

$$\sigma_{prism} = 0.8\sigma_{cube}.$$

In design we take into account the standard deviation of the modulus of elasticity by that of the strength, i.e. we associate $E_{c,0}$ with the minimum required strength rather than with the mean value of the strength. By minimum required strength we denote the threshold strength corresponding to the fractile required.

Modulus of deformation taking creep into account (E_c). The measure of creep of the concrete depends on the data of loading, since the concrete hardens with time and, thus, its deformation characteristics also vary. However, the creep of concrete is caused not only by the creep of its material but also by the fact that the load is carried initially by the solid skeleton and by the pore water as well. After a certain time the pore water partly becomes pressed out partly evaporates, so that gradually the entire stress will be carried by the internal skeleton of the concrete.

According to Dischinger's theory [9.5.2], the creep deformation begins according to the creep factor function $\varphi(t)=\varepsilon_{creep}(t)/\varepsilon_{el}$ at the time of the first loading, and the loads applied at a later date induces only that part of the creep deformation that corresponds to the remaining part of the original creep factor function. (It should be remarked that the Dischinger model can be reduced to a fictitious Maxwell fluid with the aid of a co-ordinate transformation, taking φ instead of t as the independent variable, see e.g. in [9.5.3]. However, in this case the "time" φ cannot increase to infinity, only to a certain finite value, i.e. to the final value of the creep factor φ_c of the concrete at $t=\infty$.)

On the other hand, the conception of Freyssinet assumes that the main cause of creep is the squeezing out of the pore water. As a result, we obtain the standard linear three-parameter solid as a model for the creep of concrete.

In recent years, Trost [9.8.14a] and Zerna [9.8.16] showed that the actual behaviour of the concrete lies between these two conceptions, but is closer to the standard three-parameter solid. They established the following fomula for the creep of the concrete:

$$\varepsilon_c = \frac{\sigma_0}{E_{c,0}}[1+k_0\varphi(t)]+\frac{\sigma_t}{E_{c,0}}[1+\bar{\varrho}k_t\varphi(t)].$$

The coefficient $\bar{\varrho}$ appearing in this relation depends on several factors. According to Dischinger's theory, $\bar{\varrho}=0.5$, while for the three-parameter solid $\bar{\varrho}=1.0$. Trost and Zerna suggest $\bar{\varrho}=0.7\sim0.9$. The coefficient k represents the decreasing propensity of the concrete to creep with increasing time. It has the value 1.8 at the beginning of concrete hardening, and 1.0 at the age of one month, while

16 Buckling of Shells

it decreases to $k=0.5$ for concretes older than one year. The value of k valid at the onset of the initial stress σ_0 is denoted by k_0, while that valid at the onset of σ_t at a later date t is denoted by k_t.

Corresponding to the standard linear three-parameter solid, the creep factor $\varphi(t)$ tends to a finite value $\varphi(\infty)$ which we shall call φ_c for the concrete in the following.

The value of φ_c depends on the thickness of the structure, on the quantity and quality of cement applied, on the water–cement ratio, and, finally, on the humidity of the environment of the concrete [9.8.2].

The data published in [9.8.2] suggest that, assuming average circumstances, φ_c practically depends on the strength of the concrete only, and can be described by the relation

$$\varphi_c = 4 - 2 \log_{10} \sigma_{\text{prism}}, \qquad (9.8.2)$$

where the prism strength σ_{prism} is to be substituted in N/mm².

It should be remarked that the data given so far for the concrete are valid up to 200°C only, because at higher temperatures the concrete disintegrates rapidly.

The critical loads of some structures with decreasing post-buckling load bearing capacity were determined in [9.5.11], taking the influence of linear creep exactly into account. Evaluating these results and considering what has been said in Section 9.5 we may conclude that if we consider the effect of the creep of concrete by reducing $E_{c,0}$, i.e. by assuming a modulus of deformation E_c lower than $E_{c,0}$ according to the formula:

$$E_c = \frac{E_{c,0}}{1 + \varphi_c}, \qquad (9.8.3a)$$

see [9.8.2], we commit a slight error to the benefit of safety. The well-foundedness of this formula has been proven by model tests performed on concrete shell domes [9.8.15].

In the case when only a part of the load is acting from the beginning causing σ_0, while another part begins to act only at a later date t causing σ_t, we may reduce the creep factor φ_c accordingly. By so doing we arrive at the following interpolation formula for the modulus of deformation:

$$E_c = \frac{E_{c,0}}{1 + \dfrac{\sigma_0 + k_t \bar{\varrho} \sigma_t}{\sigma_0 + \sigma_t} \varphi(t)}. \qquad (9.8.3b)$$

The meanings of k_t and $\bar{\varrho}$ were explained earlier.

For structures with increasing post-buckling load bearing capacity we know of no such investigations. The effect of creep seems to be smaller on these structures. Until more exact results are available, we suggest using Eq. (9.8.3) as an approxi-

mation also for structures with an increasing character. By so doing we certainly remain on the safe side.

If the load acts on the structure for a short time only (e.g. for a few hours), merely a part of the creep develops [9.8.2]. We may take this part of the creep into account by assuming the "short-term" deformation modulus $E_{c,sh}$, to be applied for short-term (e.g. test) loads, as 70% of the modulus of elasticity $E_{c,0}$ [9.8.13]. Hence, we obtain:

$$E_{cs,h} = 0.7 E_{c,0}. \tag{9.8.4}$$

In the following, E_c always denotes the appropriate value, i.e. for the analysis of the effect of long-term loads, $E_c = E_{c,l}$, for that of short-term loads, $E_c = E_{c,sh}$, and for the investigation of the effect of vibration, $E_c = E_{c,0}$.

9.8.2. Dimensions of Reinforced Concrete Shells

As a rule, the thicknesses of concrete and reinforced concrete structures, also included shells, deviate from the design values. Extensive series of measurements on erected reinforced concrete slabs, conducted in the Institute of Quality Control of the Building Industry (Építőipari Minőségvizsgáló Intézet, ÉMI) in Budapest, and their evaluation [9.8.10], [9.8.14] showed that the mean value of the dimensions is equal to 1.05 of the design thickness, while for the lower extreme values (fractiles) of the cross sectional dimensions we can take the design values reduced by 10 mm. For buckling, the average dimensions are decisive, and the deviations of the dimensions of the individual cross sections become decisive only in the calculation of the plastic failure load. Thus, as with other reinforced concrete constructions, for the calculation of the elastic critical loads of shells we may use the design dimensions, while for the calculation of the load p_{pl} causing plastic failure we may use the design dimensions reduced by 10 mm.

9.8.3. The Shell Buckling Rigidity Characteristic of the Reinforced Concrete Cross Section

On the basis of the reasoning to be found in [9.1.1], for the buckling analysis of reinforced concrete shells we introduce the "shell buckling rigidity characteristic" $K = \sqrt{BT}$, see Eq. (9.1.1). Here B and T are the bending and tensile stiffnesses of the shell cross section respectively.

We compute the rigidity characteristics on the basis of the second state of the reinforced concrete structures, i.e. assuming a cracked tensile zone but still linearly elastic behaviour.

In the case of reinforced concrete structures, the bending and tensile stiffnesses B and T depend on the reinforcement and on the eccentricity of the compressive force, because with increasing eccentricity the tensile zone of the concrete gradually cracks, causing a decrease in stiffness.

The rigidity characteristics of the uncracked, unreinforced concrete cross section are, neglecting Poisson's ratio, as follows:

$$B_c^{uncr} = E_c I_c = E_c \frac{t^3}{12},$$

$$T_c^{uncr} = E_c A_c = E_c t,$$

where I_c and A_c are, respectively, the moment of inertia and the area of the concrete cross section of unit width. From this we can compute the shell buckling rigidity characteristic of the uncracked full concrete cross section:

$$K_c^{uncr} = \sqrt{B_c^{uncr} T_c^{uncr}} = E_c \frac{t^2}{\sqrt{12}}. \tag{9.8.5}$$

If we apply reinforcement in the cross section, its rigidity characteristics will be increased due to the area of reinforcement which, multiplied by $E_{st}/E_c=n$ (with E_{st} as the modulus of elasticity of the reinforcement), can be considered as an additional concrete area. Hence, we have:

$$B_{rc}^{uncr} = E_c I_{rc}^{uncr},$$

$$T_{rc}^{uncr} = E_c A_{rc}^{uncr},$$

and the shell buckling rigidity characteristic of the uncracked full reinforced concrete cross section becomes:

$$K_{rc}^{uncr} = \sqrt{B_{rc}^{uncr} T_{rc}^{uncr}}. \tag{9.8.6}$$

In the formulas the subscript rc denotes that we considered the above-mentioned additional concrete area in the calculation of the rigidity characteristics. We thus have:

$$B_{rc}^{uncr} = \frac{E_c t^3}{12} [1 + 3n\mu(1 - 2\eta)^2],$$

$$T_{rc}^{uncr} = E_c t(1 + n\mu),$$

where $\mu = A_{st}/A_c$ is the ratio of reinforcement area in one direction to the cross sectional area, and $\eta = h'/t$ is the ratio of the concrete thickness covering the reinforcement to the height of the cross section, see Fig. 9.8.2.

Introducing the notation

$$K_{rc}^{uncr} = \psi_0 K_c^{uncr},$$
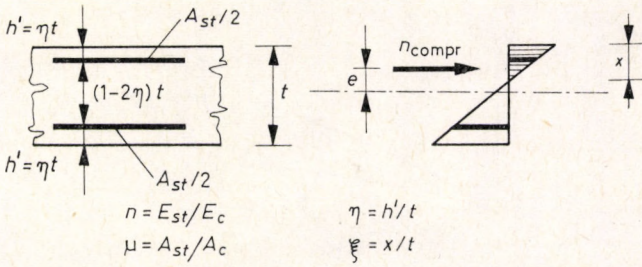
Fig. 9.8.2. Stresses in a cracked reinforced concrete shell cross section

ψ_0 can be written as follows:

$$\psi_0 = \sqrt{(1+n\mu)[1+3n\mu(1-2\eta)^2]}. \tag{9.8.7}$$

In reinforced concrete shell structures, two kinds of reinforcement are generally used: the single layer grid (placed, as a rule, in the middle of the height) and the double layer grid (placed on the two sides of the cross section). In the case of single layer grids $\eta=0.5$, while for double layer grids we may take $\eta \approx 0.2$, as a rule. We computed from Eq. (9.8.7) the values of $\psi_{0,1}$ and $\psi_{0,2}$, characteristic of the single layer middle grid and of the double layer grid (with $\eta=0.2$) respectively. These values are to be seen in Table 9.8.1 and Fig. 9.8.3.

Table 9.8.1

Values of ψ appearing in Eqs (9.8.7) and (9.8.10)

$n\mu$	0	0.05	0.10	0.15	0.20	0.30	0.40	0.50
$\psi_{0,1}$	1.000	1.025	1.049	1.072	1.095	1.140	1.183	1.225
$\psi_{0,2}$	1.000	1.052	1.104	1.156	1.208	1.312	1.416	1.520
$\psi_{\infty,1}$	0	0.139	0.212	0.269	0.316	0.393	0.457	0.513
$\psi_{\infty,2}$	0	0.178	0.285	0.373	0.453	0.597	0.730	0.855

$$K_{rc}^{uncr} = \psi_0 K_c^{uncr}; \quad K_{rc}^{crack} = \psi_\infty K_c^{uncr}$$

If the cross section cracks, its rigidity characteristics decrease. The degree of decrease depends on the eccentricity of the compressive force. When the eccentricity reaches the value of half the height of the cross section, the rigidity characteristics closely approximate the values

$$B_{rc}^{crack} = E_c I_{rc}^{crack} = \frac{E_c t^3}{12}[4\xi^3+6n\mu(1+2\xi^2+2\eta^2-2\xi-2\eta)],$$

$$T_{rc}^{crack} = E_c A_{rc}^{crack} = E_c t(\xi+n\mu),$$

$$\psi = \frac{K_{rc}}{K_c^{uncr}}$$

$$n = E_{st}/E_c$$
$$\mu = A_{st}/A_c$$
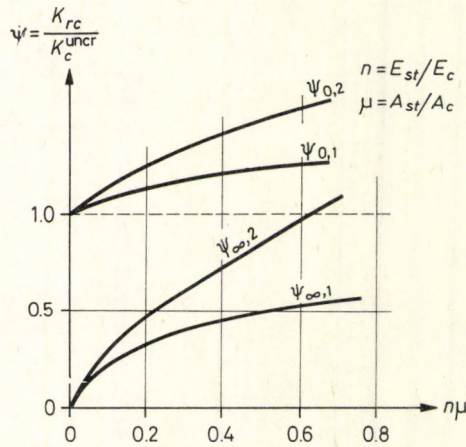
$\psi_{0,1}$: Uncracked	Reinforced concrete
$\psi_{\infty,1}$: Cracked	with single-layer reinforcement
$\psi_{0,2}$: Uncracked	Reinforced concrete
$\psi_{\infty,2}$: Cracked	with double-layer reinforcement

Fig. 9.8.3. Factors ψ for calculating
the shell buckling rigidity characteristic of reinforced
concrete shells plotted against the quantity of reinforcement

valid for infinitely large eccentricity, i.e. for bending. Here ξ denotes the ratio of the height of the compressed zone to that of the cross section, see Fig. 9.8.2.

The difference between these rigidity characteristics and those of the uncracked cross section, B_{rc}^{uncr} and T_{rc}^{uncr}, is that in B_{rc}^{crack} and T_{rc}^{crack} the stiffness of the tension zone of the concrete is omitted.

Consequently, the shell buckling rigidity characteristic of the cracked reinforced concrete cross section can be written with close approximation as follows:

$$K_{rc}^{crack} = \sqrt{B_{rc}^{crack} T_{rc}^{crack}} = E_c \sqrt{I_{rc}^{crack} A_{rc}^{crack}}.$$

This expression can be regarded as valid in the range of large eccentricities ($e > t/2$). By eccentricity e we denote the distance of the compressive force n_{compr} measured from the centroid of the full (uncracked) cross section.

In the case of a symmetric reinforcement as shown in Fig. 9.8.2, we obtain with the aid of the usual reinforced concrete theory [9.8.5]:

$$\xi = \frac{x}{t} = n\mu \left[\sqrt{1 + \frac{1}{n\mu}} - 1 \right]. \tag{9.8.8}$$

Introducing the notation

$$K_{rc}^{\text{crack}} = \psi_\infty K_c^{\text{uncr}},\tag{9.8.9}$$

we can derive from the foregoing the following expression for ψ_∞:

$$\psi_\infty = \sqrt{12(n\mu+\xi)\left[\frac{\xi^3}{3}+\frac{n\mu}{2}(1+2\xi^2+2\eta^2-2\xi-2\eta)\right]}.\tag{9.8.10}$$

The values of $\psi_{\infty,1}$ and $\psi_{\infty,2}$, valid for single layer middle reinforcement ($\eta=0.5$) and double layer reinforcement ($\eta=0.2$) respectively, are shown in Table 9.8.1 and Fig. 9.8.3. It is permissible to interpolate linearly between the values of the table.

If there is no reinforcement, then the tensile stresses disappear after cracking. The compressive forces alone have to counterbalance the bending moment acting on the cross section. Consequently, the unreinforced concrete cross section is able to take bending moment only if the compressive force acts inside the cross section.

Shrinkage and variation of temperature cause cracks in the concrete even without external forces. Hence, we may assume that from the beginning of the loading process on no tensile stresses arise in the cross section. By so doing we remain on the safe side.

The effective area of the cracked concrete cross section is

$$A_c^{\text{crack}} = 3\left(\frac{t}{2}-e\right),$$

so that its tensile stiffness becomes:

$$T_c^{\text{crack}} = E_c 3\left(\frac{t}{2}-e\right).$$

The above formulas are only valid if the compressive force acts outside the core of the cross section, i.e. if the eccentricity e exceeds the kernel radius $t/6$.

The change in curvature χ of the bending deformation is to be computed generally from the expression

$$\chi = \frac{M}{EI}.$$

In the case of the cross section without tensile strength this becomes:

$$\chi = \frac{\varepsilon}{x} = \frac{\sigma}{E_c x} = \frac{2n_{\text{compr}}}{E_c 9\left(\frac{t}{2}-e\right)^2}.$$

Equating the two expressions for χ and substituting en_{compr} for M, we obtain the bending stiffness of the cracked concrete cross section:

$$B_c^{crack} = E_c I_c^{crack} = E_c 4.5e\left(\frac{t}{2}-e\right)^2.$$

Hence, the shell buckling rigidity characteristic for the range $t/6 < e < t/2$ becomes:

$$K_c^{crack} = \sqrt{B_c^{crack} T_c^{crack}} = E_c \sqrt{13.5e\left(\frac{t}{2}-e\right)^3}. \qquad (9.8.11)$$

According to what has been said in Section 9.2, we can assume $e = cw$ for the eccentricity e without detailed analysis. The assumption $c=1$ causes an error to the benefit of safety.

9.8.4. Determination of the Upper Critical Loads of Reinforced Concrete Shells

We first take into account only the influence of cracking, i.e. the decrease of the shell buckling rigidity characteristic with increasing eccentricity. Then we consider the effect of creep through the modulus of deformation E_c, as said before. In this way we determine the elastic upper critical load of the reinforced concrete shell. Finally, using the results of Section 9.4, we establish the plastic upper critical load of the reinforced concrete shell.

Upper critical load of the elastic reinforced concrete shell. Inside the area of a buckle, the eccentricity and, consequently, also the shell buckling rigidity characteristic of the reinforced concrete varies from place to place. Nevertheless, it is the value of this rigidity characteristic valid at the maximum buckling amplitude that has the greatest influence on the buckling deformation. Considering that the value of the rigidity characteristic is greater everywhere else inside the buckle, we may assume its minimum value, pertaining to the maximum amplitude, to be valid all over the buckle. We thus commit a slight error to the benefit of safety. Hence, the rigidity of the shell will be considered to be constant, and the differential equations will have constant coefficients. The load p pertaining to some deformation w may be computed by using the shell buckling rigidity characteristic pertaining to w_{max}.

The construction based on this assumption was worked out in [9.8.4] and is shown in Fig. 9.8.4 for the homogeneous elastic cylindrical panel solved in [2.57]. The load-deformation diagram of the perfect shell is represented by the full heavy parabola-like line in the figure, branching from the point that corresponds to

(a)

(b)
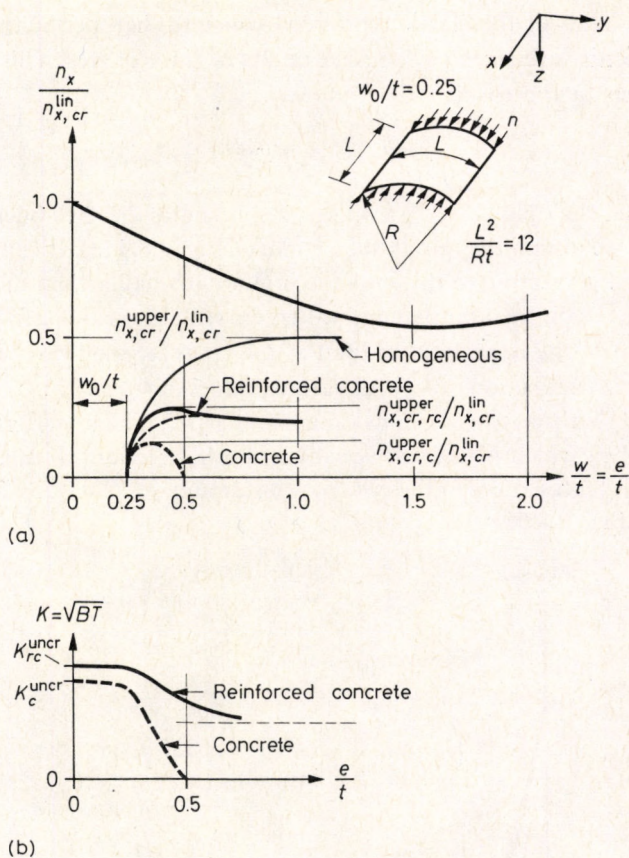
Fig. 9.8.4. Determination of the upper critical load
of the elastic reinforced concrete shell

the linear critical load. Supposing that the compressive force acts on the homogeneous shell with an eccentricity $w_0 = e_0 = 0.25\ t$, or that the shell has an initial imperfection with a maximum amplitude equal to this value, then the eccentricity w increases with increasing load intensity as shown by the thin curve, according to [2.57].

In Fig. 9.8.4 (b) we show the variation of the shell buckling rigidity characteristic K of the concrete and reinforced concrete cross sections plotted against the eccentricity $e = w$. We have to reduce the ordinates of the $p(w)$ curve valid for the homogeneous material to the same extent that the shell buckling rigidity characteristic K decreases. Thus we obtain for the reinforced concrete shell the curve drawn by the full heavy line, while for the concrete shell we arrive at the heavy dashed curve in Fig. 9.8.4 (a).

The critical loads of the elastic reinforced concrete shell pertaining to various initial eccentricities are given by the peak points of these curves. This critical load may be written in the form:

$$p^{upper}_{cr, el, rc} = \varrho_{rc} \, p^{lin, uncr}_{cr, c}. \qquad (9.8.12)$$

If we consider the rigidity K^{crack}_{rc} from the beginning as the shell buckling rigidity characteristic, we obtain the thin dashed curve of Fig. 9.8.4 (a). It can be seen that the critical load pertaining to this curve is somewhat smaller than the more exact one. Hence, by using the approximate value, we remain on the safe side.

If we determine the upper critical load of the concrete shell carcked equally in both directions as a function of w_0/t for various values of w_{cr} and p^{lower}_{cr}, as explained above, we find that it hardly depends on w_{cr} and p^{lower}_{cr}. The upper critical load of the concrete shell which is cracked equally in both directions and has no tensile strength can be represented, in the case of $w_{cr} = 2t$ and $p^{lower}_{cr} = 0.25 p^{lin}_{cr}$, by the full line curve in Fig. 9.8.5.
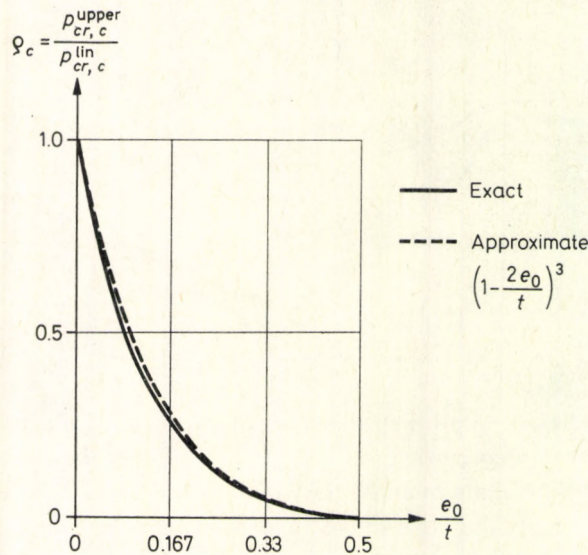
Fig. 9.8.5. The variation of the factor ϱ_c of the concrete shell as a function of the initial imperfection amplitude for the case $e_0 = w_c$

The cracks develop, in fact, not infinitely densely in the concrete shell, but at finite distances. Hence, its stiffness becomes also somewhat greater than that of the shell with no tensile strength at all. Consequently, we do not commit any error to the detriment of safety if, instead of the exact full line curve, we take the approxi-

mate dashed line curve of Fig. 9.8.5, corresponding to the simple relation:

$$\varrho_c = \left(1 - \frac{2e_0}{t}\right)^{3(1+w_0/e_0)/2}. \tag{9.8.13}$$

which is much easier to use in the following.

In the range $e_0/t \geqq 0.5$ we obviously have $\varrho_c = 0$, since the stiffnesses of the cracked concrete cross section become zero at $e_0/t = 0.5$. As we explained in the course of the analysis of the shell buckling rigidity characteristic of the reinforced concrete cross section, from $e_0/t = 0.5$ on we may consider the rigidity of the cracked, bent reinforced concrete cross section as valid; consequently, its critical load can also be computed by multiplying that of the homogeneous (uncracked concrete) shell by ψ_∞, i.e.:

$$\varrho_{rc}\left(\frac{e_0}{t} > 0.5\right) = \psi_\infty \varrho_{hom}. \tag{9.8.14}$$

The stiffnesses computed by completely neglecting the tensile stresses in the concrete will be increased by the uncracked sections of the tension zone between the cracked cross sections. On the other hand, if the cracks do not intersect the reinforcing bars at a right angle, the stiffnesses decrease. These two effects approximately cancel each other out, so that in practice we can work with the value ψ_∞.

In the uncracked parts of the shell the efficacy of the reinforcing bars which do not subtend a right angle with the directions of the principal bending moments decreases. In the case of a rectangular mesh reinforcement of equal strength in both directions this reduction becomes greatest at 45°, where its efficacy is only 0.5. Since we do not know in advance how the buckling shape will develop, it seems advisable to take this value 0.5 into consideration. Hence the stiffnesses of the uncracked reinforced concrete shell can be computed by using the factor:

$$\varrho_{rc}\left(\frac{e_0}{t} = 0\right) = \frac{1+\psi_0}{2}.$$

In the range $e_0/t \leqq 0.5$, the value of ϱ_{rc} lies between those of $\frac{1+\psi_0}{2}\varrho_{hom}$ and $\frac{1+\psi_0}{2}\varrho_c$. Detailed investigations showed that we can interpolate between these two values according to ψ_∞, see Fig. 9.8.6. Thus we have:

$$\varrho_{rc}\left(\frac{e_0}{t} \leqq 0.5\right) = \frac{1+\psi_0}{2}\varrho_c + \psi_\infty(\varrho_{hom} - \varrho_c). \tag{9.8.15}$$

Finally, the upper critical load of the elastic reinforced concrete shell can be computed from the relation:

$$p_{cr,rc}^{upper} = \varrho_{rc}\, p_{cr,hom}^{lin}. \tag{9.8.16}$$

$$\varrho = \frac{p_{cr}^{upper}}{p_{cr}^{lin}}$$

1. ϱ_c

2. $\frac{1+\Psi_0}{2}\varrho_c$

3. ϱ_{hom}

4. $\frac{1+\Psi_0}{2}\varrho_{hom}$

5. $\varrho_{rc} = \frac{1+\Psi_0}{2}\varrho_c + \Psi_\infty(\varrho_{hom}-\varrho_c)$

$$\frac{1+\Psi_0}{2}$$

$$\frac{1+\Psi_0}{2}(\varrho_{hom}-\varrho_c)$$

$$\Psi_\infty(\varrho_{hom}-\varrho_c)$$

$$\frac{1+\Psi_0}{2}\varrho_c$$

1.0 —

ϱ_c

$\Psi_\infty \cdot \varrho_{hom}$

ϱ_{rc} 0

0   0.5 $\frac{e_0}{t}$
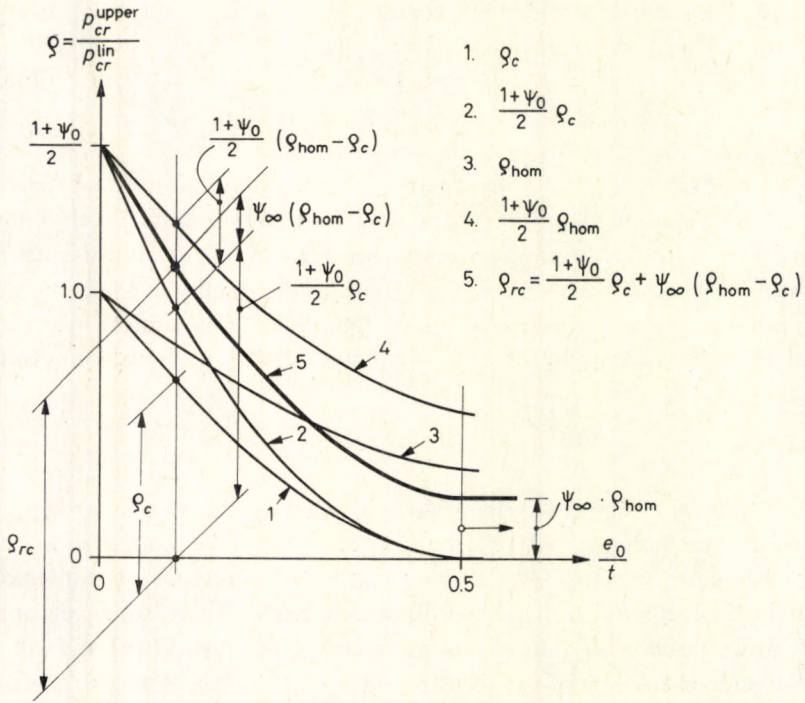
Fig. 9.8.6. Determination of the factor ϱ_{rc} of the reinforced concrete shell by interpolation

In shell structures the usual reinforcement is mostly weak, so that ψ_0 exceeds unity only slightly. If we use the approximation $\Psi_0 \approx 1$, we can further simplify the procedure as follows.

Introducing the ratio:

$$\beta = \frac{p_{cr,rc}^{upper}}{p_{cr,hom}^{upper}} = \frac{\varrho_{rc}}{\varrho_{rc}(\psi_\infty = 1)}, \tag{9.8.17}$$

the critical load of the weakly reinforced elastic concrete shell can also be computed from the expression:

$$p_{cr,rc}^{upper} = \beta p_{cr,hom}^{upper} = \beta p_{cr,c}^{upper, uncr}. \tag{9.8.18}$$

The numerical values of the factor β are compiled in Table 9.8.2. The values corresponding to $\varrho_{hom}(0.5)=0.25$ refer to shells which behave like the axially compressed cylinder or the radially compressed sphere. Hence, we also plotted these values in Fig. 9.8.7.

If the reinforcement, i.e. the rigidities, are not equal in the two directions, the shell is to be computed as orthotropic, with the different factors β_x and β_y in the two directions. In most practical cases, however, the difference between the two

Table 9.8.2

Values of the factor β (Eq. (9.8.17))

$\varrho_{hom}(0.5)$	ψ_∞	e_0/w_0	$\dfrac{e_0}{t} = 0$	0.1	0.2	0.3	0.4	0.5
1.00	1.0	0.5 1.0	1.0	1.0	1.0	1.0	1.0	1.0
	0.8	0.5 1.0	1.0	0.87 0.90	0.82 0.84	0.80 0.81	0.8	0.8
	0.6	0.5 1.0	1.0	0.75 0.80	0.64 0.69	0.61 0.63	0.6	0.6
	0.4	0.5 1.0	1.0	0.62 0.71	0.46 0.53	0.41 0.44	0.4	0.4
	0.2	0.5 1.0	1.0	0.49 0.61	0.28 0.37	0.21 0.25	0.20 0.21	0.2
	0	0.5 1.0	1.0	0.37 0.51	0.10 0.22	0.02 0.06	0 0.01	0
0.75	1.0	0.5 1.0	1.0	1.0	1.0	1.0	1.0	1.0
	0.8	0.5 1.0	1.0	0.88 0.91	0.83 0.85	0.80 0.82	0.8	0.8
	0.6	0.5 1.0	1.0	0.77 0.82	0.65 0.70	0.61 0.63	0.6	0.6
	0.4	0.5 1.0	1.0	0.65 0.73	0.48 0.55	0.41 0.45	0.40 0.41	0.4
	0.2	0.5 1.0	1.0	0.53 0.64	0.30 0.40	0.22 0.26	0.20 0.21	0.2
	0	0.5 1.0	1.0	0.42 0.55	0.13 0.24	0.02 0.08	0 0.01	0
0.50	1.0	0.5 1.0	1.0	1.0	1.0	1.0	1.0	1.0
	0.8	0.5 1.0	1.0	0.90 0.92	0.84 0.86	0.81 0.82	0.8	0.8
	0.6	0.5 1.0	1.0	0.81 0.85	0.67 0.72	0.61 0.64	0.60 0.61	0.6
	0.4	0.5 1.0	1.0	0.71 0.77	0.51 0.58	0.42 0.46	0.40 0.41	0.4
	0.2	0.5 1.0	1.0	0.61 0.69	0.34 0.44	0.23 0.28	0.20 0.21	0.2
	0	0.5 1.0	1.0	0.51 0.61	0.18 0.30	0.04 0.10	0 0.01	0

Table 9.8.2. (continued)

ϱ_{hom} (0.5)	ψ_∞	e_0/w_0	$\dfrac{e_0}{t} = 0$	0.1	0.2	0.3	0.4	0.5
0.25	1.0	0.5 / 1.0	1.0	1.0	1.0	1.0	1.0	1.0
	0.8	0.5 / 1.0	1.0	0.96 / 0.96	0.87 / 0.90	0.81 / 0.84	0.80 / 0.81	0.8
	0.6	0.5 / 1.0	1.0	0.92 / 0.93	0.74 / 0.79	0.63 / 0.67	0.60 / 0.61	0.6
	0.4	0.5 / 1.0	1.0	0.88 / 0.89	0.60 / 0.69	0.44 / 0.51	0.40 / 0.42	0.4
	0.2	0.5 / 1.0	1.0	0.84 / 0.86	0.47 / 0.58	0.26 / 0.34	0.20 / 0.22	0.2
	0	0.5 / 1.0	1.0	0.81 / 0.82	0.34 / 0.48	0.07 / 0.18	0 / 0.03	0
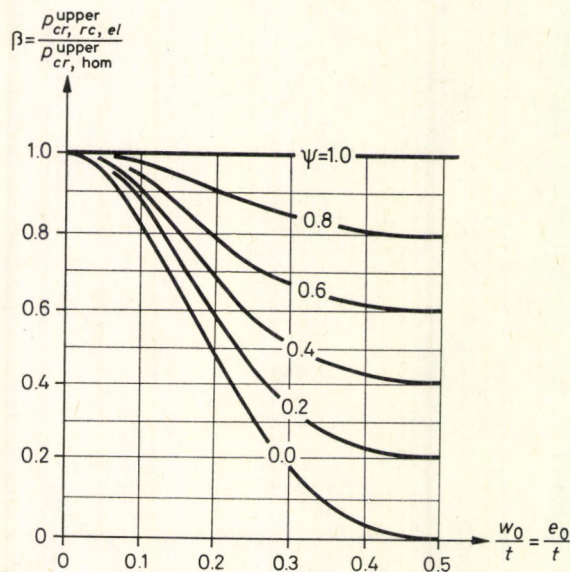
Fig. 9.8.7. The factors β of the reinforced concrete cylindrical shell as functions of the imperfection amplitude in the case of ϱ_{hom} (0.5)=0.25 and $e_0=w_0$

stiffnesses is not very significant, so that the shell can be considered as approximately isotropic with the substituting factor:

$$\beta_{\text{subst}} = \sqrt{\beta_x \beta_y}. \tag{9.8.19}$$

Upper critical load of the plastic reinforced concrete shell. The plastic behaviour of the reinforced concrete shell can be taken into consideration either by Eq. (9.4.2) or by Eq. (9.4.6). Hence, summing up the foregoing, the critical load taking into consideration all the properties of reinforced concrete shells (cracking, reinforcement, creep and plasticity) can be computed from the following formula, obtained by combining Eqs (9.4.3) and (9.8.18):

$$p_{cr,\,pl,\,cr}^{\text{upper}} = \zeta p_{cr,\,el,\,rc}^{\text{upper}} = \zeta \beta p_{cr,\,\text{hom}}^{\text{upper}}. \tag{9.8.20}$$

Here $p_{cr,\,pl,\,rc}^{\text{upper}}$ denotes the upper critical load of the reinforced concrete shell with plastic properties, $p_{cr,\,\text{hom}}^{\text{upper}}$ the upper critical load of the uncracked concrete shell considered as elastic with the modulus of deformation E_c (taking into consideration the effect of creep), ζ the factor taking the plastic properties according to Eq. (9.4.4) or (9.4.6) into account, and β the ratio of the upper critical loads of elastic reinforced concrete and elastic homogeneous shells, to be determined from Eq. (9.8.17) or Table 9.8.2.

We computed in [9.3.1] the critical loads of the experimental reinforced concrete shells reported on in [4.6], [4.30], [4.33], [9.8.7], [9.8.8], [9.8.9] and [9.8.12] by means of Eq. (9.8.20) and compared them with the experimental values. The results are plotted against (R/t) in Fig. 9.8.8.
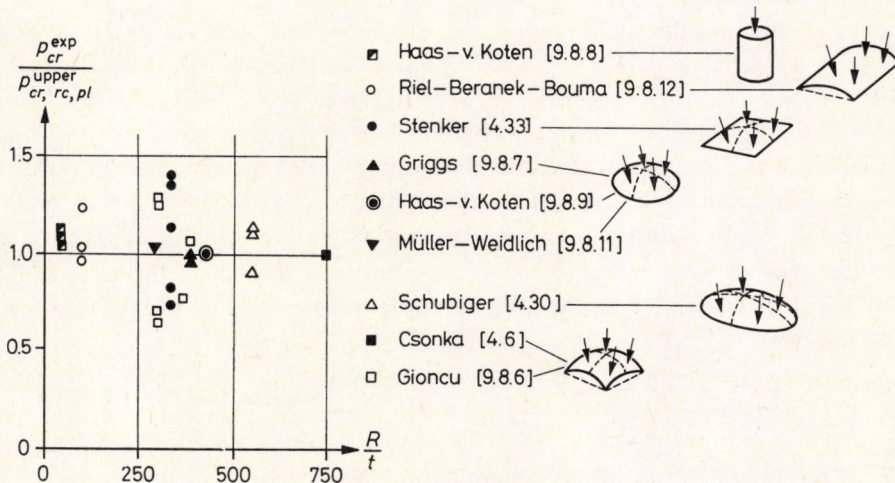
Fig. 9.8.8. Comparison of test results to be found in the literature with values calculated by the proposed method

The mean value of the ratios of the experimental to the computed critical loads is 1.02; the standard deviation is 20%. This proves that the method presented in the foregoing corresponds to reality.

If we take the special properties of the reinforced concrete into consideration by using the method presented above, the low values of critical loads of reinforced concrete shells shown in Fig. 4.2 and 4.3 rise to the average values.

9.9. Determination of Critical Loads by Model Tests and by Measurements on Erected Structures

From the foregoing it can be seen that not all stability problems of shells even of the simplest shapes have been solved in a way that is satisfactory for practical applications. Hence, the critical loads, of shells of new, more complicated shapes can be determined theoretically during the design procedure only in the most exceptional cases. Consequently, in these cases we have to resort to model tests. By so doing we may load the shell up to failure. However, besides the critical load causing failure, it is important to know whether the post-buckling load bearing capacity of the shell is constant, decreasing or increasing, because this circumstance basically influences the magnitude of the safety factor to be chosen. The demand also may arise that the shell — at least in some loading cases — should not be loaded up to failure in order to save costs, but that, nevertheless, the above data should be determined.

Plotting the buckling deformation w against the load intensity generally does not furnish a reliable answer to the above questions. That is, this diagram corresponds to one of the dashed lines of Figs. 1.1 (a), (b), (c) or (d). However, these are so similar to each other that it is impossible to find out to which one the measured diagram corresponds. Moreover, the peak point of the curve, i.e. the critical load, cannot be reliably extrapolated either. Thus, we have to resort to Southwell's plot [2.51] that transforms the load-deflection diagram of structures with initial imperfections, corresponding to Fig. 1.1 (a) into a straight line. In this case the buckling deformation w depends on the initial eccentricity w_0 and on the load P as follows:

$$w = w_0 \frac{1}{1 - P/P_{cr}^{\mathrm{lin}}} . \tag{9.9.1}$$

This relation is based on the usual assumption that the initial imperfection has the same shape as the buckling deformation, which is fulfilled in most cases with good approximation.

Introducing the displacement δ measured from the initial imperfection w_0:

$$w - w_0 = \delta, \qquad (9.9.2)$$

Equation (9.9.1) can be rearranged into the form:

$$\frac{\delta}{P} = \frac{1}{P_{cr}^{lin}} (\delta + w_0), \qquad (9.9.3)$$

which is the equation of a *straight line* according to the co-ordinates δ/P and δ. Hence, measuring the deflection δ caused by several load intensities P, and plotting the data in the co-ordinate system $[\delta/P, \delta]$, we obtain a straight line the tangent of which yields the critical load (Fig. 9.9.1). (In shell buckling problems we may write p instead of P.)
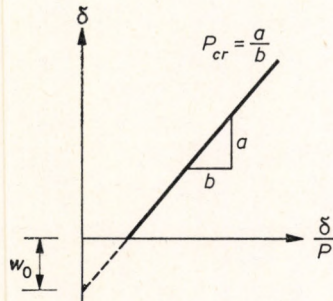
Fig. 9.9.1. The Southwell-plot for structures with constant post-buckling load bearing capacity

(a)   (b)
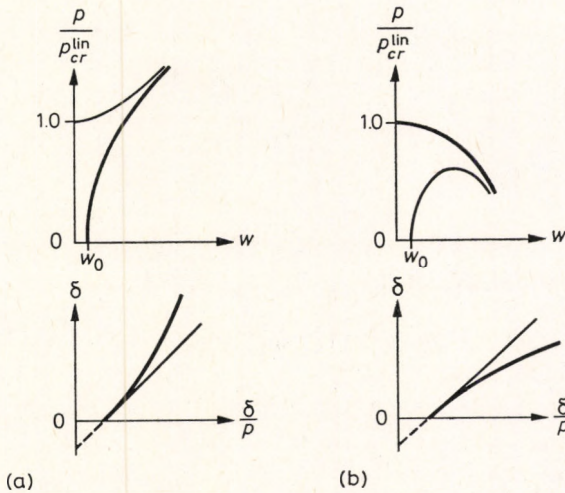
Fig. 9.9.2. Determination of the ascending or descending character of the post-buckling behaviour by the generalized Southwell-plot

Thus, Southwell's plot has the advantage of making the extrapolation of the critical load more accurate. In addition, it may also be used to find out whether the post-buckling load bearing capacity of the shell is increasing, constant or decreasing (Figs 1.1 (a), (b), (c) or (d)). That is, it can be shown [9.9.2], [9.9.3] that the Southwell plot becomes curved upwards or downwards depending on whether the post-critical load bearing capacity of the structure increases or decreases (Figs 9.9.2 (a) and (b)). Hence, if by plotting the measured values δ and δ/p, we obtain one of the curves of Fig. 9.9.2 instead of a straight line, we may decide on the increasing or decreasing post-buckling behaviour of the shell, corresponding to Fig. 1.1 (b) or Figs 1.1 (c), (d) respectively. However, as a rule, we cannot determine the critical load of the structure from these curved Southwell diagrams, so that we have to chose an appropriate safety factor corresponding to the type of post-buckling behaviour. For structures with an increasing post-buckling behaviour (see Fig. 1.1 (b)), the so-called Spencer plot proposed in [9.9.4] is in most cases able to furnish the critical load.

We have to be careful if there is a chance that the behaviour of the structure corresponds to Fig. 1.1 (e). That is, it may happen that the initial section of the load-deflection curve corresponds, e.g. to Fig. 1.1 (a), and its Southwell plot becomes straight, although the branching that occurs later results in a (sometimes sharply) decreasing post-buckling load bearing capacity.

The initial section of the Southwell plot is sometimes curved. This is mostly due to errors in the measurements at low loads, which can be eliminated by the "modified Lundgren plot", see in [9.9.4].

Another way to determine the linear critical load without destroying the structure is the *measurement of vibrations* [2.12], [9.8.3]. This method is mainly suitable for application on erected shells, but it can also be performed during model tests. It is based on the following relation, well known for compressed bars [9.9.1]:

$$N = N_{\text{dead}} \sqrt{1 - \frac{p}{p_{cr}^{\text{lin}}}}. \tag{9.9.4}$$

Equation (9.9.4) is also valid for shallow shells subjected to compressive forces of constant magnitude. Here:

p — the total load acting on the shell (dead-weight included);

p_{cr}^{lin} — the linear critical load;

N_{dead} — eigenfrequency of the unloaded shell (loaded only by its dead weight), disregarding the influence of compressive forces due to dead weight on the vibration;

N — eigenfrequency of the shell loaded by p, taking the influence of compressive forces into account.

The assumption underlying Eq. (9.9.4) is that the load p does not increase the vibrating inert mass of the shell. This is fulfilled if, e.g. the shell model is loaded by air pressure or by weights suspended on soft springs. However, if we load the structure by weights rigidly connected to it (e.g. by placing them on the shell), then we have to consider that they increase the vibrating mass of the shell, causing a reduction in its eigenfrequency (even without considering the effect of the compressive forces). Since the mass appears in the formula of the eigenfrequency in the denominator under the square root sign, Eq. (9.9.4) has to be modified as follows:

$$N = \frac{N_{\text{dead}}}{\sqrt{p/p_{\text{dead}}}} \sqrt{1 - \frac{p}{p_{cr}^{\text{lin}}}}, \qquad (9.9.5)$$

where p_{dead} denotes the dead weight.

Hence, if we measure the eigenfrequencies of the shell subjected to two different loads (possibly not very close to each other), we can write two equations for the unknowns N_{dead} and p_{cr}^{lin}, from which p_{cr}^{lin} can be calculated. This allows us to decide also on the actual critical load p_{cr}^{upper} of the structure.

Equations (9.9.4) and (9.9.5) are valid on the condition that the eigenshape of the vibration coincides with the buckling shape. However, this is not always fulfilled. Consequently, as a rule, measurements have to be performed in as many points as necessary to distinguish the vibrations of different wavelengths and to determine the corresponding eigenfrequencies separately. Then the critical loads have to be computed from every eigenfrequency and the minimum of them should be considered as the most onerous one.

As with the Southwell plot, the measurement of the vibration is also not suitable for the determination of the critical load in the case corresponding to Fig. 1.1 (e).

When using either the Southwell plot or the measurement of vibration, we impose only small deformations on the structure. Hence, neither of these methods assesses the rigidity-reducing effects of the plasticity, creep and cracks which develop in the reinforced concrete structures only in a later stage of buckling. Both methods consider, on the other hand, the actual stiffening effect of the edge supports (considered in most cases only roughly in the computation) and the influence of cracks due to the dead weight.

In summary, these methods can be applied only in correlation with and completed by the theoretical results.

9.10. The Safety Factor

The safety factor k determines the actual security against buckling. We may choose its magnitude freely, but it should depend

- on the accuracy of the theory for the computation of the critical load;
- on whether the failure of the shell occurs suddenly or slowly (decreasing, constant or increasing post-buckling load-bearing capacity);
- on the discrepancies between the theoretical model and the erected shell with respect to:

    - material quality,
    - load intensity,
    - dimensions and
    - shape;

- on the standard deviations of these effects and on the coincidence of tehse effects and of these standard deviations; finally
- on the acceptable degree of risk of failure.

These effects appear in a different manner depending on whether we determine the elastic critical load or the plastic failure load p_{pl} pertaining to a given initial imperfection. The change in the radius of curvature due to the initial imperfection has different influences on the elastic critical load $p_{cr,el}^{upper}$ and on the plastic failure load p_{pl}, because e.g. in the case of a spherical shell, R appears squared in the denominator of the elastic critical load, but to the first power in that of the plastic failure load, since $p_{pl} = 2n_{pl}/R$. Furthermore, the plastic load bearing capacity always decreases with increasing buckling deflection w, while the post-buckling elastic load bearing capacity may either decrease or increase.

For all these reasons two different safety factors, k_{el} and k_{pl}, are to be used for the elastic critical and for the plastic failure loads respectively. Thus, we can write for the allowable load of the shell $p_{cr,allow}$, according to Eq. (9.4.2) or (9.4.5), the following relations:

$$\left(\frac{k_{el}\,p_{cr,\,allow}}{p_{cr,\,el}^{upper}}\right)^2 + \left(\frac{k_{pl}\,p_{cr,\,allow}}{p_{pl}}\right)^2 = 1, \tag{9.10.1a}$$

or

$$\left(\frac{k_{el}\,p_{cr,\,allow}}{p_{cr,\,el}^{upper}}\right)^2 + \frac{k_{pl}\,p_{cr,\,allow}}{p_{pl}} = 1. \tag{9.10.2a}$$

Expressing $p_{cr,\,\text{allow}}$ from these formulas we obtain:

$$p_{cr,\,\text{allow}} = \frac{p_{cr,\,el}^{\text{upper}}}{k_{el}} \sqrt{\frac{1}{1 + \left(\dfrac{k_{pl}}{k_{el}}\dfrac{p_{cr,\,el}^{\text{upper}}}{p_{pl}}\right)^2}}. \tag{9.10.1b}$$

or

$$p_{cr,\,\text{allow}} = \frac{p_{cr,\,el}^{\text{upper}}}{k_{el}} \left[\sqrt{\frac{1}{4}\left(\frac{k_{el}}{k_{pl}}\frac{p_{pl}}{p_{cr,\,el}^{\text{upper}}}\right)^4 - \left(\frac{k_{el}}{k_{pl}}\frac{p_{pl}}{p_{cr,\,el}^{\text{upper}}}\right)^2} \right.$$
$$\left. - \frac{1}{2}\left(\frac{k_{el}}{k_{pl}}\frac{p_{pl}}{p_{cr,\,el}^{\text{upper}}}\right)^2 \right]. \tag{9.10.2b}$$

If, for simplicity, we want to use a unique safety factor $k_{el,\,pl}=k$, this has to assume an intermediate value between k_{el} and k_{pl}. However, this assumption provides no transition to the analysis of failure without buckling.

The safety of the shell against buckling can be provided in the most simple way, if we consider the most onerous, extreme values of all effects, if we determine the critical load with these data and reduce it by a safety factor. This procedure may be called the "multiplication of the partial safety factors". By so doing we are certainly safe, but uneconomical, because we do not take into consideration that, as a rule, the most unfavourable values of the different data do not coincide.

The application of the probability theory yields a more exact method, see, e.g. in [9.2.2], [9.3.3]. Accordingly, the threshold value of the critical load to be applied in design is obtained by subtracting α times the resultant standard deviation from the mean value of the experimental results (or from the critical load computed with the mean values of all data). Here, α denotes a numerical value that depends on the fractile corresponding to the risk taken.

Hence, we can compute the safety factor from the formula:

$$k = \frac{k_0}{1 - \alpha S_r}. \tag{9.10.3}$$

Here k_0 denotes a "basic" safety factor that determines the measure by which we want to "draw apart" the upper extreme value (fractile) of the load and the lower extreme value (fractile) of the load bearing capacity. If the computation model and the actual structure agree fairly well, we may assume $k_0 = 1.10$. This value should be increased if the model or the computation are of an approximate nature.

The value of α depends on the probability according to which we want to choose the safety factor. In building practice a fractile of 2.5% is generally accepted [9.8.2], from which, assuming a normal distribution, it follows that $\alpha = 2.0$.

The S_r appearing in Eq. (9.10.1) is the resultant relative standard deviation, which can be defined by the following formulas:

for k_{pl}:

$$S_{r,pl} = \sqrt{S_{\text{load}}^2 + S_{pl}^2}$$

and for k_{el}:

$$S_{r,el} = \sqrt{S_{\text{load}}^2 + S_E^2 + S_\varphi^2 + S_{cr}^2}.$$

Here:

S_{load} — the relative standard deviation of the load;

S_{pl} — that of the plastic load bearing capacity of the structure (i.e. of the force causing plastic failure without buckling);

S_E — that of the effect of the modulus of elasticity of the concrete;

S_φ — that of the effect of the creep of the concrete;

S_{cr} — that of the critical load causing elastic buckling.

By "relative" we denote "normalized with respect to the mean value".

Since the relative standard deviations of both the load and the force causing plastic failure are about 10%, consequently $S_{\text{load}}=0.10$, $S_{pl}=0.10$.

For reinforced concrete shells we obtained from the data of Fig. 9.8.7 the value $S_{\text{exp}}=0.2$. The standard deviation of the critical loads of the cylindrical and spherical metal models (with decreasing post-buckling load bearing capacity) is about the same. We evaluated separately the data of the various authors, shown in Figs 2.3 and 4.2, in the range $300 < R/t < 1300$, and found that the standard deviation S_{exp}, that can be considered as equal to S_{cr}, was in every case less than 0.23. Hence we can assume $S_{cr}=0.23$.

(In the range $R/t < 300$ plastic deformations predominate, but the reports on these experiments did not publish enough results to take this effect into account. On the other hand, the range $R/t > 1300$ lies above the R/t ratios used in practice.)

The authors of [9.8.15] obtained from their very extensive test results performed on concrete dome models the average values $S_{\text{exp}}=0.12$ for instantaneous loading and $S_{\text{exp}}=0.20$ for long-time loading (creep buckling). Evaluating these tests, a value $S_\varphi=0.16$ for the standard deviation of the effect of the creep on the critical load is arrived at. Metal shells do not creep at normal temperatures, so that for them the value $S_\varphi=0$ is appropriate. (We have no usable data for the creep of metals at high temperatures.)

When calculating the modulus of elasticity $E_{c,0}$ from the nominal strength of the concrete, we automatically obtain a certain standard deviation for $E_{c,0}$. However, $E_{c,0}$ also shows an additional standard deviation, which proved to be $S_{E,c}=0.1$ in the evaluation of the experimental results published in [9.8.13]. For steel, half this value for the additional standard deviation can be assumed, i.e. $S_{E,s} \approx 0.05$.

Hence we obtain the following resultant standard deviations:

— for metal shells:

$$S_{r,el} = \sqrt{S_{\text{load}}^2 + S_E^2 + S_{cr}^2} = \sqrt{0.1^2 + 0.05^2 + 0.23^2} = 0.256,$$

and

$$S_{r,pl} = \sqrt{S_{load}^2 + S_{pl}^2} = \sqrt{0.1^2 + 0.1^2} = 0.14;$$

— for concrete and reinforced concrete shells:

$$S_{r,el} = \sqrt{S_{load}^2 + S_E^2 + S_\varphi^2 + S_{cr}^2} = \sqrt{0.1^2 + 0.1^2 + 0.16^2 + 0.23^2} = 0.314,$$

and

$$S_{r,pl} = \sqrt{S_{load}^2 + S_{pl}^2} = \sqrt{0.1^2 + 0.1^2} = 0.14.$$

These values yield, according to Eq. (9.10.3), the following safety factors for axially compressed cylinders and radially compressed spheres made of metals:

$$k_{el,decreasing} = \frac{1.10}{1-2(0.256)} = 2.25 \approx 2.30,$$

and

$$k_{pl} = \frac{1.1}{1-2(0.14)} = 1.53 \approx 1.55.$$

If we want to use a unique safety factor, the value $k=2.3$ can be assumed. For the aforementioned shells made of reinforced concrete we obtain:

$$k_{el,decreasing} = \frac{1.10}{2-2(0.314)} = 2.96 \approx 3.0,$$

and

$$k_{pl} = \frac{1.1}{2-2(0.14)} = 1.55.$$

As a unique safety factor $k=3.0$ can be assumed.

The post-critical load bearing capacity of unreinforced concrete shells is equal to zero, while shells made of steel and of reinforced concrete do have some load bearing capacity in the post-buckling range. Hence, it is reasonable to increase the basic safety factor k_0 by about 20%, i.e. to assume $k_0=1.35$.

We thus arrive at the values $k_{el}=3.7$, $k_{pl}=1.9$ and as a unique factor $k=3.7$ for concrete shells.

These safety factors should be increased

— if the theory used is only approximate;
— if the computation model does not agree with the actual structure;
— if the data on the material properties are not reliable enough.

We determined the critical loads of several erected large reinforced concrete domes described in [4.6], [9.10.1], [9.10.2], [9.10.3], [9.10.4], [9.10.5], and plotted them in Fig. 9.10.1, compared with their actual loads. These data show that most structures have a safety factor greater than two. Two domes exhibited a safety

Fig. 9.10.1. Safety factors of some erected reinforced concrete domes
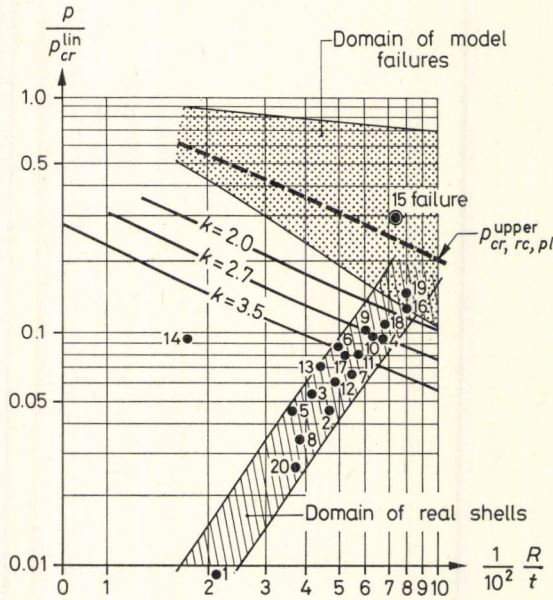
1. Jena, GDR	7. Windward, USA	14. Rome, Italy
2. Jena, GDR	8. Wales, GB	15. Gödöllő, Hungary
3. Matsuyama, Japan	9. Albuquerque, USA	16. Saloniki, Greece
4. Ingoviskoza Werke, FRG	10. Belgrade, Yugoslavia	17. Puerto Rico, USA
5. Hilling, USA	11. Belgrade, Yugoslavia	18. Cleadon, GB
6. Hamburg, FRG	12. Algeciras, Spain	19. Lyons, France
	13. Novosibirsk, SU	20. Massachusetts, USA

factor somewhat inferior to two, and one showed a safety factor inferior to one. This latter structure, in fact, collapsed. On the whole, a safety factor between 2.5 and 3.0 seems to be realistic for shells with decreasing post-buckling load bearing capacity.

However, this value of the safety factor is exaggerated for shell structures whose post-buckling load bearing capacity does not decrease. For structures with a constant load bearing capacity (Fig. 1.1 (a)), $S_{cr} \approx 0.18$ can be assumed. Consequently, the relative standard deviation of such metal shells becomes $S_r = 0.21$, and for their unique safety factor we obatin from Eq. (9.10.3) for metal shells:

$$k_{\text{constant}} = \frac{1.1}{1 - 2(0.21)} = 1.90.$$

For reinforced concrete shells $S_r=0.28$ and, consequently:

$$k_{constant} = \frac{1.1}{1-2(0.28)} = 2.50.$$

The safety factor of unreinforced concrete shells becomes:

$$k_{constant} = \frac{1.35}{1-2(0.28)} = 3.07 \approx 3.1.$$

In the case of an increasing post-buckling load bearing capacity, the "loss of stability" does not mean failure. Hence we can use the factor $k_{increasing} \geq 1.75$ for the benefit of safety.

For shells with post-buckling load bearing capacity decreasing at a lower rate than that of the axially compressed cylinder or the radially compressed sphere, some intermediate safety factor between $k_{constant}$ and $k_{decreasing}$ seems to be reasonable. With the aid of the value $\varrho_{hom}(0.5)$, characteristic of the rate of decrease (see Section 9.2), the following approximate interpolating formula can be set up:

$$k_{intermediate} \approx k_{constant} + (k_{decreasing} - k_{constant}) \frac{1 - \varrho_{hom}(0.5)}{0.75}.$$

For some values of $\varrho_{hom}(0.5)$ the safety factors are given in Table 9.10.1.

<center>Table 9.10.1.</center>

<center>Values of $k_{intermediate}$</center>

$\varrho_{hom}(0.5)$	0.25	0.50	0.75	1.00
Metal	2.30	2.17	2.04	1.90
Reinforced concrete	3.00	2.83	2.67	2.50
Unreinforced concrete	3.70	3.50	3.30	3.10

10. Numerical Examples

10.1. Buckling Analysis of a Reticulated Cylindrical Cooling Tower

Let us check the stability of a reticulated steel cooling tower, shown in Fig. 10.1. For the sake of simplicity, we shall investigate only the upper section of the tower with a characteristic mesh to be seen in Fig. 10.2. We shall take only vertical compressive forces into account. In conformity with what was said in Section 8.3, we shall substitute the reticulated structure by a statically equivalent continuum.
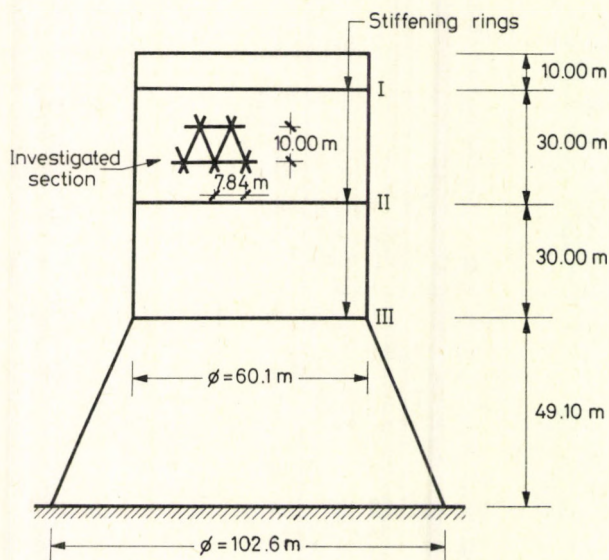
Fig. 10.1. Overall view of the reticulated cooling tower

The stiffening rings serve two purposes. First, they carry the ring-directed bending moments due to wind. Secondly, they stiffen the reticulated shell against buckling in the sense that they prevent the "overall-" and "free-edge-" type buckling modes described in detail in Section 5.4 for hyperbolic cooling towers. These
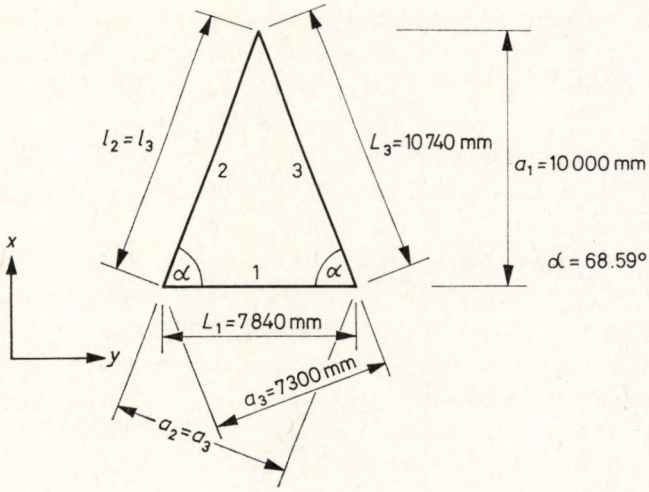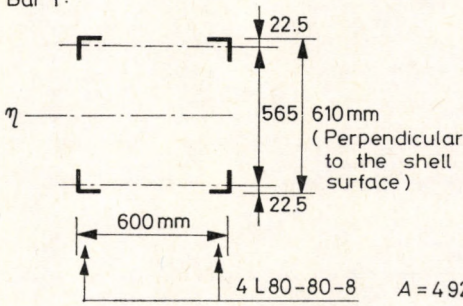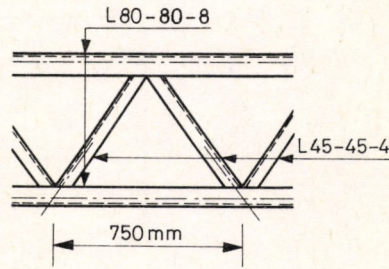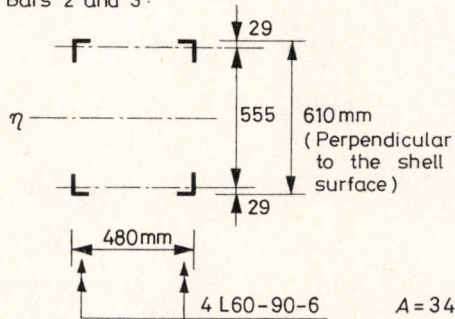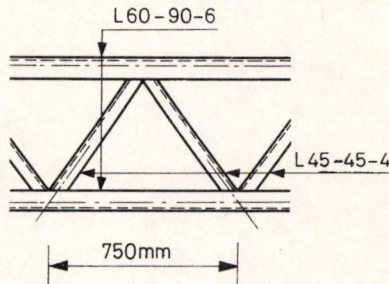
Fig. 10.2. Details of the reticulated shell

buckling modes may also occur on cylindrical shells with free edges, *cf.* the explanation after Eq. (2.14) and the low linear critical load for the cylinder with free edges. Hence, the stiffening rings should have a rigidity sufficiently great to comply with these two requirements.

Since the individual bars are themselves trusses, they can either be considered as unique bars and the structure as a single-layer grid, or we may regard the whole structure as a double-layer reticulated shell.

Considering the structure as single-layered, the extensional and bending rigidities of the grid, valid for the replacement continuum, can be computed from the data of the individual bars. Neglecting the torsional rigidities of the individual members (resulting in an error of about 3%), we obtain the rigidity characteristics of the equivalent orthotropic shell (see Eqs (7.1), (7.2) and (7.3)) from the formulas of [8.3.2] as follows:

Auxiliary quantities:

$$e_1 = \frac{EA_1}{a_1} = \frac{200 \text{ kN/mm}^2 (4920 \text{ mm}^2)}{10 \text{ m}} = 98.40 \text{ kN/mm},$$

$$e_2 = e_3 = \frac{EA_2}{a_2} = \frac{200 (3470)}{7.30} = 95.07 \text{ kN/mm},$$

$$i_1 = \frac{EI_1}{a_1} = \frac{200 \text{ kN/mm}^2 (3.9237) 10^8 \text{ mm}^4}{10 \text{ m}} = 7.8474 \text{ MN m},$$

$$i_2 = i_3 = \frac{EI_2}{a_2} = \frac{200 (2.6433) 10^8}{7.30} = 7.2419 \text{ MN m}.$$

The tensile stiffnesses become:

$$\bar{T}_x = e_1 + 2e_2 \cos^4 \alpha = 98.40 + 2(95.07) \cos^4 68.59° = 101.78 \text{ kN/mm},$$

$$\bar{T}_y = 2e_2 \sin^4 \alpha = 142.8 \text{ kN/mm},$$

$$\bar{T}' = 2e_2 \sin^2 \alpha \cos^2 \alpha = 21.96 \text{ kN/mm},$$

$$\bar{T}_{xy} = 2\bar{T}' = 43.92 \text{ kN/mm}.$$

From these we compute the equivalent rigidities according to Eqs (7.2):

$$T_x = 98.40 \text{ kN/mm},$$

$$T_y = 138.06 \text{ kN/mm},$$

$$T_{xy} = 47.16 \text{ kN/mm}.$$

The bending stiffnesses are:

$$\bar{B}_x = i_1 + 2i_2 \cos^4 \alpha = 8.1046 \text{ MNm},$$

$$\bar{B}_y = 2i_2 \sin^4 \alpha = 10.8809 \text{ MNm},$$

$$\bar{B}' = 2i_2 \sin^2 \alpha \cos^2 \alpha = 1.6728 \text{ MNm},$$

$$\bar{B}_{xy} = 2\bar{B}' = 3.3457 \text{ MNm}.$$

From these we obtain the equivalent rigidities:

$$B_x = 8.1046 \text{ MNm},$$

$$B_y = 10.8809 \text{ MNm},$$

$$B_{xy} = 5.0185 \text{ MNm},$$

The linear critical axial force is obtained from Eq (7.11) with $p=0$ by selecting that value of $\mu = l_x/l_y$ for which $n_{x,cr}^{lin}$ becomes a minimum. Performing the calculation for several μ-values we find:

$$n_{x,cr}^{lin} = 1.464 \text{ MN/m} \quad \text{for} \quad \mu = l_x/l_y = 0.94.$$

Since the flanges of the individual bars are connected by bracings (see Fig. 10.2), we compute their transverse shearing rigidity in order to assess the "sanwich-effect" (Section 8.1).

Calculating the shearing deformation of the bracing by the energy method yields

$$\varrho = 0.0985 \text{ m/MN}$$

for the continuum. The product $\varrho n_{cr,0}^{lin}$ thus assumes the value $0.1442 < 4$, so that the shell can be considered "rigid" against transverse shear. From Fig. 8.1.3 we read off the reduction factor for the linear critical load:

$$1 - 0.25(\varrho n_{cr,0}^{lin}) = 0.9640,$$

and we obtain the actual critical load, taking the sandwich-effect into account as well:

$$n_{x,cr}^{lin, sandw} = 0.964(1.464) = 1.411 \text{ MN/m}.$$

For assessing the reduction of $n_{x,cr}^{lin, sandw}$ due to initial imperfections we compute the parameter $1/\gamma$ (7.8):

$$\frac{1}{\gamma} = \frac{B_y T_x}{B_x T_y} = 0.957 \approx 1.0.$$

According to Fig. 7.7, the post-buckling behaviour of our orthotropic shell is very close to that of the isotropic one. In order to use the reduction factors for

the latter, plotted against w_0/t, we have to compute the wall thickness t' of the "equivalent" isotropic shell. If we now consider the structure as a double-layer reticulated shell, Eq. (8.3.4) clearly shows that t' is independent of the rigidity of the shell and depends only on the distance between the centroids of the two flanges (see Fig. 10.2):

$$t' = 0.56 \text{ m } \sqrt{3} = 0.97 \text{ m}.$$

(The same result is obtained from Eq. (8.3.1) of the single-layer shell, if GI_t is neglected.)

Assuming an initial imperfection of $w_0 = \pm 100$ mm we obtain:

$$w_0/t' = 0.1/0.97 \approx 0.10.$$

From Fig 2.7 or 2.8 we read off a reduction factor of 0.6. Consequently, the elastic upper critical load of the structure becomes:

$$n_{x,cr}^{\text{upper}} = 0.6 n_{x,cr}^{\text{lin, sandw}} = 0.6(1.411) = 0.847 \text{ MN/m}.$$

To assess the interaction of overall and local bucklings (Section 8.3.3) we compute the specific axial force causing buckling in one member.

Disregarding, for simplicity, the buckling of the flanges between the bracing bars, we obtain for the Euler critical force of the skew member 2 or 3 (Fig. 10.2):

$$F_E = \frac{\pi^2 EI}{l^2} = \frac{\pi^2 (200 \text{ kN/mm}^2) 2.6433(10^8) \text{ mm}^2}{(10.74 \text{ m})^2} =$$
$$= 4.523 \text{ MN}.$$

The compressive force causing plastic yielding of the same member is

$$F_{pl} = A\sigma_y = 3470 \text{ mm}^2 (240 \text{ N/mm}^2) = 833 \text{ kN}.$$

The force causing plastic buckling will be computed by Ritter's formula (equivalent to a Dunkerley-type relation:

$$\frac{1}{F_{cr,pl}} = \frac{1}{F_E} + \frac{1}{F_{pl}},$$

see e.g. in [2.32]):

$$F_{cr,pl} = \frac{F_E}{1 + \dfrac{F_E}{F_{pl}}} = \frac{4.523}{1 + \dfrac{4.523}{0.833}} = 0.703 \text{ MN}.$$

This corresponds to a specific axial load on the cylinder of the magnitude:

$$n_{x,pl} = \frac{2 F_{cr,pl} \sin 68.59°}{7.84 \text{ m}} = 0.1671 \text{ MN/m}.$$

Considering this value as n_{pl}, we may use Eqs (9.4.5) and (9.4.6) for assessing the interaction of (plastic) local buckling and overall shell buckling:

$$\zeta = \frac{0.1671}{0.847} \sqrt{\frac{1}{4}\left(\frac{0.1671}{0.847}\right)^2 + 1} - \frac{1}{2}\left(\frac{0.1671}{0.847}\right)^2 = 0.1788,$$

$$n_{x, cr, pl}^{upper} = 0.1788(0.847) = 0.1514 \text{ MN/m}.$$

The safety of the cylinder against buckling is thus sufficient if the actual axial load does not exceed 0.065 MN/m:

$$k = \frac{0.1514 \text{ MN/m}}{0.065 \text{ MN/m}} = 2.33 > 2.3.$$

10.2. Stability Analysis of a Reinforced Concrete Dome

Let us perform the stability analysis of the domes presented in [9.9.4], formed according to spherical surfaces with the radius $R=56.2$ m, over a square ground plan of 48×48 m (Fig. 10.3). The shells are supported by vertical arches which rest on column rows, so that the shells cannot exert lateral thrust. The shells have a thickness of 90 mm which increases to 200 mm in the corners. For lack of data we suppose that the shell wall has been thickened to 140 mm along the edges. They are made of concrete with cube strength of 22 N/mm², reinforced by mild St 37 steel ($\sigma_{ult}=370$ N/mm²). $\varnothing 6$ mm/250 mm reinforcing meshes were applied, in the central zone as single-layer reinforcement and along the edges in double
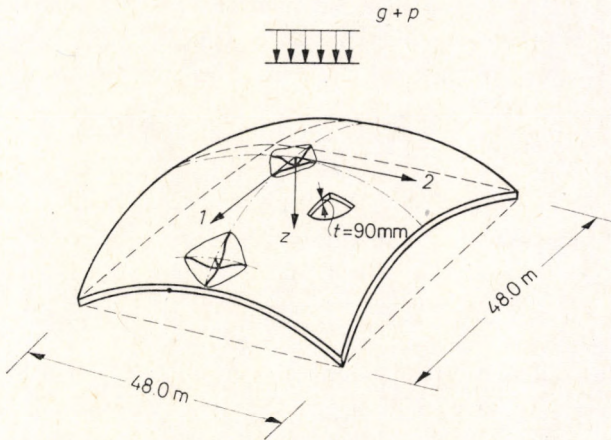
Fig. 10.3. Overall view of the reinforced concrete dome

layer arrangement near the surfaces of the shell wall. The area of reinforcement in one direction is, accordingly, 113 mm²/m in the single-layer and 226 mm²/m in the double-layer zone.

The reference mentioned above does not give the insulation, etc. layers of the structure. Hence we perform the weight analysis with estimated data, assuming 90 mm thickness in the central part of the shell, while near the edges, at the middle of the buckle to be expected, we take 140 mm thickness:

	Central part:	Near the edges:
10 mm damp course	0.15 kN/m²	0.15 kN/m²
90 mm cork heat insulation	0.14 kN/m²	0.14 kN/m²
r. c. shell	2.16 kN/m²	3.36 kN/m²
	2.45 kN/m²	3.65 kN/m²

We further assume 0.8 kN/m² snow load.
The prism strength of the concrete is:

$$\sigma_{prism} = 0.8\sigma_{cube} = 0.8\,(22) = 17.6 \text{ N/mm}^2.$$

The modulus of elasticity is given by Eq. (9.8.1):

$$E_{c,0} = 55000 \frac{17.6}{15+17.6} = 29700 \text{ N/mm}^2.$$

The final value of the creep factor is determined from Eq. (9.8.2):

$$\varphi_c = 4 - 2 \log 17.6 = 1.51.$$

Three quarters of the load consist of dead load while the remaining 25% is the snow load occurring only at a later date and for a not very long duration. Hence, we set $k_t = 0.5$ for the snow load and, to the benefit of safety, we assume $\bar{\varrho} = 1$. Accordingly, we may compute the modulus of deformation from Eq. (9.8.3b):

$$E_c = \frac{29700}{1 + \dfrac{0.75 + 0.5\,(0.25)}{0.75 + 0.25}\,1.51} = 12830 \text{ N/mm}^2.$$

The ratio of the moduli of deformation of steel and concrete is:

$$n = \frac{E_{st}}{E_c} = \frac{200000}{12830} = 15.6.$$

Due to the different stress states, the two kinds of reinforcement and the variable thickness, we have to investigate the stability of the shell at three places: in the middle of the shell, near the edges and in the corners. We present here the stability analyses at the centre and near the edge.

Stability analysis at the centre of the shell:

$$n\mu = 15.6 \frac{113}{90000} = 0.0196.$$

Interpolating from Table 9.8.1 we obtain

$$\psi_{0,1} = 1.000 + 0.025 \frac{0.0196}{0.050} = 1.010,$$

$$\psi_{\infty,1} = 0.139 \frac{0.0196}{0.050} = 0.0545.$$

In the middle part of the shell the bending moment is zero, hence the imperfection amplitude consists only of the accidental part: $w_{0,\text{design}} = w_{0,\text{accid}}$. Assuming an average value, we have from Eq. (9.2.7):

$$w_{0,\text{design}} = 0.05(90) + \frac{56200}{2000} \left(\frac{1}{\dfrac{5620/9}{1000} + \dfrac{1000}{5620/9}} \right) = 17.12 \text{ mm}.$$

$$e_{0,\text{design}} = 0.67(17.12) = 11.47 \text{ mm}.$$

Equation (9.8.13) yields:

$$\varrho_c = \left[1 - \frac{2(11.47)}{90} \right]^{\frac{3}{2}(1+1.5)} = 0.333,$$

and from Eq. (9.2.1) and Table 9.1.1 we obtain

$$\varrho_{\text{hom}} = \frac{1}{1 + 6\dfrac{17.12}{9}} = 0.467.$$

Equation (9.8.15) gives:

$$\varrho_{rc} = 1.005(0.441) + 0.0545(0.467 - 0.333) = 0.342,$$

Equation (4.7):

$$p_{cr,\text{hom}}^{\text{lin}} = 1.2 \frac{12830(90)^2}{(56200)^2} = 0.0395 \text{ N/mm}^2 = 39.5 \text{ kN/m}^2,$$

Equation (9.8.16):

$$p_{cr,rc} = 0.342(39.5) = 13.51 \text{ kN/m}^2.$$

We compute the plastic failure load neglecting the reinforcement, assuming a 10 mm tolerance in the thickness and considering only that part of the concrete cross section on which the load is acting centrally:

$$p_{pl} \approx \frac{2\sigma_{\text{prism}} t}{R} \left(1 - \frac{2e_0}{t} \right) = \frac{2(17.6)80}{56200} \left[1 - \frac{2(11.47)}{80} \right] =$$
$$= 0.03574 \text{ N/mm}^2 = 35.74 \text{ kN/m}^2,$$

18 Buckling of Shells

Equation (9.4.4):

$$\zeta = \frac{35.74}{13.51}\sqrt{\frac{1}{4}\left(\frac{35.74}{13.51}\right)^2 + 1} - \frac{1}{2}\left(\frac{35.74}{13.51}\right)^2 = 0.887.$$

Hence, the upper critical load of the reinforced concrete shell becomes:
Equation (9.8.20):

$$p_{cr,rc}^{upper,\,pl} = 0.887(13.51) = 11.98 \text{ kN/m}^2.$$

The load perpendicular to the shell surface consists of the shell's own weight and the snow load:

$$p_{actual} = 2.45 + 0.8 = 3.25 \text{ kN/m}^2.$$

The safety factor thus becomes:

$$k = \frac{p_{cr,rc}^{upper,\,pl}}{p_{actual}} = \frac{11.98}{3.25} = 3.69 > 3.0$$

which is sufficient.

Stability analysis near the edges:

(Here we shall show the use of the separated safety factors k_{el} and k_{pl}.)

$$n\mu = \frac{15.6(226)}{14000} = 0.0252.$$

Interpolating from Table 9.8.1:

$$\psi_{0,2} = 1.000 + 0.052\,\frac{0.0252}{0.050} = 1.026,$$

$$\psi_{\infty,2} = 0.178\,\frac{0.0252}{0.050} = 0.0897.$$

The membrane forces, in the vicinity of the maximum amplitude of the buckle to be expected, have approximately the following values:

$$n_2 \approx 1.5\,\frac{pR}{2}; \quad n_1 \approx 0.5\,\frac{pR}{2},$$

so that $n_2/n_1 = 0.33$.
We read off Fig. 4.18 that

$$p_{cr,hom}^{lin} = 0.8\,\frac{Et^2}{R^2} = 0.8\,\frac{12830(140)^2}{(56200)^2} = 0.0637 \text{ N/mm}^2 =$$

$$= 63.7 \text{ kN/m}^2.$$

From Eq. (9.2.3) we obtain:

$$\varrho_{hom}(0.5) \approx \frac{1}{6}\left[1+5\frac{0.108(1.2)}{0.8}\right] = 0.30,$$

Equation (9.2.2): $\qquad A \approx 2\left(\frac{1}{0.3}-1\right) = 4.63.$

Due to the restraining effect of the columns, we may consider the edge of the shell as clamped. The eccentricity at the place of the maximum positive bending moment can be taken from [9.4.2]:

$$e_{calc} = 0.133t = 0.133(140) = 18.62 \text{ mm}. \quad w_{calc} \approx \frac{18.62}{0.67} = 27.8.$$

$$w_{acc} = 0.05(140) + \frac{56200}{2000}\left(\frac{1}{\frac{56200/140}{1000}+\frac{1000}{56200/140}}\right) = 13.6 \text{ mm}.$$

$$e_{acc} = 0.67(13.6) = 9.1 \text{ mm}.$$

We obtain the eccentricity of the membrane forces from Eq. (9.2.4):

$$e_0 = 19.62+0.8(9.1) = 25.9 \text{ mm},$$

and the amplitude of the imperfection:

$$w_0 = \frac{25.9}{0.67} = 38.7 \text{ mm}.$$

Furthermore:

Equation (9.8.13): $\qquad \varrho_c = \left(1-2\frac{25.9}{140.0}\right)^{\frac{3}{2}(1+1.5)} = 0.177,$

Equation (9.2.1):

$$\varrho_{hom} = \frac{1}{1+4.63\frac{w_0}{t}} = \frac{1}{1+4.63\frac{38.7}{140.00}} = 0.439,$$

Equation (9.8.15):

$$\varrho_{rc} = 1.013(0.177)+0.089(0.439-0.177) = 0.203,$$

Equation (9.8.16): $\qquad p_{cr,rc} = 0.203(63.7) = 12.92 \text{ kN/m}^2,$

$$p_{pl} = \frac{2\sigma_{prism}t}{R}\left(1-2\frac{e_0}{t}\right) =$$

$$= \frac{2(17.6)13.0}{5620.0}\left(1-2\frac{2.59}{13.0}\right) = 0.049 \text{ N/mm}^2 \rightarrow 49 \text{ kN/m}^2.$$

The safety factors are: $k_{el}=3.0$, $k_{pl}=1.55$, and $p_{cr,\,allow}$ is given by Eq. (9.10.2b):

$$p_{cr,\,allow} =$$

$$= \frac{12.92}{3.0}\left[\frac{49.00}{12.92}\left(\frac{3.0}{1.55}\right)\sqrt{\frac{1}{4}\left(\frac{49.00}{12.92}\right)^2\left(\frac{3.0}{1.55}\right)^2+1}-\frac{1}{2}\left(\frac{49.00}{12.92}\right)^2\left(\frac{3.0}{1.55}\right)^2\right] = 4.22.$$

The component of the load perpendicular to the shell surface is computed (with α as the angle of the surface) as

$$p_{prep} = g_{own\,weight}\cos\alpha + p_{snow}\cos^2\alpha =$$

$$= 3.65\,(0.904)+0.8\,(0.904)^2 = 3.95 \text{ kN/m}^2.$$

Since $p_{perp} < p_{cr,\,allow}$, the safety of the shell against buckling is sufficient.

List of Figures Taken from Other Sources

References

Chapter 1

[1.1] Fung, Y. C. and Sechler, E. E., Instability of Thin Elastic Shells. Structural Mechanics, (Proc. 1st Symp. Naval Struct. Mech., Stanford Univ. Calif. 1958) 115—168. Pergamon Press, Oxford–London–New York–Paris, 1960

[1.2] Hoff, N. J., Some Recent Studies of the Buckling of Thin Shells. Aeronaut. Journ. (London) **73** 1057–70 (1969)

[1.3] Hutchinson, J. W. and Koiter, W. T., Postbuckling Theory. Applied Mechanics Reviews **23** 1353–66 (1970)

[1.3a] Budiansky, B. and Hutchinson, J. W., A Survey of Some Buckling Problems. AIAA Journal **4** 1505–1510 (1966)

[1.4] Nash, W. A., Instability of Thin Shells. Applied Mechanics Surveys. Spartan Books, Washington, D. C., 1966

[1.4a] Nash, W. A., Recent Advances in the Buckling of Thin Shells. Applied Mechanics Reviews **13** 161–164 (1960)

[1.5] Handbook of Structural Stability. Edited by the Column Research Committee of Japan. Corona Publ. Co. Ltd. Tokyo, 1971

[1.6] Brush, D. O. and Almroth, B. O., Buckling of Bars, Plates and Shells. McGraw-Hill, New York, 1975.

[1.7] Thompson, J. M. T. and Hunt, G. W., A General Theory of Elastic Stability. John Wiley & Sons, London–New York–Sydney–Toronto, 1973.

[1.8] Tvergaard, V., Buckling Behaviour of Plate and Shell Structures. Theoretical and Applied Mechanics. (Preprints of the IUTAM Congress, Delft, 1976.) Ed.: Koiter. North-Holland, Amsterdam–New York–Oxford, 1976

Chapter 2

[2.1] Almroth, B. O., Postbuckling Behavior of Axially Compressed Circular Cylinders. AIAA Journ. **1** 630–633 (1963)

[2.2] Almroth, B. O., Influence of Imperfections and Edge Restraint on the Buckling of Axially Compressed Cylinders. NASA CR–432. April, 1966

[2.3] Batdorf, S. B., A Simplified Method of Elastic-Stability Analysis for Thin Cylindrical Shells. I. Donnell's Equation, NACA TN 1341, 1947. II. Modified Equilibrium Equation, NACA TN 1342, 1947

[2.4] Budiansky, B., Post-Buckling Behavior of Cylinders in Torsion. Theory of Thin Shells. (IUTAM, Second Symposium, Copenhagen, 1967) Ed.: Niordson. Springer, Berlin–Heidelberg–New York, 212–233, 1969

[2.5] Budiansky, B. and Amazigo, J. C., Initial Post-Buckling Behavior of Cylindrical Shells under External Pressure. Journ. Math. Phys. **47** 223–235 (1968)

[2.6] Bürgermeister, G., Steup, H. and Kretschmar, H., Stabilitätstheorie, Teil II. Akademie-Verlag, Berlin, 1963

[2.6a] Chwalla, E. and Kollbrunner, C. F., Beiträge zum Knickproblem des Bogenträgers und des Rahmens. Stahlbau, **11** 73–78, 81–84, 94–96 (1938)

[2.7] Dierks, K., Zur Kreiszylinderschale unter Manteldruck. Abhdl. der Braunschweigischen Wissenschaftl. Gesellschaft. **17** 139–153 (1965)

[2.8] Donnell, L. H., A New Theory for the Buckling of Thin Cylinders under Axial Compression and Bending. Transactions ASME **56** 795 (1934)

[2.9] Donnell, L. H. and Wan, C. C., Effect of Imperfections on Buckling of Thin Cylinders and Columns under Axial Compression. Journ. Appl. Mech. **17** 73–83 (1950)

[2.10] Donnell, L. H., Effect of Imperfections on Buckling of Thin Cylinders under External Pressure. Journ. Appl. Mech. **23** 569–575 (1956)

[2.11] Donnell, L. H., Effect of Imperfections on Buckling of Thin Cylinders with Fixed Edges under External Pressure. Proc. 3rd U. S. Nat. Congr. Appl. Mech. New York. American Society of Mechanical Engineers, 1958

[2.12] Dulácska, E., Experimental Determination of the Critical Load of Shell Structures. Proc. Symposium IASS (Budapest, 1965). Építéstudományi Intézet, Budapest, 1965

[2.13] Dulácska, E., Vibration and Stability of Anisotropic Shallow Shells. Acta Techn. Acad. Sci. Hung. **65** 225–260 (1969)

[2.14] Dym, C. L. and Hoff, N. J., Perturbation Solutions for the Buckling Problems of Axially Compressed Thin Cylindrical Shells of Infinite or Finite Length. Journ. Appl. Mech. **35** 754–762 (1968)

[2.15] Esslinger, M., Hochgeschwindigkeitsaufnahmen vom Beulvorgang dünnwandiger, axialbelasteter Zylinder. Stahlbau **39** 73–75 (1970)

[2.16] Fischer, G., Über den Einfluss der gelenkigen Lagerung auf die Stabilität dünnwandiger Kreiszylinderschalen unter Axiallast und Innendruck. Zeitschrift für Flugwissenschaften **11** 111–119 (1963)

[2.17] Flügge, W., Statik und Dynamik der Schalen, 3. Aufl. Springer, Berlin, 1962

[2.17a] Flügge, W., Stresses in Shells. Springer, Berlin–Heidelberg–New York, 1973

[2.17b] Harris, L. A., Suer, H. S., Suene, W. T. and Bendjamen, R. J., The Stability of Thin-walled Unstiffened Circular Cylinders. Journ. Aeronaut. Sci. **24** No. 8 (1947)

[2.18] Hoff, N. J., Madsen, W. A. and Mayers, J., Postbuckling Equilibrium of Axially Compressed Circular Cylindrical Shells. AIAA Journ. **4** 126–133 (1966)

[2.19] Hoff, N. J. and Soong, T. C., Buckling of Circular Cylindrical Shells in Axial Compression. Int. Journ. Mech. Sci. **7** 489–520 (1965)

[2.20] Hutchinson, J., Axial Buckling of Pressurized Imperfect Cylindrical Shells. AIAA Journ. **3** 1461–66 (1965)

[2.21] Kármán, Th. von and Tsien, H. S., The Buckling of Thin Cylindrical Shells under Axial Compression. Journ. Aeronaut. Sci. **9** 303–312 (1941)

[2.22] Kempner, J., Postbuckling Behavior of Axially Compressed Circular Cylindrical Shells. Journ. Aeronaut. Sci. **21** 329–335 (1954)

[2.23] Kirste, L., Abwickelbare Verformung dünnwandiger Kreiszylinder. Österr. Ing. Archiv **8** 149–151 (1954)

[2.24] Koiter, W. T., Over de stabiliteit van het elastisch evenwicht. (On the stability of the elastic equilibrium.) Thesis, Delft. H. J. Paris, Amsterdam, 1945. English translation: NASA, Techn. Transl. F 10 833, 1967

[2.25] Koiter, W. T., Elastic Stability and Post-Buckling Behavior. Proc. Symp. Nonlinear Problems. University of Wisconsin Press, Madison 257–275 (1963)

[2.26] Koiter, W. T., The Effect of Axisymmetric Imperfections on the Buckling of Cylindrical Shells under Axial Compression. Proc. Royal Netherlands Academy of Sciences, Amsterdam, Series B, Vol. **66** 265–279 (1963)

[2.27] Korányi, I., Stabilitási kérdések a mérnöki gyakorlatban. Kihajlás a síkban. (Stability Problems in Engineering Practice, Buckling in the Plane.) Akadémiai Kiadó, Budapest, 1965

[2.28] Kromm, A., Jahrbuch der Deutschen Luftfahrt-Forschung. p. 1832, 1940

[2.29] Leggett, D. M. A. and Jones, R. P. N., The Behaviour of a Cylindrical Shell under Axial Compression when the Buckling Load has been Exceeded. Aeronautical Research Council, London, R. & M. 2190, (1942)

[2.30] Litle, W. A., Reliability of Shell Buckling Predictions. Research Monograph No. 25. Cambridge, Mass., M. I. T. Press, 1964

[2.31] Loo, T. T., Effects of Large Deflections and Imperfections on the Elastic Buckling of Cylinders under Torsion and Axial Compression. Proc. 2nd U. S. Nat. Congr. Appl. Mech. New York, American Society of Mechanical Engineers, 345–357, 1955

[2.32] Lundgren, H., Cylindrical Shells. Vol. 1. Copenhagen. The Institution of Danish Civil Engineers, 1960

[2.33] Madsen, W. A. and Hoff, N. J., The Snap-through and Post-buckling Equilibrium Behavior of Circular Cylindrical Shells under Axial Load. Stanford University, Department of Aeronautics and Astronautics, Report No. 227, Stanford, California (1965)

[2.34] Mayers, J. and Rehfield, L. W., Further Nonlinear Considerations in the Postbuckling Behavior of Axially Compressed Circular Cylindrical Shells. Proc. 9th Midwestern Mechanics Conference (Wisconsin, Madison, 1965) John Wiley & Sons, New York, 1967

[2.35] Menyhárd, I., Héjszerkezetek számítása és szerkesztése. (Analysis and design of shell structures.) Műszaki Könyvkiadó, Budapest, 1966

[2.36] Michielsen, H. F., The Behavior of Thin Cylindrical Shells after Buckling under Axial Compression. Journ. Aeronaut. Sci. **15** 738–744 (1948)

[2.37] Narasimhan, K. Y. and Hoff, N. J., Snapping of Imperfect Thin-Walled Circular Cylindrical Shells of Finite Length. Journ. Appl. Mech. **38** 162–171 (1971)

[2.38] Nash, W. A., Buckling of Initially Imperfect Cylindrical Shells Subject to Torsion. Journ. Appl. Mech. **24** 215–130 (1957)

[2.39] Neufville, R. L., de and Connor, J. J. jr., Postbuckling Behavior of Thin Cylinders. Journ. Eng. Mech. Divis. (Proc. ASCE) **94** EM2, 585–602 (1968)

[2.39a] Pearson, C. E., General Theory of Elastic Stability. Quart. Appl. Math. **14** 133–144 (1956)

[2.40] Pflüger, A., Stabilitätsprobleme der Elastostatik. Springer, Berlin–Göttingen–Heidelberg, 1950

[2.41] Pflüger, A., Zur praktischen Berechnung der axial gedrückten Kreiszylinderschale. Stahlbau **32** 161–165 (1963)

[2.42] Pflüger, A., Zur praktischen Berechnung der Kreiszylinderschale unter Manteldruck. Stahlbau **35** 249–252 (1966)

[2.43] Ponomarev, S. D., Raschety na prochnost' v mashinostroenii. Tom. 7. Ustoĭchivost'. Rezinovye elementy. Mashgiz, Moskva, 1959

[2.44] Schnell, W., Zur Stabilität dünnwandiger längsgedruckter Kreiszylinderschalen bei zu-
        sätzlichem Innendruck. Proc. Symp. Theory of Thin Elastic Shells (Delft, 1959).
        North-Holland Publ. Co., Amsterdam, 167–188, 1960
[2.45] Seide, P. and Weingarten, V. I., On the Buckling of Circular Cylindrical Shells under
        Pure Bending. Journ. Appl. Mech. **28** 112–116 (1961)
[2.45a] Sendelbeck, R. S. and Hoff, N. J., Loading Rig in Which Axially Compressed Thin
        Cylindrical Shells Buckle Near Theoretical Values. Experimental Mechanics **12**
        372–376 (1972)
[2.45b] Simitses, G. J. and Aswani, M., Buckling of Thin Cylinders under Uniform Lateral
        Loading. Journ. Appl. Mech. **41** 827–829 (1974)
[2.45c] Singer, J. and Babcock, C. D., On the Buckling of Rings under Constant Directional
        and Centrally Directed Pressure. Journ. Appl. Mech. **37** 215–218 (1970)
[2.46] Stein, M., Some Recent Advances in the Investigation of Shell Buckling. AIAA Journ.
        6 2339–45 (1968)
[2.47] Sturm, R. G., A Study of the Collapsing Pressure of Instability of Thin-Walled Cylinders.
        Bulletin No. 329. University of Illinois Engineering Experimental Station (1941)
[2.48] Tennyson, R. C., Buckling Modes of Circular Cylindrical Shells under Axial Compression.
        AIAA Jorun. **7** 1481–87 (1969)
[2.49] Thielemann, W. and Esslinger, M., Einfluss der Randbedingungen auf die Beullast von
        Kreiszylinderschalen. Stahlbau **33** 353–361 (1964)
[2.50] Thielemann, W. and Esslinger, M., Beul- und Nachbeulverhalten isotroper Zylinder unter
        Aussendruck. Stahlbau **36** 161–175 (1967)
[2.51] Timoshenko, S. P. and Gere, J. M., Theory of Elastic Stability. McGraw-Hill, New York,
        1961
[2.52] Voblykh, V. A., O vliianii nachal'nykh otkloneniĭ na velichinu kriticheskoĭ nagruzki dlia
        krugovykh tsilindricheskih obolochek. Prikladnaia Mekhanika **1** 17–26 (1965)
[2.53] Weingarten, V. I., Morgan, E. J. and Seide, P., Elastic Stability of Thin-Walled Cylindrical
        and Conical Shells under Axial Compression. AIAA Journ. **3** 500–505 (1965)
[2.54] Weingarten, V. I. and Seide, P., Elastic Stability of Thin-Walled Cylindrical and Conical
        Shells under Combined External Pressure and Axial Compression. AIAA Journ. **3**
        913–920 (1965)
[2.55] Windenburg, D. E. and Trilling, C., Collapse by Instability of Thin Cylindrical Shells
        under External Pressure. Trans. Am. Soc. Mech. Engrs. **56** 819–825 (1934)
[2.56] Wlassow, W. S., Allgemeine Schalentheorie und ihre Anwendung in der Technik. Akade-
        mie-Verlag, Berlin, 1958
        Vlasov, V. Z., Obshchaia teoriia obolochek i ee prilozheniia v tekhnike. Gostekhizdat,
        Moskva, 1949
[2.57] Wolmir, A. S., Biegsame Platten und Schalen. Verlag für Bauwesen, Berlin, 1962
        Vol'mir, A. S., Gibkie plastinki i obolochki. Gostekhizdat, Moskva, 1956
[2.58] Yamaki, N., Otomo, K. and Matsuda, K., Experiments on the Postbuckling Behavior of
        Circular Cylindrical Shells under Compression. Experimental Mechanics **15** 23–28
        (1975)
[2.59] Yamaki, N., Experiments on the Postbuckling Behavior of Circular Cylindrical Shells
        under Torsion. In: Buckling of Structures (IUTAM Symposium Cambridge – USA,
        1974). Ed. B. Budiansky. Springer-Verlag, Berlin–Heidelberg–New York, 1976.
[2.60] Yamaki, N. and Matsuda, K., Postbuckling Behavior of Circular Cylindrical Shells under
        Torsion. Ing.-Archiv **45** 79–89 (1976)

Chapter 3

[3.1] Baruch, M., Harari, O. and Singer, J., Low Buckling Loads of Axially Compressed Conical Shells. Journ. Appl. Mech. **37** 384–392 (1790)

[3.2] Lackman, L. and Penzien, J., Buckling of Circular Cones under Axial Compression. Journ. Appl. Mech. **27** 458–460 (1960)

[3.3] Niordson, F. I. N., Buckling of Conical Shells Subjected to Uniform External Lateral Pressure. Transactions of the Royal Institute of Technology, Stockholm. No. 10. 1947

[3.4] Seide, P., Axisymmetrical Buckling of Circular Cones under Axial Compression. Journ. Appl. Mech. **23** 625–628 (1956)

[3.5] Seide, P., On the Buckling of Truncated Conical Shells under Uniform Hydrostatic Pressure. Proc. Symp. Theory of Thin Elastic Shells (Delft, 1959). North-Holland Publ., Amsterdam, 1960

[3.6] Seide, P., The Stability of Thin Conical Frustrums Subjected to Axial Compression and External Pressure. TRW Space Technology Labs., Inc. (1960) Unpublished

[3.7] Sendelbeck, R. L. and Singer, J., Further Experimental Studies of Buckling of Electroformed Conical Shells. AIAA Journ. **8** 1532–34 (1970)

Chapter 4

[4.1] Adam, H. P. and King, P. A., Experimental Investigation of the Stability of Monocoque Domes Subjected to External Pressure. Experimental Mechanics **5** 313–320 (1965)

[4.2] Archer, R. R. and Famili, J., On the Vibration and Stability of Finitely Deformed Shallow Spherical Shells. Journ. Appl. Mech. **32** 116–120 (1965)

[4.2a] Buchert, K. P., Buckling of Shells and Shell-like Structures. K. P. Buchert and Assoc., Columbia, 1973

[4.3] Budiansky, B., Buckling of Clamped Shallow Spherical Shells. Proc. Symp. Theory of Thin Elastic Shells (Delft, 1959). North-Holland Publ., Amsterdam, 1960

[4.4] Bushnell, D., Nonlinear Axisymmetric Behavior of Shells of Revolution. AIAA Journ. **5** 432–439 (1967)

[4.4a] Bushnell, D., Buckling of Spherical Shells Ring-Supported at the Edges. AIAA Journ. **5** 2041–46 (1967)

[4.5] Carlson, R. L., Sendelbeck, R. L. and Hoff, N. J., Experimental Studies of the Buckling of Complete Spherical Shells. Experimental Mechanics **7** 281–288 (1967)

[4.5a] Chien, H. K. and Lien, W., The Nonlinear Elastic Stability of Elliptical Paraboloid Shallow Shells under Uniform External Load. Scientia Sinica **2** 273 (1966)

[4.6] Csonka, P., The Buckling of a Spheroidal Shell Curved in Two Directions. Acta Techn. Acad. Sci. Hung. **14** 425–437 (1956)

Die Verformung und nachträgliche Verstärkung einer kuppelartigen Schale in Ungarn. Bautechnik **35** 69–72 (1958)

[4.7] Danielson, D. A., Buckling and Initial Postbuckling Behavior of Spheroidal Shells under Pressure. AIAA Journ. **7** 936–944 (1969)

[4.7a] Dostanova, S. Kh. and Raĭzer, V. D., Issledovanie ustoĭchivosti pologih obolochek polozhitel'noĭ krivizny metodom lokal'nykh variatsiĭ. Stroit. Mekh. i. Rasch. Sooruzh. 34–39 (1973)

[4.8] Dulácska, E., On the Critical Load of Shells. IASS Bulletin, No. 39. (Sept. 1969) 31–36

[4.9] Evan-Iwanowski, R. M. and Loo, T. C., Deformations and Stability of Spherical Shells under Action of Concentrated Loads and Uniform Pressure. Techn. Report 834 (11), No. 4. Syracuse University Research Institute, 1962

[4.9a] Famili, J. and Archer, R. R., Finite Asymmetric Deformation of Shallow Spherical Shells. AIAA Journ. 3 506–510 (1965)

[4.9b] Fitch, J. R., The Buckling and Postbuckling Behavior of Spherical Caps under Concentrated Loads. Int. Journ. Solids Struct. 4 421–446 (1968)

[4.9c] Fitch, J. R. and Budiansky, B., Buckling and Postbuckling Behavior of Spherical Caps under Axisymmetric Loads. AIAA Journ. 8 686–693 (1970)

[4.10] Friedrichs, K. O., On the Minimum Buckling Load for Spherical Shells. Th. v. Kármán Anniversary Vol. 1941. p. 258

[4.10a] Gabril'iants, A. G. and Feodos'ev, F. I., Ob osesimmetrichnykh formakh ravnovesiia uprugoĭ sfericheskoĭ obolochki, nakhodiashcheisia pod deĭstviem ravnomerno raszpredelennogo davleniia. Prikl. Mat. i. Mekh. 25 No. 6 (1961)

[4.10b] Galletly, G. D., On the Buckling of Shallow Spherical Caps Subjected to Uniform External Pressure. AIAA Journ. 14 1331—1333 (1976)

[4.11] Hergenröder, A. and Rüsch, H., Recent Findings in the Testing of Models. Proc. Symp. Shell Research, (Delft, 1961) North-Holland Publ., Amsterdam, 1961

[4.12] Homewood, R. H., Brine, A. C. and Johnson, A. E. Jr., Experimental Investigations for the Buckling Instability of Monocoque Shells. Proc. Soc. Experimental Stress Analysis 18 88–96 (1961)

[4.13] Huang, N. C., Unsymmetrical Buckling of Thin Shallow Spherical Shells. Journ. Appl. Mech. 31 447–457 (1964)

[4.14] Hutchinson, J. W., Imperfection Sensitivity of Externally Pressurized Spherical Shells. Journ. Appl. Mech. 34 49–55 (1967)

[4.15] Hyman, B. I. and Healey, J. J., Buckling of Prolate Spheroidal Shells under Hydrostatic Pressure. AIAA Journ. 5 1469–77 (1967)

[4.16] Kao, R. and Perrone, N., Asymmetric Buckling of Spherical Caps with Asymmetrical Imperfections. Journ. App. Mech. 38 172–178 (1971)

[4.16a] Kao, R., A Note on Buckling of Spherical Caps with Initial Asymmetric Imperfections. Journ. Appl. Mech. 39 842–844 (1972)

[4.17] Kaplan, A. and Fung, Y. C., A Nonlinear Theory of the Bending and Buckling of Thin Elastic Shallow Shells. NACA TN 3212 (1954)

[4.18] Kármán, Th. von and Tsien, H. S., The Buckling of Spherical Shells by External Pressure. Journ. Aeronaut. Sci. 7 43 (1939)

[4.19] Klöppel, K. and Jungbluth, O., Beitrag zum Durchschlagproblem dünnwandiger Kugelschalen. (Versuche und Bemessungsformeln.) Stahlbau 22 121–130 (1953)

[4.20] Klöppel, K. and Roos, E., Beitrag zum Durchschlagproblem dünnwandiger, versteifter und unversteifter Kugelschalen für voll- und halbseitige Belastung. Stahlbau 25 49–60 (1956)

[4.21] Koga, T. and Hoff, N. J., The Axisymmetric Buckling of Initially Imperfect Complete Spherical Shells. Int. Journ. Solids Struct. 5 679–697 (1969)

[4.22] Koiter, W. T., The nonlinear Buckling Problem of a Complete Spherical Shell under Uniform External Pressure, I, II, III, and IV. Proc. Kon. Nederl. Akad. Wet. Series B. 72 40–123 (1969)

[4.23] Koten, H., van and Haas, A. M., The Influence of the Edge Stiffness and of the Angle of Aperture on the Stability of a Spherical Shell. Large-span Shells. (Proc. IASS-Congr. Leningrad, 1966) Tsinis, Moscow. 1968

[4.24] Koten, H. van and Haas, A. M., The Stability of Doubly Curved Surfaces Having a Positive Gaussian Curvature Index. Heron, 17 No. 4 (1970–71)

[4.25] Krenzke, M. A. and Kiernan, T. J., Elastic Stability of Near-Perfect Shallow Spherical Shells. AIAA Journ. 1 2855–57 (1963)

[4.25a] Loo, T. C. and Evan-Iwanowski, R. M., Interaction of Critical Pressures and Critical Concentrated Loads Acting on Shallow Spherical Shells. Journ. Appl. Mech. 33 612–616 (1966)

[4.26] Mushtari, H. M. and Surkin, R. G., O nelineĭnoĭ teorii ustoĭchivosti uprugogo ravnovesiia sfericheskoĭ obolochki pri deĭstvii ravnomerno raspredelennogo vneshnego davleniia. Prikl. Mat. i. Mekh. 14 573 (1950)

[4.26a] Mushtari, Kh. M., K teorii ustoĭchivosti sfericheskoĭ obolochki pod deĭstviem vneshnego davleniia. Prikl. Mat. i Mekh. 19 No. 2 (1955)

[4.27] Neut, A., van der, De elastische stabiliteit van de dunwandige bol. (The elastic stability of the thin-walled sphere.) Thesis. Delft, 1932

[4.28] Parmerter, R. R., The Buckling of Clamped Shallow Spherical Shells under Uniform Pressure. Thesis. California Institute of Technology, 1963

[4.28a] Pozo Frutos, F., del and Pozo Vindel, F., del, Elastic Buckling of Non-perfect Spherical Shells of Constant Thickness. Proc. IASS World Congress, Madrid, 1, 1.173–1.179 1979

[4.28b] Rauch, H. E., Jacobs, N. H. and Marz, J. L., Buckling of a Complete Spherical Shell Under Uniform External Pressure. Studies in Appl. Math. 58 141–158 (1978)

[4.28c] Reissner, E., On Axisymmetric Deformations of Thin Shells of Revolution. Proc. of Symposia in Applied Mathematics. 3 27–52 (1950) McGraw-Hill, New York–Toronto–London

[4.29] Schmidt, H., Ergebnisse von Beulversuchen mit doppelt gekrümmten Schalenmodellen aus Aluminium. Proc. Symp. Shell Research (Delft, 1961), North-Holland Publ., Amsterdam, 1961

[4.30] Schubiger, E., Die Schalenkuppel im vorgespannten Beton der Kriche Felix und Regula in Zürich. Schweizerische Bauzeitung, 68 223–228 (1950)

[4.31] Seaman, L., The Nature of Buckling in Thin Spherical Shells. Thesis. Cambridge, Mass. Department of Civil Engineering, M. I. T., 1961

[4.32] Simitses, G. J. and Cole, R. T., Effect of Load Behavior on the Buckling of Thin Spherical Shells under Pressure. Journ. Appl. Mech. 35 420–422 (1968)

[4.33] Stenker, H., Gesamtbericht von Grossversuchen an doppelt gekrümmten Montageschalen für raumabschliessende Geschossdecken. Wissensch. Zeitschr. Hochschule für Architektur und Bauwesen Weimar, 8 181–202 (1961)

[4.33a] Sunakawa, M., A Note on the Stability of Shells. Proceedings of the 22nd Japanese National Congress of Applied Mechanics, 1972. Published in: Theoretical and Applied Mechanics, 22, University of Tokyo Press, Tokyo, Japan, 1974

[4.33b] Sunakawa, M. and Ichida, K., A High Precision Experiment on the Buckling of Spherical Caps Subjected to External Pressure. Institute of Space and Aeronautical Science Report No. 508, March 1974, University of Tokyo, Tokyo, Japan

[4.34] Thompson, J. M. T., The Elastic Instability of a Complete Spherical Shell. Aeronaut. Quart. 13 189–201 (1962);

The Post-Buckling of a Spherical Shell by Computer Analysis. Proc. World Conference on Shell Structures, San Francisco, 1961. National Academy of Sciences, Washington, D. C., 1964

[4.35] Thurston, G. A., A Numerical Solution of the Nonlinear Equations for Axisymmetric Bending of Shallow Spherical Shells. Journ. Appl. Mech. **28** 557–568 (1961)

[4.36] Thurston, G. A., A New Method for Computing Axisymmetric Buckling of Spherical Caps. Journ. Appl. Mech. **38** 179–184 (1971)

[4.37] Thurston, G. A. and Penning, F. A., Effect of Axisymmetric Imperfections on the Buckling of Spherical Caps under Uniform Pressure. AIAA Journ. **4** 319–327 (1966)

[4.38] Tsien, H. S., A Theory for the Buckling of Thin Shells. Journ. Aeronaut. Sci. **9** 373–384 (1941)

[4.39] Wang, L. R. L., Discrepancy of Experimental Buckling Pressures of Spherical Shells. AIAA Journ. **5** 357–359 (1967)

[4.40] Wang, L. R. L., Rodriquez-Agrait, L. and Litle, W. A., Effect of Boundary Conditions on Shell Buckling. Journ. Eng. Mech. Divis. (Proc. ASCE) **92** EM6 101–116 (1966)

[4.41] Wedellsborg, B. W., Critical Buckling Load on Large Spherical Shells. Journ. Struct. Divis. (Proc. ASCE) **88** ST1 111–121 (1962)

[4.42] Weinitschke, H. J., On Asymmetric Buckling of Shallow Spherical Shells. Journ. Math. Phys. **44** 141–163 (1965)

[4.43] Zoelly, R., Über ein Knickproblem an der Kugelschale. Thesis. Zürich, 1915

Chapter 5

[5.1] Aimond, F., Etude statique des voiles minces en paraboloide hyperbolique travaillant sans flexion. Publ. IABSE, **4** (1936)

[5.1a] Apeland, K., A Note on the Stability Problem of Shallow Translational Shells. Journ. Appl. Mech. **27** 586–588 (1960)

[5.2] Cole, P. P., Abel, J. F. and Billington, D. F., Buckling of Cooling Tower Shells: State-of-the-Art. Journ. Struct. Divis. (Proc. ASCE) **101** ST6 1185–1203 (1975)

[5.3] Cole, P. P., Abel, J. F. and Billington, D. P., Buckling of Cooling Tower Shells: Bifurcation Results. Journ. Struct. Divis. (Proc. ASCE) **101** ST6 1205–1222 (1975)

[5.4] Der, T. J. and Fidler, R., A Model Study of the Buckling Behavior of Hyperbolic Shells. Proc. Inst. Civ. Eng. **41** 105 (1968)

[5.5] Dulácska, E., Vibration and Stability of Anisotropic Shallow Shells. Acta Techn. Acad. Sci. Hung. **65** 225–260 (1969)

[5.5a] Dulácska, E., Buckling of the Saddle-shaped Hypar Acting like an Arch. Acta Techn. Acad. Sci. Hung. **91** 441—417 (1980)

[5.6] Dulácska, E., Nagy, J. and Bódi I., Overall Buckling of Hyperbolic Shells of Revolution. with Unmovable Lower Edges. Acta Techn. Acad. Sci. Hung. **92** 167—187 (1981)

[5.7] Flügge, W. and Geyling, F. T., A General Theory of Deformations of Membrane Shells. Publ. IABSE **17** 23–46 (1957)

[5.8] Geyling, F. T., A General Theory of Deformations of Membrane Shells. Thesis. Stanford University, Stanford, Calif. 1953

[5.9] Gioncu, V. and Ivan, M., Instabilitatea structurilor din plăci curbe subțiri. (Buckling of shell structures.) Ed. Acad. Republ. Soc. România, 1978

[5.10] Hampe, E., Kühltürme. Verlag Bauwesen, Berlin, 1975

[5.10a] Hauptenbuchner, B., Zur Stabilität einer hyperbolischen Paraboloidschale. Thesis. Technische Universität Dresden, 1978

[5.11] Hayman, B. and Chilver, A. R., The Effect of Structural Degeneracy on the Stability of Cooling Towers. Proc. IASS Colloquium on Cooling Towers. Brussels, May 1971

[5.12] Hutchinson, J. W., Initial Post-buckling Behavior of Toroidal Shell Segments. Int. Journ. Solids, Struct. **3** 97–115 (1967)

[5.13] Jankó, L., Analyse der Verhältnisses zwischen Membran- und Biegeschnittkräften in Sattel-förmigen, flachen, normalkraftfrei gelagerten HP-Schalen unter gleichmässig verteilter Belastung. Acta Techn. Acad. Sci. Hung. **91** 19—55 (1980)

[5.14] Jankó, L., Untersuchung der Stabilität sattelförmiger, flacher, normalkraftfrei gelagerter HP-Schalen unter gleichmässig verteilter Belastung. Acta Techn. Acad. Sci. Hung. **91** 265–301 (1980)

[5.15] Jankó, L., Untersuchung der Gleichgewichtszustände sattelförmiger, flacher, normalkraft-frei gelagerter HP-Schalen unter gleichmässig verteilter Belastung, mit besonderer Berücksichtigung des Durchschlagens und der Abzweigung. Acta Techn. Acad. Sci. Hung. **91** 419—467 (1980)

[5.15a] Jankó, L., Initial Postbuckling Behaviour of Shallow Saddle-shaped Hypar Shells, Supported by Shear Diaphragms, under Uniform Load. Acta Techn. Acad. Sci. Hung. **91** 419–467 (1980)

[5.16] Kaluza, R. and Mateja, O., Problems of the Influence of Irregular Displacements of Foundation on the State of Stress and Displacement of a Hyperboloidal Cooling Tower. IASS-Bulletin No. **62** 47–59 (1976)

[5.17] Kohli, J., Beitrag zum axialsymmetrischen Ausbeulen einer einschaligen Hyperboloid-schale. Thesis. Karslruhe, 1968

[5.18] Kollár, L., Die dehnungslosen Formänderungen von Schalen. Konstruktiver Ingenieur-bau-Berichte **20**. Ruhr-Universität Bochum. Vulkan-Verlag W. Classen, Essen, 1974

[5.19] Krätzig, W., Statische und dynamische Stabilität der Kühlturmschale. Naturzug-Kühl-türme. Konstruktiver Ingenieurbau-Berichte **1**. Ruhr-Universität Bochum. Vulkan-Verlag W. Classen, Essen, 1968

[5.20] Krätzig, W. B., Grosse Naturzug-Kühltürme aus Stahlbeton. VGB Kraftwerkstechnik **55** 191–197 (1975)

[5.21] Langhaar, H. L., Boresi, A. P. and Miller, R. E., Stability of Hyperboloidal Cooling Tower. Journ. Eng. Mech. Divis. (Proc. ASCE) **95** EM5 753–779 (1970)

[5.22] La Tegola, A., Sulla stabilità dell'equilibrio del giuscio piatto a forma di paraboloide iper-bolico. Giornale del Genio Civile **105** 809–817 (1967)

[5.23] Leet, K. M., Study of Stability in the Hyperbolic Paraboloid. Journ. Eng. Mech. Divis. (Proc. ASCE) **92** EM1 169–181 (1966)

[5.23a] Lehmkämper, O., Versteifte Kühlturmschalen aus Stahlbeton. Technisch-wissenschaft-liche Mitteilungen Nr. 78-6. Institut für Konstruktiven Ingenieurbau, Ruhr-Univer-sität Bochum, 1978

[5.23b] Leone, D. J. and Wang. L. R.-L., Buckling of Hyperbolic Paraboloid Shells. Journ. Eng. Mech. Divis. (Proc. ASCE) **101** EM3 295–299 (1975)

[5.24] Lukasievich, S. and Szyszkowski, W., On the Stability and Post-buckling Equilibrium of Shells of Revolution. Zeitschr. angew, Math. Mech. **8** 635 (1971)

[5.25] Mateja, O., O badaniach nad statecznoscią hiperboloidalnych chłodni wieżowych. (Analysis of the static properties of hyperbolic cooling towers.) Inżynierie i budownictwo **23** 428–431 (1966)

[5.26] Mungan, I., Buckling Stress States of Hyperboloidal Shells. Journ. Struct. Divis. (Proc. ASCE) **102** ST10 2005—20 (1976)

[5.27] Rabich, R., Die Membrantheorie der einschalig hyperbolischen Rotationschalen, Baupla-nung-Bautechnik **7** 310–320 (1953)

[5.28] Ralston, A., On the Problem of Buckling of a Hyperbolic Paraboloidal Shell Loaded by Its Own Weight. Journ. Math. Phys. **35** 53–59 (1956)

[5.29] Reissner, E., On Some Aspects of the Theory of Thin Elastic Shells. Journ. Boston Soc. Civ. Eng. **17** 100–133 (1956)

[5.30] Rosemeier, G., Zur Stabilität von Hypar- und Hyperboloidschalen. Bauingenieur **48** 437–444 (1973)

[5.31] Veronda, D. R. and Weingarten, V. I., Stability of Hyperboloidal Shells. Journ. Struct. Divis. (Proc. ASCE) **101** ST7 1585–1602 (1975)

[5.32] Vlaszov, V. Z. and Garai, T., Nyomatékmentes forgáshéjak kinematikai határozatlanságának feltétele. (Condition for the kinematic indeterminacy of momentless shells of revolution.) A Magyar Tudományos Akadémia VI. Műszaki Oszt. Közl. **19** 211–223. (1956)

[5.33] Walther, H. J. and Wölfel, R., Stabilitätsverhalten hyperbolischer Kühlturmschalen unter Windbelastung. Bauplanung-Bautechnik **32** 510–512 (1978)

[5.34] Wianeczki, J., Stabilité d'une coque en forme d'hyperboloide de révolution sous des charges uniformément réparties sur les bords et symétriques par rapport à son axe. Cahiers de la Rech. **19** (1965)

[5.35] Wittek, U., Überblick und theoretische Einführung in das Stabilitätsverhalten von Kühlturmschalen. Kühlturm-Symposium 1977. Konstruktiver Ingenieurbau-Berichte **29/30**. Ruhr-Universität Bochum. Vulkan-Verlag W. Classen, Essen, 1977

[5.36] Yeh, C. H. and Shieh, W. Y. J., Stability and Dynamic Analysis of Cooling Tower. Journ. Power Divis. (Proc. ASCE) **99** PO2 339–347 (1973)

Chapter 6

[6.1] Brazier, L. G., On the Flexure of Thin Cylindrical Shells and Other ,,Thin" Sections. Proc. Royal Society, London, Ser. A. **116** 104–114 (1927)

[6.2] Chwalla, E., Kippung von Trägern mit einfachsymmetrischen, dünnwandigen und offenen Querschnitten. Sitzunsgberichte der Akademie der Wissenschaften in Wien, Abt. II. a, 153, H. 1–10, 1944

[6.3] Dulácska, E., Stability of Eccentrically Compressed Shell-arches. Acta Techn. Acad. Sci. Hung. **45** 351–359 (1964)

[6.4] Kármán, Th., von, Über die Formänderung dünnwandiger Rohre, insbesondere federnder Ausgleichsrohre. VDI-Zeitschrift **55** 1889–95 (1911)

[6.5] Kollár, L., Statik und Stabilität der Schalenbogen und Schalenbalken, W. Ernst und Sohn, Berlin–München–Akadémiai Kiadó, Budapest, 1973

[6.6] Szittner, A., A Budapesti Sportcsarnok modellkísérlete. (Model test for the Budapest Sports Hall.) Az IASS magyar tagozatának héjszerkezeti kollokviuma, Budapest, 1968. Nov. Építéstudományi Intézet. 203–219

[6.7] Weinel, E., Über Biegung und Stabilität eines doppelt gekrümmten Plattenstreifens. Zeitschr. angew. Math. Mech. **17** 366–369 (1937)

Chapter 7

[7.1] Almroth, B. O., Postbuckling Behavior of Orthotropic Cylinders under Axial Compression. AIAA Journ. **2** 1795–99 (1964)

[7.2] Baruch, M. and Singer, J., Instability of Conical Shells. Aeronaut. Quart. **16** 187–204 (1965)

[7.3] Bodner, S. R., General Instability of a Ring-Stiffened Circular Cylindrical Shell under Hydrostatic Pressure. Journ. Appl. Mech. **24** 269–277 (1957)

[7.4] Bushnell, D., Symmetric and Nonsymmetric Buckling of Finitely Deformed Eccentrically Stiffened Shells of Revolution. AIAA Journ. **5** 1455–62 (1967)

[7.5] Crawford, R. F. and Schwartz, D. B., General Instability and Optimum Design of Grid-Stiffened Spherical Domes. AIAA Journ. **3** 511–515 (1965)

[7.6] Dulácska, E., Stability of Anisotropic Hyperbolic Paraboloid Shells. Acta Techn. Acad. Sci. Hung. **59** 123–130 (1967)

[7.7] Ebner, H., Angenäherte Bestimmung der Tragfähigkeit radial versteifter Kugelschalen unter Druckbelastung. Proc. IUTAM-Symposium on the Theory of Thin Elastic Shells, North-Holland Publ. Co., Amsterdam, 95–121, 1960

[7.8] Fischer, M., Versuche zur Ermittlung des Tragverhaltens einer hyperbolischen Paraboloid-schale aus einlagigen Trapezprofilblechen. Stahlbau, **41** 110–115, 145–150 (1972)

[7.9] Gerard, G., Compressive Stability of Orthotropic Cylinders. Journ. Aerospace Sci. **29** 1171–79 (1962)

[7.10] Girkmann, K., Flächentragwerke. 5. Aufl. Springer, Wien, 1959

[7.11] Hayashi, T., Torsional Buckling of Orthogonal Anisotropic Cylinders. 8th Int. Congr. of Appl. Mech. 1952

[7.12] Holston, A., Buckling of Inhomogeneous Anisotropic Cylindrical Shells by Bending. AIAA Journ. 9 1837–41 (1968)

[7.13] Krolak, M., Stateczność ortotropowej powłoki stożkowej ściskanej osiowo – w ujęciu nieliniowyn. (The stability of orthotropic conical shells under axial compressive load according to the nonlinear theory.) Archivum Budowy Maszyn **16** 333–351 (1969)

[7.14] Lakshmikantham, C. and Gerard, G., Minimum Weight Design of Stiffened Cylinders. Aeronaut. Quart. **21** 45–68 (1970)

[7.15] Mah, G. B., Almroth, B. O. and Pittner, E. V., Buckling of Orthotropic Cylinders. AIAA Journ. 6 598–602. (1968)

[7.16] March, H. W., Buckling of Long Thin Plywood Cylinders in Axial Compression. Forest Prod. Laboratory, Rep. No. 1322-A. (Sept. 1943)

[7.17] McDermott, J. F., Single-Layer Corrugated-Steel-Sheet Hypars. Journ. Struct. Divis. (Proc. ASCE) **94** ST6 1279–93 (1968)

[7.18] Meyer, R. R. and Bellifante, R. J., Fabrication and Experimental Evaluation of Common Cones Having Waffle-like Stiffening. Douglas Aircraft Corp. Rept. SM–47742 (Nov. 1964)

[7.19] Milligan, R., Gerard, G. and Lakshmikantham, C., General Instability of Orthotropically Stiffened Cylinders under Axial Compression. AIAA Journ. **4** 1906–13 (1966)

[7.20] Milligan, R. and Gerard, G., General Instability of Orthotropically Stiffened Cylinders under Torsion. AIAA Journ. **5** 2071–73 (1967)

[7.20a] Reese, C. D. and Bert, C. W., Buckling of Orthotropic Sandwich Cylinders under Axial Compression and Bending. Journ. Aircraft. **11** 207–212 (1974)

[7.21] Schapitz, E., Festigkeitslehre für den Leichtbau. 2. Aufl. VDI-Verlag, Düsseldorf, 1963

[7.22] Schnell, W. and Brühl, Ch., Die längsgedrückte orthotrope Kreiszylinderschale bei Innendruck. Zeitschr. Flugwiss. **7** 201–207 (1959)

[7.23] Schulz, V., Zur Beulstabilität anisotroper Zylinderschalen aus glasfaserverstärktem Kunststoff. Bauingenieur 47 157–163 (1972)

[7.24] Simitses, G., Instability of Orthotropic Cylindrical Shells under Combined Torsion and Hydrostatic Pressure. AIAA Journ. 5 1463–69 (1967)

[7.25] Singer, J. and Fersht, R., Buckling of Orthotropic Conical Shells under External Pressure. Journ. Appl. Mech. 29 212–214 (1962)

[7.26] Singer, J., Buckling of Orthotropic and Stiffened Conical Shells. NASA TN. Collected Papers on Instability of Shell Structures, 463–479, 1962

[7.27] Singer, J., The Influence of Stiffener Geometry and Spacing on the Buckling of Axially Compressed Cylindrical and Conical Shells. Theory of Thin Shells. IUTAM Symposium Copenhagen, 1967. Springer, Berlin–Heidelberg–New York, 1969. 234–263

[7.28] Singer, J., Arbocz, J. and Babcock, Ch. D., Buckling of Imperfect Stiffened Cylindrical Shells under Axial Compression AIAA Journ. 9 68–75 (1971)

[7.29] Stein, M., Sanders, J. L. and Crate, H., Critical Stress of Ring-Stiffened Cylinders in Torsion. NACA Report No. 989 (1951)

[7.29a] Tennyson, R. C., Chan, H. K. and Muggeridge, D. B., The effect of Axisymmetric Shape Imperfections on the Buckling of Laminated Anisotropic Circular Cylinders. Canadian Aeronautics Space Inst. Trans. of Inst. 4 131–139 (1971)

[7.30] Thielemann, W. F., New Developments in the Nonlinear Theories of the Buckling of Thin Cylindrical Shells. Aeronautics and Astronautics. Proc. Durand Centennial Conference at Stanford University (1959). Pergamon Press, Oxford–London–New York–Paris, 1960

[7.31] Timoshenko, St. and Woinowsky-Krieger, S., Theory of Plates and Shells. (Second Edition). McGraw-Hill Book Comp., New York–Toronto–London, 1959

[7.32] Weller, T. and Singer, J., Further Experimental Studies on Buckling of Integrally Ring-Stiffened Cylindrical Shells under Axial Compression. Experimental Mechanics 14 267–273 (1974)

Chapter 8

[8.1.1] Allen, H. G., Analysis and Design of Structural Sandwich Panels. Pergamon Press, Oxford–London–Edinburgh–New York–Toronto–Sydney–Paris–Braunschweig, 1969

[8.1.2] Habip, L. M., A Survey of Modern Developments in the Analysis of Sandwich Structures. Appl. Mech. Reviews 18 (1965)

[8.1.3] Hegedűs, I., Buckling of Axially Compressed Cylindrical Sandwich Shells. Acta Techn. Acad. Sci. Hung. 89 377–387 (1979)

[8.1.4] Lin, M. S. and Popov, E. P., Buckling of Spherical Sandwich Shells. Experimental Mechanics 9 433–440 (1969)

[8.1.5] March, H. and Kuenzi, E., Buckling of Cylinders of Sandwich Construction. Forest Products Lab., Rep. 1830 (Dec. 1957)

[8.1.6] Plantema, J. P., Sandwich Construction. The Bending and Buckling of Sandwich Beams, Plates, and Shells. John Wiley and Sons, New York–London–Sydney, 1966.

[8.1.7] Sylvester, R. J., Buckling of Sandwich Cylinders under Axial Load. Journ. Aeronaut. Sci. 29 863–872 (1962)

[8.1.8] Teichmann, F. K., Wang, C. and Gerard, G., Buckling of Sandwich Cylinders under Axial Compression. Journ. Aeronaut. Sci. 18 398–406 (1951)

[8.1.9] Yao, J. C., Buckling of Sandwich Sphere under Normal Pressure. Journ. Aeronaut. Sci. 29 264–305 (1962)

[8.2.1] Baruch, M. and Singer, J., Effect of Eccentricity of Stiffeners on the General Instability of Stiffened Cylindrical Shells under Hydrostatic Pressure. Journ. Mech. Eng. Sci. **5** 23–27 (1963)

[8.2.2] Biezeno, C. B. and Grammel, R., Technische Dynamik. 2. Auflage, Bd. I., Springer-Verlag, Berlin–Göttingen–Heidelberg, 1953

[8.2.2a] Block, D. L., Card, M. F. and Mikulas, M. M., Buckling of Eccentrically Stiffened Orthotropic Cylinders. NASA Langley Research Center, TN D–2960 (August, 1965)

[8.2.2b] Byskov, E. and Hutchinson, J. W., Mode Interaction in Axially Stiffened Cylindrical Shells. AIAA Journ. **15** 941–48 (1977)

[8.2.2c] Card, M. F. and Jones, R. M., Experimental and Theoretical Results for Buckling of Eccentrically Stiffened Cylinders, NASA TN D–3639 (Oct. 1966)

[8.2.3] Chwalla, E., Die Formeln zur Berechnung der "voll mittragenden Breite" dünner Gurt- und Rippenplatten. Stahlbau **9** 73–78 (1936)

[8.2.3a] Dulácska, E. and Kollár, L., Augenäherte Berechnung des Momentenzuwachses und der Stabilität von gedrückten Rahmenstielen. Die Bautechnik **37** 98–109 (1960)

[8.2.3b] Dulácska, E. Vasbeton faltartók tervezési kérdései (Design problems of reinforced concrete wall-beams). Mélyépítéstudományi Szemle **16** 466–475 (1966)

[8.2.4] Ebner, H., Theorie und Versuche zur Festigkeit von Schalenrümpfen. Luftfahrt-Forschung **14** 93–115 (1937)

[8.2.4a] Esslinger, M. and Geier, B., Postbuckling Behavior of Structures. Springer-Verlag, Wien–New York, 1975 (CISM Courses and Lectures No. 236)

[8.2.5] Geier, B., Beullasten versteifter Kreiszylinderschalen. Jahrbuch 1965 der Wissenschaftlichen Gesellschaft für Luft und Raumfahrt, 440–447

[8.2.6] Giencke, E., Die Grundgleichungen für die orthotrope Platte mit exzentrischen Steifen. Stahlbau **24** 128–129 (1955)

[8.2.6a] Hedgepeth, J. M. and Hall, D. B., Stability of Stiffened Cylinders. AIAA Journ. **3** 2275–86 (1965)

[8.2.6b] Hutchinson, J. W. and Amazigo, J. C., Imperfection-Sensitivity of Eccentrically Stiffened Cylindrical Shells. AIAA Journ. **5** 392–401 (1967)

[8.2.7] Jankó, L., Die mit den Längsrippen mitwirkende Breite der Zylinderschale. Acta Techn. Acad. Sci. Hung. **84** 97–124 (1977)

[8.2.8] Koiter, W. T., Buckling and Post-Buckling Behaviour of a Cylindrical Panel under Axial Compression. National Luchtvaartlaboratorium (Nat. Aeron. Res. Inst.) Amsterdam, Report S. **476** (1956)

[8.2.8a] MacNeal, R. H., Winemiller, A. F. and Bailie, J. A., Elastic Stability of Cylindrical Shells Reinforced by One or Two Frames and Subjected to External Radial Pressure., AIAA Journ. **4** 1431–33 (1966)

[8.2.9] Marguerre, K., Die mittragende Breite der gedrückten Platte. Luftfahrt-Forschung **14** 121–128 (1937)

[8.2.9a] Murzewski, J., Load-Carrying Capacity of Stiffened Non-circular Cylinders in Bending. Bull. Acad. Polonaise des Sciences. **15** No. 8 495–504 (1967)

[8.2.10] Neut, A. van der, The General Instability of Stiffened Cylindrical Shells under Axial Compression. Nationaal Luchtvaartlaboratorium (Nat. Aeron. Res. Inst.) Amsterdam, Report S. 314 (1947)

[8.2.11] Pflüger, A., Zum Beulproblem der anisotropen Rechteckplatte. Ing.-Archiv **16** 111–120 (1947)

[8.2.12] Pflüger, A., Das Beulproblem der orthotropen Platte mit Hohlsteifen. Zeitschr. Flugwiss. **5** 178–181 (1957)

[8.2.12a] Rehfield, L. W., Design of Stiffened Cylinders to Resist Axial Compression. Journ. Spacecraft & Rockets **10** 346–349 (1973)

[8.2.12b] Shanley, F. R., Simplified Analysis of General Instability of Stiffened Shells in Pure Bending. Journ. Aeronaut. Sci. **16** 590–592 (1949)

[8.2.13] Sinegr, J., Baruch, M. and Harari, O., Inversion of the Eccentricity Effect in Stiffened Cylindrical Shells Buckling under External Pressure, Journ. Mech. Eng. Sci. **8** 363–373 (1966)

[8.2.13a] Singer, J. and Haftka, R. T., Buckling of Discretely Stringer-Stiffened Cylindrical Shells and Elastically Restrained Panels. AIAA Journ. **15** 847–850 (1975)

[8.2.14] Singer, J., Meer, A. and Baruch, M., Buckling of Cylindrical Panels under Lateral Pressure. Aeronaut. Journ. (London) **73** 169–172 (1969)

[8.2.15] Stuhlmann, C., De Luzio, A. and Almroth, B., Influence of Stiffener Eccentricity and End Moment on Stability of Cylinder in Compression. AIAA Journ. **4** 872–877 (1966)

[8.2.16] Tamate, O. and Sekine, H., Post-Buckling Behaviour of Thin Curved Panels under Axial Compression. Bulletin Japan. Soc. Mech. Engrs. **12** 415–420 (1969)

[8.2.17] Trenks, K., Beitrag zur Berechnung orthogonal anisotroper Rechteckplatten, Bauingenieur **29** 372–377 (1954)

[8.2.18] Walker, A. C., Interactive Buckling of Structural Components. Sci. Progr. Oxf. **62** 579–597 (1975)

[8.2.19] Wang, J. T. S. and Lin, Y. J., Stability of Discretely Stringer-Stiffened Cylindrical Shells. AIAA Journ. **11** 810–814 (1973)

[8.2.20] Yang, T. Y. and Kunoo, K., Buckling of Cylindrical Shells with Smeared-Out and Discrete Orthogonal Stiffeners. AIAA Journ. **15** 1704–1711 (1977)

[8.3.1] Forman, S. E. and Hutchinson, J. W., Buckling of Reticulated Shell Structures. Int. Journ. Solids Struct. **6** 909–932 (1970)

[8.3.2] Kerek, A., Berechnung von einschichtigen, auf Biegung beanspruchten, anisotropen Fachwerkschalen. Acta Techn. Acad. Sci. Hung. **79** 383–411 (1974)

[8.3.3] Kollár, L. and Hegedűs, I., Analysis and Design of Space Frames by the Continuum Method. Elsevier, Amsterdam and Akadémiai Kiadó, Budapest (in the press).

[8.3.4] Lind, N. C., Local Instability Analysis of Triangulated Dome Frameworks. Struct. Eng. **47** 317–324 (1969)

[8.3.5] Wright, D. T., Membrane Forces and Buckling in Reticulated Shells. Journ. Struct. Divis. (Proc. ASCE) **91** ST1 173–201 (1965)

[8.3.6] Wright, D. T., A Continuum Analysis for Double Layer Space Frame Shells. Publ. IABSE **26** (1966)

[8.4.1] Abdel-Sayed, G., Critical Shear Loading of Curved Panels of Corrugated Sheets. Journ. Eng. Mech. Divis. (Proc. ASCE) **96** EM6 (1970) 895–911

[8.4.2] Kollár, L., On the Extensional Rigidities of Corrugated and Folded Shells. Wood, Ferrocoment and Plastics in Shells and Spatial Structures. Proc. IASS Symposium (Ed. P. A. Tupamäki) University of Oulu, Oulu, Finland, June 1980

[8.4.3] McDermott. J. F., Single-Layer Corrugated-Steel-Sheet Hypars. Journ. Struct. Divis. (Proc. ASCE) **94** ST6 (1968) 1279–93

[8.4.4] Nilson, H. A., Light Gage Steel Sheet Roofs. World Conference on Shells Structures Proc. San Francisco, Calif. 1962

Chapter 9

[9.1.1] Dulácska, E., Der Steifigkeitskennwert der Schalenbeulung. Acta Techn. Acad. Sci. Hung. **87** 457–467 (1978)

[9.2.1] Árbócz, J., The Effect of General Imperfections on the Buckling of Cylindrical Shells. Journ. Appl. Mech. **30** 28–38 (1960)

[9.2.2] Bolotin, V. V., Statistische Methoden in der Baumechanik. Deutsche Bauinformation. Deutsche Bauakademie zu Berlin. Schriftenreihe der Bauforschung. Reihe Technik und Organisation **44** Berlin, 1972
Bolotin, V. V., Statisticheskie metody v stroitel'noĭ mekhanike, Moskva, Stroĭizdat, 1965

[9.2.3] Dickie, J. F.–Broughton, P., Stability Criteria for Shallow Arches. Journ. Eng. Mech. Divis. (Proc. ASCE) **97** EM3 951–965 (1971)

[9.2.4] Dulácska, E., Die bei der Untersuchung des Beulverhaltens von Schalen in Betracht zu ziehende Anfangsausmittigkeit. Acta Techn. Acad. Sci. Hung. **86** 157–167 (1978)

[9.2.5] Wang, St. S-K., Plastic Buckling of Point-loaded Spherical Shells. Journ. Eng. Mech. Divis. (Proc. ASCE) **97** EM1 77–93 (1971)

[9.3.1] Dulácska, E., Die Beulung von Stahlbetonschalen. Acta Tech. Acad. Sci. Hung. **86** 93–115 (1978)

[9.3.2] Dulácska, E., Buckling of Reinforced Concrete Shells. Journ. Struct Divis. (Proc. ASCE) **107** ST 12 2381—2401 (1981)

[9.3.3] Dulácska, E., Explanation of the Chapter on Stability of the "Recommendations for Reinforced Concrete Shells and Folded Plates", and a Proposal to its Improvement. IASS Bulletin, **77** (1982)

[9.4.1] Dulácska, E., Praktische Stabilitätsuntersuchung von zentrisch gedrückten Tragwerken aus Material mit veränderlichem Elastizitätsmodul. Bautechnik **49** 340–345 (1972)

[9.4.2] Dulácska, E., Buckling of Elastic-Plastic Shells. IASS-Bulletin No. 68 (Dec. 1978) 15–20

[9.4.3] Emerton, R. K. and Morris, N. F., Symmetric Buckling of Inelastic Spherical Shells. Journ. Eng. Mech. Divis. (Proc. ASCE) **98** EM6 1417–31

[9.4.4] Grimaldi, A., Sull'Imbozzamento Elasto-Plastico dei Cilindri in Parete Sottile. (On the elasto-plastic buckling of thin-walled cylinders.) Giornale del Genio Civile **111** 83–107 (1973)

[9.4.5] Herber, K. H., Vorschlag von Berechnung für Beul- und Traglasten von Schalen. Stahlbau **35** 142–151 (1966)

[9.4.6] Hutchinson, J. W., On the Postbuckling Behavior of Imperfection-sensitive Structures in the Plastic Range. Journ. Appl. Mech. **39** 155–162 (1972)

[9.4.7] Ježek, K., Die Festigkeit von Druckstäben aus Stahl. Springer, Wien, 1937

[9.4.8] Kaganov, M. E. and Manevich, A. I., Osesimmetrichnoe vypuchivanie uprugoplasticheskikh tsilindricheskikh obolochek. Stroitelnaya Mekhanika i Raschet Sooruzhenĭ No. 2 (Apr. 1977) 25–28

[9.4.9] Pflüger, A., Zur praktischen Berechnung der axialgedrückten Kreiszylinderschale. Stahlbau **32** 161–165 (1963)

[9.4.10] Sureshwara, B., Lee, L. H. N. and Ariman, T., Inelastic Buckling of Shallow Spherical Shells under External Pressure. Trans. ASME J. Eng. Ind. Series B, **95** 208–214 (1973)

[9.4.11] Zielnica, J., Wyznaczenie obciążenia krytycznego cienkiej powłoki stożkowej w oparciu to theorie plastycznego płynięcia. (Determination of the critical loads of thin conical shells with the aid of the theory of plasticity.) Archiwum Budowy Maszyn **23** 283–299 (1976)

[9.5.1] Bailey, R. W., Creep of Steel under Simple and Compound Stresses and the Use of High Initial Temperature in Steam Power Plants. Trans. Tokyo Sect. Meeting of the World Power Conference Tokyo 1089 (1929)

[9.5.2] Dischinger, F., Untersuchungen über die Knichsicherheit, die elastische Verformung und das Kriechen des Betons bei Bogenbrücken, Bauingenieur **18** 487–520, 539–552, 595–621 (1937)

[9.5.3] Distefano, J. N., Creep Buckling of Slender Columns. Journ. Struct. Divis. (Proc. ASCE) **91** ST3 127–150 (1965)

[9.5.3a] Dulácska, E., The Influence of Creep on the Stability of Shells. Wood, Ferrocement and Plastics in Shell and Spatial Structures. Proc. IASS Symposium. (Ed. P. A. Tupamäki). University of Oulu, Oulu, Finland, June 1980. 87–97

[9.5.4] Findley, W. N., Lai, J. S. and Onaran, K., Creep and Relaxation of Nonlinear Visco-elastic Materials. In: Lauwerier, H. A. and Koiter, W. T., North-Holland Series in Applied Mathematics and Mechanics. North Holland Publ. Comp., Amsterdam–New York, 1976

[9.5.5] Finnie, L. and Heller, W. R., Creep of Engineering Materials. McGraw-Hill. New York–Toronto–London, 1959

[9.5.6] Fleischhaker, W., Zur Beulstabilität von axial belasteten Kreiszylinderschalen aus kriechendem Material. Bautechnik **53** 62–65 (1976)

[9.5.7] Flügge, W., Viscoelasticity. Springer, Berlin–Heidelberg–New York, 1975

[9.5.8] Hoff, N. J., Theory and Experiment in the Creep Buckling of Plates and Shells. IUTAM-Symposium, Cambridge, USA (1974). In: Buckling of Structures (Ed. Budiansky, B.) Springer, Berlin–Heidelberg–New York, 1976

[9.5.9] Hoff, N. J., High Temperature Effects in Aircraft Structures. Pergamon Press, London–New York–Paris–Los Angeles, 1958

[9.5.10] Hoff, N. J., Creep Buckling of Plates and Shells. Proc. 13th Int. Conf. Theor. Appl. Mech. Moscow Univ., 1972. Springer, Berling, 1973

[9.5.11] Huang, N. Ch., Nonlinear Creep Buckling of Some Simple Structures. University of California, San Diego. Report IRPA-66-80, 1960

[9.5.12] Huang, N. Ch., Axisymmetrical Creep Buckling of Clamped Shallow Spherical Shells. Journ. Appl. Mech. **32** 323–330 (1965)

[9.5.13] Hult, J., Creep in Engineering Structures. Blaisdell Publ. Co. Waltham, Mass., 1966

[9.5.14] Jones, N., Creep Buckling of a Complete Spherical Shell. Journ. Appl. Mech. **43** 450–454 (1976)

[9.5.15] Kempner, J., Viscoelastic Buckling. In: Handbook of Engineering Mechanics (Ed. Flüge, W.). McGraw-Hill Book Comp., New York–Toronto–London, 1962

[9.5.16] Kollár, L., A kúszás hatása a szerkezetek kritikus terhére. (The influence of creep on the critical loads of structures.) Mélyépítéstudományi Szemle **18** 472–479 (1968)

[9.5.17] Norton, F. H., Creep of Steel at High Temperatures. McGraw-Hill, New York, p. 67, 1929

[9.5.18] Obrecht, H., Creep Buckling and Postbuckling of Circular Cylindrical Shells under Axial Compression. Int. Journ. Solids Struct. **13** 337–355 (1977)

[9.5.19] Odquist, F. K. G., Mathematical Theory of Creep and Creep Rupture. Clarendon Press, Oxford, 1966

[9.5.20] Vicat, L. T., Note sur l'allongement progressif du fil de fer soumis à diverses tensions. Annales, Ponts et Chaussées, Mémoires et Docum. **7** (1834).

[9.7.1] Dulácska, E., A fa lassú alakváltozásáról. (On the creep of wood.) Magyar Építőipar p. 763, (1967)

[9.7.2] Gillwald, W. and Luthard, H., Beitrag zur Dauerstandfestigkeit von Vollholz- und Holzspanplatten. Holztechnologie **7** 25–29 (1966)

[9.7.3] Graf, O., Beobachtungen über den Einfluss der Grösse der Belastungsfläche auf die Wiederstandsfähigkeit von Bauholz gegen Druckbelastung quer zur Faser. Bauingenieur **2** 498–501 (1921)

[9.7.4] Hintersdorf, G., Tragwerke aus Plasten, Verlag für Bauwesen, Berlin, 1972

[9.7.5] Perkitny, T. and Perkitny, J., Vergleichende Untersuchungen über die Verformungen von Holz-, Span- und Faserplatten bei langdauernder konstanter Biegebelastung. Holztechnologie **7** 265–270 (1966)

[9.7.6] Tennyson, R. C. and Muggeridge, D. B., Buckling of Laminated Anisotropic Imperfect Circular Cylinders under Axial Compression. Journ. Spacecraft & Rockets **10** 143–148 (1973)

[9.8.1] Buchert, K. P., Stress and Buckling Analysis of Cracked Reinforced Concrete Shells Using the Split Rigidity Concept. In: Nonlinear Behaviour of Reinf. Concr. Spatial Structures (IASS-Symposium, 1978, Darsmtadt). Werner, Düsseldorf, 255–266

[9.8.2] C. E. B., Empfehlungen zur Berechnung und Ausführung von Stahlbetonbauwerken. Deutscher Beton-Verein E. V. 1966

[9.8.3] Dulácska, E., Stabilitätsuntersuchung der Schalenkonstruktionen. Large-span Shells (Proc. IASS-Congr. Leningrad, 1966). Tsinis, Moscow, 1968

[9.8.4] Dulácska, E., Die Beulung von Stahlbetonschalen. Acta Techn. Acad. Sci. Hung. **86** 93–115 (1978)

[9.8.5] Dunham, C. W., The Theory and Practice of Reinforced Concrete. McGraw-Hill, New York, 1966

[9.8.6] Gioncu, V., Cercetări experimentale priving stabilitatea cupolelor pe contur pătrat. (Experimental research on the buckling of domes over square ground planes.) Stud. Cerc. Mec. Apl. **32** 641–651 (1973)

[9.8.7] Griggs, H., Buckling of Reinforced Concrete Shells. Journ. Eng. Mech. Divis. (Proc. ASCE) **97** EM3 687–700 (1971)

[9.8.8] Haas, A. M. and van Koten, H., On the Buckling Behaviour of Doubly Curved Shells. RILEM Symposium, Buenos Aires, 1971

[9.8.9] Haas, A. M. and van Koten, H., The Stability of Doubly Curved Thin Shells. RILEM Symposium, Buenos Aires, 1971

[9.8.10] Korda, J. and Móna, J., A vasbeton szerkezetek méreteiben mutatkozó tényleges eltérések és azok számításba vétele. (The actual deviations in the dimensions of reinforced concrete structures and their consideration.) ÉMI-Jelentés, Budapest, 1969

[9.8.11] Müller, F. P. and Weidlich, C., An Experimental Investigation of the Stability of Shallow Spherical Shells of Reinforced Concrete Subjected to Uniformly Distributed Load. In: Nonlinear Behaviour of Reinforced Concr. Spatial Structures (IASS Symposium, 1978, Darmstadt). Werner, Düsseldorf, 319–328, 1978

[9.8.12] Riel, A. C., Beranek, W. J. and Bouma, A. L., Tests on Shell Roof Models of Reinforced Mortar. Proc. of the Second Symposium on Concrete Shell Roof Construction (July, 1957, Oslo), Teknisk Ukeblad, Oslo

[9.8.13] Roš, M., Die materialtechnischen Grundlagen und Probleme des Eisenbetons im Hinblick auf die zukünftige Gestaltung der Stahlbeton-Bauweise. EMPA-Bericht No. 162 (1950)

[9.8.14] Szepesszentgyörgyi, O., ÉMI Tudományos Beszámoló az állandó terhekre vonatkozó ISO előírás kidolgozása c. témáról. (Scientific report of the Institute for Quality Control of the Building Industry on the subject: Elaboration of the ISO-Regulations on Dead Loads). Budapest, 1966

[9.8.14a] Trost, H., Auswirkungen des Superpositionsprinzips auf Kriech- und Relaxationsprobleme bei Beton und Spannbeton. Beton- und Stahlbetonbau **62** 230–238, 261–269 (1967)

[9.8.15] Vandepitte, D., Rathé, J. and Weymeis, G., Experimetntal Investigation into the Buckling and Creep Buckling of Shallow Spherical Caps Subjected to Uniform Radial Pressure. Proc. IASS World Congress, Madrid, **1**, 1.1–1.15, 1979

[9.8.16] Zerna, W., Spannungs-Dehnungs-Beziehung für Beton bei einachsiger Beanspruchung. In: Aus Theorie und Praxis des Stahlbetonbaues. W. Ernst und Sohn, Berlin–München, 1969

[9.9.1] Hohenemser, K. and Prager, W., Dynamik der Stabwerke. Springer, Berlin, 1933

[9.9.2] Kollár, L., On the Behaviour of Shells in the Postbuckling Range. IASS Bulletin No. **39** (Sept. 1969) 41–51

[9.9.3] Roorda, J., Some Thoughts on the Southwell Plot. Journ. Eng. Mech. Divis. (Proc. ASCE) **93** EM6 (1967) 37–48.

[9.9.4] Spencer, H. H. and Walker, A. C., Critique of Southwell Plots with Proposals for Alternative Methods. Experimental Mechanics **15** 303–310 (1975)

[9.10.1] Born, J., Schalen, Faltwerke, Rippenkuppeln und Hängedächer. Werner, Düsseldorf, 1962

[9.10.2] Guyon, V. L. and Jeanbloch, T., Salle des sports de Salonique. Large-span Shells (Proc. IASS-Congr. Leningrad, 1966). Tsinis, Moscow, 1968

[9.10.3] Joedicke, J., Schalenbau. Dokumente der modernen Architektur. Krämer, Stuttgart, 1962

[9.10.4] Krstić, M., Die Verwendung von Schalen aus vorgespannten Beton an der neuen Messe in Belgrad. Bauingenieur **33** 299–301 (1958)

[9.10.5] Sanchez-Arcas, M., Form und Bauweise der Schalen. Verlag für Bauwesen, Berlin, 1961

Subject Index